



HAL
open science

Current controlled negative differential resistance in niobium dioxide

Ali Fakih

► **To cite this version:**

Ali Fakih. Current controlled negative differential resistance in niobium dioxide. Materials Science [cond-mat.mtrl-sci]. Sorbonne Université, 2019. English. NNT : 2019SORUS099 . tel-03371422

HAL Id: tel-03371422

<https://theses.hal.science/tel-03371422v1>

Submitted on 8 Oct 2021

HAL is a multi-disciplinary open access archive for the deposit and dissemination of scientific research documents, whether they are published or not. The documents may come from teaching and research institutions in France or abroad, or from public or private research centers.

L'archive ouverte pluridisciplinaire **HAL**, est destinée au dépôt et à la diffusion de documents scientifiques de niveau recherche, publiés ou non, émanant des établissements d'enseignement et de recherche français ou étrangers, des laboratoires publics ou privés.

Sorbonne Université

École doctorale 397 - Physique et Chimie des Matériaux

Institut de minéralogie, de physique des matériaux et de cosmochimie

Current Controlled Negative Differential Resistance in Niobium Dioxide

Par Ali FAKIH

Thèse de doctorat de Physique

Dirigée par Abhay SHUKLA

Présentée et soutenue publiquement le 05/11/2019

Devant un jury composé de :

Mme. GUILLOUX-VIRY Maryline	Professeure	Rapportrice
M. JANOD Etienne	Directeur de Recherche CNRS	Rapporteur
M. GARREAU Yves	Professeur	Examineur
M. MARANGOLO Massimiliano	Professeur	Examineur
M. SHUKLA Abhay	Professeur	Directeur de thèse
M. BISCARAS Johan	Maîtres de conférences	Co-encadrant, invité

“A body will not become weak where the intention is strong.”

Ja'far Al-Sadiq (A.S)

Pointing his finger to a huge stone he said: “Abu Shakir, do you see the stone which is in the foot of that portico? To you it seems lifeless and motionless because you do not see the brisk motion which is inside the stone. Again, it is lack of knowledge or your ignorance which would not let you believe that there is motion inside the stone. The time will come when the learned people would see the motion which is in the stone.”

Ja'far Al-Sadiq (A.S)
more than 1200 years ago...

Acknowledgement



For all the hands which I have seen and which I have not that contributed to the success of this work...

My deepest gratitude goes to my parents who are like the sun in the sky, my mother provides me with warmth and my father supports me with light. Without their care and love I wouldn't be here.

I would like to thank every person who contributed to this dissertation. Starting with my adviser Professor Abhay Shukla who has always been positive during the work. Even in the hard times, he was still enthusiastic, gave us hope and invigorated our spirits. His energetic character gave us a lot of boosts in our work. Next comes my other adviser Assistant Professor Johan Biscaras who has always been a helpful hand in conducting experiments and teaching us the different techniques. He did not bother to answer questions, explain theories, etc... I have really gained a lot of experience from my advisers in managing a scientific project, like how to plan, be systematic, write a scientific article, prepare a presentation... I would also like to thank the team members that were present during my thesis whom I have enjoyed time being with them (discussions, talking of different subjects and topics...) starting from oldest colleague: Edoardo Sterpetti, Wenyi Wu, Fang Wang, Sagar Gupta, Amit Pawbake, Hugo Kowalczyk and Onkar Shinde who arrived last but comes first on my colleague list. Onkar was a special colleague and a

good lunch partner. He has also contributed in this work in one way or another by helping in performing the experiments and giving tips based on his previous experience in electronics.

Stepping out of the group, I would also like to thank other colleagues whom I was in contact with for different experiments. Loic Becerra from INSP who taught me how to use the sputtering machine, Hicham Moutaabbid who taught me how to use the furnaces at the IMPMC lab. Also, thanks to Dr. Ricardo Lobo for pilot experiments with infrared spectroscopy. A special thanks to Dr. Jean-Jacques Ganem who has given me access to their high-vacuum furnace at INSP and teaching me how to use it, in addition to the nice discussions we had. Also I would like to thank our XRD experts Benoit Baptiste and Ludovic Delbes. Ludovic was also a very special colleague. I also thank Seyed Mohammad Al Bahreini, who was a post doc. at IMPMC, for his wise advice and for the rich discussions we had together.

In addition to the academic staff, there are two other categories whom I had friends among, and they have sometimes made my day... From the cleaning staff I would like to thank Kala and Tiba who were always smiling. In addition, thanks the security guards like Lyes, Khaled and Mahdi who were sometimes there to have some words when I stayed for a late hour at night in the university.

Hoping I did not forget anyone in campus. Outside the university there are a lot of people to thank, but to keep it short I will say that I thank all my friends and brothers who were there to make life in a foreign country beautiful and colorful. Seyed Sajad Zafranchilar would be the star of those friends along with Seyed Baqir. There is also M. Ali Zreik who has taken good care of me during my stay in Paris to a point that I am embarrassed by his kindness.

Finally, over the seas, back in Lebanon, rests a patient fiance whom I thank her for her love and three years of bearing the distances apart... And again, I thank my family, my brothers Naim and Imad for being supportive, mother and father.

Not to forget of course, Labex MATISSE who funded this project, a special thanks to them as well.

“This work was supported by French state funds managed by the ANR within the Investissements d’Avenir programme under reference ANR-11-IDEX-0004-02, and more specifically within the framework of the Cluster of Excellence MATISSE led by Sorbonne Universités”.

Contents

1	Introduction and Background	1
1.1	State of the Art	1
1.2	Nano-scale Materials: Correlated Electron Systems	2
1.3	Niobium and Niobium Oxides	3
1.4	Niobium Dioxide NbO₂	7
1.4.1	Physical Structure	7
1.4.2	Electronic Band Structure and The Density of States	7
1.5	Metal-Insulator Transition MIT	11
1.5.1	Mott Transition	11
1.5.2	Anderson Localization	13
1.5.3	Peierls Transition	14
1.6	Doping of 2D Materials	15
1.7	Conduction Mechanism: Defect Contribution	17
1.8	Negative Differential Resistance	19
1.8.1	Types of Negative Differential Resistance	20
1.9	Conduction Mechanism in NbO₂ Under Current Application	21
1.9.1	Poole-Frenkel Conduction Mechanism	21
2	Experiments	24
2.1	Sample Fabrication Techniques	24
2.1.1	Substrate Preparation	25
2.1.2	Radio Frequency (RF)-Magnetron Sputtering	26
2.1.3	NbO₂ from Nb films by oxidation	28
2.1.4	Crystalline NbO₂ From Sputtered Amorphous NbO₂ films	30
2.2	Characterization Techniques	31
2.2.1	Raman Spectroscopy	31
2.2.2	Atomic Force Microscopy AFM	35
2.2.3	X-Ray Diffraction	37
2.3	Device Fabrication and Measurement Techniques	41
2.3.1	The van der Pauw Method	41
2.3.2	Sample Shaping	43
2.3.3	Gold Contact Deposition	46
2.3.4	Measurement Setup	47
2.3.5	Glass Structure	47
2.3.6	Space Charge Doping Technique SCD	49

3	NbO₂ Thin Film Synthesis	50
3.1	Introduction	50
3.2	Nb Thin Film Preparation	50
3.3	Nb Oxidation by Slow Annealing	52
3.4	Nb Oxidation by Flash Annealing	56
3.4.1	Nb films at Slower Rate	56
3.5	Summary on Ambient Nb Thin Film Oxidation	60
3.6	NbO₂ Thin Films by RF-Magnetron Sputtering	61
3.7	Sputtering Experiments	65
3.7.1	Effect of Target-Substrate Distance $H_{\text{substrate}}^{\text{target}}$	65
3.7.2	Effect of Substrate Temperature T_{sub}	68
3.7.3	Effect of Process Gas Pressure P_{Ar}	70
3.8	Post Annealing Process Optimization	75
3.8.1	Effect of Post Annealing Time	75
3.8.2	Effect of Post annealing Temperature	77
3.9	Electronic Properties and Doping NbO₂ Thin Films	82
3.9.1	Space Charge Doping of NbO₂ Films	84
3.10	High Temperature Raman Measurements	86
3.11	Conclusion	88
4	Negative Differential Resistance in NbO₂: Origins	89
4.1	Introduction	89
4.2	Studies Under Electric Field	90
4.2.1	Vertical Measurements and Sheet Resistance	91
4.2.2	Discussion and Conclusion Concerning the Transition by Applying E-Field	95
4.3	CC-NDR in NbO₂	96
4.4	NDR in crystalline and amorphous NbO₂	98
4.4.1	Hysteresis in the measured NDR	98
4.4.2	Origin of Hysteresis	102
4.4.3	Hysteresis and Thermal Equilibrium	102
4.4.4	Heat Dissipation and Current Distribution in Sample and Substrate	104
4.4.5	NDR and Sample Temperature	106
4.5	NDR and Structural Changes	107
4.5.1	Stable Current Application	107
4.5.2	Pulsed Current Application	110
4.6	Numerical Modeling of CC-NDR in NbO₂	113
4.7	Conclusion	116
5	Conclusion	117
	Appendices	120
A	Raman Spectra on Target Before and After Unsealing	121

List of Figures

1.1	(a) Voltage and (b) current controlled I-V curves displaying the threshold switching and the negative differential resistance characteristics respectively [8].	1
1.2	The Nb-O phase diagram shows the existence of four thermodynamically stable phases of niobium–oxygen system (Nb, NbO, NbO ₂ and Nb ₂ O ₅) with very narrow single-phase fields and negligible deviations from the exact stoichiometry [42]. “Reprinted from Progress in Material Science, 80, C. Nico, T. Monteiro, M.P.F. Graca, Niobium oxides and niobates physical properties: Review and prospects, 3, Copyright (2016), with permission from Elsevier.”	4
1.3	The niobium-oxygen system: main oxides and some of their structural and electrical properties (conductivity σ given at $\sim 0^\circ - 25^\circ\text{C}$) as a function of the formal Nb-oxidation state [62].	6
1.4	(a) The high temperature rutile structure of NbO ₂ (metallic NbO ₂). (b) The tetragonal distorted rutile structure of NbO ₂ at low temperature (semiconducting NbO ₂) [70].	7
1.5	When ligands approach a metal cation in a spherical form (symmetric from all directions), the energy of all five d orbitals increases due to electrostatic repulsion. However, when the ligands approach along the vertices of an octahedron, the d orbitals split into two groups of different energies: the d_{z^2} and the $d_{x^2-y^2}$ orbitals which have respectively higher energies, and the d_{xy} , d_{yz} and d_{xz} which have respectively lower energies. Image ref. [75].	8
1.6	The band structure diagram of NbO ₂ in the vicinity of the Fermi level in both crystalline states (a) rutile and (b) distorted rutile (tetragonal) phases [74].	9
1.7	The total and orbital-resolved density of states of NbO ₂ , as displayed by O’Hara et al., in the tetragonal distorted rutile phase. [28]. “Reproduced from Journal of Applied Physics, 116, A. O’Hara, T. Nunley, A. Posadas, S. Zollner, A. Demkov, Electronic and optical properties of NbO ₂ , 213705, Copyright (2014), with the permission of AIP publishing.”	10
1.8	Band diagram illustrating the Mott transition.	12
1.9	In the absence of disorder (a) the chain of ions can be considered as a series of potential wells where the electron can tunnel through these wells without alternating the wave function. However, when impurities are strongly present (b), the electron experiences different potentials at different sites and the wave function becomes localized. [84].	13

1.10	Lattice distortion due to Nb-Nb dimerization. After dimirization, the lattice constant is doubled.	14
1.11	Impact of lattice distortion on the Brillouin Zone (a) before distortion (b) after distortion	15
1.12	A typical structure of ionic liquid gated field effect transistor.	16
1.13	A Schematic of the band structure with localized states (shaded) and the mobility edges E_V or E_C	18
1.14	(a) N-type negative differential resistance (VC-NDR). (b) S-type negative differential resistance (CC-NDR).	21
2.1	A photo of the sputtering system (a) an electronic closet for controlling target-substrate distance, substrate temperature and power (b) power source (c) deposition chamber with a valve for controlling Ar flow.	25
2.2	An AFM image for the soda lime glass used shows that it has a smooth surface (rms = 0.207 nm).	25
2.3	The RF-Magnetron Sputtering process. The power applied allows the formation of plasma (Ar^+ ions and free electrons) in the chamber containing Ar gas. Ar^+ ions in the plasma bombard the target surface striking out Nb atoms from the target. These atoms are collected on surfaces in their paths and eventually on the glass substrates.	27
2.4	(a) First adsorption of oxygen molecules on the surface of the metal occurs. O_2 molecules are physisorbed at the surface by Van der Waals forces. Then chemisorption represented by metal-oxygen bonds takes place. An oxide layer is formed and further oxidation continues in a direction perpendicular to the surface. The oxide growth proceeds depending on the species (b) at the surface of the oxide layer, if the metal ions are diffusing or (c) at the metal-oxide interface if the oxygen atoms are diffusing.	29
2.5	Schematic of the sample holder that was put in the furnace for monitoring the sheet resistance while the temperature was systematically increased.	30
2.6	A photo of the furnace used to crystallize amorphous NbO_2 samples into crystalline NbO_2	31
2.7	In a Rayleigh scattering, the molecule is excited to a virtual state due to the photon-phonon interaction, and returns back to its original state emitting a photon with the same energy. In Raman scattering, the photon-phonon interaction excites the molecule into a virtual state, and the molecule returns either to a higher vibrational state (Stokes scattering) emitting a lower energy photon or to a lower vibrational state (Anti-Stokes scattering) emitting a photon with a higher energy.	32
2.8	Photograph of the HORIBA Raman spectrometer present in our lab.	34
2.9	The Raman apparatus configuration.	34
2.10	AFM apparatus: (a) Schematic of the AC operating mode of the AFM. The tip is made to oscillate by a function generator through a piezoelectric. A laser is emitted at the back of the oscillating cantilever. Deflections of the laser beam are recorder, and an AFM image is generated. (b) A magnified image of the tip hovering over the sample during the scan. Depending on the cantilever scanning mode, attractive or repulsive forces are taken into account.	36

2.11	Different operating modes of the cantilever with respect to the van der Waal Forces between the tip and the sample. In contact AFM, as the tip-sample distance is relatively small, the significant forces are the repulsive forces. In non contact mode, as the tip-sample distance is relatively large, the significant forces are the attractive forces. In tapping mode, both attractive and repulsive forces are taken into account as the tip oscillates along the z-axis.	37
2.12	Photo of the x-ray diffractometer used to perform XRD measurements.	38
2.13	Illustration of Bragg's law in the real space. X-rays reaching the sample will diffract only when the path difference between the reflected rays leads to a constructive interference, i.e $n\lambda = 2d_{hkl}\sin\theta$	38
2.14	(a) Bragg Brentano geometric configuration: both the x-ray source and the detector move simultaneously at an angle θ w.r.t the sample surface. (b) Grazing Incidence configuration : The source is fixed at a very small angle α w.r.t the sample while the detector rotates and collects diffracted radiations from the film.	39
2.15	A typical x-ray diffraction peak. Grain size of the relevant peak can be estimated from the FWHM of the peak, and the inter planar distances can be derived from the peak's position 2θ	40
2.16	The van der Pauw geometry. (a) Current is injected and collected along contacts 1 and 2, meanwhile the voltage V_{34} is measured. Then R_V is calculated. (b) The current is injected and collected along contacts 2 and 3 and the voltage V_{41} is measured. Then R_H is calculated. These two resistances are then substituted in the sheet resistance equation for obtaining the sheet resistance of the film.	41
2.17	Graph representing the relation between the correction factor f and the ration r of vertical and horizontal resistances [162].	43
2.18	Sample shaping obtained by procedure involving PMMA.	44
2.19	(a) The NbO_2 film of the glass substrate was scratched, then gold was deposited in van der Pauw geometry on top of the film. The dimensions of the mask are also shown. (b) A sample after such a shaping method was done on it.	44
2.20	Gold contact geometry on Si, SiO_2 substrates. Thermal resistant scotch tape was used to mask the films.	45
2.21	Photo of the evaporator used for gold contact depositions.	46
2.22	A schematic showing the measurement apparatus. The sample is mounted on a cryostat. A heater allows the increase in temperature, while $He_{(l)}$ is used to drop the temperature.	47
2.23	Glass atomic structure. Firm silicon oxide bonds compose the building block of glass, and <i>free</i> unbridged sodium ions are randomly distributed over the structure. The non-bridging oxygen form the anionic counterparts of Na and Ca cations.	48
2.24	Testing the mobility of ions through the glass while applying a voltage $V_G = 10V$ and increasing the temperature to 400K. The current starts to increase at ~ 340 K which defines the thermal activation energy for ionic mobility in soda-lime glass.	48

2.25	The space charge doping technique. The left side of the figure shows the n-doping of the film deposited on glass as a consequence of positive voltage application at the gate. The right side shows the p-doping process in which a negative voltage is applied at the gate. In the middle, the Fermi level shifts towards the conduction band with n-doping, or towards the valence band with p-doping.	49
3.1	X-ray diffraction patterns for a 47 nm thin film on (a) Soda lime glass substrate (b) Borofloat glass substrate with the relative Gaussian peak fitting of each (red color). (XRD was performed using $\text{Cu K}\alpha_1$ radiation).	52
3.2	AFM image of a niobium thin film on soda-lime glass substrate. The film is polycrystalline film of grain size in the order of few tens of nm.	52
3.3	Graph illustrating the phase transitions of Nb we expected to see as a function of time when the temperature of the system was increased and held at 300°C to begin with.	53
3.4	Graphs showing the oxidation process of Nb thin films on 2 soda-lime (a) SL1 and (b) SL2 and 2 borofloat (c) BF1 and (d) BF2 glass substrates.	54
3.5	Macroscopic photos of an Nb film before and after oxidation.	54
3.6	Optical microscopic images for SL2 and BF1 samples after their oxidation. The inhomogeneity can be clearly seen.	55
3.7	X-ray diffraction patterns for the samples oxidized earlier (a) SL1 (b) SL2, (c) BF1 and (d) BF2. No peaks appear in any of the diffractograms. (XRD was performed using $\text{Cu K}\alpha_1$ radiation).	55
3.8	The variation of the film thickness as a function of deposition time at two different temperatures: RT and 450°C . The black and the red lines are the linear fittings of the RT and 450°C depositions respectively.	57
3.9	(a) X-ray diffractograms of Nb thin films at different substrate temperatures. (b) The variation of the lattice constant of Nb unit cell as a function of substrate temperature. (XRD was performed using $\text{Cu K}\alpha_1$ radiation).	58
3.10	(a), (b) and (c) Optical images of some samples oxidized at different times and different temperatures. (d) Raman spectra taken at different regions in film (b).	58
3.11	The Raman Spectra of a 125 nm film with an <i>exaggerated</i> illustration of the film composition after (a) 2 min oxidation, (b) an additional 1.5 min oxidation, and (c) and extra 1 min oxidation.	59
3.12	The x-ray diffraction pattern of the 125 nm film after oxidation. (XRD was performed using $\text{Cu K}\alpha_1$ radiation)	59
3.13	A diagram showing the previous methods performed in attempt to oxidize Nb thin films into NbO_2	60
3.14	A photo of the purchased target. The dark blue-grey color is a sign of stoichiometric NbO_2 phase.	61
3.15	Raman spectrum of the purchased NbO_2 target while sealed in its vacuum protection sac.	62
3.16	X-ray diffraction pattern of the purchased NbO_2 target taken in ambient conditions. The green curves represent Gaussian fittings added up to fit an asymmetric diffraction peak. (XRD was performed using $\text{Co K}\alpha_1$ radiation).	64

3.17	Graph showing the sheet resistance R_S and the thickness as a function of the target-substrate distance.	65
3.18	Raman spectra of the as-deposited niobium oxide films sputtered at different target-substrate distances.	67
3.19	Optical photos of the samples before and after annealing at different target-substrate distances (a) 6.5 cm (b) 7.5 cm (c) 8.5 cm and (d) 9 cm.	67
3.20	Raman spectra of the post annealed niobium oxide films originally sputtered at different target-substrate distances.	68
3.21	Graph showing the sheet resistance R_S and the thickness as a function of the substrate temperature T_S	69
3.22	Raman spectra of the as-deposited niobium oxide films sputtered at different substrate temperatures.	69
3.23	Graph showing the sheet resistance R_S and the thickness as a function of the substrate temperature P_{Ar}	70
3.24	Raman spectra of the as-deposited niobium oxide films sputtered at different process gas pressure P_{Ar}	71
3.25	Optical photos of the samples before and after annealing at different argon pressures (a) 0.2 mbar and (b) 0.5 mbar.	72
3.26	Raman spectra of the post annealed niobium oxide films originally sputtered at different argon pressure.	72
3.27	(a) Optical photo taken for a totally crystalline NbO_2 film taken from the opposite side of the film (through the glass substrate). (b) The Raman spectra taken of the trenches and islands taken from the opposite side of the sample.	73
3.28	(a) 10 μm AFM image of the NbO_2 film showing the trench like structure and nucleated islands. (b) 200 nm AFM image showing the grains size in the film.	73
3.29	X-ray diffraction pattern for the NbO_2 film obtained after annealing for 2 hrs at 600°C. Measurement was taken in the Bragg Brentano configuration. (XRD was performed using $Co K\alpha_1$ radiation).	74
3.30	Optical photos of NbO_2 films annealed at 600°C at different times (a) 2 hrs (b) 4 hrs and (c) 6 hrs.	75
3.31	Raman spectra of two NbO_2 films one annealed at 600° for 2 hrs and the other for 4 hrs.	76
3.32	Optical photos of NbO_2 films annealed for 4 hrs at (a) 550°C (b) 600°C and (c) 800°C.	77
3.33	(a) Raman spectra of three NbO_2 films on Si substrate annealed for 4 hrs at 550°C, 600°C and 800°C. (b) Raman spectrum of the shallow non-crystalline region in figure 3.32 (a).	78
3.34	Raman spectra of NbO_2 films on different substrates after annealing. In particular Raman spectra of the Si and Si/SiO ₂ films match nanostructured NbO_2 films of reference [172]. The green curves represent Gaussian fittings added up to fit an asymmetric peak.	79

3.35	X-ray diffractograms of NbO ₂ films on different substrates: glass, Si and SiO ₂ before and after annealing them. Figures (a) and (b) show the results of experiments done in the Bragg-Brentano configuration, while figures (c) and (d) show the results of experiments done in the grazing incidence geometry. The green curves represent Gaussian fittings added up to fit an asymmetric diffraction peak. (XRD was performed using Co K α_1 radiation).	81
3.36	The resistivity of an amorphous NbO ₂ film and a crystalline NbO ₂ film deposited on a glass substrate between 300 K and 400 K.	82
3.37	Arrhenius plot of film conductivity from 300 K to 400 K.	83
3.38	N-doping an NbO ₂ film at 400 K using Space Charge Doping Technique.	85
3.39	Photo of the linkam where the sample was kept during the measurement at RT (left) and at 1000°C (right).	86
3.40	(a) Optical photos showing the evolution of the NbO ₂ crystalline film. After 700°C the crystallinity disappears. (b) Raman spectra of the NbO ₂ film. We notice that the NbO ₂ peaks start vanishing at 700°C. After which only the Si peaks appear.	87
3.41	A graph showing the variation of temperature as a function of Si peak position.	88
4.1	(a) A schematic drawing of the device used by Kumar et al. [24]. (b) A schematic of the device used in our work (left) along with its relative photo (right).	91
4.2	I-V curves of the central contact C to the gate contact (black) and of a peripheral contact of relatively smaller area to the gate contact (blue) taken at stabilized temperature of 320 K. Both curves show diode-like characteristics; however, the threshold voltage V_{th1} across the peripheral contact is higher than that across the central one.	92
4.3	I-V curves across the central-gate contacts V_{CG} taken at different stabilized temperatures. The threshold voltage V_{th1} shifts to the right (lower voltages in absolute value), and the hysteresis size becomes smaller as the temperature increases.	92
4.4	Graph showing the variation of R_S (left axis) and the current I_{GC} (right axis) as a function of the voltage V_{GC} . As V increases to 94 V (V_{th1}), the current shows a jump in the curve, while R_S shows a steep drop to a less resistive state. Then as V decreases to 36 V (V_{th2}), the current/ R_S display a sharp drop/jump respectively.	93
4.5	(a) I-V and (b) R_S curves of measurements taken across the gate-central contact GC at different compliances. The threshold voltages vary as the compliance varies for I-V and R_S -V curves.	94
4.6	(a) I-V curve showing that the hysteresis obtained while sweeping voltage was not a real hysteresis. Testing the voltage at the sample by adding a secondary keithley showed that the actual voltage at the sample after compliance is reached is not the same displayed on the primary keithley. (b) The drop in voltage remains constant at the threshold value V_{th2} until the primary keithley's sweep hits the same value and then both voltages continue to decrease in parallel.	95

4.7	V(I) curves between central-peripheral TC and peripheral-peripheral TZ contacts. The V(I) curves show CC-NDR resistance in NbO ₂ with a hysteresis. Notice the dependence of the voltage on the path area of the current. Contacts which provide narrower current path (TZ) have higher current density and eventually higher voltages.	97
4.8	Gold contacts deposited on crystalline and amorphous NbO ₂ samples.	98
4.9	V(I) curves for crystalline (Si ₃₁ ¹⁰⁰) and amorphous (Si ₃₂ ¹⁰⁰) NbO ₂ . Both curves show negative differential resistance and also exhibit a hysteresis. The blue curve lies above the black curve indicating that the resistivity of crystalline NbO ₂ is higher than that of amorphous NbO ₂	99
4.10	Graph showing the different parameters I(mA), V(V), R(kΩ) and P(Watts) as a function of time. The power represents the heat dissipated and eventually the change temperature.	101
4.11	V(I) curves obtained at different step size durations at two temperatures (a) 300 K and (b) 320 K.	102
4.12	V(I) curve results obtained during the thermal equilibrium test at two different temperatures (a) 320 K and (b) 400 K. The different colors in each figure represent different current values at which pauses were made in both forward and backward sweeps. The peaks and troughs at each current represent the stabilization voltage. The inset in panel (a) shows the relaxation of the voltage during the pause at 5 mA during the forward sweep (black) and the backward sweep (red).	103
4.13	(a) Schematic of the cross section of the NbO ₂ device with a conductive Si substrate. (b) Calculated current density distribution in the NbO ₂ and Si when voltage is applied between the contacts for the geometry defined in (a). The current distribution indicates that most of the current if not all the current passes vertically downwards from the NbO ₂ film to the Si substrate and then vertically upwards from the Si substrate to the NbO ₂ film. (c) and (d) are schematics that show the differences between the current flow direction in the NbO ₂ device on Si and glass substrate respectively. (e) and (f) show the circuit representation of these two devices. (g) V(I) curves showing on NbO ₂ devices with Si and glass substrate. In the former a large current is needed for the NDR to occur while in the sample with glass substrate much less current is needed for NDR to happen. The difference in current is due to the different effective cross-sectional areas of the two geometries.	105
4.14	(a) Optical photos of the contacts made for the studies of V(I) curves on the glass substrate. (b) V(I) curves obtained at different contact separation. Shorter distance between contacts induced lower maximum voltages in the V(I) curves.	106
4.15	Effect of temperature on the V(I) curves of crystalline and amorphous NbO ₂ films. For both samples as the temperature increases the hysteresis becomes less and the curves tend to flatten.	107
4.16	Raman apparatus setup used to make Raman spectroscopy on samples while taking V(I) measurements.	108

4.17	Raman spectroscopy at different current values on (a) Si_{31}^{100} (b) Si_{32}^{100} . Both films did not show any structural change during the transport process. However, all peaks shift to lower energies as the temperatures increases due to heat dissipation.	109
4.18	The voltage and the temperature variation as a function of current in both (a) crystalline and (b) amorphous samples. The temperature were calculated by studying the Si Raman peak shifts as described in section 3.10.	110
4.19	(a) and (b) show an optical image of sample Si_{31}^{100} before and after pulsing respectively. (c) Shows the Raman spectra before pulsing and after applying 50 pulses of 100 mA. No noticeable change can be remarked. . .	111
4.20	(a) and (b) show an optical image of sample Si_{32}^{100} . After pulsing, a track can be seen along the direction of the pulse. (c) Raman spectra of different regions on the sample, it is noticed that the more the pulses, the darker the region, the better the crystallinity and the more intense Raman signal. . .	112
4.21	V(I) curves of sample Si_{32}^{100} before and after 10 pulses. After pulsing, the V(I) curve shifts upwards due to the higher resistivity of the crystalline NbO_2 compared to that of amorphous.	112
4.22	(a) Model of the variation of temperature as a function of current using Newton's law of cooling in the static limit. (b) Curves of the different models used to fit the experimental data of V(I) curves.	114
A.1	(a) Raman spectrum before unsealing the target. (b), (c) and (d) Successive Raman spectra taken after unsealing the target.	121

List of Tables

1.1	Niobium oxide crystal phases [42]. The main oxides of niobium are shown as well as the different crystalline polymorphs. “Reprinted from Progress in Material Science, 80, C. Nico, T. Monteiro, M.P.F. Graca, Niobium oxides and niobates physical properties: Review and prospects, 14, Copyright (2016), with permission from Elsevier.”	5
2.1	Niobium oxides resistivities at 300°C and the respective sheet resistance of each oxide for an 80 nm sample.	30
3.1	Parameters used to obtain thin Nb films of thickness ~ 47 nm.	51
3.2	Parameters used to achieve a relatively lower deposition rate $R = 6\text{nm}/\text{min}$ of Nb thin films.	56
3.3	Sputtering parameters for testing the effect of target-substrate distance on the film quality.	65
3.4	Sputtering parameters for testing the effect of substrate temperature on the film quality.	68
3.5	Sputtering parameters for testing the effect of Ar pressure on the film quality.	70
3.6	Table showing the indices of plane directions with the corresponding XRD peak positions 2θ of thin NbO_2 films deposited on the three substrates: glass, Si, and SiO_2 . β and L are the peak’s full width at half maximum and the grain size respectively. The asterisk sign corresponds to Nb_2O_5 peaks.	80
4.1	Sputtering parameters of sample Si_{36}^{100} used in the studies to test the effect of electric field on the NbO_2 transition.	90
4.2	The different components of critical points on the hysteresis of curves of figure 4.9.	100
4.3	The time required for the voltage to stabilize while the measurement was paused at specific current values in a sweep from 0 to 100 mA (at 320 K).	104
4.4	List of parameters used in the conduction models for fitting the V(I) curves. *The fitting parameter σ_0 for Poole-Frenkel model with $a=2$ is multiplied by a factor of $8/5$ [15] so it becomes 19360.	115
4.5	Effective thermal resistance of the different models used to fit our measured data.	115

Abstract

English Version

Niobium dioxide (NbO_2) has been recently gaining a lot of interest in the fields of solid state physics and technological nano-devices. On one hand, NbO_2 undergoes a structural distortion accompanied by an electronic phase transition where the material changes from an insulating state at room temperature into a metallic state at temperatures above ~ 1080 K. On the other hand, NbO_2 exhibits a negative differential resistance phase under the application of electric current, a phenomenon known as current-controlled negative differential resistance CC-NDR. These two characteristics in NbO_2 promote it to be good candidate to develop many functional devices used for variety of applications such as electric switching and memory devices. However, despite the potentialities of NbO_2 , the understanding of this material is still incomplete as literature reporting many research work on NbO_2 show contradictory or inconsistent information. One possible reason of this lack of consistency could emerge from the difficulty in the film fabrication of pure phase NbO_2 and the different means in synthesizing them.

In this thesis, we have fabricated thin films of NbO_2 by RF-magnetron sputtering technique on amorphous and crystalline substrates (glass and Si). The deposited films were always amorphous, and annealing treatment of the as-deposited films was necessary to achieve crystallinity. Annealing tests revealed that increasing both the annealing duration and the annealing temperature gives rise to better crystalline films. Optimized amorphous NbO_2 films had a resistivity $\rho_{\text{amo}} \sim 5 \Omega \text{ cm}$ while the crystalline films had a $\rho_{\text{cry}} \sim 50 \Omega \text{ cm}$ both which are less than the bulk crystalline NbO_2 $\rho_{\text{bulk}} \sim 10^4 \Omega \text{ cm}$. Upon performing electronic studies on NbO_2 , we witnessed CC-NDR with a hysteresis in the $V(I)$ curves. We showed that hysteresis in CC-NDR is due to temperature inhomogeneity. Simultaneous electronic transport and Raman measurements show that CC-NDR is not associated to a phase transition (the phase is always insulating). Moreover, we showed that there is a similar temperature driven change in conductivity in both the amorphous and the crystalline samples, however, the amorphous sample is a better electronic and thermal conductor. Finally, we proved that the CC-NDR may be simply explained by the creation of carriers by temperature in a semiconductor, without the need for invoking more complicated transport mechanisms.

Résumé

La commutation à seuil est un phénomène de commutation résistive volatile qui a été découvert depuis les années 1960. Il a été observé dans une grande variété d'oxydes de métaux de transition; par exemple: VO_2 , Ti_2O_3 , Fe_3O_4 , NbO_2 etc. Lors d'un balayage de tension, le dispositif commute entre deux phases avec une différence de conductivité remarquable: un état isolant (OFF) et un état passant (ON), mais une fois la tension supprimée, le dispositif revient à son état isolant d'origine, état OFF. Cette commutation ON-OFF est souvent accompagnée d'une hystérèse, l'activation (OFF à ON) arrivant à une tension appelée "tension de seuil" et la désactivation à une tension inférieure appelée "tension de maintien". Dans certains matériaux comme le dioxyde de vanadium VO_2 , de tels changements s'accompagnent d'une transition de phase entre deux structures cristallines différentes, dans d'autres comme le dioxyde de niobium, la situation est moins claire. Dans cette thèse, nous analyserons les aspects liés aux comportements contrôlés par le courant et la température et étudierons les mécanismes physiques impliqués dans la commutation à seuil observée dans NbO_2 .

Le phénomène de résistance différentielle négative contrôlée par le courant (CC-NDR) a été observé dans plusieurs matériaux à différentes températures et son origine est débattue. Par exemple, une conduction non linéaire a été observée dans les caractéristiques tension-courant $V(I)$ des manganites $\text{Pr}_{1-x}\text{Ca}_x\text{MnO}_3$ présentant un ordre de charge et un ordre antiferromagnétique. Selon les études, plusieurs mécanismes ont été invoqués, comme la création de filaments métalliques avec un ordre ferromagnétique, ou un effet de chauffage par effet Joule. Par ailleurs, un modèle analytique de la caractéristique tension-courant $V(I)$ basés sur la loi d'Ohm et la loi de la chaleur de Newton a été établi pour expliquer le CC-NDR dans des dispositifs de type memristors à base de TiO_2 , dans lesquels l'effet Joule semble également à l'origine de la CC-NDR. Ce mécanisme a aussi été invoqué pour expliquer la CC-NDR dans le matériau SmB_6 (isolant de type Kondo).

Le dioxyde de niobium (NbO_2) a récemment suscité un vif intérêt dans les domaines de la physique des solides et des nano-technologies. D'une part, le NbO_2 subit une distorsion structurale accompagnée d'une transition de phase électronique où le matériau isolant à basse température devient métallique pour des températures supérieures à 1000 K. Cette transition Métal - Isolant (MIT) à température relativement haute par rapport à d'autres matériaux comme VO_2 peut présenter un intérêt pour des applications hautes températures, ou encore des dispositifs où l'effet de la chaleur doit être séparé des effets de champs électriques. D'autre part, NbO_2 présente une phase de résistance différentielle négative contrôlée par le courant (CC-NDR). Cependant, l'origine physique

de ce phénomène est sujette à controverse. Selon les études, il pourrait être causé soit par une instabilité thermique à basse température induite par le transport électronique; soit par une transition métal isolant de Mott haute température. Pour l'instant, l'explication la plus acceptée de ce phénomène est l'auto-échauffement par effet Joule local. En effet, la puissance dissipée par effet Joule dans un matériau augmente localement sa température. Dans un semiconducteur de bande-interdite moyenne, l'augmentation de la température locale induit une chute de la résistivité et ainsi une résistance différentielle négative.

Les phénomènes de commutation à seuil et de résistance différentielle négative observées dans NbO_2 en font un bon candidat pour développer diverses applications comme des dispositifs à mémoire, des commutateurs logiques, des oscillateurs, des amplificateurs, etc... Cependant la compréhension des phénomènes physiques à l'oeuvre dans ce matériau est encore parcéllaire, la littérature faisant états de nombreuses recherches contradictoires ou avec des résultats incohérents. Une raison possible de ce manque de cohérence pourrait venir de la difficulté de synthétiser la phase NbO_2 pure et d'en fabriquer des couches minces.

Dans cette thèse, nous avons choisi de travailler sur les films minces de NbO_2 . Nous nous sommes demandés quels phénomènes interviennent quand le NbO_2 subit des modifications de conductivité dans des conditions d'utilisations typiques? Comment la structure (amorphe, cristalline) influence-t-elle les propriétés électroniques? Des transitions de phases structurelles ou électroniques ont-elles lieu? Comment modéliser simplement les changements observés?

Pour répondre à ces questions, nous avons fabriqués des films minces stoechiométriques de NbO_2 amorphes et cristallins. En raison de l'existence de plusieurs oxydes intermédiaires et non stoechiométriques, cette étape s'est avérée difficile et longue. Nous avons ensuite fait des dispositifs simples qui ne reproduisent pas la géométrie utilisée dans les dispositifs de type memristor utilisée dans la littérature mais permettent un meilleure contrôle du matériau, de sa phase et de sa caractérisation électrique et spectroscopique. Ce travail inclue la caractérisation courant-tension et les mesures de résistivité en fonction de la température, la spectroscopie Raman, y compris lors de la caractérisation électrique, et enfin, l'utilisation de modèles simples pour vérifier la nature des phénomènes conduisant à la Résistance différentielle négative contrôlée en courant dans NbO_2 .

Initialement, nous avons essayé de fabriquer des films minces de NbO_2 par oxydation ex-situ de films de niobium obtenus par pulvérisation magnétron. Cependant, nous avons constaté que, à partir de films de niobium cristallins et homogènes, l'oxydation ex-situ produit des films non-stoechiométrique et inhomogènes de manière non-reproductible. Par conséquent, la technique alternative adoptée a été la pulvérisation magnétron radio-fréquence à partir d'une cible stoechiométrique de NbO_2 . Nous avons ainsi déposé des couches minces de NbO_2 sur différents substrats: verre, Si et SiO_2 . Après optimisation des paramètres de pulvérisation, nous avons constaté que les films obtenus sont systématiquement amorphes et un recuit à haute température est nécessaire pour obtenir un film polycristallin. Nous avons également étudié l'influence des paramètres du recuit sur la cristallinité des films. Un temps de recuit plus long entraîne une plus grande taille de grain, et une température plus élevée conduit à une meilleure cristallinité. Cependant la température de recuit est limitée pour les films déposés sur substrat de verre car ces

derniers se ramollissent au delà de 600 °C. Les couches minces obtenues sur les différents substrats ont été caractérisées par spectroscopie Raman et diffraction X qui ont montré des résultats satisfaisants concernant la structure et la stoechiométrie. La caractérisation électronique a également été réalisée à l'aide de diverses mesures de transport dans un cryostat sous vide secondaire dans une plage de température entre 3-400 K.

A partir des mesures de résistance de couche sur les films déposés sur substrats de verre, nous avons conclu que la résistivité du NbO₂ cristallin est d'environ 50 Ωcm, soit environ un ordre de grandeur plus grand que celle de l'amorphe à 5 Ωcm. De plus, des diagrammes d'Arrhenius de chaque film, nous avons extrait l'énergie d'activation du NbO₂ cristallin et celle des films amorphes qui sont respectivement 0,27 eV et 0,18 eV. Cela concorde avec le fait que le NbO₂ amorphe a une conductivité supérieure à celle du NbO₂ cristallin. Les tentatives de dopage électrostatique des films déposés sur substrats de verre (cristallins et amorphes) par la technique de dopage par charge d'espace développée au laboratoire ont produit les changements de résistivité d'environ un ordre de grandeur, mais aucun changement de phase n'a pu être observé. Plusieurs raisons peuvent être invoquées pour expliquer cette observation. Le dopage électrostatique (comme le dopage chimique) peut être inefficace si le potentiel chimique est accroché aux états de défauts dans la bande interdite de sorte qu'il ne peut pas être amené jusqu'à une bande électronique. De plus un changement de phase peut également être empêché par la localisation dans les échantillons très désordonnés. Enfin, une interface substrat-échantillon non idéale peut également nuire à l'efficacité du dopage électrostatique.

D'autres mesures ont été effectuées pour étudier les origines de la commutation de seuil et les phénomènes de résistance différentielle négative qui se produisent dans NbO₂. Dans les expériences contrôlées en tension, nous avons montré, à la fois par les caractéristiques I-V et par les mesures de résistivités, que les limites des appareils de mesures peuvent introduire des comportements de transition de seuil avec de grandes hystérèses. De tels artefacts peuvent être évités en contrôlant le courant injecté dans le dispositif au lieu de la tension. Les mesures effectuées dans cette configuration ont montré une résistance différentielle négative contrôlée par le courant. Des mesures systématiques des dispositifs sur des substrats de silicium et de verre nous ont permis de trouver les conclusions suivantes :

- Aucun changement de phase électronique ou structurel n'est observé dans les films minces de NbO₂ en mode CC-NDR. En particulier, même dans le domaine NDR avec de grands changements de résistivité, les échantillons cristallins et amorphes restent isolants puisque leur résistance diminue toujours avec l'augmentation de la température.
- Les éventuels changements de phases observés dans la littérature peuvent être dus au changement amorphe-cristallin qui se produit au-dessus de 550 °C. La transition isolant-métallique qui se produit à environ 800 °C n'est probablement jamais observée dans de tels dispositifs.
- La température est le paramètre qui induit ce changement de résistivité par activation thermique des porteurs. Les changements de température sont induits locale-

ment par la puissance dissipée par le courant dans le dispositif et la conductivité thermique intrinsèquement basse de NbO_2 .

- Les variations de températures mesurées et extraites à partir de l'ajustement des modèles de la conductivité concordent raisonnablement, ce qui indique que le phénomène est raisonnablement bien compris. Cependant, le modèle d'activation thermique le plus simple représente assez bien les observations sans qu'il soit nécessaire d'invoquer des modèles plus complexes.

Le phénomène de NDR dans NbO_2 est ainsi le résultat de la variation de la conductivité électrique par la génération thermique de porteurs de charge dans un phénomène de rétroaction où la puissance du courant dissipée par le dispositif détermine la température locale. Si l'appareil est utilisé à une température où les porteurs de charge générés thermiquement sont suffisamment nombreux, aucune NDR n'est observée. Dans le cas du NbO_2 amorphe, cette température est aussi basse que 400 K et peut être estimée à environ 100 K plus élevé pour le NbO_2 cristallin.

Le NDR est présent dans les dispositifs NbO_2 amorphes et cristallins. Cependant, la conductivité électrique et thermique du NbO_2 amorphe est supérieure à celle du NbO_2 cristallin, ce qui signifie que la plage I-V où se trouve la NDR est différente dans chaque matériau. La transformation amorphe-cristalline se situe entre 800 K et 900 K, tandis que la transition métal-isolant de Mott se produit à 1080 K dans le matériau cristallin. Ces transitions ne sont pas impliquées dans les phénomènes de NDR dans nos dispositifs. Aucune transition de phase, ni structurale ni électronique, ni aucun phénomène irréversible ne pourraient être liés au NDR dans nos échantillons.

Puisque ce phénomène de résistance différentielle négative implique des variations considérables de la conductivité électrique générée par le changement de température, il peut être trouvé dans les semi-conducteurs ou les isolants où une telle variation est possible grâce à l'énergie thermique. Mais pour qu'une variation importante de la conductivité électrique puisse être observée, des changements considérables de la température locale doivent pouvoir se produire par effet Joule. Cela implique une faible conductivité thermique dans le matériau. En effet, la conductivité thermique du NbO_2 est deux ordres de grandeur plus faible que celle du silicium.

Chapter 1

Introduction and Background

1.1 State of the Art

Threshold switching is a volatile resistive switching phenomenon that has been reported since the 1960's [2]. It has been observed in a wide variety of transition metal oxides such as VO_2 , Ti_2O_3 , Fe_3O_4 , NbO_2 etc... [3–6]. The characteristics of threshold switching are shown in figure 1.1. Upon running voltage sweeps, the device switches between two phases with a remarkable difference in conductivity: an insulating state (OFF) and a conducting state (ON), but once the voltage is removed, the device returns to its original insulating state, OFF state. This On-OFF switching is often accompanied by a hysteresis, see figure 1.1 (a), which switches ON at voltage called “threshold voltage” and switches back OFF at a lower voltage known as “hold voltage”. While in some materials such as vanadium dioxide VO_2 [7], such changes are accompanied by a phase transition with different crystalline structure, in others the situation is less clear. In this thesis, we concentrate on aspects related to current controlled and temperature controlled behavior and investigate the physical mechanisms involved.

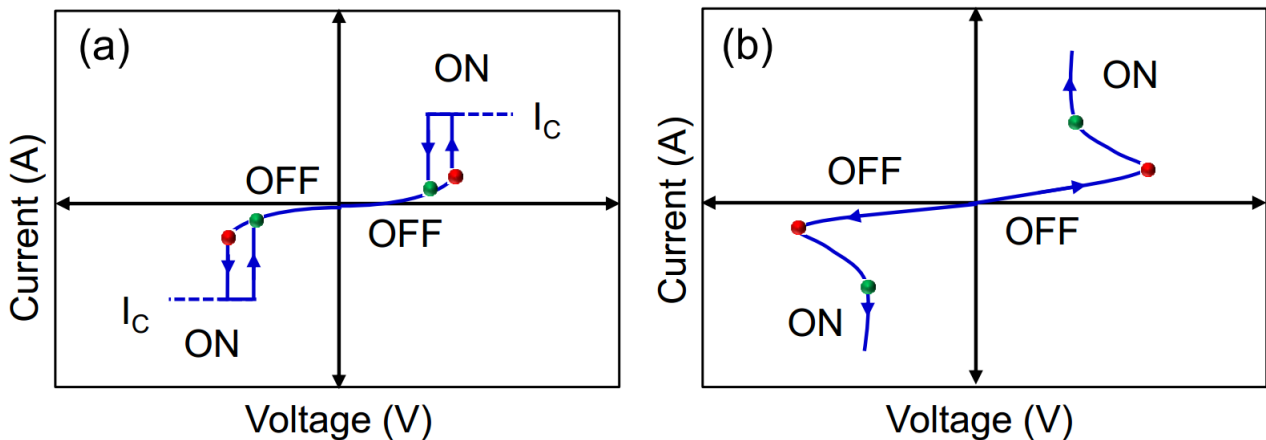


Figure 1.1: (a) Voltage and (b) current controlled I-V curves displaying the threshold switching and the negative differential resistance characteristics respectively [8].

The phenomenon of current-controlled negative differential resistance, figure 1.1 (b), has been observed in systems for different ranges of temperature with an ongoing debate concerning the origins of this behavior. Nonlinear conduction has been observed in the $V(I)$ curves of $\text{Pr}_{0.63}\text{Ca}_{0.37}\text{MnO}_3$ single crystals below 240 K (in the charge order (CO) state) with a temperature induced transition discounted [9]. Asamitsu et al. [10] conclude that the resistivity states changes in $\text{Pr}_{0.7}\text{Ca}_{0.3}\text{MnO}_3$ are due to thermal effects. On the other hand, Alexandarov et al. [11] established an analytical model of the voltage-current $V(I)$ characteristics based on polaronic transport and Ohm's Law and Newton's law of cooling to explain the CC-NDR in TiO_2 memristors. They showed that Joule heating was at origins of the CC-NDR in TiO_2 . CC-NDR was also detected in SmB_6 (Kondo insulator) at a temperature below 10 K [12] in the non linear resistance of the I-V characteristics of the material, and attributed to Joule self-heating as well.

NbO_2 is a metal oxide that is an insulator at room temperature but shows a transition to metallic behaviour at a temperature above ~ 1080 K. In addition to this property, NbO_2 exhibits NDR which is current driven. There has been a decade-long controversy on physical origins of this phenomenon, whether the NDR is caused by a low-temperature non-linear-transport driven thermal instability [13–16] or whether it is caused by a high temperature Mott metal-insulator transition [17–23]. Kumar et al. [24] demonstrated that two NDR regimes exist in NbO_2 one which is at low temperature (~ 400 K) and the other at ~ 1000 K both which are Joule-heating driven although the mechanisms vary at these different temperatures. Until now, Joule self heating has been the most accepted explanation of the NDR phenomenon. The increase of the current in a sample means that the power also increases and eventually the temperature. This increase in the temperature drives a semi-conductor with suitable energy gap, thermal and electrical conductivity from high to low resistivity state and CC-NDR is observed.

The advantage of being able to fabricate CC-NDR devices easily would be commercially recommended. These devices can contribute as elementary material to advanced circuit technologies such as resistance-based memory technologies that use memristive, phase change, conductive bridge or spin-torque memory elements [15] in crossbar array architectures. Such technologies are evolving rapidly as they have high potentialities for providing fast, low-power, non-volatile random access memory (NV-RAM) which can enhance the memory and storage in computer architectures.

1.2 Nano-scale Materials: Correlated Electron Systems

In recent years, there has been considerable interest in the field of nanomaterial devices because of the compelling ways in which their properties can be manipulated. Nanostructures have gained a lot of attention due to striking, new physics as well as many exciting applications revolutionising cutting-edge technology and everyday life [25, 26]. For example, the nature of motion of an electron is drastically changed upon lowering the dimensionality of the material by forming nanostructures [27]. Nanostructures are often ideal technological solutions, ranging from uses in microelectronics, information storage, food processing, health industry and waste purification to energy generation and storage [25, 26]. The fact that at the nano-scale the material's properties can differ from the

bulk has triggered researchers' curiosity to investigate and understand the physical origin of these differences.

Among the centerpieces of modern condensed matter physics are correlated electron systems. In these systems many intriguing phenomena such as superconductivity, ferroic order, interfacial two dimensional electron gases and metal-insulator transition occur [28]. Moreover, thanks to the development in the ultra-fast pump probe techniques and cold atom physics, researchers were able to extend their studies to out of equilibrium systems [29] where new unusual electronic states are revealed which could not be *seen* in the equilibrium regime. Many metal oxides have shown to possess highly correlated electronic systems of which they exhibited a metal-insulator transition that originated from different transport mechanisms depending on the investigated material [30–36].

In this thesis we investigate transport and electronic properties of niobium dioxide NbO₂ 2D thin films, a transition metal oxide which, when the conditions are satisfied, undergoes a metal-insulator transition. I start by introducing the material under study. Then I give an overview on metal-insulator transition describing some of its different types. Furthermore, I introduce electrostatic, field effect doping, since part of the work in this thesis is engaged in doping NbO₂ films using the doping technique developed by my host team, known as “Space Charge Doping” [37]. Finally, I will explain the central topic of this thesis; a phenomenon seen in NbO₂ known as current-controlled negative differential resistance (CC-NDR) or S-NDR (because of the I-V curve shape which looks like the letter S) or threshold switching [38].

1.3 Niobium and Niobium Oxides

Niobium¹, the 41st element of the periodic table with electron configuration [Kr]4d⁴5s¹, was first discovered in the year 1801 by the English chemist Charles Hatchett [39]. It adopts a BCC structure with a lattice constant of 3.3 Å [40]. In comparison with many other metals, niobium has a relatively high melting point of about 2468 °C. It is also corrosion resistant which makes it a good candidate for industrial applications. At room temperature niobium has a grey color with good ductility. When exposed to air for a long period, the color of niobium changes to blue [41].

Despite their known aptitudes in many technological applications, niobium oxide systems still lack complete understanding. On one hand, literature shows contradictory reports or inconsistent information on these oxides [42–44]. On the other hand, there are difficulties in fabricating pure stoichiometric phases of some oxides which shows a narrow window of thermodynamic stability [45].

Depending on the exposed conditions, niobium oxidizes into three main stable oxides: niobium monoxide, niobium dioxide and niobium pentoxide. A brief overview is discussed on niobium monoxide and niobium pentoxide, where as niobium dioxide will be discussed in detail.

- Niobium monoxide (NbO), the 2⁺ charge state of Nb is a superconductor with a critical temperature $T_C \sim 1.38$ K [46,47]. The stability of this oxide lies in a narrow

¹Initially it was called columbium in honor of the place of its discovery

stoichiometric range NbO_x where $0.96 \leq x \leq 1.02$ [48], and it was shown that a slight shift in the oxygen ratio (towards NbO_2 , NbO_{1+x} where $0 < x < 1$) causes a sharp increase in its electrical resistivity. However, a small decrease in the oxygen ratio (NbO_{1+x} where $-1 < x < 0$), or equivalently an increase in the Nb ratio, induces an increase in the superconducting critical temperature [46]. Although NbO is not widely used in technological applications, it is still a good candidate for niobium-based solid electrolytic capacitors since it possesses improved properties concerning oxygen diffusion [49–53].

- Niobium pentoxide (Nb_2O_5), also known as 5^+ charge state of Nb: is the most thermodynamically stable phase in the Nb-O system [54, 55]. It is an insulator which can exist in an amorphous state or in one of several polymorphic crystalline forms. The physical properties of (Nb_2O_5) depend on the polymorph type, the fabrication parameters and the synthesis technique used [56–60].

Principal oxides are shown in the Nb-O phase diagram of figure 1.2 reported by Masalski [61] and presented by [42]. Many metastable suboxides as well as metastable phases of niobium oxides [62] also exist as shown in figure 1.3. Table 1.1 also presents the crystal systems, lattice parameters and the space groups of the different phases of niobium oxides [42].

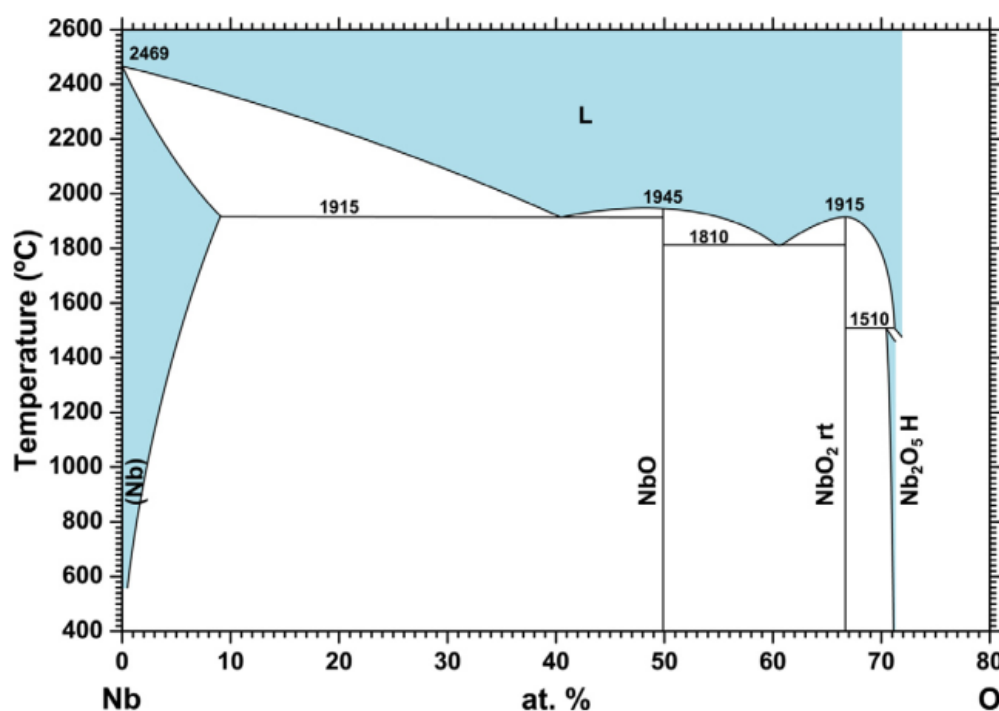


Figure 1.2: The Nb-O phase diagram shows the existence of four thermodynamically stable phases of niobium–oxygen system (Nb, NbO, NbO₂ and Nb₂O₅) with very narrow single-phase fields and negligible deviations from the exact stoichiometry [42]. “Reprinted from Progress in Material Science, 80, C. Nico, T. Monteiro, M.P.F. Graca, Niobium oxides and niobates physical properties: Review and prospects, 3, Copyright (2016), with permission from Elsevier.”

From the above overview, it can be clearly seen that obtaining pure phases of a stable niobium oxide is not an easy mission as narrow windows in stoichiometry and temperature have to be satisfied.

Phase	Crystal system	Lattice parameters	Space group
NbO	Cubic	$a = 4.210 \text{ \AA}$	O_h^1
NbO ₂	Tetragonal	$a = 13.695 \text{ \AA}$ $c = 5.981 \text{ \AA}$	C_{4h}^6
	Rutile	$a = 4.55 \text{ \AA}/a = 4.841 \text{ \AA}$ $c = 2.86 \text{ \AA}/c = 2.992 \text{ \AA}$	D_{4h}^{14}
	Monoclinic	$a = 12.03 \text{ \AA}$ $b = 14.37 \text{ \AA}$ $c = 10.36 \text{ \AA}$ $\beta = 121.17^\circ$	C_{2h}
Nb ₁₂ O ₂₉	Monoclinic	$a = 15.686 \text{ \AA}$ $b = 3.831 \text{ \AA}$ $c = 20.71 \text{ \AA}$ $\beta = 121.17^\circ$	C_{2h}^3
	Orthorhombic	$a = 3.832 \text{ \AA}$ $b = 2.740 \text{ \AA}$ $c = 28.890 \text{ \AA}$	D_{2h}^{17}
Nb ₂₂ O ₅₄	Monoclinic	$a = 15.749 \text{ \AA}$ $b = 3.824 \text{ \AA}$ $c = 17.852 \text{ \AA}$ $\beta = 102.03^\circ$	C_{2h}^1
	Orthorhombic	$a = 6.175 \text{ \AA}/a = 6.144 \text{ \AA}$ $b = 29.175 \text{ \AA}/b = 29.194 \text{ \AA}$ $c = 3.930 \text{ \AA}/c = 3.940 \text{ \AA}$	D_{2h}^9
B-Nb ₂ O ₅	Monoclinic	$a = 12.73 \text{ \AA}$ $b = 4.88 \text{ \AA}$ $c = 5.56 \text{ \AA}$ $\beta = 105.1^\circ$	C_{2h}^6
H-Nb ₂ O ₅	Monoclinic	$a = 21.153 \text{ \AA}/a = 21.163 \text{ \AA}$ $b = 3.8233 \text{ \AA}/b = 3.824 \text{ \AA}$ $c = 19.356 \text{ \AA}/c = 19.355 \text{ \AA}$ $\beta = 119.80^\circ$	C_{2h}^1
N-Nb ₂ O ₅	Monoclinic	$a = 28.51 \text{ \AA}$ $b = 3.830 \text{ \AA}$ $c = 17.48 \text{ \AA}$ $\beta = 120.8^\circ$	C_{2h}^3
Z-Nb ₂ O ₅	Monoclinic	$a = 5.219 \text{ \AA}$ $b = 4.699 \text{ \AA}$ $c = 5.928 \text{ \AA}$ $\beta = 108.56^\circ$	C_2^1
R-Nb ₂ O ₅	Monoclinic	$a = 12.79 \text{ \AA}$ $b = 3.826 \text{ \AA}$ $c = 3.983 \text{ \AA}$ $\beta = 90.75^\circ$	C_{2h}^3
M-Nb ₂ O ₅	Tetragonal	$a = 20.44 \text{ \AA}$ $c = 3.832 \text{ \AA}$	D_{4h}^{17}
P-Nb ₂ O ₅	Tetragonal	$a = 3.876 \text{ \AA}$ $c = 25.43 \text{ \AA}$	D_4^{10}
TT-Nb ₂ O ₅	Pseudo-hexagonal	$a = 3.607 \text{ \AA}/a = 3.600 \text{ \AA}$ $c = 3.925 \text{ \AA}/c = 3.919 \text{ \AA}$	-
	Monoclinic	$a = 7.23 \text{ \AA}$ $b = 15.7 \text{ \AA}$ $c = 7.18 \text{ \AA}$ $\beta = 119.08^\circ$	

Table 1.1: Niobium oxide crystal phases [42]. The main oxides of niobium are shown as well as the different crystalline polymorphs. "Reprinted from Progress in Material Science, 80, C. Nico, T. Monteiro, M.P.F. Graca, Niobium oxides and niobates physical properties: Review and prospects, 14, Copyright (2016), with permission from Elsevier."

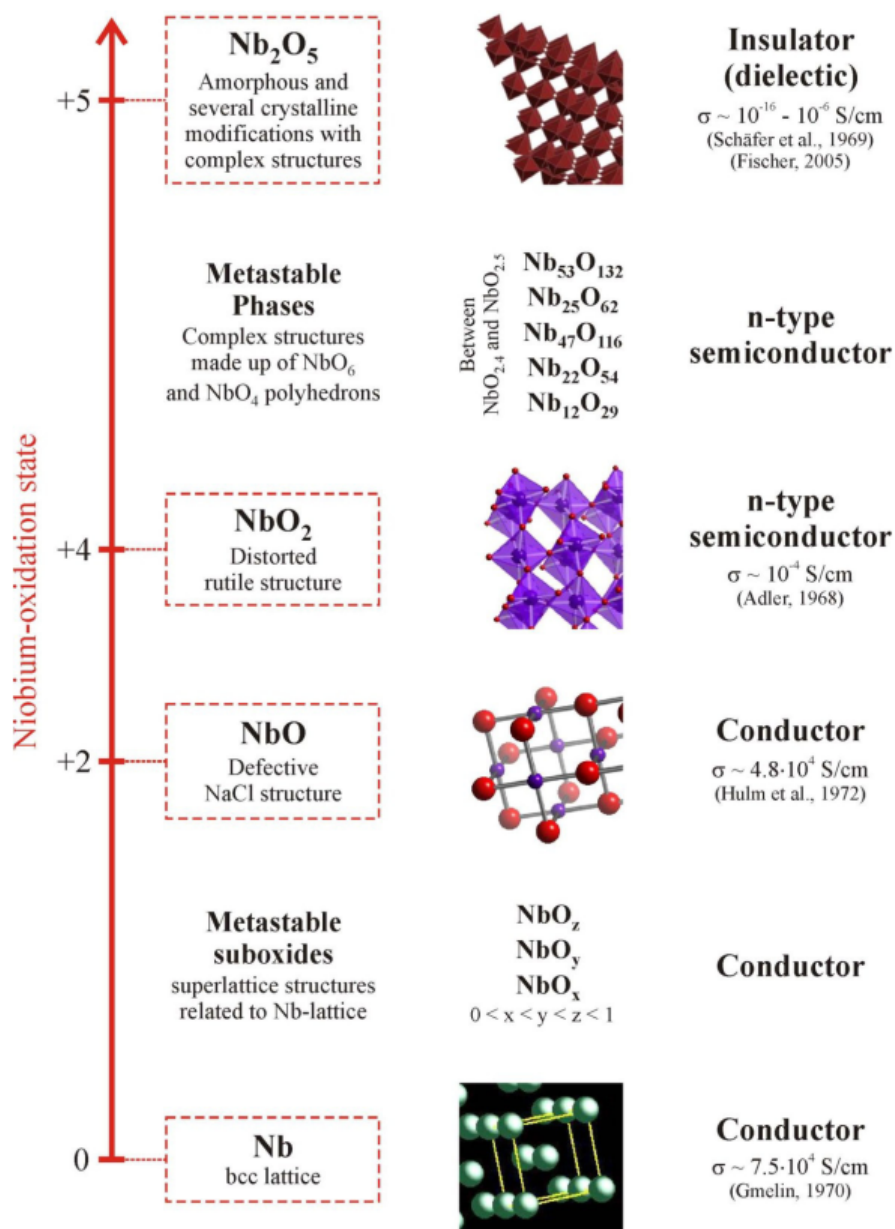


Figure 1.3: The niobium-oxygen system: main oxides and some of their structural and electrical properties (conductivity σ given at $\sim 0^\circ - 25^\circ\text{C}$) as a function of the formal Nb-oxidation state [62].

1.4 Niobium Dioxide NbO_2

1.4.1 Physical Structure

Among the niobium oxides, Niobium dioxide (NbO_2), the 4^+ charge state of Nb, is interesting to study because it has a insulator to metal transition. In its semiconducting phase at low temperatures (LT), NbO_2 adopts a tetragonal distorted rutile structure and space group $I4a_1/a$ [63,64]. It is characterized by chains of edge-sharing NbO_6 octahedrons which are linked together at the corners, see figure 1.4 (b). Along the edge-sharing chains, the Nb-Nb distances are alternately 2.80 and 3.20\AA corresponding to the dimerization of the Nb atoms which is most likely to be a direct impact of a Peierls instability [28,66,90]. As the temperature of NbO_2 is raised to high temperatures (HT) $\sim 800^\circ\text{C}$ and above, it undergoes an electronic phase transition where it becomes metallic. This transition is accompanied by a structural phase transition in which the structure becomes undistorted rutile [63,67–69] as shown in figure 1.4 (a). The relations between the lattice parameters of both structures the tetragonal at LT and the rutile at HT are as follows:

$$a_T \simeq 2\sqrt{2} a_R$$

and

$$c_T \simeq 2 c_R$$

where $a_R = 4.84\text{\AA}$ and $c_R = 2.99\text{\AA}$ [70].

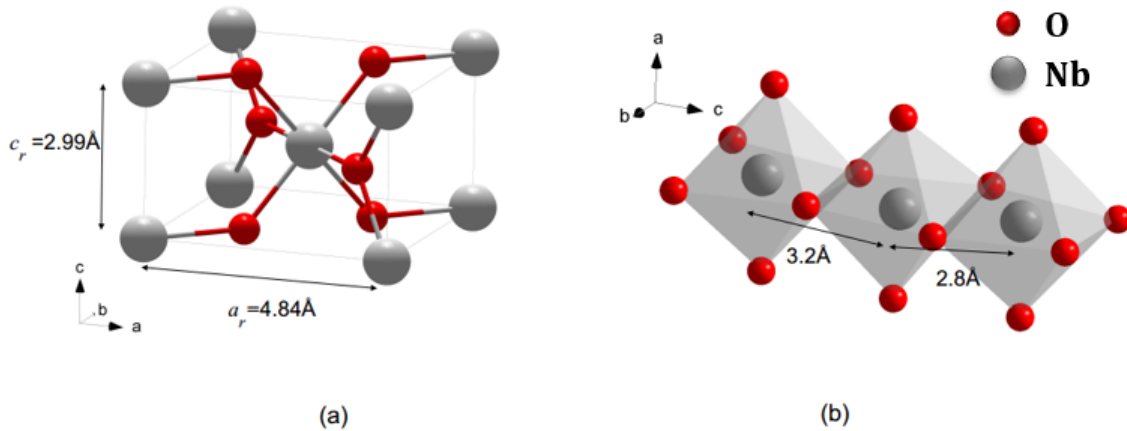


Figure 1.4: (a) The high temperature rutile structure of NbO_2 (metallic NbO_2). (b) The tetragonal distorted rutile structure of NbO_2 at low temperature (semiconducting NbO_2) [70].

1.4.2 Electronic Band Structure and The Density of States

1.4.2.1 Crystal Field Theory

Developed by Hans Bethe [71] and John Hasbrouck van Vleck [72], the crystal field theory CFT explains the breaking of orbital degeneracy in transition metal oxide complexes due

to the presence of ligands. Ligands can approach the metal atom forming different structural geometries and eventually, based on the geometry, different metal-ligand bonds. Depending on the strength of these bonds, the energy of the system is altered.

Transition metal physics is dominated by electrons that can occupy the d orbitals. For a free transition metal in the absence of any crystal field, the 5 d orbitals are degenerate i.e. that they all have the same energy. However, in an octahedral field, just like the case in NbO_2 [73,74], six ligands approach along the $\pm z$ axis, $\pm x$ axis and along the $\pm y$ axis. When a ligand encounters a lobe of the central atom's d orbitals, it raises the energy hence the d_{z^2} and the $d_{x^2-y^2}$ orbitals which lie along the x, y and z axes are raised in energies, whereas they d_{xy} , d_{yz} and d_{xz} are out of the way of the ligands and are of lower energy, see figure 1.5.

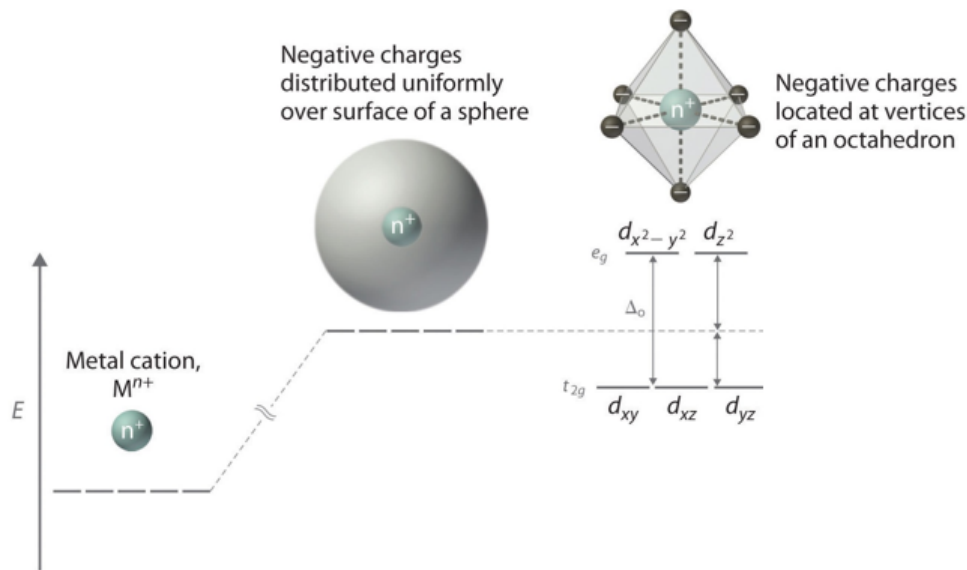


Figure 1.5: When ligands approach a metal cation in a spherical form (symmetric from all directions), the energy of all five d orbitals increases due to electrostatic repulsion. However, when the ligands approach along the vertices of an octahedron, the d orbitals split into two groups of different energies: the d_{z^2} and the $d_{x^2-y^2}$ orbitals which have respectively higher energies, and the d_{xy} , d_{yz} and d_{xz} which have respectively lower energies. Image ref. [75].

1.4.2.2 Electronic Band Structure

Having a lot in common with its parent oxide VO_2 , the energy band diagram of NbO_2 can be described based on the molecular orbital as presented by Lateron and Goode-nough [73] on VO_2 . The bonding between Nb and O atoms during the formation of NbO_2 gives rise to a $4d^1$ system. Moreover, the hybridization of Nb 4d and O 2p orbitals results in energy bands in the vicinity of the Fermi energy. This hybridization further leads to the π -type and σ -type overlap having t_{2g} and e_g symmetry respectively. This emerges from the octahedral symmetry of NbO_6 . The antibonding states are primarily 4d orbitals of Nb, while the bonding states are mainly 2p orbitals of O. The separation between σ and σ^* is wide due to the fact that before hybridization Nb 4d and O 2p levels

are widely separated. Moreover, because the p-d overlap of the σ bonding is stronger, the σ - σ^* splitting is larger than that of the π - π^* . Nevertheless, the degeneracy of the antibonding π (t_{2g}) bands is lifted due to the orthorhombic distortion and leads to their splitting into $d_{||}$ and e_g^π .

In the rutile phase, the e_g^π and the $d_{||}$ overlap with the Fermi level crossing the bands. Hence, the two bands are partially filled which is at origin of the metallic state of this phase, see figure 1.6. On the other hand, in the tetragonal distorted rutile phase, the $d_{||}$ band splits into two bands: the bonding $d_{||}$ band and the antibonding $d_{||}^*$ band. The former being located below the Fermi energy while the latter lies above E_F . This splitting in the $d_{||}$ band arises from a Peierls transition that occurs when the system in changing from its metallic rutile phase to the insulating tetragonal phase. This transition occurs along the c-axis in which, periodically, every two Nb atoms approach each other leading to a doubling in the lattice constant and eventually in the reduction of the Brillouin Zone where the system can gain more energy by opening a gap at the boundaries of this new Brillouin Zone, and hence the splitting of the $d_{||}$ into $d_{||}$ and $d_{||}^*$. In addition, a shift in the now depopulated e_g^π band occurs towards higher energies leaving a band gap behind, see figure 1.6 (b).

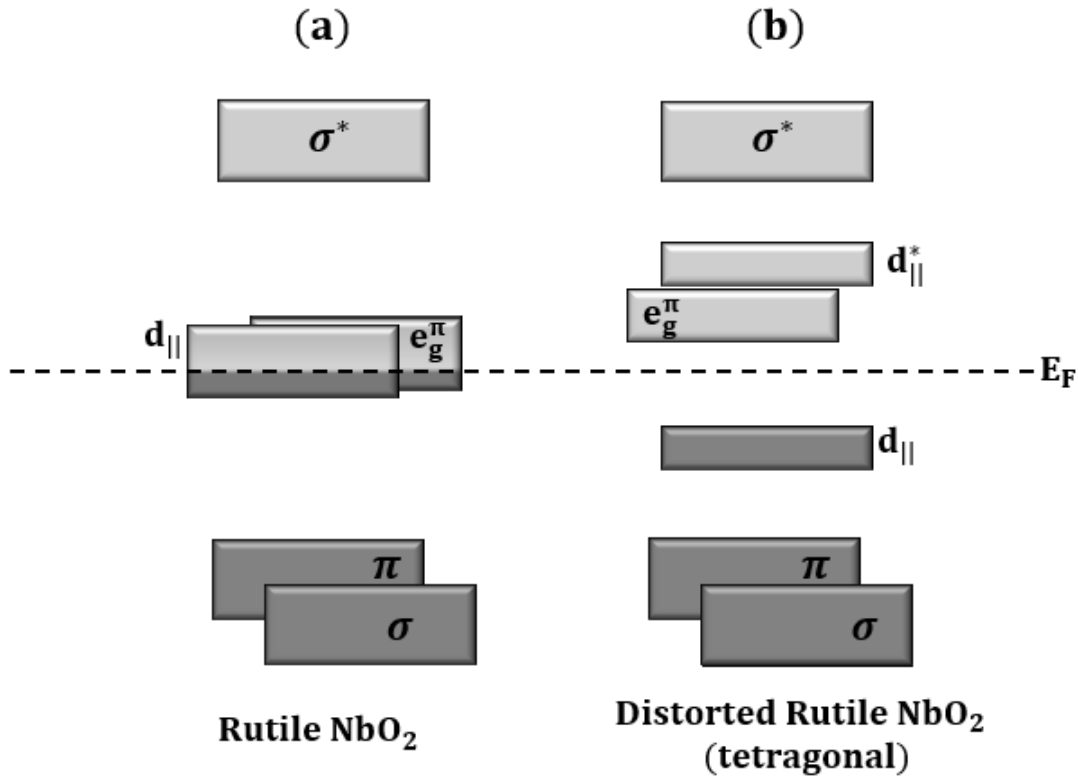


Figure 1.6: The band structure diagram of NbO_2 in the vicinity of the Fermi level in both crystalline states (a) rutile and (b) distorted rutile (tetragonal) phases [74].

1.4.2.3 Density of States of NbO_2

One main reason that attracted our attention to this material, NbO_2 , is the calculated density of states (DOS) which is shown in Figure 1.7 [28]. The Fermi level E_F of NbO_2

in the LT regime lies in the energy band gap E_g . This gap is still interestingly not precisely known, yet its size ranges from ~ 0.5 eV (from the RT estimation of the optical gap) [76, 77] to 1.2 eV [78]. Values in between were also reported, for example, by fitting to conductivity measurements [78], it was found to be 1.16 eV. Moreover, measurements including a combination of inverse photoemission spectroscopy (IPS), ultraviolet photoemission spectroscopy (UPS) and x-ray photoemission spectroscopy (XPS) reveal that E_g is at least 1 eV [79]. And recently, a theoretical calculation, by O'Hara et al. [28], was made using the local density approximation (LDA) to calculate the band gap and it was found to be an indirect gap of 1.15 eV [28].

The difference in these values is very likely to be attributed to the variance in the synthesis techniques, sample quality and stoichiometry and the measurement techniques. However, what we can clearly see is that at the edges of the band gap (both to the left and to the right of the band gap) we see peaks in the density of states.

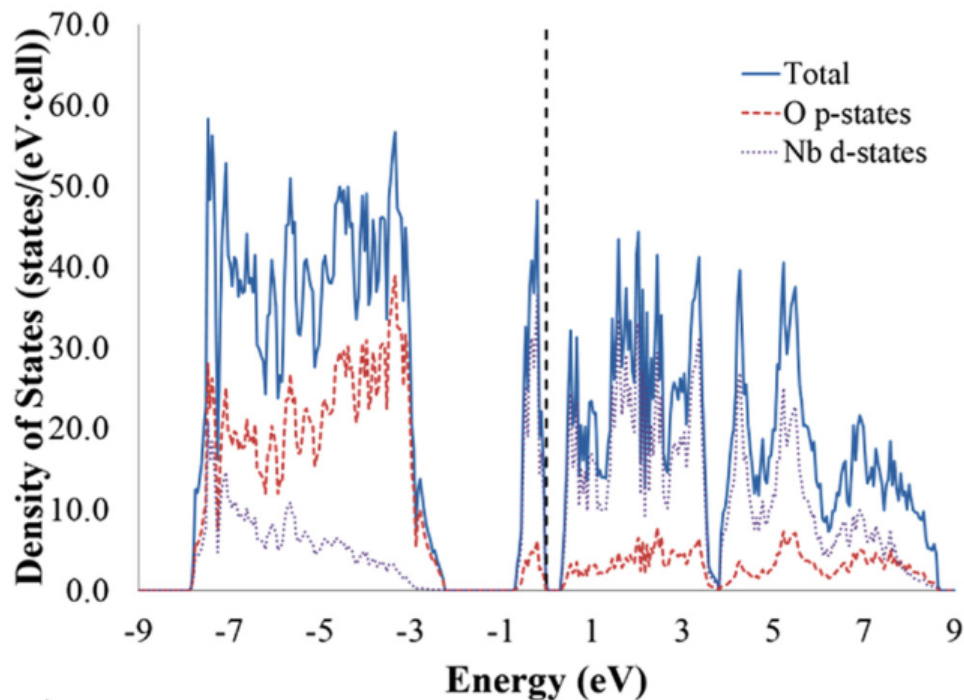


Figure 1.7: The total and orbital-resolved density of states of NbO_2 , as displayed by O'Hara et al., in the tetragonal distorted rutile phase. [28]. “Reproduced from Journal of Applied Physics, 116, A. O'Hara, T. Nunley, A. Posadas, S. Zollner, A. Demkov, Electronic and optical properties of NbO_2 , 213705, Copyright (2014), with the permission of AIP publishing.”

There are different parameters that can be modified for generating phase transitions such as temperature [80] (temperature controlled MIT [81]), pressure [82, 83] (bandwidth controlled MIT [81]), electronic density by chemical doping (filling controlled MIT [81]), and electric field [80] or eventually electrostatic doping. As far as electrostatic doping is concerned, it is only possible for an ultra-thin nanometer thick region in a thin film field effect transistor like device as will be explained later. So far, we have known that NbO_2 undergoes a metal-insulator transition by impact of temperature, and that for the transition to happen a relatively high temperature is needed. Being aware of the peaks

at the edges of the band gap in the DOS, we asked ourselves: Is it possible to trigger an electronic transition by means of electrostatic doping? That is, can we dope the sample enough so that the Fermi level is forced to coincide with a DOS peak causing a jump in the carrier density and a transition into the metallic state? Another question we asked ourselves: In case the transition occurred, will this electronic transition be accompanied by a structural transition or not? To understand better, I proceed by introducing a background on the significance of metal-insulator transition phenomenon.

1.5 Metal-Insulator Transition MIT

Intense research, both theoretical and experimental, has been undertaken in order to unravel the mechanism and the physical concepts behind the metal-insulator transition which can be seen in many transition metal oxides. MIT can take place due to different phenomena. Depending on the material, the simpler type of MIT can be: a Mott transition which arises from an electron-electron interaction, a Peierls transition which is due to an electron-phonon interaction, or the transition that can stem from a disorder-induced localization known as Anderson localization [84]. These transitions can be triggered by external stimuli which can be thermal, strain, optical, magnetic, electrical, etc.

1.5.1 Mott Transition

When electron-electron interactions are not negligible and can no more be treated simply as a perturbation to the system, but rather contribute to the energetic state of that system, we are then talking about correlated electronic systems [85–87]. Mott transition describes the transition from an insulating to a metallic state of a material in light of electron correlated systems. The Mott insulating state was first found in some transitional metal oxides with odd number of electrons per lattice site thus expected to be metallic according to the classical band theory.

For illustration, consider a lattice with N primitive unit cells and one electron on each site. In the simple band theory, the band degeneracy would be $2N$ (taking into account the spin degeneracy). The theory predicts that the material would be metallic with a half-filled conduction band. The conduction thus happens by electrons hopping through the lattice from one site to another. However, when the electron is to hop from its original site to a new site, which is already occupied by another electron, it will experience Coulombic repulsion from the electron in the new site, and if the Coulombic repulsion energy U is much larger than the electrons' kinetic energy, electrons would be bound to their original site instead of being itinerant in the lattice, in other words, there is a competition between the band width W and the Coulombic potential U . In the absence of the potential there are double degenerate bands. As Coulombic potential increases, the bands start to split, and the transition occurs when $U = W$ which is marked by opening a gap at the Fermi level. Finally, when the potential is greater than the band width, two non-degenerate bands are formed. Thus the original single-half filling band is split into a full lower band (lower Hubbard band, LHB) and an empty higher band (upper Hubbard band, UHB) as shown in figure 1.8. The magnitude of the band splitting is the Coulombic repulsion energy U . This physics is well captured by the well known Hubbard model.

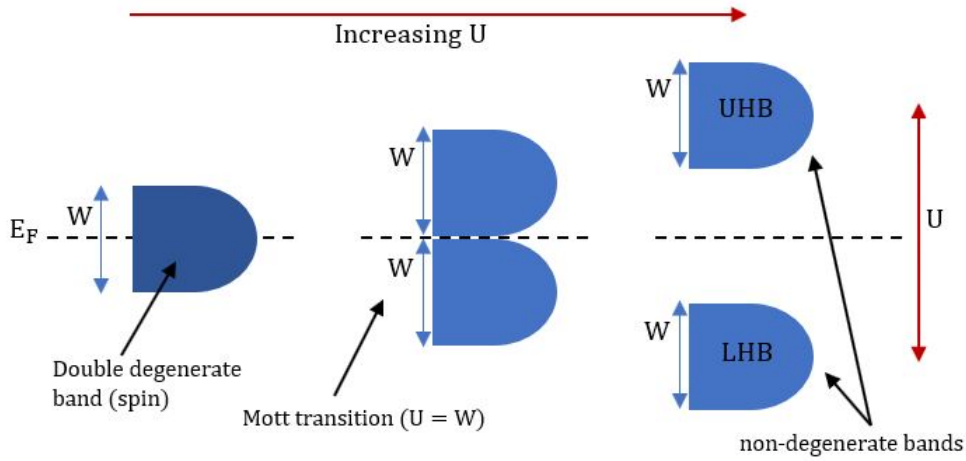


Figure 1.8: Band diagram illustrating the Mott transition.

The transition from the insulating state to the conducting state can be triggered by external factors. For example, adding enough thermal energy can stimulate the transition of electrons from the LHB to the UHB. Another way is to change the bandwidth W of the material by changing the atomic spacing which can be done by applying a pressure. In other situations, MIT can be induced by the change in band-filling, realized by doping the UHB or the LHB with electrons or holes relatively. Experimental observation showed that there is a critical free carrier density n_c required to induce the MIT at $T = 0K$. Mott proposed the criterion [87] for the MIT to occur:

$$n_c^{1/3} a_H \approx 0.25 \quad (1.1)$$

where a_H is the Bohr radius of electrons.

1.5.2 Anderson Localization

Briefly speaking, this type of insulating behaviour is a consequence of lattice disorder such as the presence of impurities or vacancies. These disorders can attenuate electron transport by scattering and eventually decrease their mean free path and thereby the material's conductivity. The concept of the Anderson Localization [88] is as follows:

Let us consider a one dimensional lattice, and each site acts a potential well which traps (confines) the electrons at low temperatures. In the absence of disorder, the eigen wave functions as well as the eigen energies are the same at different sites, and therefore, the electrons can tunnel through the potential barriers without any problem, see figure 1.9 a(a). On the other hand, if disorder is highly present, this means that the lattice is not any more uniform and the potential well depths vary, see figure 1.9 (b). This means that the eigen functions as well as the eigen energies at each site also vary and from perturbation theory, the eigen wave function will be dominated by a single site wave function. In other words, electrons will become localized and the conduction will start to disappear at low temperatures [89]. From what preceded, it has become obvious that this kind of localization comes from the wave-like aspect of the electrons.

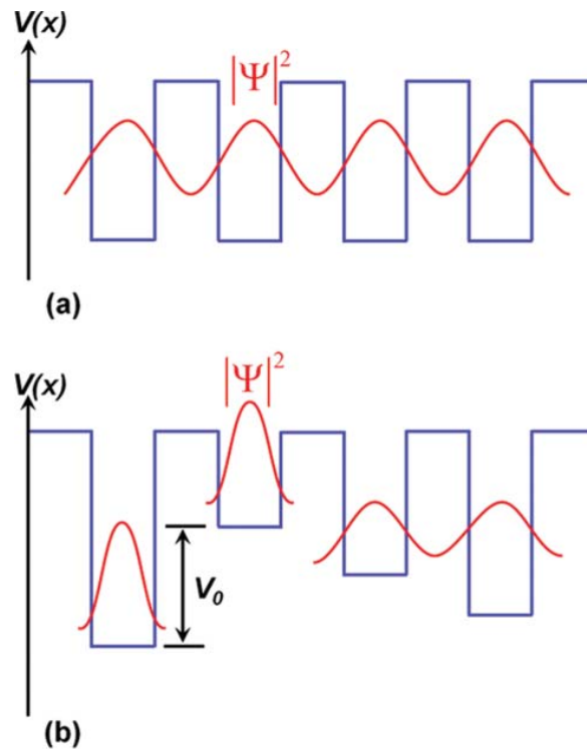


Figure 1.9: In the absence of disorder (a) the chain of ions can be considered as a series of potential wells where the electron can tunnel through these wells without altering the wave function. However, when impurities are strongly present (b), the electron experiences different potentials at different sites and the wave function becomes localized. [84].

1.5.3 Peierls Transition

The physical background of the Peierls instability [90] is based on energetic considerations. When one takes into account not only the electronic contribution to the total energy but also to the elastic energy of the ions (phonon excitation), it can happen that the ground state energy is reduced by a lattice distortion.

For illustration, consider a niobium Nb one-dimensional lattice of lattice constant c with one electron per atom. It can happen that the total energy of the system is minimized by dimerization, that is by two atoms periodically getting closer to each other in a manner that the period of the solid becomes twice that of the underlying lattice ($2c$ instead of c), see figure 1.10.

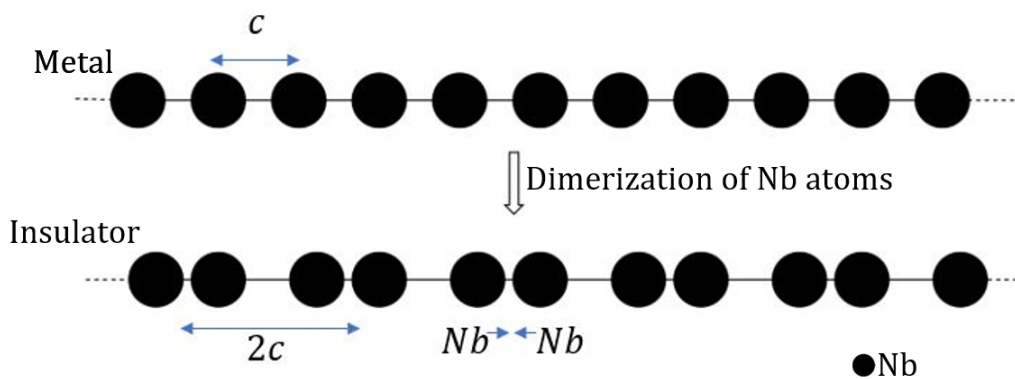


Figure 1.10: Lattice distortion due to Nb-Nb dimerization. After dimerization, the lattice constant is doubled.

In this way, the size of the original Brillouin Zone is halved, and as result, diffraction of the electron wave function will occur at the boundaries of the new Brillouin Zone. This diffraction causes the E vs. k relation to distort in the vicinity of the Bragg planes (or Brillouin Zone boundaries) for nearly free electrons. This distortion causes some of the energy levels to become forbidden and eventually opening a band gap, see figure 1.11. And as the fermi energy E_F lies in this gap, the material becomes insulating.

By considering references [91, 92], one will realize that the authors associate the Peierls instability in niobium dioxide to softening of some phonon modes - when a phonon energy becomes zero (becomes 'soft') at some non-vanishing wave vector q , it suggests that the system is likely to become structurally unstable against a periodic distortion with wave vector q . In addition to that O'Hara [28] also attributes this transition *purely* to a structural distortion.

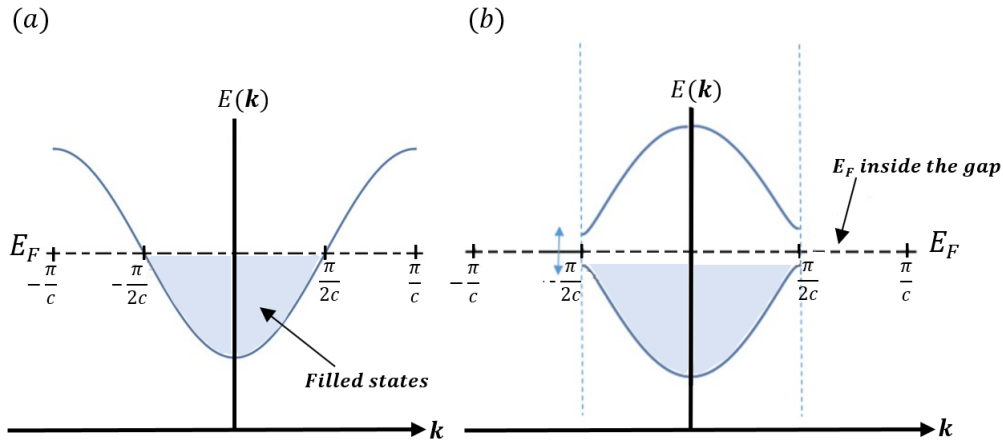


Figure 1.11: Impact of lattice distortion on the Brillouin Zone (a) before distortion (b) after distortion

1.6 Doping of 2D Materials

Now that we understand some features of NbO_2 , and the fact that we can trigger the electronic properties by doping it, let us recall what doping is:

Doping a semiconductor means to introduce impurities, intentionally, in order to modulate the electronic properties of the host material. By doping, more allowed energies are introduced within the band gap. These new allowed energies depend on the dopant type; if the impurity is an electron donor, new states are created near the conduction band, where as if the dopant is an electron acceptor, then the new state appear in the vicinity of the valence band.

When doping requires the introduction of a foreign dopant into the host material, then this type of doping is called chemical doping because it requires introduction of a new chemical species. Although widely used in the semiconductor technology, chemical doping presents drawbacks and side effects. For example, the formation of impurity phases can reduce intergranular connectivity [93], the impurities can cause structural defects in the sample, unwanted chemical reactions can occur and finally doping may be inhomogeneous.

In order to avoid such problems, other doping techniques are used which are based on electrostatic considerations and implemented in devices with the field effect transistor geometry. One of these techniques is known as ionic liquid doping. A schematic of this doping technique is shown in figure 1.12.

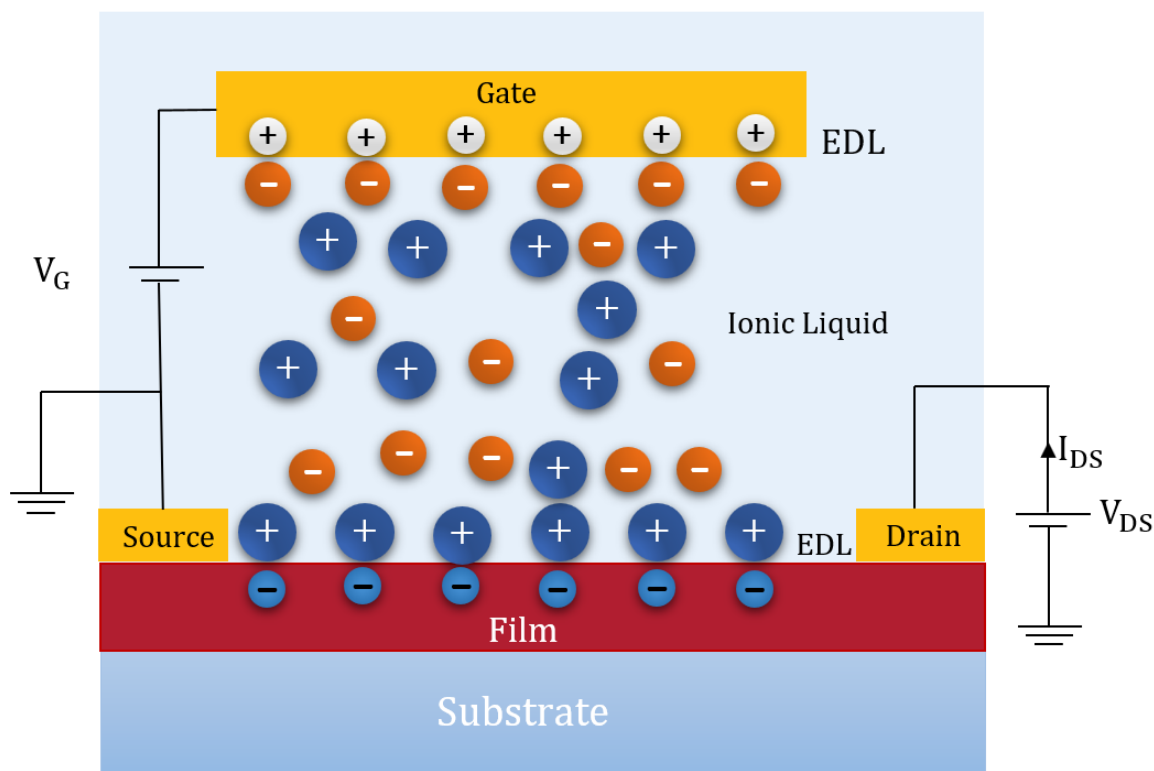


Figure 1.12: A typical structure of ionic liquid gated field effect transistor.

As its name implies, ionic liquid doping exploits the presence of organic cations and inorganic anions in the liquid for the doping process. As can be seen in figure 1.12, the ionic liquid covers the source and drain contacts of the field effect transistor, the film to be doped (channel) and the gate electrode which is separated from the channel by the dielectric. Depending on the doping type of interest, a positive or negative voltage is applied at the gate. The application of a voltage, say positive, at the gate causes an electric field in the dielectric and a two direction migration. Anions will be attracted towards the positive electrode (gate) where as the cations will be repelled to the opposite side towards the film. The accumulation of the cations at the film's surface attracts electrons within the film to the top few layers and eventually n-doping it. The interface layered structure of charges (positive charges from the ionic liquid and negative charges from the film) is called the electric double layer (EDL).

Aside of being a powerful doping technique, ionic liquid doping also has its draw backs as it is upper and lower bounded by temperature limitations. Dropping to a low temperature can cause the freezing of the ions with a consequent drastic reduction of their mobility, and augmenting to a high temperature can cause a contribution of the ionic charges to measurements carried out such as transport measurements.

A similar technique, but with less constraints on its functional window², is the developed technique by my host group, the so called "Space Charge Doping Technique" which, instead of using cations and anions of the ionic liquid, takes advantage of the glass structure and the presence of free cations in its doping process. This technique will be described

²Concerning temperature margins, with Space Charge Doping measurements as low as 3 K may be reached; however, the upper temperature is limited by the softening temperature of glass $\sim 600\text{C}$.

in details in next chapter.

Electrostatic doping has shown that it can achieve a high carrier density $10^{14} - 10^{15} \text{ cm}^{-2}$ [37, 94] as compared to conventional gate oxides which can normally induce a carrier density of $\sim 10^{13} \text{ cm}^{-2}$ before dielectric breakdown [95].

Doping of NbO_2 thin films using Space Charge Doping Technique was one part of the thesis; however, the major part of the work was on the studies of the threshold switching in NbO_2 . In what follows, the modelization of the transport and conduction mechanism of NbO_2 in two different situations is described. On one hand, the conduction in NbO_2 as a function of temperature alone is previewed, and on the other hand, when an electric current is applied, the so called current controlled negative differential resistance (CC-NDR) phenomenon.

1.7 Conduction Mechanism: Defect Contribution

In general, films synthesized by deposition or sputtering techniques are not defect free films - they are not perfect. Due to the presence of localized defects within the film and depending on the density of the defect, the contribution of the charge carriers hopping between these localized states can play a significant role in the electronic transport mechanism and may vary in different temperature zones [96]. Apart from the density of the defect states, when the system's temperature is relatively low, the influence of hopping through defected states can also be important. Miller and Abrahams [97] dealt with such systems by considering random resistance networks.

The absence of long-range order in non-crystalline semiconductors leads to the formation of localized states. By referring to Anderson's [98] and Mott's [89] view on strong localization on the electronic structure, the defect states are located beyond the non-localized states as broad tails (see figure 1.13) extending into the gap and separated by energy levels known as *mobility edge* (E_V or E_C). In addition to non-crystalline semiconductors, it has also been demonstrated that localized band-tail states can occur due to the presence of defects at grain boundaries which cause static energetic disorder. Thus the electrical transport can take place by carriers excited into the band-tail states and hop between localized states. The conductivity can then be written as:

$$\sigma(T) = \sigma_0 \exp\left(-\frac{W}{k_B T}\right) \quad (1.2)$$

Where

$$W = (E_A - E_F) + E_h \text{ or } (E_F - E_B) + E_h \quad (1.3)$$

with E_h being the hopping activation energy and the energy differences $(E_A - E_F)$ or $(E_F - E_B)$ the carrier excitation energy. Note that the energy E_h is proportional to the temperature [99].

In some specific cases, where the DOS in the vicinity of the Fermi level E_F is small [100], and the DOS of the defect states has a maximum at a certain energy E_m hopping of

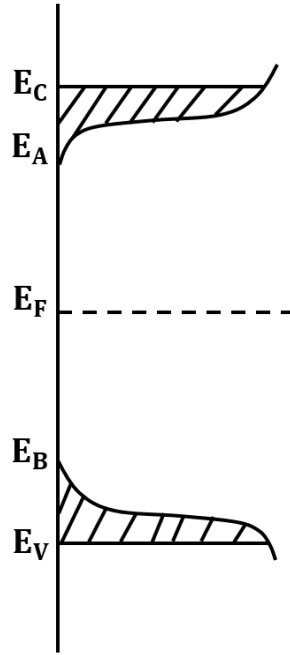


Figure 1.13: A Schematic of the band structure with localized states (shaded) and the mobility edges E_V or E_C .

carriers can happen where they move to the nearest neighbor sites. This is known as the nearest neighbor hopping (NNH) and this hopping mechanism has a conductivity

$$\sigma_{\text{NNH}}(T) = \sigma_{0,\text{NNH}} \exp\left(-\frac{W_{\text{NNH}}}{k_B T}\right) \quad (1.4)$$

where W is the absolute value of difference between the energy where the DOS of the defect has a maximum and the Fermi level $W_{\text{NNH}} = |E_m - E_F|$.

In the low temperature regime, the hopping process is a little different as the states near the Fermi level E_F (that is the states of the smaller DOS) can be more significant in the conduction mechanism, further, as compared to the distance between the nearest neighbor, the hopping distance here is much larger, and it is also temperature dependent. This type of hopping is known as *variable range hopping* (VRH) since it is not restricted to near neighbors. In modeling the VRH, Mott considered the DOS in the vicinity of the Fermi level as a finite constant. The Mott conductivity thus becomes:

$$\sigma_{\text{Mott}}(T) = \sigma_{0,\text{Mott}} \exp\left(-\frac{T_{\text{Mott}}}{T}\right)^{1/(1+d)} \quad (1.5)$$

where d is the dimension of the studied material.

The reason why Mott, in the VRH model, can consider the DOS near Fermi level ($N(E_F)$) as a constant is because he neglects the Coulombic interactions between the hopping sites and assumes that they are negligible. However, if we were to take these interactions into account, energetic considerations will appear where there will be a redistribution of the carriers on the states near the Fermi level in order to reduce the total energy. This happening, it results in a *Coulomb gap* at the Fermi level with $N(E_F)$. Supposing that

the DOS in the vicinity of the fermi level can be described by $N(E) = c|E - E_F|^n$ with c being a constant and n an integer, then the following expression holds [101–103].

$$\sigma(T) = \sigma_0 \exp\left(-\frac{T_0}{T}\right)^{(n+1)/(n+4)} \quad (1.6)$$

Efros-Shlocskii VRH is one of the familiar cases which is observed when $n = 2$ where the conduction can then be written as [104]

$$\sigma_{\text{ES}}(T) = \sigma_{0,\text{ES}} \exp\left(-\frac{T_{\text{ES}}}{T}\right)^{1/2} \quad (1.7)$$

1.8 Negative Differential Resistance

In some non linear electronic devices a phenomenon occurs in which increasing the voltage (current) across the device's terminals leads to the decrease in the current (voltage) through it. This is known as negative resistance [105, 106]. The behavior is in contrast to an ordinary Ohmic resistor, where following Ohm's law the voltage (current) increases when the current (voltage) is increased with the resistance R ($1/R$) being the proportionality constant and eventually resulting in a positive resistance or a positive and eventually constant value for dv/di [107]. Moreover, the functionality of negative resistance in an electric circuit is the opposite of that of positive resistance. While the latter dissipates (consumes) power from the current passing through it, the former generates power [108, 109] and in some favorable conditions can also amplify the power of an electric signal [110–112]. This special behavior of negative differential resistance materials or devices has made them candidates for a variety of technological applications. Such material can be used in electronic oscillators and amplifiers [113, 114], they are also used in switching and memory circuits [115] serving as a memristor [116] since some of them have a hysteresis or a bistable state [124]. Gas discharge tubes [117, 118], tunnel diodes [118, 119], Gunn diodes [120] and parametric amplifiers [121] are all examples of devices that show negative differential resistance.

Two types of resistance can be defined in a non-linear device: A static or absolute resistance which is the ration of the voltage to the current [122, 123]:

$$R_s = \frac{v}{i} \quad (1.8)$$

and from its name, it is the linear positive constant resistance that we usually encounter in circuits. The differential resistance is the ratio of the change in the voltage over the change in current which can be written as:

$$r_{\text{diff}} = \frac{dv}{di} \quad (1.9)$$

The term *negative* differential resistance (NDR) points out that the variation of the voltage and the current is inverse, in other words, when one of them increases, the other decreases, so we can write:

$$\frac{dv}{di} < 0 \quad (1.10)$$

Due to the nonlinearity, the behaviour of NDR devices is more complicated than that of Ohmic resistance devices. In addition to its behavior, the voltage or current range at which this phenomenon occurs is only limited to a certain region [112, 125] and varies depending on the applied current or voltage to the device. Thus there is no real ‘negative resistor’, as compared to a positive resistor, which exhibits a negative resistance over a wide range of voltage or current.

1.8.1 Types of Negative Differential Resistance

Two types of negative differential resistance can be distinguished:

- Voltage controlled negative differential resistance (V-CNDR)

This type of NDR is also known as the “N” type negative differential resistance which comes from the shape of the curve it forms while increasing the voltage in the I-V plot, see figure 1.14 (a). In such devices, the current is a single valued and continuous function of the voltage; however, the voltage is a multivalued function of the current [126]. The curve can be divided into three regions regions 1, 2 and 3. In region 1, as the voltage increases, the current also increases (positive resistance) till it reaches a maximum of i_1 at v_1 . Then in the second region (marked in red) which represents the region of the negative differential resistance, as v increases further, the current starts to decrease till it reaches a minimum i_2 at v_2 . Beyond this, in the third region, as the voltage increases more, the current increases as well showing also a positive resistance. In this manner the letter N is formed and whence the name “N” type. Tunnel diodes [127], resonant tunneling diodes [128] and Gunn diodes [129] are devices that exhibit a voltage controlled negative differential resistance.

- Current controlled negative differential resistance (CC-NDR)

It is the dual of the V-CNDR, and it is also known as the “S” type negative differential resistance which also originates from the shape of the curve, see figure 1.14 (b). Opposite to the former type, here the voltage is a single valued function of the current, whereas the current is a multivalued function of the voltage [126]. Here, the curve can also be divided into three portions; 1 and 3 which show positive resistance, and the region in between (2) which exhibits the negative differential resistance. This behavior of current controlled negative differential resistance is seen in NbO_2 [24, 133] films and other metal oxide devices [130], in addition to other devices such as IMPATT diodes [129] and gas discharge tubes [118].

While most devices have only a single region where the negative differential resistance appears, devices with multiple separate negative differential resistance can also be synthesized [131, 132]. Such devices have more than a single stable state and are used in digital and logic circuits.

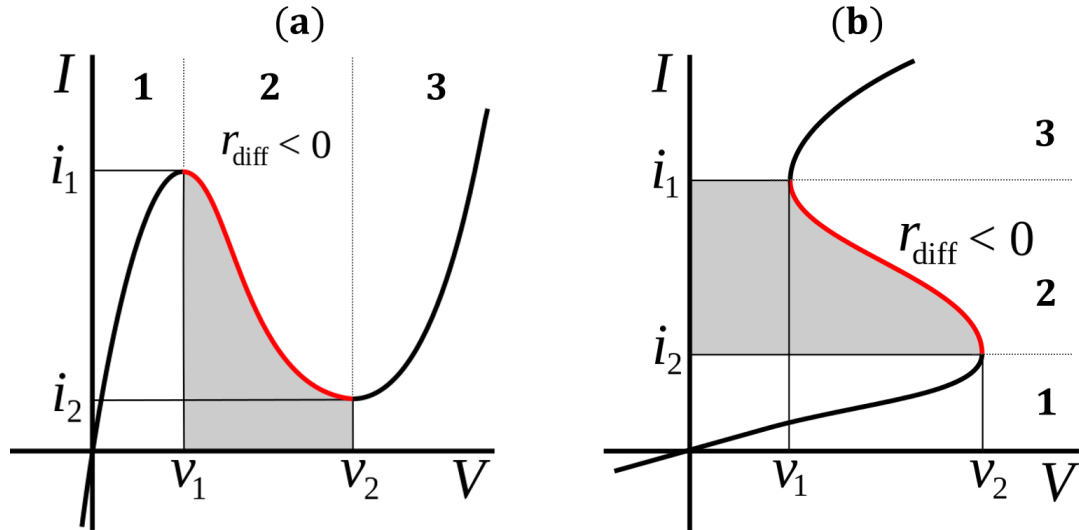


Figure 1.14: (a) N-type negative differential resistance (VC-NDR). (b) S-type negative differential resistance (CC-NDR).

1.9 Conduction Mechanism in NbO₂ Under Current Application

Unlike devices which can be usually treated as a fundamental circuit component or a combination of them such as resistor, capacitor and inductor, and where the conduction mechanism can be described in a single equation, the conduction mechanism in negative differential resistance electric components is not as simple. It requires more than one equation to characterize it completely. The basic understanding of the mechanism is implemented in these two simple equations:

$$v = R(w) i \quad (1.11)$$

$$\frac{dw}{dt} = f(t) \quad (1.12)$$

Where w is a state variable which depends on time.

The first equation essentially states that there is a quasi-static conductance relation between mean voltage and current, but the resistance in that equation depends upon the state of the device at any given point in time. Then there is another equation which is a time-dependent equation that shows how the state variable evolves in time, and both of these equations are needed in order to model the observed CC-NDR phenomenon.

1.9.1 Poole-Frenkel Conduction Mechanism

Researchers studying the conduction mechanism of NbO₂ under the effect of current application [15, 16, 24, 133–135, 137] may have had different interpretations describing the phenomenon, but they all agree that their results could be fit best by the Poole-Frenkel Mechanism or a refined version of it.

Conduction in insulators is not really zero³, as long as the temperature is above 0 K, then it is possible to find electrons in the conduction band of a certain semiconductor/insulator due to thermal excitation. However, these electrons are bound localized states in the vicinity of the atoms, and they are not free to explore the full dimension of the solid. Random fluctuations in the temperature, which happen occasionally, provide electrons with enough energy to get excited to the conduction band. Once there, the electron is able to travel through the crystal for a short period of time before it relaxes again to another localized state of a different atom. However, if a strong electric field is applied, the electrons take advantage of the energy provided in the field to get excited into the conduction band and thus less thermal energy is required to do the stimulation. Moreover, being pulled by the electric field, the electron's lifetime in the conduction band increases and it will be able to move more frequently.

Considering all the above, the standard quantitative expression for the Poole-Frenkel effect is [138, 139]:

$$j \propto E \cdot \exp\left(\frac{-e(\Phi_B - \sqrt{eE/(\pi \epsilon)})}{k_B T}\right) \quad (1.13)$$

where j is the current density, E is the applied electric field, e is the elementary charge, Φ_B is the voltage barrier (in zero applied electric field) that an electron must cross to move from one atom to another in the crystal, ϵ is the dynamic permittivity, k_B is Boltzmann's constant, and T is the temperature.

Slesazek et al. [16] used the standard Poole-Frenkel equation mentioned above and proposed a model that describes the behaviour of NbO_2 based filamentary switching devices, by a temperature activated Poole-Frenkel conduction mechanism.

The above equation describes the current-voltage relation; however, for a complete characterization of the CC-NDR phenomenon another equation is needed which describes the evolution of the state variable, and in the case of NbO_2 , it is the temperature.

In their NbO_2 based device, Kumar et al. [24] have shown that there existed two CC-NDR regimes one at low temperature (~ 400 K) and the other at ~ 1000 K, and both were induced due to Joule's heating so that the temperature was the state variable of the system. They demonstrated that the NDR observed is due to self heating via bulk conduction mechanism that is well described by three dimensional Pool-Frenkel conduction modified by the presence of donors and traps. The two equations necessary for describing their model are:

$$i = v \sigma_0 \frac{A}{d} e^{\frac{-E_a}{k_B T}} \left[\frac{1}{2} + \left(\frac{k_B T}{\beta \sqrt{v/d}} \right)^2 \left(1 + \left(\frac{\beta \sqrt{v/d}}{k_B T} - 1 \right) e^{\frac{\beta \sqrt{v/d}}{k_B T}} \right) \right] \quad (1.14)$$

and the dynamic equation for the state variable is the Newton's law of cooling expressed in terms of memristor current and voltage,

$$\frac{dT}{dt} = \frac{iv}{C_{th}} - \frac{T - T_{amb}}{C_{th} R_{th}(T)} \quad (1.15)$$

³This is why they are referred to as *poor conductors* and not as *non-conductors*.

where in equation 1.14⁴, A is the lateral device area, d is the thickness of NbO_2 , E_a is the activation energy, σ_0 (depends on the dimensions of the film) and β are material properties described elsewhere in [15]. β has the form of $\beta = \sqrt{e^3/\pi \epsilon_0 \epsilon_i}$, with e being the electron charge, ϵ_0 the electric permittivity of vacuum and ϵ_i the high frequency dielectric constant. In the other equation T_{amb} is the ambient temperature, C_{th} and R_{th} are the thermal capacitance and effective thermal resistance respectively.

Although different approaches have been used in describing the conduction mechanism in NbO_2 the characteristic equations were based on developed or modified version the Poole-Frenkel model along with the Newton's law of cooling.

⁴There is actually a mistake in ref. [24] for equation 1.14. The error is not present in earlier ref. [15].

Chapter 2

Experiments

In this chapter the experiments and techniques which were performed during this thesis are described, and the concept behind each experiment is explained. All experiments were carried out at Sorbonne University in Paris.

2.1 Sample Fabrication Techniques

In material science, thin films are generally fabricated by a deposition technique. Deposition techniques can be distinguished into two broad categories depending on whether the process is primarily physical or chemical. When physical forces are engaged in the deposition process, the deposition is known as “Physical Vapor Deposition” (PVD). On the other hand, depositions which involve chemical processes are known as “Chemical Vapor Deposition” (CVD).

Our aim in this project is to study the electronic properties and investigate the metal-insulator transition in thin films of NbO_2 , and for that, we first had to prepare thin films of the desired material. There were two available options in which the films were prepared. One way was by fabricating Nb thin films sputtered from a niobium target and then oxidizing them in an oven (ex situ), and the other was by sputtering from an NbO_2 target.

The niobium and niobium dioxide thin films were prepared by a Physical Vapor Deposition technique known as RF-Magnetron Sputtering. Experiments were held in the clean room of INSP¹ at Sorbonne University, and the sputtering machine used is SCM-400 ALCATEL. A photo of the sputtering system is shown in figure 2.1.

¹Institut des NanoSciences de Paris



Figure 2.1: A photo of the sputtering system (a) an electronic closet for controlling target-substrate distance, substrate temperature and power (b) power source (c) deposition chamber with a valve for controlling Ar flow.

2.1.1 Substrate Preparation

Four types of substrates were used in this thesis: 0.5 mm thick borofloat glass (BF), soda-lime glass (SL) of 0.5mm thickness, phosphorous n-doped Si $\langle 100 \rangle$ of $279 \pm 25 \mu\text{m}$ thickness and has a resistivity of $\rho = 1 - 10 \Omega\cdot\text{cm}$ and boron p-doped Si $\langle 100 \rangle \pm 0.5^\circ$ of $500 - 550 \mu\text{m}$ thickness with a 285 nm SiO_2 layer on top and has a resistivity of $\rho = 0.07 - 0.13 \Omega\cdot\text{cm}$. The choice of this type of glass substrate will be explained later in section 2.3.5 as it has a direct relation with the electrostatic doping technique used. Moreover, an AFM experiment performed on a SL glass sample (image shown in figure 2.2) shows that it has an rms of 0.207 nm. That of BF is 0.227 nm.

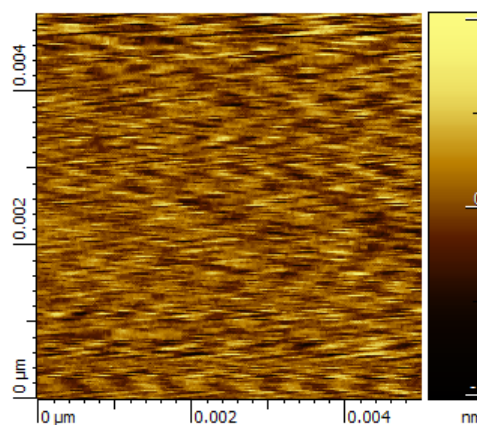


Figure 2.2: An AFM image for the soda lime glass used shows that it has a smooth surface (rms = 0.207 nm).

The substrate preparation was as follows: Wafers of soda-lime glass were first cut into small squared substrates of $\sim 1 \times 1 \text{ cm}^2$ using a diamond-tip pen. The substrates were then put in a small beaker filled with acetone and left at 45°C for ~ 4 min on in ultrasonic bath (Fisher Scientific FB15047). The substrates were then transferred into another beaker containing ethanol and the former process was repeated. Finally, the substrates were taken out, and nitrogen gas was used to dry off the remaining ethanol on the substrates. The same cleaning treatment was done to the silicon substrates. In addition to ex situ cleaning process, substrates were also in situ cleaned by plasma etching for $\sim 2\text{-}3$ min before deposition.

2.1.2 Radio Frequency (RF)-Magnetron Sputtering

The term sputtering refers to the removal of material from a target by the bombardment of high-energy particles. The technique was first discovered in the 1850's, then in the mid 1970's [140] a magnetically enhanced sputtering known as magnetron sputtering had emerged, and thanks to modern vacuum technology, it is now possible to deposit films of extremely high quality.

The RF-Magnetron Sputtering system we used consists of a sputtering chamber, two pumps (primary pump and secondary pump) for achieving high vacuum, a power source set and an electronic closet for controlling plasma generation and temperature.

The inside of a sputtering chamber is shown in figure 2.3. The Niobium target is fixed on a copper² plate over the magnetron which is cooled by a circulating water flow. In order to insure highly pure deposition the chamber is evacuated to a base pressure of $\sim 10^{-7}$ mbar. Then the chamber is back-filled with the process gas Argon. The conditions inside the chamber are thus satisfied to initiate the process.

In an RF-Sputtering, the power supply is a high voltage RF source often fixed at 13.56 MHz. When this power is applied, radio waves emerged are able to ionize the Argon atoms inside the chamber, thus creating a plasma of Ar^+ ions and free electrons.

As an AC voltage is used, a negative electric potential is applied to the Nb target during one half of a cycle. This electric potential will cause the free electrons to accelerate away from the target and in the same time will cause the Ar^+ ions to accelerate towards the target and knock off niobium atoms from the Nb target. The ejected niobium atoms will then collect on the surfaces in their paths and eventually will collect on the sample substrate. During the bombardment of Nb atoms, some electrons, called secondary electrons, are also ejected from the target. These electrons play the same role as the primary electrons in the plasma.

In the second half-cycle, where a positive potential is applied at the target, the Ar^+ ions at surface of the target are repelled and forced back into the plasma. These positively charged ions will recombine with free electrons (either primary or secondary electrons) to create a neutral atom again. The plasma glow generated is due to the recombination of electrons with free Ar^+ ions into a lower energy state.

²Thermal properties of copper enhance the cooling process during the sputtering

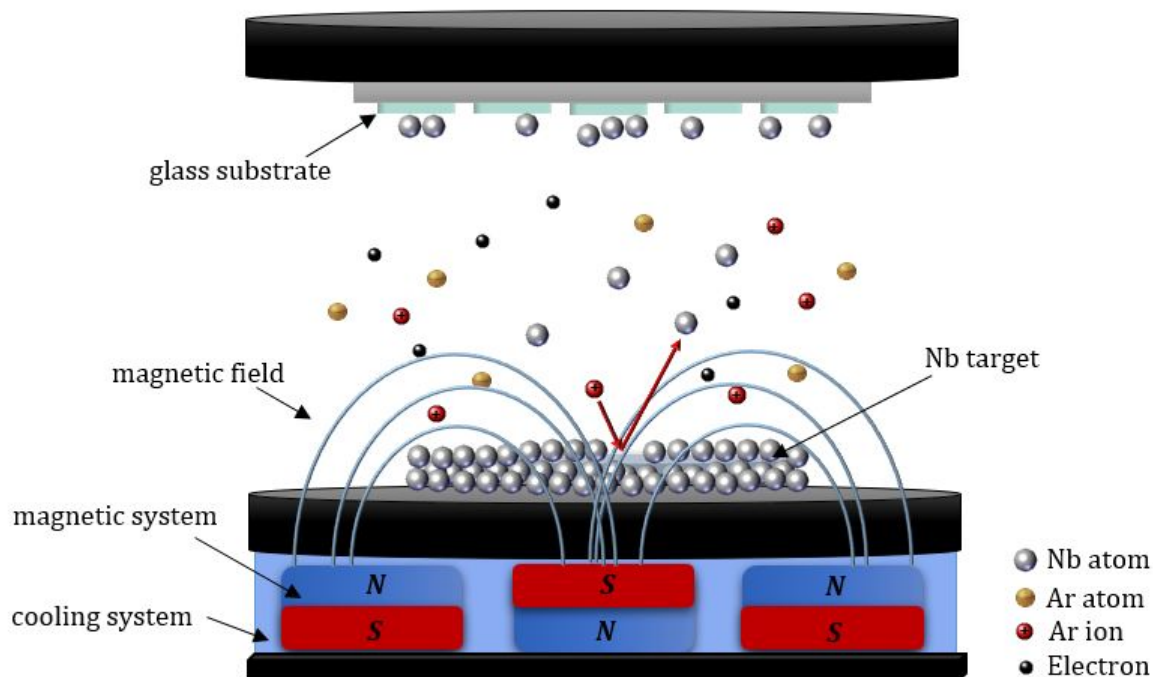


Figure 2.3: The RF-Magnetron Sputtering process. The power applied allows the formation of plasma (Ar^+ ions and free electrons) in the chamber containing Ar gas. Ar^+ ions in the plasma bombard the target surface striking out Nb atoms from the target. These atoms are collected on surfaces in their paths and eventually on the glass substrates.

Magnets behind the cathode are used to trap electrons in a magnetic field directly above the target surface. Extensive circuitous paths carved by these electrons, when trapped in the magnetic field, enhances their probability of ionizing Argon gas molecules. This, in turn, significantly increases the rate at which the target material is bombarded and subsequently deposited onto the substrate. The process is repeated at a constant rate until the desired thickness is achieved, then the power is removed from the cathode ending the process.

The privilege of using RF-power rather than DC-power becomes more significant when dealing with insulating targets such as the NbO_2 target. Basically, during sputtering, the working gas will be ionized, and as a result, many positive ions will be produced within the chamber and accumulate on the surface of the target. In the case where the target is conducting, free electrons in the target will neutralize the Ar^+ ions; however, if the target were insulating, the accumulated Ar^+ ions will remain attached onto the target surface which increases the density of defects in the films. When DC-power is used it would not be possible to remove those ions. In order to avoid this problem, an AC-power is used instead of DC, and as explained above during half a cycle bombardment of atoms occurs and during the other half, the surface of the target is cleaned.

In an RF-sputtering process, there are several parameters that affect the quality of the films. Argon pressure [141, 142], target-substrate distance [142, 143], sputtering power [141], substrate temperature [144] and post annealing temperature [145] are very important parameters that influence the structure, morphology and the deposition rate

of the deposited films. Moreover, as the sputtering machine differs, the range of a certain parameter may differ as well. In the sputtering machine used in this thesis, the ranges were constrained as follows:

Target – Substrate distance $H_{\text{substrate}}^{\text{target}}$: 6.5 cm to 9 cm

RF – Power : $P \leq 300\text{W}$

Argon pressure p_{Ar} : 0.01 mbar to 1 mbar

Substrate temperature $T_{\text{substrate}}$: RT to 600°C

In fact, the real temperature subjected onto the substrate was less than the input temperature as the system was not well thermally calibrated.

2.1.3 NbO₂ from Nb films by oxidation

In this method of fabrication, we have oxidized Nb thin films in two different approaches of which in only one of them we were able to detect the presence of the NbO₂ phase. However, before describing what was done it is better to get an insight on the oxidation process that takes place in a metal.

2.1.3.1 Oxidation Theory

The oxidation of a metallic thin film in an oxygen medium starts by the adsorption of oxygen at the surface of the film. The process involves two adsorption mechanisms: physisorption and chemisorption. In the former, van der Waals interactions bind the oxygen molecules to the metal surface, while in the latter the oxygen molecules are dissociated into oxygen atoms, then the valence electrons of the metal and oxygen atoms are rearranged and chemical bonds are formed.

Once the critical oxygen concentration is attained at the surface [146], the oxide clusters start to nucleate and coalesce to form a continuous layer which acts as a barrier. After this, further oxidation continues in the direction perpendicular to the surface.

Supposing that the oxygen molecules are dissociated at the oxide surface, and assuming that after dissociation they are charged, the progress of the oxidation reaction necessitates the diffusion of either the metal, oxygen or both species through the oxide layer. This diffusion is driven by a potential known as the Mott-potential [147] which exists between the positively charged interface and the negatively charged surface. The potential depends on the electronegativity between the metal and oxygen.

If the potential is strong enough, one of the species (or both) will diffuse through the oxide layer and continues the growth of the layer. The oxidation may take place at the surface in which the metallic ions diffuse from the interface to the oxide surface, or at the metal-oxide interface, where the oxygen ions diffuse from the surface to the interface (see figure 2.4). It can also happen that both species diffuse simultaneously and the reaction happens anywhere in the oxide. This all depends on the reacting species. On the other hand, if the Mott potential is not strong enough to diffuse any of the species, a passivating layer is created, and the oxidation process is ceased.

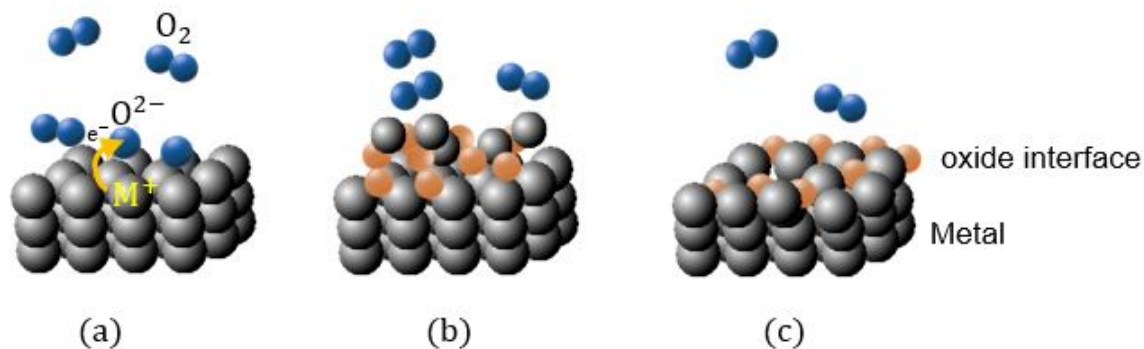


Figure 2.4: (a) First adsorption of oxygen molecules on the surface of the metal occurs. O₂ molecules are physisorbed at the surface by Van der Waals forces. Then chemisorption represented by metal-oxygen bonds takes place. An oxide layer is formed and further oxidation continues in a direction perpendicular to the surface. The oxide growth proceeds depending on the species (b) at the surface of the oxide layer, if the metal ions are diffusing or (c) at the metal-oxide interface if the oxygen atoms are diffusing.

2.1.3.2 First Approach: Oxidation by Slow Annealing

After Nb films were sputtered and characterized (to verify their composition and crystallinity), setup for film oxidation was prepared. The sample was fixed on the center of a 4 cm × 6 cm ceramic plate by a sample holder. Four 2 cm × 2 cm copper plates were fixed at the edges of the ceramic plate by screws and flat washers as shown in figure 2.5. Connections between the corners³ of the sample and the neighboring copper plate were made by wire bonding (25 μm aluminum wires), whereas connections between the copper plates and the measuring apparatus were done using 0.65 mm copper wires protected by ceramic pearls. This configuration allows to measure the sheet resistance of the sample during the oxidation process.

In this approach of niobium oxidation, the film was put in a furnace (47900 THERMOLYNE Furnace) in atmospheric pressure, and the temperature was gradually raised, while the sheet resistance was monitored. The oxidation was to be stopped (by taking the sample out of the furnace) once the desired NbO₂ sheet resistance was reached. Table 2.1 shows the resistivities of the main niobium oxides obtained from references and the expected sheet resistance for a film of 80 nm thickness.

The sheet resistance R_S was calculated using the following equation:

$$R_S = \frac{\rho}{t} \quad (2.1)$$

where ρ is the resistivity of the oxide and t is the thickness.

³The van der Pauw geometry for sheet resistance measurements requires that the connections are made at the peripheral of the measured material.

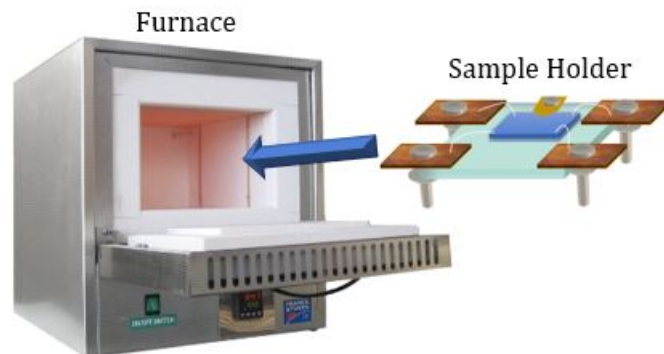


Figure 2.5: Schematic of the sample holder that was put in the furnace for monitoring the sheet resistance while the temperature was systematically increased.

Niobium oxide	NbO	NbO ₂	Nb ₂ O ₅
Resistivity ρ (Ω m) at 300°C	$\sim 3 \times 10^{-7}$ [148]	~ 2 [149]	> 1818 [150]
Sheet resistance R_S (Ω / \square)	3.75	2.5×10^7	2.27×10^{10}

Table 2.1: Niobium oxides resistivities at 300°C and the respective sheet resistance of each oxide for an 80 nm sample.

2.1.3.3 Second Approach: Oxidation by Flash Annealing

Another trial to reach the crystalline NbO₂ phase was by flash or sudden annealing of thin films of niobium. While remaining at atmospheric pressure, the temperature was raised to elevated temperatures (450°C or 500°C), and then a sample was deposited on a cylindrical ceramic placed in the same furnace previously used. Experiments at different time intervals were done and then the films were characterized. Unlike the previous experiment, the sheet resistance was not directly monitored due to the short time of phase change. Rather, the sheet resistance was measured ex-situ with a probe station, and then Raman Spectroscopy and XRD were performed.

2.1.4 Crystalline NbO₂ From Sputtered Amorphous NbO₂ films

Niobium dioxide thin films were also produced by RF-magnetron sputtering. A circular niobium dioxide target was bought from EDGETECH INDUSTRIES LLC. After sputtering with the appropriate parameters amorphous NbO₂ films were obtained. For crystallization, these films were then annealed in the furnace Nabertherm GmbH present at INSP, shown in figure 2.6, under vacuum (10^{-6} mbar $< p < 10^{-5}$ mbar) and at different temperatures. The furnace is equipped with a primary and a secondary pump, and a tube containing the sample holder which can be moved using a magnetic handle to put it in and out of the furnace. Crystallization results are discussed in the next chapter.



Figure 2.6: A photo of the furnace used to crystallize amorphous NbO_2 samples into crystalline NbO_2 .

2.2 Characterization Techniques

Raman spectroscopy and x-ray diffraction were performed to study the composition, phase and crystallinity of the samples, whereas Atomic Force Microscopy was used to measure the thickness of the films and to study the morphology of the samples' surfaces.

2.2.1 Raman Spectroscopy

Raman spectroscopy is a technique used to probe the vibrational modes (phonons) of a material in the range of optical frequencies (THz). It enables the extraction of different information about that material such as: the chemical content, bond properties, symmetries of a material, etc...

The phenomenon was discovered in 1928 by the Indian physicist C.V. Raman [151], for which he was awarded the Nobel Prize in 1930 [152]. It arises from the interaction of an electromagnetic wave with the optical phonons of the solid. The interaction results in two types of scattered radiations: i- elastically scattered radiations which have the same frequency ν_0 as the incident electromagnetic wave known as “elastic or Rayleigh scattering” ($\nu = \nu_0$); ii- inelastically scattered radiations that have different frequencies ν than that of the incident ($\nu \neq \nu_0$) known as Raman scattering. The latter process is 10^3 to 10^6 less probable to occur, thus the intensity of the Raman light will be much less than an elastically scattered one.

In Rayleigh scattering, the photon-phonon interaction polarizes the electron cloud and raises the molecule to a “virtual” energy state. This excitation has a very short life time (in the order of 10^{-14} seconds) after which the molecule returns back to its ground state accompanied by a photon emission. And since it has dropped back to its original state, then the photon released has the same energy as that of the incident, and eventually it has the same wave length ($\lambda = \lambda_0$).

On the other hand, after the photon-phonon interaction in a Raman scattering, the photons loose or gain energy during the scattering process. If the molecule is excited to a virtual state and then drops back to a higher vibrational state, then the emitted photon has less energy and a larger wave length ($\lambda > \lambda_0$) than the incident photon. This scattering is known as Stokes scattering. However, if the molecule was already in an excited state, and after scattering, it drops back to its ground state, then the emitted photon has more energy and a smaller wave length ($\lambda < \lambda_0$) than the incident photon. This is known as Anti-Stokes scattering. Figure 2.7 shows the different types of scatterings.

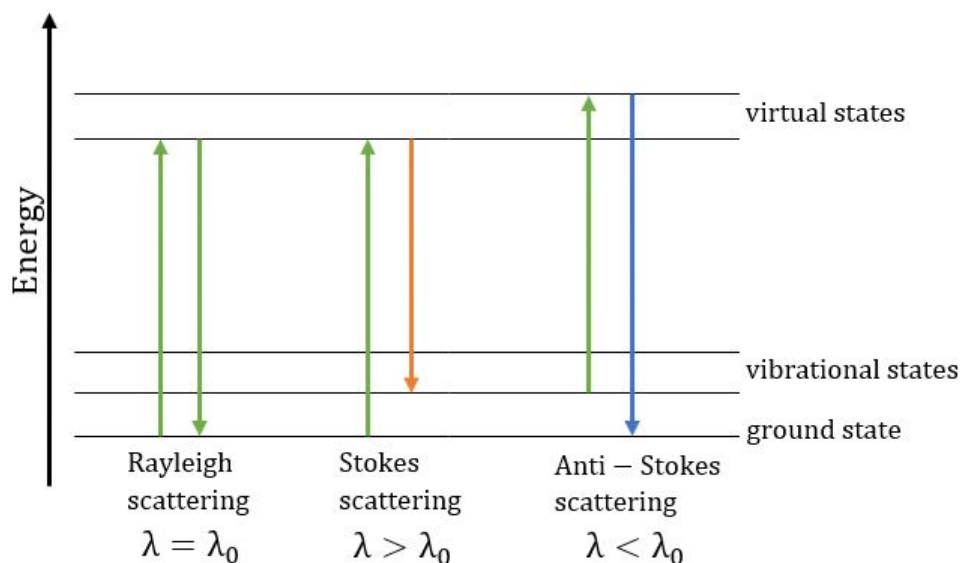


Figure 2.7: In a Rayleigh scattering, the molecule is excited to a virtual state due to the photon-phonon interaction, and returns back to its original state emitting a photon with the same energy. In Raman scattering, the photon-phonon interaction excites the molecule into a virtual state, and the molecule returns either to a higher vibrational state (Stokes scattering) emitting a lower energy photon or to a lower vibrational state (Anti-Stokes scattering) emitting a photon with a higher energy.

2.2.1.1 Origin of the Raman Effect

When emitted on a material, an electromagnetic wave of electric field \mathbf{E} interacts with the material via the dipole moment $\boldsymbol{\mu}$ of that material. At first order, $\boldsymbol{\mu}$ can be written as:

$$\boldsymbol{\mu} = \boldsymbol{\mu}_0 + \alpha \mathbf{E} \quad (2.2)$$

where $\boldsymbol{\mu}_0$ is the permanent (field free) dipole moment and α is the polarizability of the material. Raman effect is concerned with the second term $\alpha \mathbf{E}$ of the equation, where as the first term is related to the infrared absorption effect. In general, α depends on the orientation of \mathbf{E} , it describes the deformation of the electron clouds induced due to the presence of the presence of an EM wave. At first order, the induced dipole moment can be written as:

$$\mathbf{P} = \alpha \mathbf{E} \quad (2.3)$$

The dipole moment's periodic vibrations explain the emission of scattered radiation. Static polarizability α_0 is at origin of elastic scatterings, while oscillating polarizability due to molecular vibrations produces the Raman scattering.

For clarity, let us consider the simplest case of a homo-diatomic molecule, take for example: H_2 . This molecule has a stretching type of vibration of frequency ν_v or pulsation $\omega_v = 2\pi\nu_v$. The displacement of the atoms due to the vibration can be expressed as:

$$dR = R_0 \cos(\omega_v t + \beta) \quad (2.4)$$

where R_0 is the maximum displacement about the equilibrium position and β an arbitrary phase. This displacement is small, and for that the polarizability may be expressed as a Taylor expansion in the form:

$$\alpha = \alpha_0 + \left(\frac{\partial \alpha}{\partial R} \right)_0 dR \quad (2.5)$$

If we express the incident electric field of pulsation ω_0 as:

$$\mathbf{E} = \mathbf{E}_0 \cos(\omega_0 t) \quad (2.6)$$

Then:

$$\mathbf{P} = \alpha \mathbf{E} = \alpha_0 \mathbf{E}_0 \cos(\omega_0 t + \beta) + \left(\frac{\partial \alpha}{\partial R} \right)_0 R_0 \cos(\omega_v t + \beta) \times \mathbf{E}_0 \cos(\omega_0 t) \quad (2.7)$$

Which we can write as:

$$\mathbf{P} = \alpha_0 \mathbf{E}_0 \cos(\omega_0 t) + \frac{1}{2} \left(\frac{\partial \alpha}{\partial R} \right)_0 R_0 \mathbf{E}_0 \{ \cos[(\omega_0 - \omega_v)t - \beta] + \cos[(\omega_0 + \omega_v)t + \beta] \} \quad (2.8)$$

A closer look at the above expression shows that the induced dipole moments are created at three distinct pulsations: ω_0 , $(\omega_0 - \omega_v)$ and $(\omega_0 + \omega_v)$. The first corresponds to the incident frequency and thus elastic scattering. The second, represents the Stoke scattering. And the last term is for the Anti-Stoke scattering.

Eq.2.8 also shows that unless there is a change in the polarizability α , the Raman effect can not occur. That is to view a Raman scattering:

$$\left(\frac{\partial \alpha}{\partial R} \right)_0 \neq 0 \quad (2.9)$$

This is known as the selection rule for the Raman effect. If the previous relation is satisfied, a vibration is said to be Raman active.

2.2.1.2 Apparatus Configuration and Raman Spectroscopy on NbO_2

The internal optical system of the Raman spectrometer used in this thesis is presented in figure 2.9. The measurements were performed using Xplora Raman spectrometer (HORIBA Jobin-Yvon) shown in figure 2.8 in back scattering geometry and in ambient conditions.

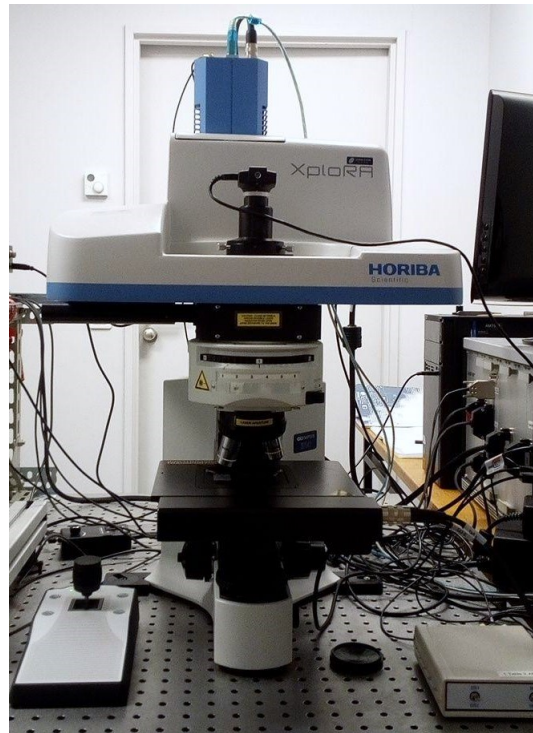


Figure 2.8: Photograph of the HORIBA Raman spectrometer present in our lab.

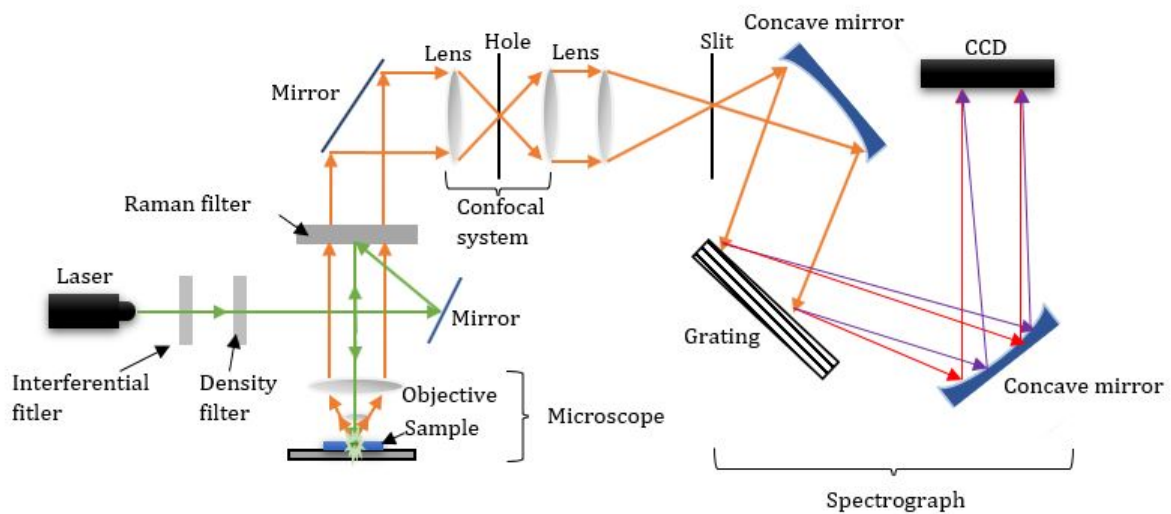


Figure 2.9: The Raman apparatus configuration.

The main parts of the apparatus are: the laser, the microscope, the confocal system and the spectrograph.

Two monochromatic wavelengths are available in the laser: 532 nm and 638 nm for green and red beam respectively. The laser power arriving at the sample is 12 mW; however, filters can be used to reduce the laser intensity arriving at the sample in order to avoid

damage that may be caused by heat. In our experiments, a 50% filter was used and thus a power of 6 mW. Then comes the microscope which is a crucial component of the system since it is responsible for the spatial resolution of the measurement. It has three objectives: 10 \times , 50 \times and 100 \times . The 100 \times objective has been used almost for all the measurements of thin films in this thesis because, thanks to its numerical aperture (NA) of 0.9, it is the objective with the best axial resolution compared to the former two objectives. Note that when using the green beam and the 100 \times objective, a spot of 0.72 μm strikes the sample. As for the slit and the hole, they are responsible for spectral and axial resolutions respectively. Finally, there is the spectrograph which is composed of a series of concave mirrors and a grating that separates the different wavelengths of the Raman signal (a grating of 1200 g/mm was used in our experiments).

The scattered light is detected by the CCD detector. Then the data are analyzed, and from the frequency and relative intensities of the Raman peaks it is possible to identify the material's composition and crystallinity.

2.2.2 Atomic Force Microscopy AFM

The first scanning probe microscopy (SPM) appeared in 1981 with the invention of the scanning tunneling microscope (STM) by Gerd Binnig and Heinrich Rohrer who were awarded a Nobel prize in physics in 1986 [153]. In the same year, another breakthrough was made by Gerd Binnig, Calvin Quate and Christoph Gerber, who invented the atomic force microscope (AFM) [154]. While the STM is restricted to conducting samples to allow the measurement of the tunneling current, the AFM can be used on any sample as it is based on van der Waals forces (VWF) between the tip and the surface. AFM is therefore more versatile than STM and has been used in this thesis on our insulating samples.

As shown in figure 2.10, a typical AFM apparatus consists of three main parts: a laser, a cantilever with a sharp tip mounted to a Piezoelectric (PZT) actuator and a position sensitive photodiode detector for receiving the laser beam reflected off the end-point of the cantilever.

The principle of AFM operation is to scan the tip over the sample surface with feedback mechanisms that enable the PZT scanners to maintain the tip at a constant force or height above the sample surface. The AFM can operate in three modes: non-contact mode, contact mode, and tapping mode. The interaction forces between the tip and sample in all of the three modes can be distinctly identified on a force–displacement curve like the one shown in figure 2.11.

In the non-contact mode, which is the one adapted in our measurements, the cantilever tip hovers about 50–150 Å above the sample surface to detect the attractive VWF acting between the tip and the sample. As the tip approaches the sample surface, the van der Waals attractive forces between the tip and the sample cause changes in both the amplitude and the phase of the cantilever vibration. These changes are monitored by a z-piezo system feedback loop to control the tip-sample distance. The precise high speed feedback loop prevents the cantilever tip from crashing into the surface keeping the tip sharp and leaving the surface untouched. By using the feedback loop to correct for these

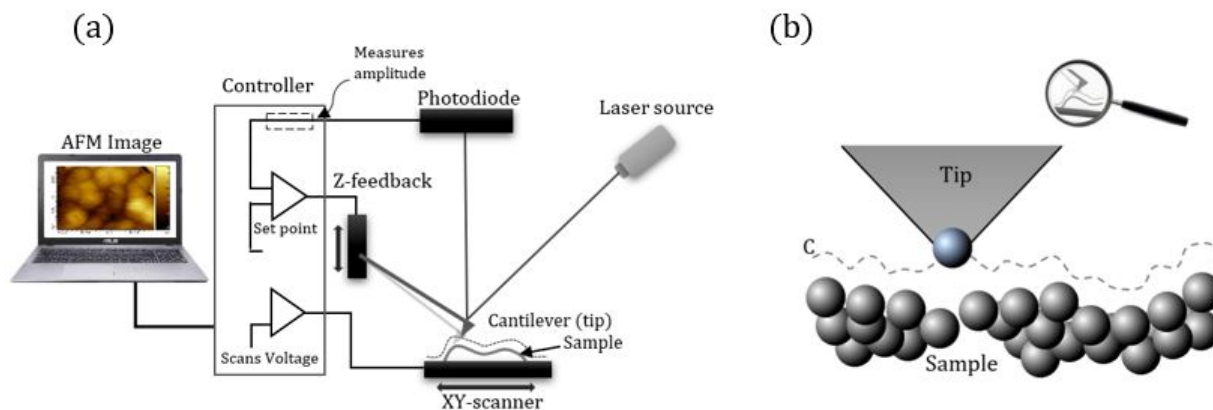


Figure 2.10: AFM apparatus: (a) Schematic of the AC operating mode of the AFM. The tip is made to oscillate by a function generator through a piezoelectric. A laser is emitted at the back of the oscillating cantilever. Deflections of the laser beam are recorder, and an AFM image is generated. (b) A magnified image of the tip hovering over the sample during the scan. Depending on the cantilever scanning mode, attractive or repulsive forces are taken into account.

amplitude deviations one can generate an image of the surface topography. Many data can be extracted from these images such as grain size [155], bonding angles [156], surface roughness [157], crystal shape [158], film thickness [159] etc... Since non contact-AFM imaging involves the tip hovering at a fixed distance away from the sample surface, the minimal tip-sample interaction yields better resolution than contact-AFM. In our studies, the setup used for AFM measurements is a Scanning Probe Microscope SmartSPM-1000 instrument (AIST-NT). We used it to determine the films' thicknesses and the surface morphology of Nb and NbO₂. AFM images will be displayed and discussed in the next chapter.

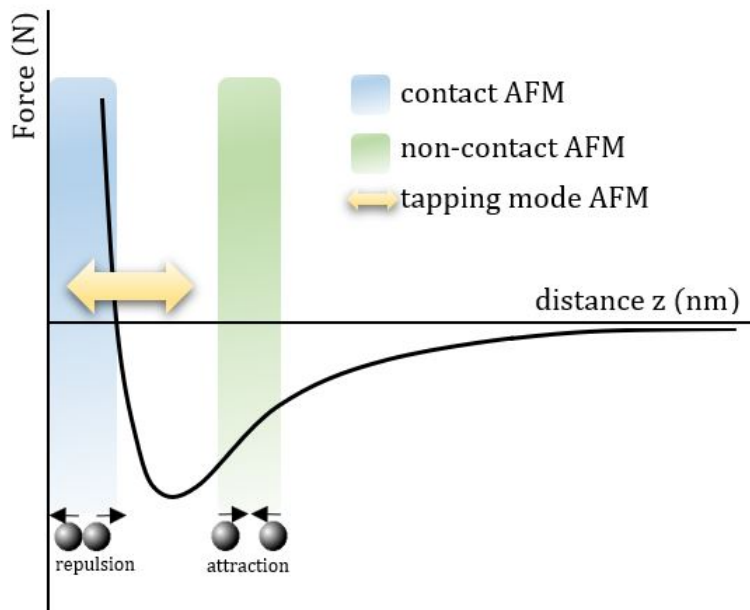


Figure 2.11: Different operating modes of the cantilever with respect to the van der Waal Forces between the tip and the sample. In contact AFM, as the tip-sample distance is relatively small, the significant forces are the repulsive forces. In non contact mode, as the tip-sample distance is relatively large, the significant forces are the attractive forces. In tapping mode, both attractive and repulsive forces are taken into account as the tip oscillates along the z-axis.

2.2.3 X-Ray Diffraction

In a crystalline solid, the lattice spacing between two atoms is in the order of an angstrom (10^{-10} m). Therefore, to produce a diffraction pattern, the electromagnetic probe must be at this order of magnitude, or, energetically speaking the radiation must have an energy of:

$$\hbar\omega = \frac{hc}{\lambda} = \frac{hc}{10^{-10}} = 12.4 \text{ keV} \quad (2.10)$$

Such high energies are characteristics of X-ray radiations. And this makes X-ray Diffraction (XRD) technique a powerful non-destructive tool commonly used to characterize crystal structures. The XRD instrument used in this thesis is PANALYTICAL X'pert Pro MPD diffractometer shown in figure 2.12⁴, and the wave length we used is the copper K_{α_1} with wave length $\lambda = 1.5406 \text{ \AA}$, or cobalt K_{α_1} with wave length $\lambda = 1.7902 \text{ \AA}$.

⁴Note that in all the XRD diffractograms a polinomial background is substracted.

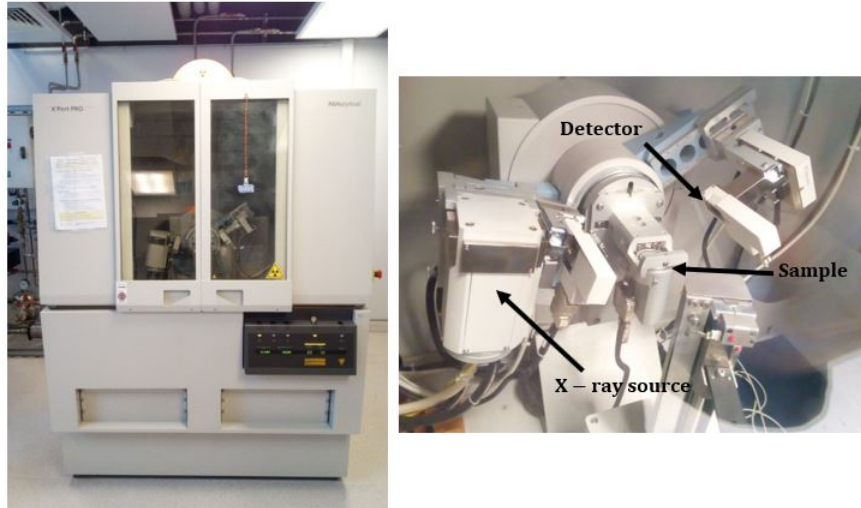


Figure 2.12: Photo of the x-ray diffractometer used to perform XRD measurements.

2.2.3.1 X-ray Diffraction Principle

In 1913, William Henry Bragg and William Lawrence Bragg [160] discovered that a crystalline material gave remarkably characteristic patterns when subjected to X-ray radiation.

Consider an array of a 2-dimensional lattice with lattice spacing d as shown in figure 2.13. When x-rays of wave length λ arrive at the crystal lattice, they are scattered off the lattice planes by the surrounding electrons and reflected in all directions at different angles. Only those rays that are specularly reflected may interfere constructively according to the following equation:

$$n\lambda = 2d_{hkl}\sin\theta \quad (2.11)$$

where n is an integer known as the order of reflection, d_{hkl} is the distance separating the family of planes (hkl) and θ is the angle of incidence of the x-ray.

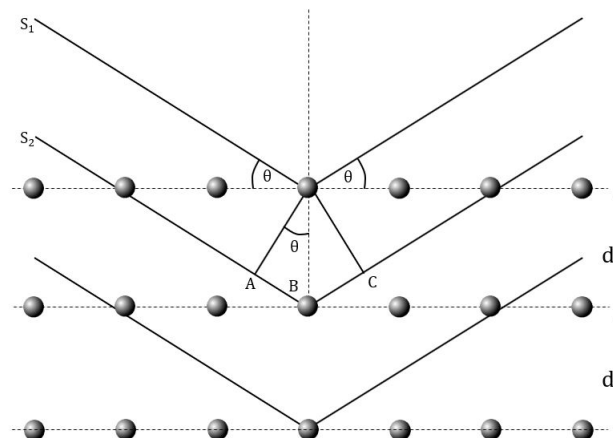


Figure 2.13: Illustration of Bragg's law in the real space. X-rays reaching the sample will diffract only when the path difference between the reflected rays leads to a constructive interference, i.e $n\lambda = 2d_{hkl}\sin\theta$.

Different geometries can be used to measure diffraction patterns, such as the "Bragg-Brentano" (a.k.a " θ - 2θ ") geometry where source and detector move symmetrically around the sample, or the "Grazing Incidence" geometry where the X-ray source is fixed. The difference between the two geometries is shown in figure 2.14.

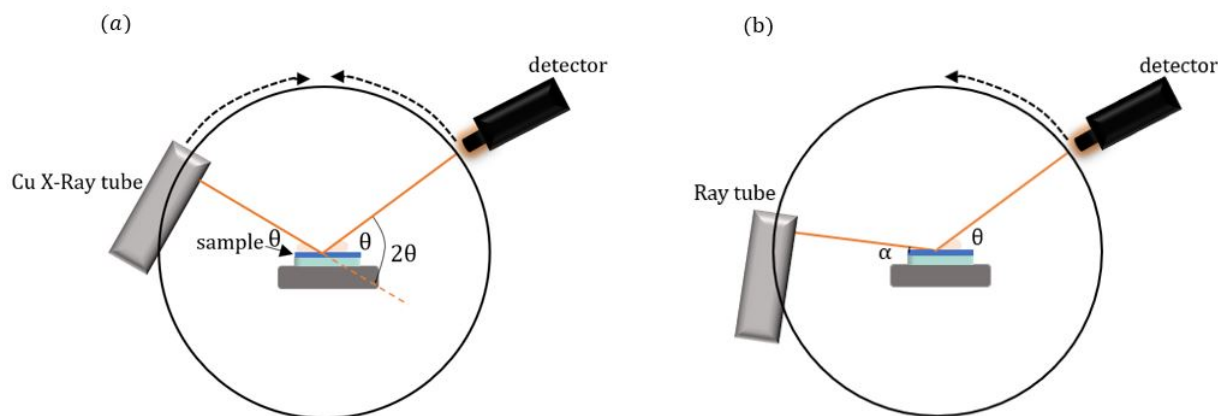


Figure 2.14: (a) Bragg Brentano geometric configuration: both the x-ray source and the detector move simultaneously at an angle θ w.r.t the sample surface. (b) Grazing Incidence configuration: The source is fixed at a very small angle α w.r.t the sample while the detector rotates and collects diffracted radiations from the film.

In symmetrical reflection, 2.14 (a), the angle of incidence and the angle of reflection are both equal, and they range from several to few tens of degrees, for example in our experiments we worked in a window of 20 - 90° . This results in a deep penetration of the x-ray radiation into the sample (tens of microns in general). In the case where the substrate is a crystalline material like silicon, and the film is much thinner than the substrate, intensive peaks will be collected from the substrate. However, when an amorphous substrate such as glass is used, only peaks from the film will appear regardless of the measurement geometry. In this configuration, upon scanning the sample, both the source and the detector are made to rotate at the same rate and the detector records the diffraction intensities from the thin film.

On the other hand, when the film is very thin, an asymmetrical-reflection measurement would be more suitable. In such configuration, the angle of incidence is kept constant at a very small angle, for example we used 1° , while the detector is set to rotate up to several tens of degrees. By that, the penetration depth can be decreased drastically and the background signal is suppressed, and the footprint of the beam increased on the sample. This also results in a lowering of resolution due to the apparent source size.

The thicknesses of our Nb and NbO₂ films ranged between 5 and 330 nm, i.e, they are relatively very thin compared to the substrates' thicknesses which are 0.5-0.55 mm for glass substrates and $0.279 \pm 25\mu\text{m}$ for Si (100) substrates. However, as mentioned above the glass substrates will not produce any new peaks as they are amorphous, so we used both configurations, and indeed, in the asymmetric the background contribution was less intense compared to the symmetric one. As for films on silicon wafers, the silicon peaks are easily identified in either configuration.

2.2.3.2 Grain Size Estimation From Diffraction Peaks

Peak analysis of the diffraction pattern allows us to extract several pieces of information of the studied material. In figure 2.15, from the peak's position 2θ we can find the distance between reflection planes (hkl). Another important parameter which we can measure from a peak is the grain size of the material oriented in a certain direction (at a certain peak position). This is calculated by finding the full width at half the maximum intensity (FWHM). Then substituting convenient values in the Scherrer equation [161], we can estimate the corresponding grain size.

$$L = \frac{K\lambda}{\beta \cos\theta} \quad (2.12)$$

where L is the grain size, K is a dimensionless shape factor close to unity and β is the FWHM. The peak positions and FWHM's in this study were obtained after subtracting the background and fitting the peaks by Gaussian functions in order to have more precise results.

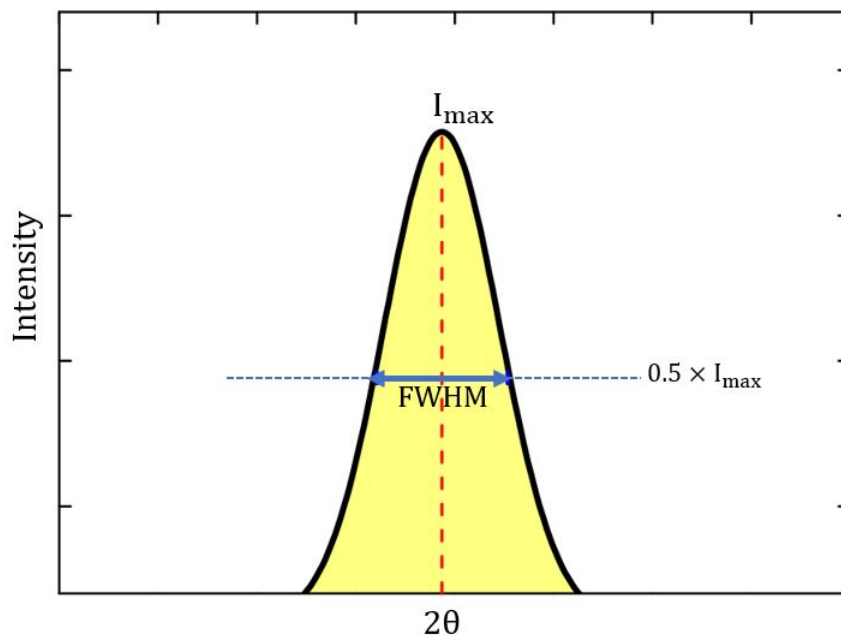


Figure 2.15: A typical x-ray diffraction peak. Grain size of the relevant peak can be estimated from the FWHM of the peak, and the inter planar distances can be derived from the peak's position 2θ .

2.3 Device Fabrication and Measurement Techniques

After the films were deposited on glass and silicon substrates and then fully characterized, devices with these samples were fabricated. The device fabrication required that the samples were first shaped, and then gold contacts were deposited on top using shadow masks. The masks were structured to deposit contacts in the van Der Pauw geometry.

2.3.1 The van der Pauw Method

The van der Pauw method was developed by Leo J. van der Pauw in 1958 [162]. It is a technique widely used in 2D materials to measure the resistivity and the Hall coefficient of a sample. From these measurements, one can extract other information such as the doping type (p or n), the sheet carrier density and the mobility of the majority carriers. The strength of this method lies in that it can explore the properties of a material regardless of its shape as long as a few conditions are satisfied: the sample must have no isolated holes in the tested region, it should be flat with a uniform thickness, the sample should be homogeneous and isotropic ⁵, the contacts must be placed at the peripheral of the sample and their areas are required to be much smaller than that of the sample itself (at least by one order of magnitude) [163].

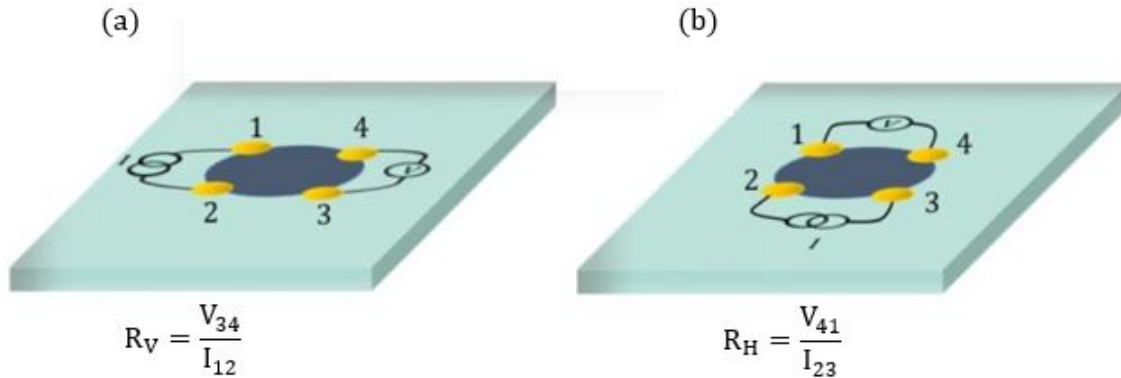


Figure 2.16: The van der Pauw geometry. (a) Current is injected and collected along contacts 1 and 2, meanwhile the voltage V_{34} is measured. Then R_V is calculated. (b) The current is injected and collected along contacts 2 and 3 and the voltage V_{41} is measured. Then R_H is calculated. These two resistances are then substituted in the sheet resistance equation for obtaining the sheet resistance of the film.

To explain how the sheet resistance R_S is measured consider the illustration in figure 2.16. The sample deposited on glass is shaped in a circular form and the gold contacts are deposited on the edges of the sample as shown in the figure. The contacts are numbered from 1 to 4 in a counter-clock wise manner. First, a direct current I is injected at contact 1 and collected at contact 2 (I_{12}), and the direct voltage V_{34} ($V_4 - V_3$) is measured. Then a resistance $R_{12,34}$ is calculated such that:

$$R_{12,34} = \frac{V_{34}}{I_{12}} \quad (2.13)$$

⁵In the case of anisotropic samples, there will be more than one resistivity (ex. ρ_x, ρ_y) depending on the direction.

A similar measurement is done, but this time the current is made to flow from contact 2 to 3 (I_{23}), and the voltage V_{41} is measured. The resistance $R_{23,41}$ is thus:

$$R_{23,41} = \frac{V_{41}}{I_{23}} \quad (2.14)$$

Van der Pauw showed that the actual sheet resistance can be calculated from the above two resistances by the relation:

$$e^{-\pi R_{12,34}/R_S} + e^{-\pi R_{23,41}/R_S} = 1 \quad (2.15)$$

In the case where the sample is perfect in terms of shape and homogeneity then the two resistances $R_{12,34}$ and $R_{23,41}$ are equal ($R_{12,34} = R_{23,41} = R$), R_S will be:

$$R_S = \frac{\pi R}{\ln 2} \quad (2.16)$$

A more precise value of R_S can be obtained by measuring the reciprocal of each of the resistances calculated above. That is, in the first case, instead of feeding contact 1 with current, collecting it at contact 2 and measuring V_{34} , current is injected in contact 3, collected in contact 4, and V_{12} is measured. $R_{34,12}$ is then calculated. And similarly we find $R_{41,23}$.

A further improvement can be done by measuring the above resistances while reversing the polarity of the current source and the voltmeter⁶, i.e. calculating $R_{21,43}$ and $R_{43,21}$, and a similar approach is done for the resistances along the horizontal direction. Finally, an average is taken for the vertical and the horizontal resistances R_V and R_H respectively :

$$R_V = \frac{R_{12,34} + R_{34,12} + R_{21,43} + R_{43,21}}{4} \quad (2.17)$$

and

$$R_H = \frac{R_{23,41} + R_{41,23} + R_{32,14} + R_{14,32}}{4} \quad (2.18)$$

The final equation for R_S can be written in the form:

$$R_S = \frac{\pi}{\ln 2} \frac{R_V + R_H}{2} f \quad (2.19)$$

where f is a correction factor which take takes into account the inhomogeneity of the sample through the ration r , where r is defined as:

$$r = \frac{R_V}{R_H} \quad \text{if } R_V < R_H$$

⁶The advantage of reversing polarity is canceling out any offset voltages such as the thermoelectric potentials caused by the Seebeck effect.

or

$$r = \frac{R_H}{R_V} \quad \text{if } R_H < R_V$$

and f is given by the implicit equation:

$$\cosh\left(\frac{r-1}{r+1} \frac{\ln 2}{f}\right) = \frac{1}{2} \exp\left(\frac{\ln 2}{f}\right) \quad (2.20)$$

As can be seen from the above equation f can not be derived analytically and is calculated numerically. The graph of f present in van der Pauw's paper [162] is shown in figure 2.17.

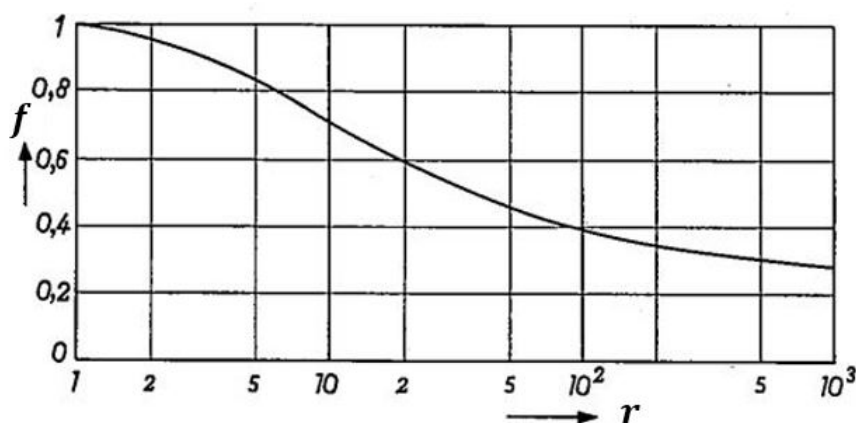


Figure 2.17: Graph representing the relation between the correction factor f and the ratio r of vertical and horizontal resistances [162].

The resistivity ρ is then calculated by multiplying the sheet resistance R_S with the thickness t of the material.

$$\rho = R_S t \quad (2.21)$$

2.3.2 Sample Shaping

Shaping the sample helps improve the accuracy of the measured sheet resistance. A more symmetric sample would lead to better results. However, niobium metal and its oxides are difficult to etch. One way to etch niobium is by exposing a sample to a microwave glow discharge in a Cl_2/Ar mixture [164], but this method was not available in the lab. Another way is to chemically etch it by using hydrogen fluoride acid (HF) acid or a mixture of acids where HF is one of its reactants [165]. Unfortunately, upon testing the effect of HF on a niobium film deposited on glass, we noticed that HF was also *attacking* the glass substrate beneath the film.

A successful way to shape the samples was to define the shape before the deposition of the films as follows: After the glass substrates were cleaned, all the glass surface was covered with PMMA except for a region with the shape of interest. The substrate was put on a hot plate for 90 s at 180°C so that the PMMA bakes [166]. Then the sputtering was done. After sputtering, the samples were put in acetone solution for 30 min at $\sim 50^\circ\text{C}$, and the PMMA was removed, along with the film deposited on top, leaving on the glass only the

uncovered region (where niobium/niobium dioxide exists). However, the melting point of PMMA is $\sim 220 - 250^\circ\text{C}$ [167] which makes an upper limit for the substrate temperature used so that the PMMA does not melt and pollute the target or the sputtering chamber. Yet it is still efficient when the substrate is at relatively low temperatures. Figure 2.18 shows an outcome of such a shaping approach.

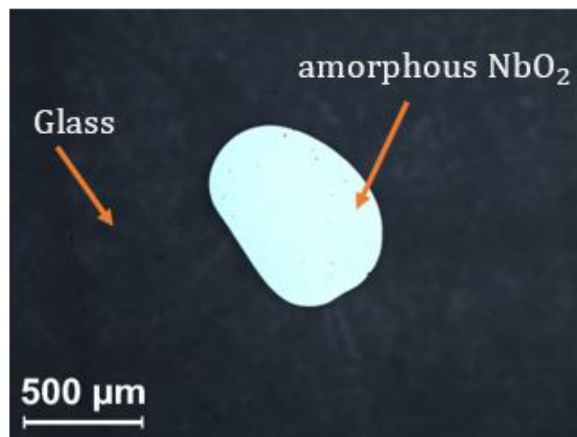


Figure 2.18: Sample shaping obtained by procedure involving PMMA.

Due to temperature limitations described above, using this method was not really recommended. So, we have finally shaped the samples mechanically. That was done by scratching the NbO_2 film on the glass using a diamond pen in a way that we conserve the van der Pauw geometry. Figure 2.19 shows a schematic of shaping the glass. The scratches between the contacts were made to isolate the contacts from each other in the directions perpendicular to the scratches, and so that the whole measurement would take place in the central region of the film. The scratches on the film under the gold contacts were made so that the gold reaches the glass at some regions for the sake of the Space Charge Doping technique.

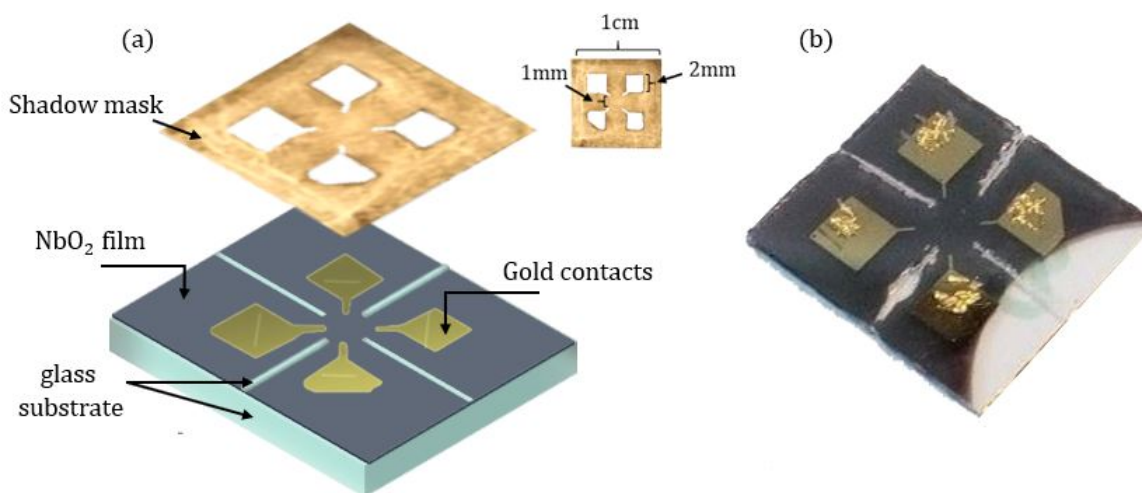


Figure 2.19: (a) The NbO_2 film of the glass substrate was scratched, then gold was deposited in van der Pauw geometry on top of the film. The dimensions of the mask are also shown. (b) A sample after such a shaping method was done on it.

On the other hand, for samples with Si or SiO₂ substrates thermal resistant scotch tape was used to deposit the gold contacts, and the contact shapes were a little different, see figure 2.20. In addition to sheet resistance measurements, we wanted to study lateral and vertical properties of the film. After the gold deposition, small gold precursors were hammered and flattened to form smooth plates, and then they were stuck on the gold contacts using silver paste. The reason for this step is to avoid the penetration of the needle probe used in wire bonding into the inner layers of the film/substrate.

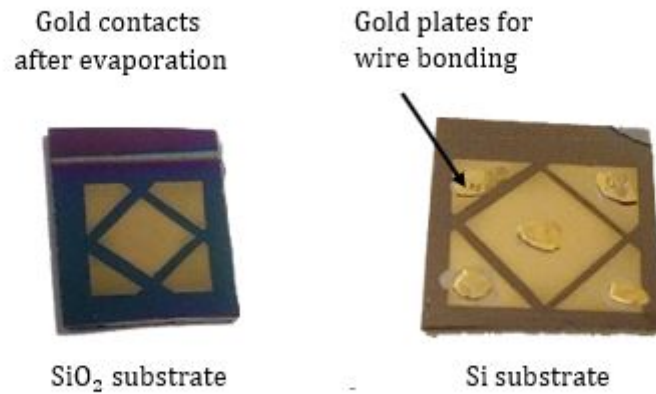


Figure 2.20: Gold contact geometry on Si, SiO₂ substrates. Thermal resistant scotch tape was used to mask the films.

2.3.3 Gold Contact Deposition

Gold contacts had to be deposited on the samples for the sake of measurements. In order to deposit the gold in a defined shape, shadow masks or thermal resistant scotch tape was used depending on the device to be fabricated. The deposition was made in the clean room of INSP laboratory using the Evaporator “VINCI PVD-4E” shown in figure 2.21. In this evaporator, almost all procedure are automatically done. The *recipe* of interest is chosen from the computer and the system takes care of the rest. However, the principle of functioning of the Edwards Evaporator is briefly explained.



Figure 2.21: Photo of the evaporator used for gold contact depositions.

The chamber of the evaporator is a cylinder with a height of ~ 70 cm and a diameter of ~ 45 cm. At the top of the inner part of the chamber there is a sample holder with a large mask beneath it, and at the bottom lie three crucibles of different metals each having a mask on top. First, the chamber is evacuated until pressure is less than 5×10^{-6} mbar. The crucible is heated by a flow of current running through it, and when the temperature of gold evaporation is reached and the evaporation is steady, the mask is opened above the gold crucible as well as below the sample holder and gold is deposited on the samples. When the process is done, the venting of the chamber is achieved by injecting N_2 . Usually, a thickness of 100-150 nm of gold was deposited onto the samples.

After the contacts were deposited, connections between the cryostat sample holder copper pads and the sample contacts were made via wire bonding technique using 25 microns aluminum wires.

2.3.4 Measurement Setup

A schematic of the apparatus which was used to perform the different electronic experiments is shown in figure 2.22. First, the sample is mounted on a cryostat, then air is pumped out where a vacuum $< 10^{-6}$ mbar can be attained. This cryostat uses a heater and liquid He flow to reach temperatures in the range 3 - 420 K. The cryostat is placed inside an electromagnet capable of reaching a magnetic field of 2 T.

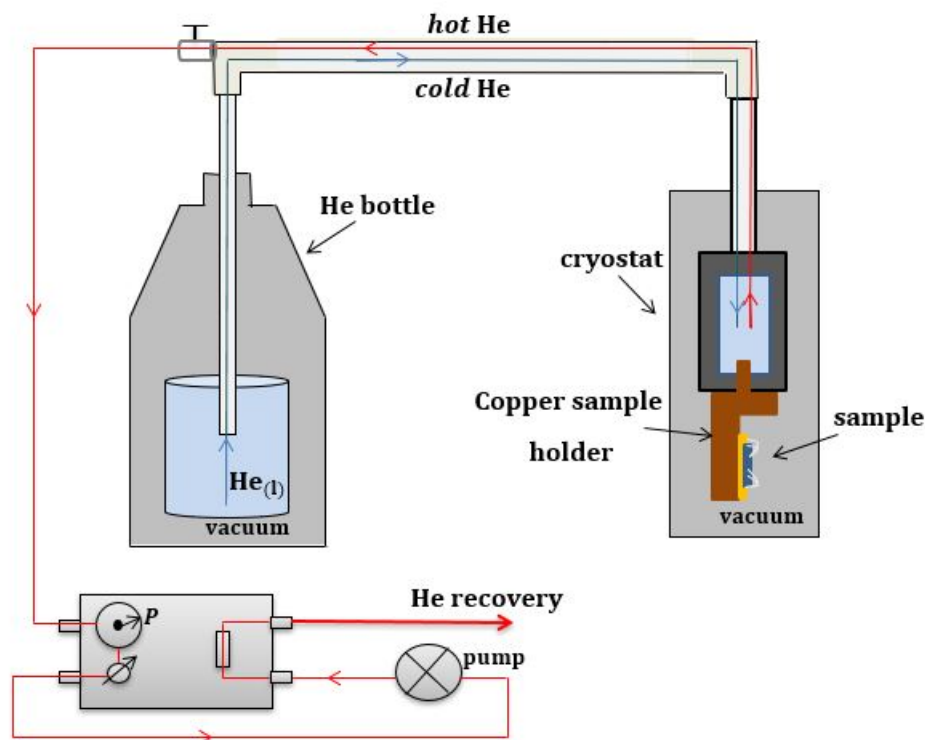


Figure 2.22: A schematic showing the measurement apparatus. The sample is mounted on a cryostat. A heater allows the increase in temperature, while $\text{He}_{(l)}$ is used to drop the temperature.

2.3.5 Glass Structure

Glass, e.g. soda-lime, is made of an amorphous silicon oxide network with SiO_4 tetrahedrons as building blocks. It also includes sodium and calcium oxides as network modifiers [168], see figure 2.23. Once these modifiers are introduced along with SiO_2 , some of the Si-O-Si bridges are broken. The non-bridging oxygen units (NBO) become the anionic counterparts of Na^+ and Ca^{2+} . The covalent bonds between the silicon atoms and oxygen atoms are strong bonds, and so are the divalent ionic bond between Ca^{2+} and O^{2-} . This makes the Na^+ ions the most mobile species in the structure. At room temperature, the ionic conductivity is negligible. However, when enough thermal energy is provided the ionic mobility is activated and the conductivity increases.

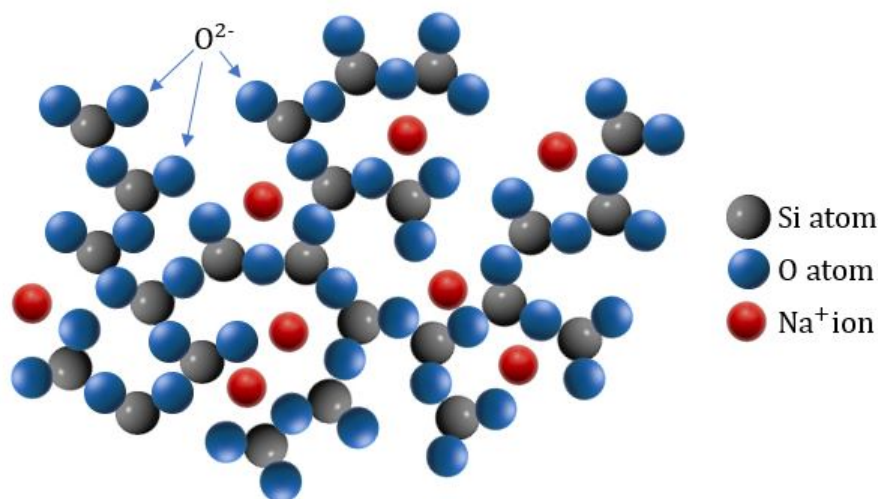


Figure 2.23: Glass atomic structure. Firm silicon oxide bonds compose the building block of glass, and *free* unbridged sodium ions are randomly distributed over the structure. The non-bridging oxygen form the anionic counterparts of Na and Ca cations.

An externally applied electric field can trigger a drift in the Na^+ in the direction of the field. A test for the activation temperature of the mobility was made by applying 10 V and monitoring the current. It was found that the activation temperature is ~ 340 K, see figure 2.24. At any time, the ionic mobility can be diminished by a rapid cooling of the system using $\text{He}_{(l)}$. The ions are then *frozen* in their sites.

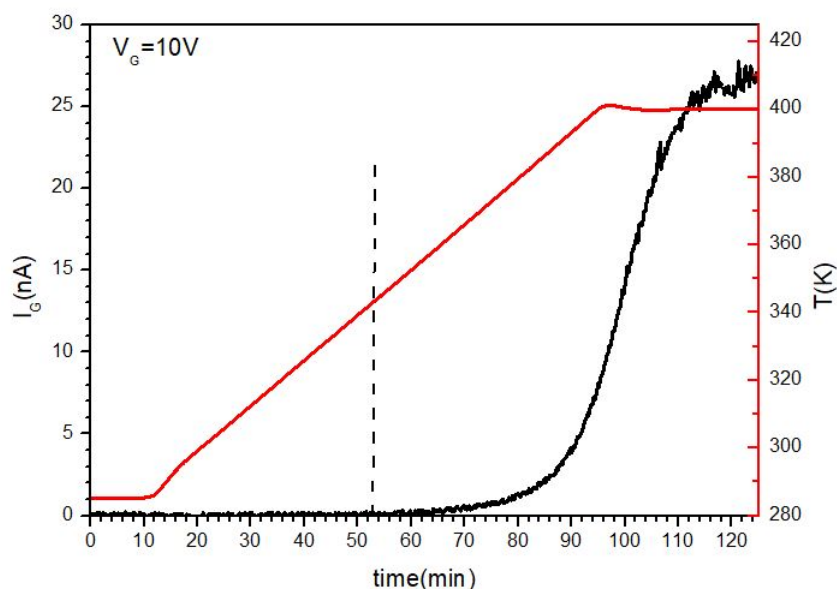


Figure 2.24: Testing the mobility of ions through the glass while applying a voltage $V_G = 10\text{V}$ and increasing the temperature to 400K. The current starts to increase at ~ 340 K which defines the thermal activation energy for ionic mobility in soda-lime glass.

Since soda-lime glass has typically a higher concentration of sodium ions than other conventional glasses such as borofloat, it is more efficient for the space charge doping technique describe hereafter.

2.3.6 Space Charge Doping Technique SCD

Space Charge Doping is an electrostatic doping technique invented by my host team, led by Professor A.SHUKLA, in the year 2015 [37]. This technique exploits the motion of Na^+ ions in its doping mechanism. The doping process is schematized in figure 2.25 below.

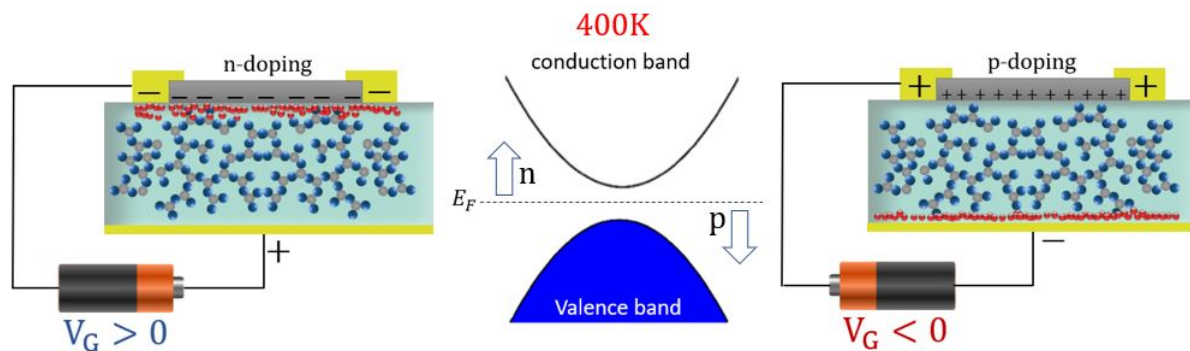


Figure 2.25: The space charge doping technique. The left side of the figure shows the n-doping of the film deposited on glass as a consequence of positive voltage application at the gate. The right side shows the p-doping process in which a negative voltage is applied at the gate. In the middle, the Fermi level shifts towards the conduction band with n-doping, or towards the valence band with p-doping.

In the beginning, the system is pumped to low pressure ($\sim 10^{-6}$ mbar). After this, the temperature is raised up to 400 K where the Na^+ ions are now free to move in random motion. To n-dope the 2D film, a positive voltage is applied at the gate, figure 2.25 (left). This causes Na^+ ions to migrate to the opposite side of the glass and create a positive space charge. Hence, the top layer of glass is now positively charged. This in turn causes the attraction of more electrons to the bottom layers of the film, eventually n-doping it, and thus shifting the Fermi level towards the conduction band. An electrostatic field in the range of 10^9V/m is created between these oppositely charged layers (positive layers in glass and negative layers in the film). The field along with the doping, can be conserved by quenching the system while keeping the voltage applied. In this way, the Na^+ ions' mobility is suppressed and they become fixed at the interface with the doped film. Similarly, to p-dope the film, a negative gate voltage is applied at the gate, see figure 2.25 (right), causing the migration of Na^+ ions towards the bottom layers in the glass leaving the top part negatively charged due to the presence of the non-bridging oxygen which in turn leads to the repulsion of electrons in the film leaving empty sites behind and thus a positively charged film. This means that the Fermi level will shift towards the valence band. The voltage range used with this technique was between -280 V and +280 V when p or n doping respectively, and studies were made at temperatures between 3 and 400 K.

The electrostatic Space Charge Doping Technique has been applied on different materials, and it has shown pleasant results. With $\text{Bi}_2\text{Sr}_2\text{CaCu}_2\text{O}_{8+x}$ (BSCCO) samples, for example, a carrier density beyond 10^{14}cm^{-2} ($\sim 1 \times 10^{15} \text{cm}^{-2}$) was reached [169]. It has also shown to be reversible [37] i.e. it is possible to dope then undope a film. Furthermore, since the technique is an electrostatic technique and does not involve the introduction of foreign material in the doping process, this keeps the film safe of unwanted chemical reactions that may occur in other doping process such as chemical doping.

Chapter 3

NbO₂ Thin Film Synthesis

3.1 Introduction

In this chapter the different synthesis techniques to obtain NbO₂ thin films with correct structure and stoichiometry are discussed. Synthesis was done on different substrates: glass (amorphous), single crystalline and polycrystalline Si substrates. Two approaches were considered; one by depositing Nb films followed by ex situ oxidation, and the other was depositing directly from a stoichiometric NbO₂ target followed by an in situ annealing of the films. In the latter approach, we were able to synthesize nanocrystalline NbO₂ thin films. This chapter is the basis of a manuscript which has been submitted for publication.

3.2 Nb Thin Film Preparation

We have discussed at length the reasons for studying NbO₂ thin films and devices in Chapter 1. Most earlier work concerns the study of NbO₂ based devices [16, 24, 135, 170, 171]. These devices show an insulator-metal like transition on the application of current, or more accurately, a current controlled negative differential resistance regime [24]. While devices often use variable stoichiometry NbO_x (with x varying from 2 to 2.5) and amorphous as-deposited phases which eventually crystallize with temperature or voltage [135], it is desirable to directly grow the NbO₂ phase, both amorphous and crystalline, on a variety of substrates, using a single, reproducible method. Numerous works have reported the growth of NbO₂ films using different evaporation [28, 74, 79, 172], deposition [1, 173, 174] or sputtering techniques [79, 178, 179, 181–185] with either in-situ or post-deposition oxidation and crystallization and on a variety of substrates ranging from glass, aluminum oxide to single crystal silicon. Note that the bulk resistivity of NbO₂ is $1 \times 10^4 \Omega\text{cm}$ [1] and that of Nb₂O₅ is $2 \times 10^7 \Omega\text{cm}$ [186]. In between these two phases NbO₂ (Nb charge state 4+) and Nb₂O₅ (Nb charge 5+) several non-stoichiometric, polymorphic or meta-stable phases exist which complicates fabrication of pure phases, especially that of NbO₂ [?, 1, 28, 74, 79, 172–174, 178, 179, 181–185].

The choices made for the fabrication of NbO₂ films were driven by the objectives of this thesis and the material constraints with respect to available equipment and techniques. We also made the fundamental decision to fabricate films ourselves instead of collaborating with a group already possessing the expertise. This, despite the inherent difficulty in doing so because we felt the need to have complete mastery over the sample, given the

complexity of the phenomena involved and also so as to maintain flexibility on sample availability and number according to experimental needs.

The objectives fixed by the thesis were to examine the possibility of electrostatically doping NbO₂ across an insulator-metal transition on one hand and to investigate the mechanisms of the CC-NDR phenomenon on the other. While CC-NDR can be investigated on films grown on various substrates, electrostatic doping is only possible on glass substrates as explained in earlier chapters. The decision was thus taken to grow films on glass (amorphous and insulating), SiO₂ on Si (polycrystalline and insulating) and Si (single crystal and semiconducting) substrates.

The material constraints were that we had access to thermal evaporation and RF-magnetron sputtering techniques, without the possibility of in-situ oxidizing atmosphere. Post-annealing could be in air or in non-oxidizing Argon atmosphere. Given the high evaporation temperature of Nb, we thus decided to use the sputtering method exclusively with two types of targets, a pure Nb target and a stoichiometric NbO₂ target. Films could thus be oxidized in air at high temperature or annealed in a non-oxidizing atmosphere after deposition. All these routes were tried as explained below, until the optimal solution was found.

Recall that in the Space Charge Doping technique the most important region in the doping process is the glass-film interface. This is where all the action takes place. Indeed, it was required to have a few layer film on the glass substrate. Thin films of ~ 47 nm thickness were prepared using RF-magnetron sputtering according to the parameters stated in table 3.1.

Parameter	Target Etching	Substrate Etching	Deposition
Ar pressure (mbar)	0.5	0.1	0.1
power (Watts)	100	100	100
tension (V)	450	400	400
target-substrate distance (cm)	8	8	8
substrate temperature (°C)	300	300	300
rate (nm/min)	31.5	-	31.5

Table 3.1: Parameters used to obtain thin Nb films of thickness ~ 47 nm.

The deposition was made on borofloat and soda lime glass substrates. After the deposition, XRD was performed to test the samples' crystallinity. A copper K_α x-ray source was used of wavelength 1.54 Å. Moreover, since the films are relatively thin (relative to the substrate thickness) the setup was made in the grazing incidence geometry. The results of a film on soda lime glass sample and a borofloat glass sample, after subtracting the polynomial background, are shown in figure 3.1 with their respective peak fittings which were done using the Gaussian function.

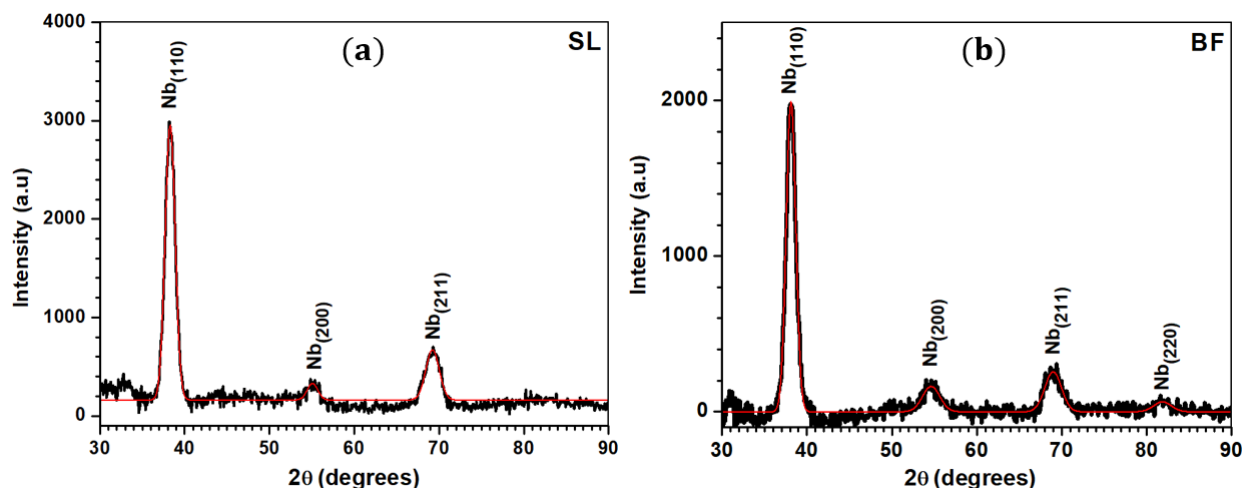


Figure 3.1: X-ray diffraction patterns for a 47 nm thin film on (a) Soda lime glass substrate (b) Borofloat glass substrate with the relative Gaussian peak fitting of each (red color). (XRD was performed using $\text{Cu K}\alpha_1$ radiation).

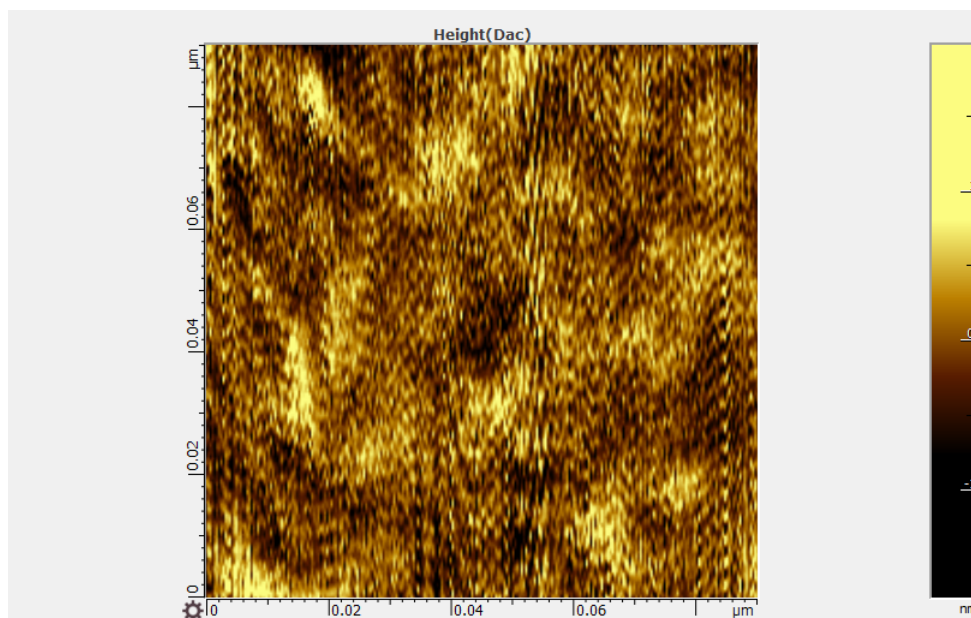


Figure 3.2: AFM image of a niobium thin film on soda-lime glass substrate. The film is polycrystalline film of grain size in the order of few tens of nm.

3.3 Nb Oxidation by Slow Annealing

Following their characterization, the films were set up in the oxidation-in-air apparatus described earlier in section 2.1.3.2. We expected *jumps* in the sheet resistance¹ in time as the temperature was increased with a ramp when the oxygen stoichiometry changed from one oxide phase to another as illustrated schematically in figure 3.3. The annealing was made at a rate of $\sim 1.5^\circ\text{C}/\text{min}$ and held at 300°C for monitoring.

¹The values of the sheet resistance in the graph are chosen according to the expected sheet resistances of the main niobium oxides in table 2.1.

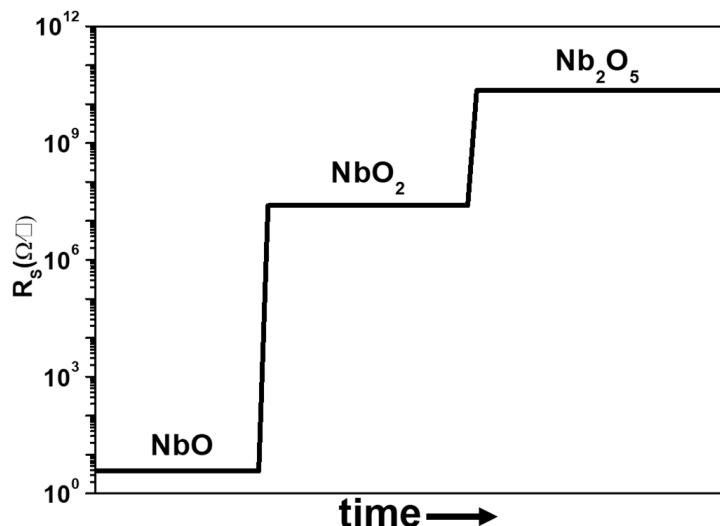


Figure 3.3: Graph illustrating the phase transitions of Nb we expected to see as a function of time when the temperature of the system was increased and held at 300°C to begin with.

Experimentally, the samples oxidized in a non-systematic manner as we can see in the graphs of figure 3.4. Figures 3.4 (a) and (b) show the oxidation of two films on soda-lime glass substrate. It can be seen that for SL1 it took about 25 hrs to make a jump in the sheet resistance and that was after elevating the system to a higher temperature (after which we lost track of the measurement). On the other hand, it took SL2 18 hrs to make a jump in the sheet resistance. Similar behavior was noticed for films on borofloat glass samples shown in figures 3.4 (c) and (d) where in BF1 a transition happened nearly 14 hrs after the measurement started, while in BF2 even after 22 hrs no transition was recorded. Although we started with the same conditions for all four different samples, yet the oxidation mechanism was different.

Also, it can be seen, even by the naked eye, that the the oxidation is inhomogeneous. Different regions of the film show different color contrast indicating that there is a mixture of phases in the film - the lighter the region the more oxidized is the film. Figures 3.5 and 3.6 show oxidized films at the macroscopic and microscopic level respectively. It can be clearly seen at both scales that the films were inhomogeneously oxidized. The loss of track of the sheet resistance measurements can be attributed to this inhomogeneity in the films where probably around at least one of the contacts the film has turned very insulating and blocked the passage of the current and eventually blocked the measurement. Moreover, x-ray measurements, shown in figure 3.7, of the samples reveals that the oxidized samples were amorphous.

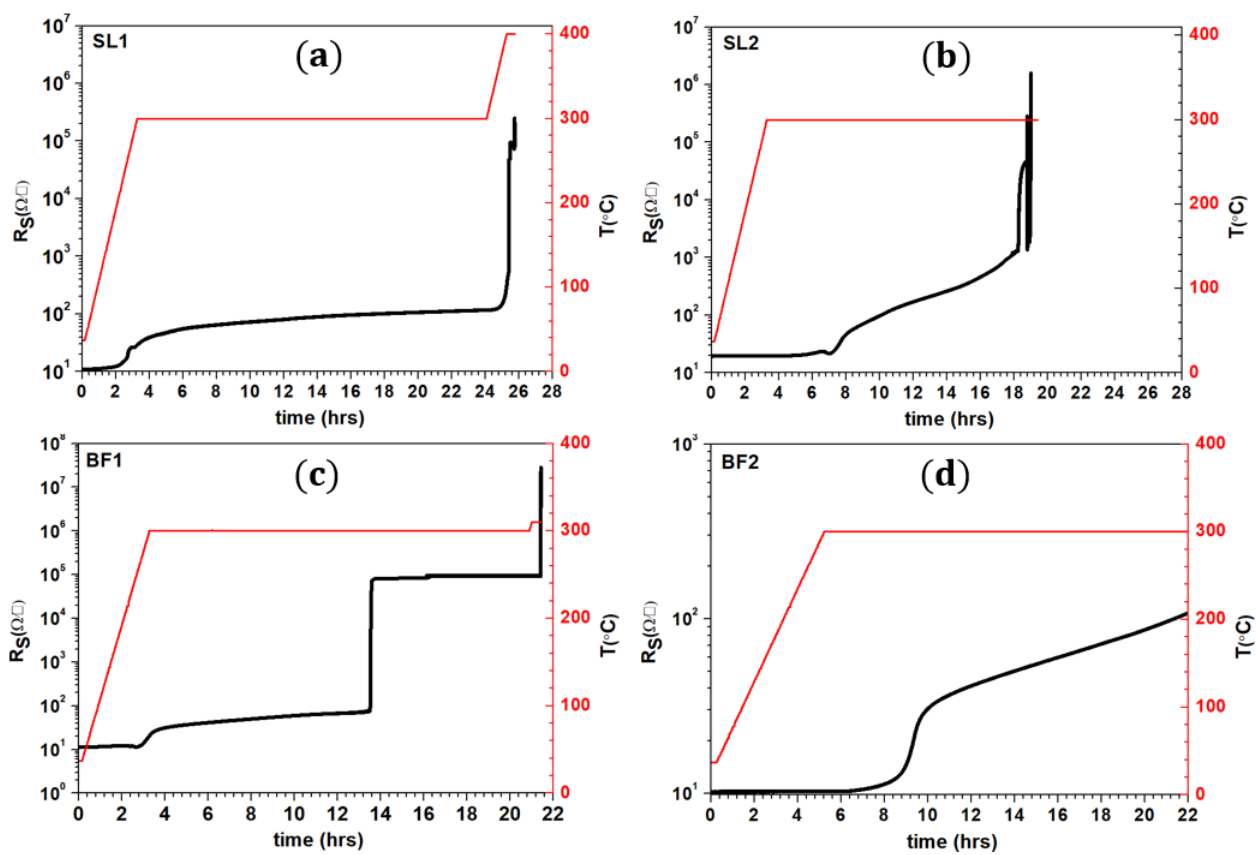


Figure 3.4: Graphs showing the oxidation process of Nb thin films on 2 soda-lime (a) SL1 and (b) SL2 and 2 borofloat (c) BF1 and (d) BF2 glass substrates.

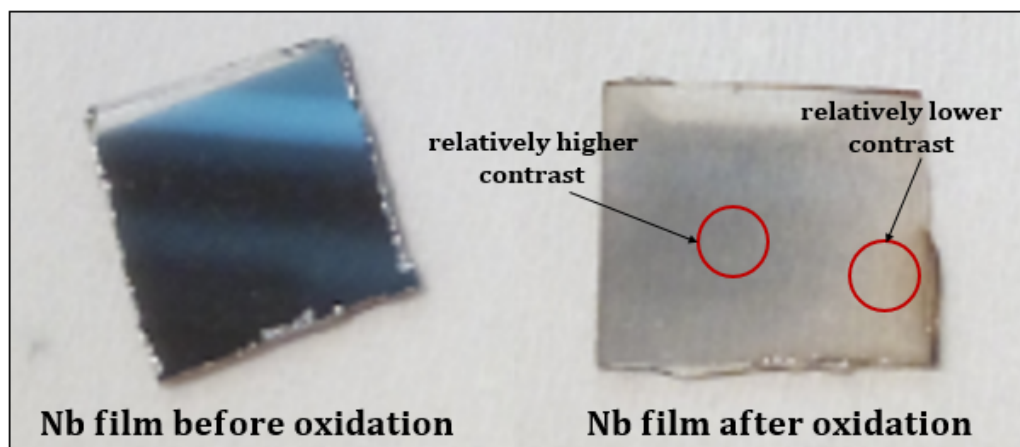


Figure 3.5: Macroscopic photos of an Nb film before and after oxidation.

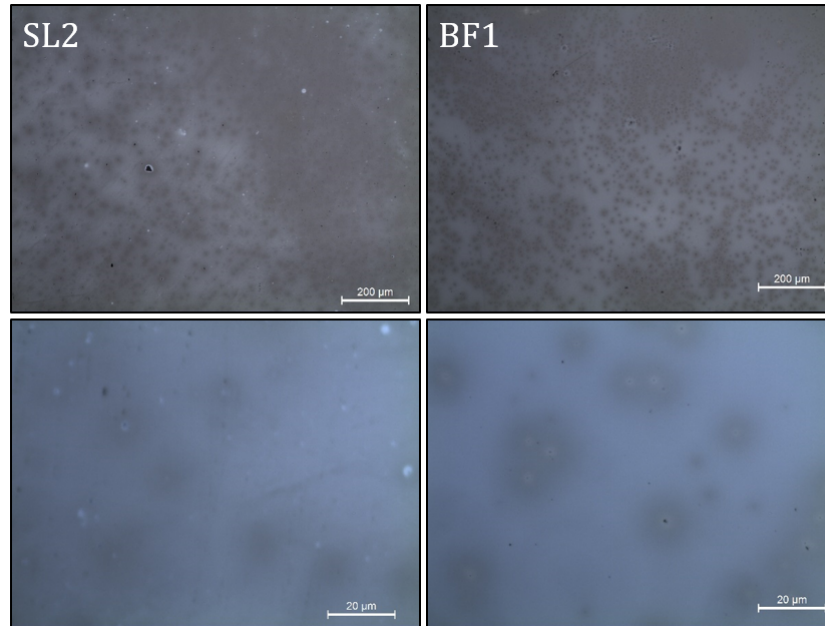


Figure 3.6: Optical microscopic images for SL2 and BF1 samples after their oxidation. The inhomogeneity can be clearly seen.

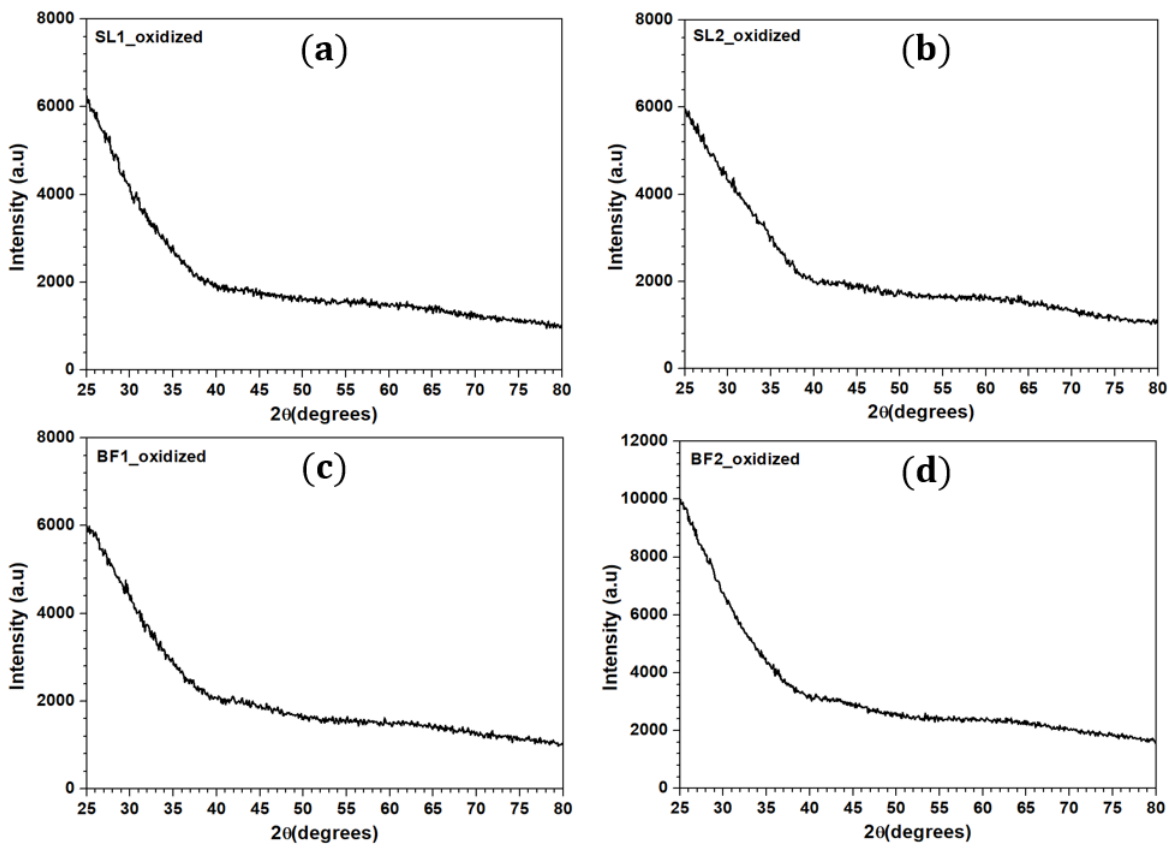


Figure 3.7: X-ray diffraction patterns for the samples oxidized earlier (a) SL1 (b) SL2, (c) BF1 and (d) BF2. No peaks appear in any of the diffractograms. (XRD was performed using Cu $K\alpha_1$ radiation).

3.4 Nb Oxidation by Flash Annealing

In this method, instead of placing the sample inside the oven and gradually increasing the temperature while monitoring the sheet resistance, the temperature of the oven was raised to a certain temperature (the range was [500°C, 600°C]), and the sample was introduced into the oven for a specific time after which it was immediately taken out.

3.4.1 Nb films at Slower Rate

Although the previous Nb sputtering parameters produced good Nb films, we decided to decrease the deposition rate of Nb film fabrication for better thickness control and better crystallinity. For this we have decreased the sputtering power by few watts and increased the distance $H_{\text{substrate}}^{\text{target}}$ to its maximum of 9 cm. Indeed, the sputtering rate was significantly reduced by a factor of ~ 5 , and the new rate has become 5 to 6 nm/min. The new sputtering parameters for Nb thin films are presented in table 3.2.

Parameter	Target Etching	Substrate Etching	Deposition
Ar pressure (mbar)	0.5	0.1	0.1
power (Watts)	100	100	80
tension (V)	450	400	190
target-substrate distance (cm)	9	9	9
substrate temperature (°C)	RT	RT	RT
rate (nm/min)	6	-	6

Table 3.2: Parameters used to achieve a relatively lower deposition rate $R = 6\text{nm}/\text{min}$ of Nb thin films.

The films were characterized by XRD, and were found to be polycrystalline Nb. Deposition at room temperature (RT) and at 450°C were made with different sputtering time, and the sample thickness was measured each time using AFM. The graph of figure 3.8 shows the results of this experiment. By fitting the points linearly we deduced that depositions at RT and at 450°C have the same rate of deposition of about 6 nm/min. They also show that we can control the rate of deposition with the power and the sample target distance in a precise manner.

The x-ray diffractograms² of the samples at different substrate temperatures are shown in figure 3.9 (a), and their respective lattice constants are shown in figure 3.9 (b). The high substrate temperature films have a higher lattice constant than the RT film indicating that they are strained. The lattice constant was obtained by initially calculating the inter planar distances from the Bragg equation:

$$d_{\text{hkl}} = \frac{\lambda}{2 \sin(\theta_{\text{hkl}})}$$

²Aside the measurement held at room temperature which was performed at a different time than the others, two other peaks appear in the remaining diffractograms. These two peaks refer to platinum metal Pt which is found in the xrd chamber. Notice, they always had the same position in the different diffraction patterns which means they do not come from the film.

after which the lattice constant ‘a’ was extracted according to the cubic structure unit cell equation [187]:

$$d_{hkl} = \frac{a}{\sqrt{h^2 + k^2 + l^2}} \quad (3.1)$$

After obtaining films at a slow rate, experiments by flash annealing were commenced.

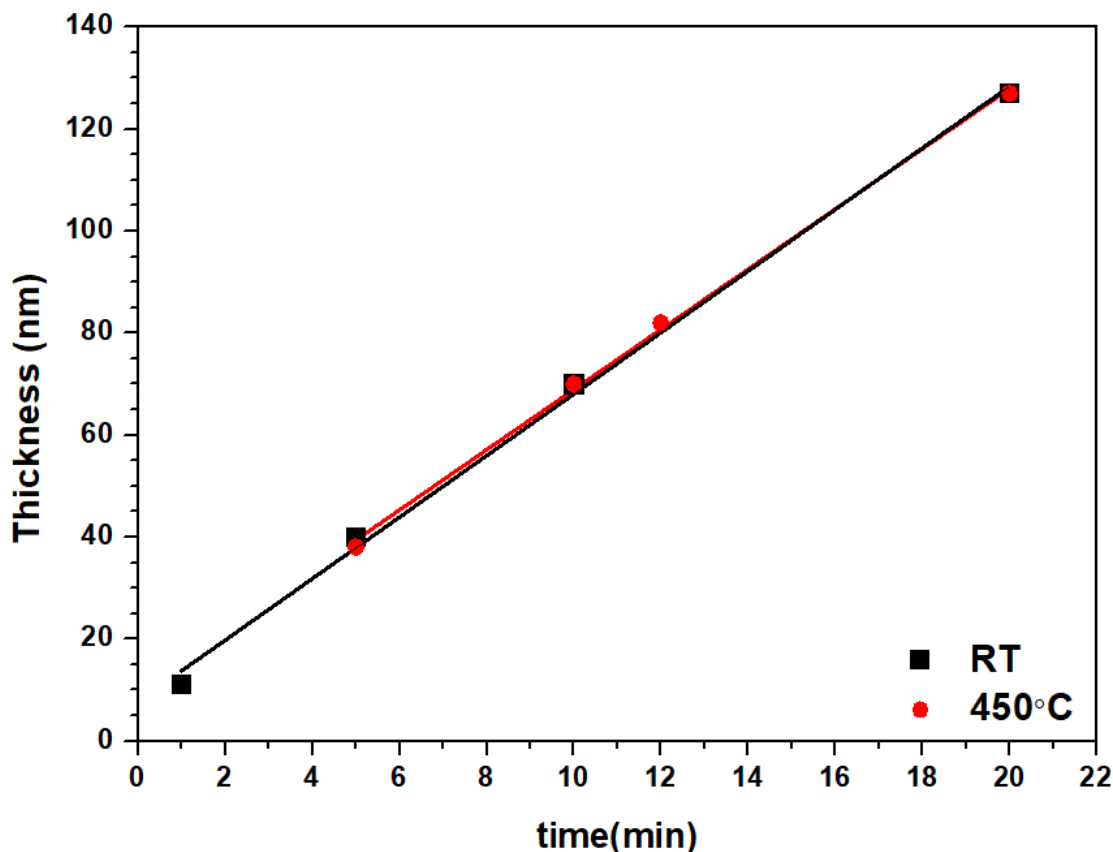


Figure 3.8: The variation of the film thickness as a function of deposition time at two different temperatures: RT and 450°C. The black and the red lines are the linear fittings of the RT and 450°C depositions respectively.

Our main findings are depicted in Figure 3.10, where Raman signatures of crystalline NbO₂ are clearly identified (which is an improvement over the slow oxidation process); however, the samples are not homogeneous and the process is not reproducible, as seen in the pictures. In Figure 3.11, we further show that the same sample flash oxidized for increasing time periods shows an improvement of the Signal to background ratio R implying in a very simple model schematized in the figure that the NbO₂ volume in the sample with respect to Nb, and NbO₂ is maximized. Although, x-ray diffraction, which takes a more averaged and macroscopic view of the crystalline phases in the sample in figure 3.12 shows only NbO₂ phase, there is still inhomogeneity in the film and presence of other amorphous oxide phases is suspected. It is thus clear that we have to find another way of making stoichiometric, homogenous NbO₂ films.

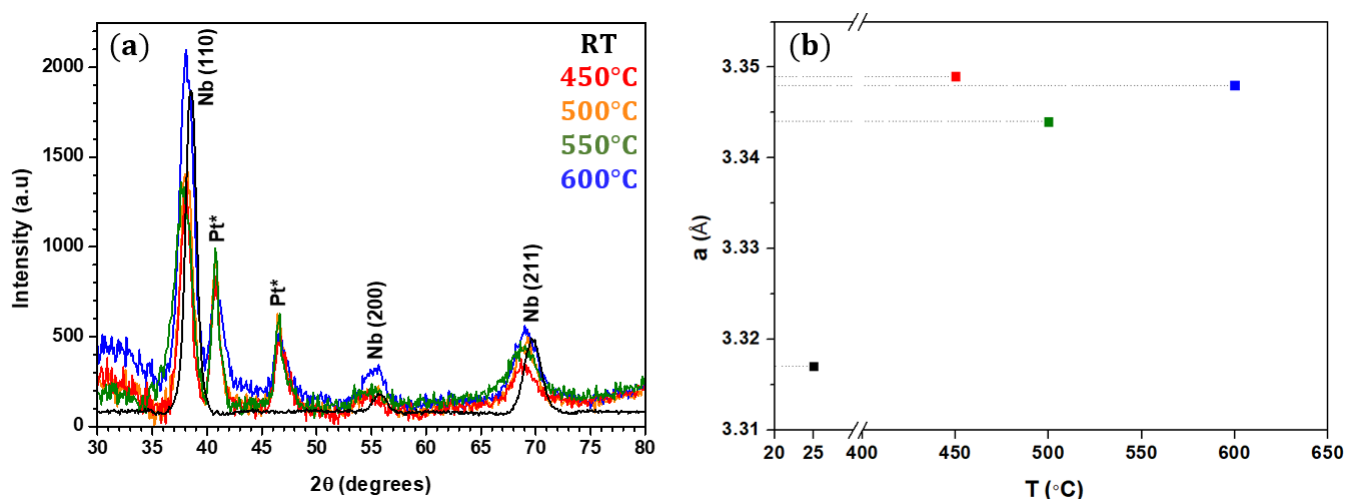


Figure 3.9: (a) X-ray diffractograms of Nb thin films at different substrate temperatures. (b) The variation of the lattice constant of Nb unit cell as a function of substrate temperature. (XRD was performed using $\text{Cu K}\alpha_1$ radiation).

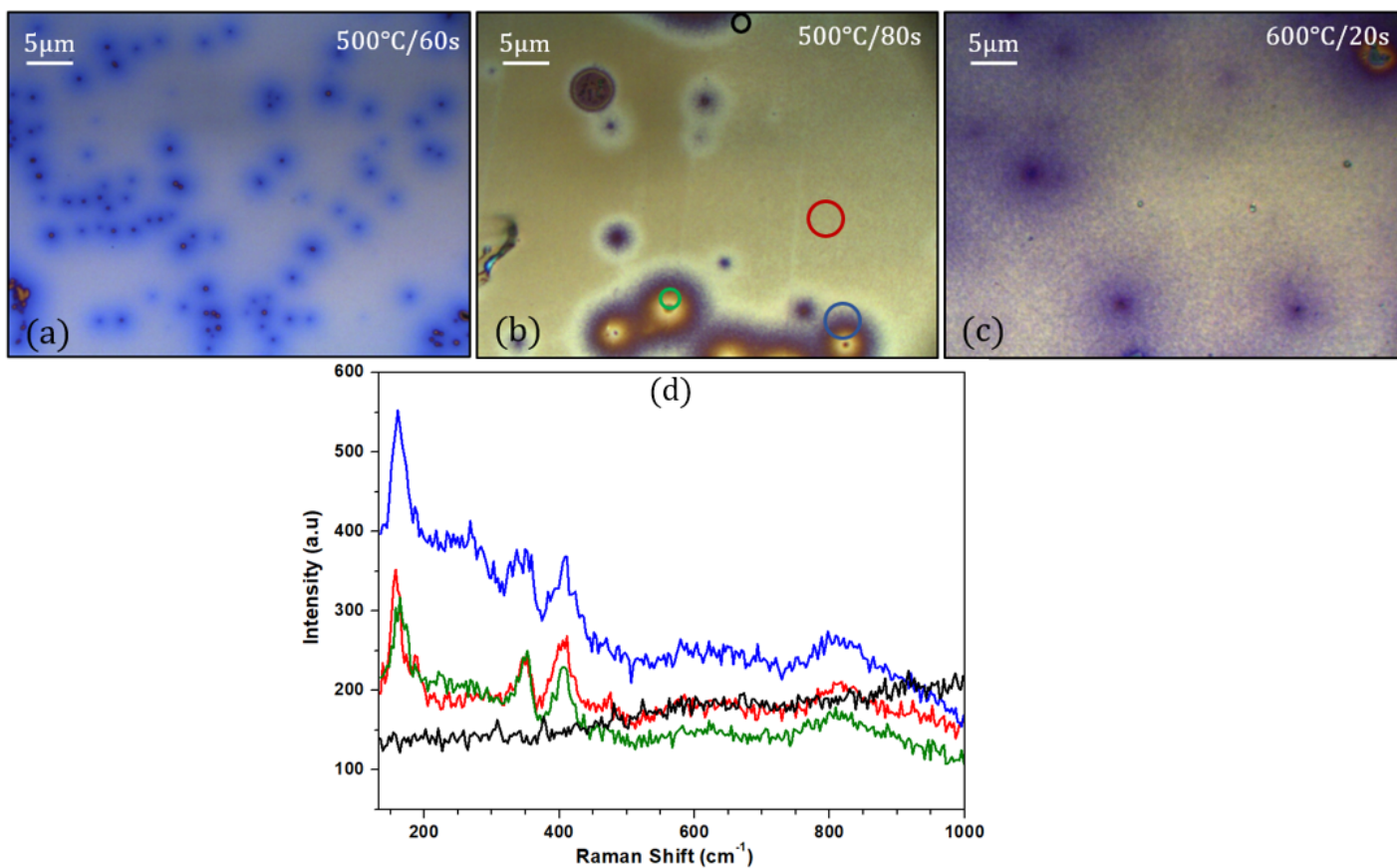


Figure 3.10: (a), (b) and (c) Optical images of some samples oxidized at different times and different temperatures. (d) Raman spectra taken at different regions in film (b).

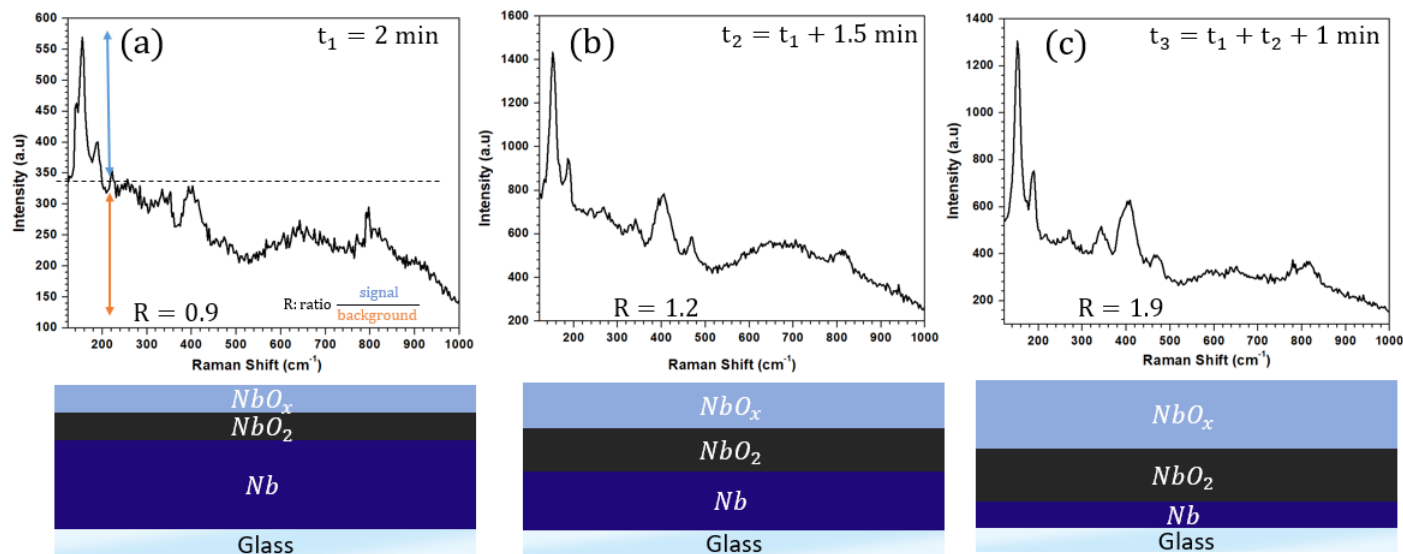


Figure 3.11: The Raman Spectra of a 125 nm film with an *exaggerated* illustration of the film composition after (a) 2 min oxidation, (b) an additional 1.5 min oxidation, and (c) and extra 1 min oxidation.

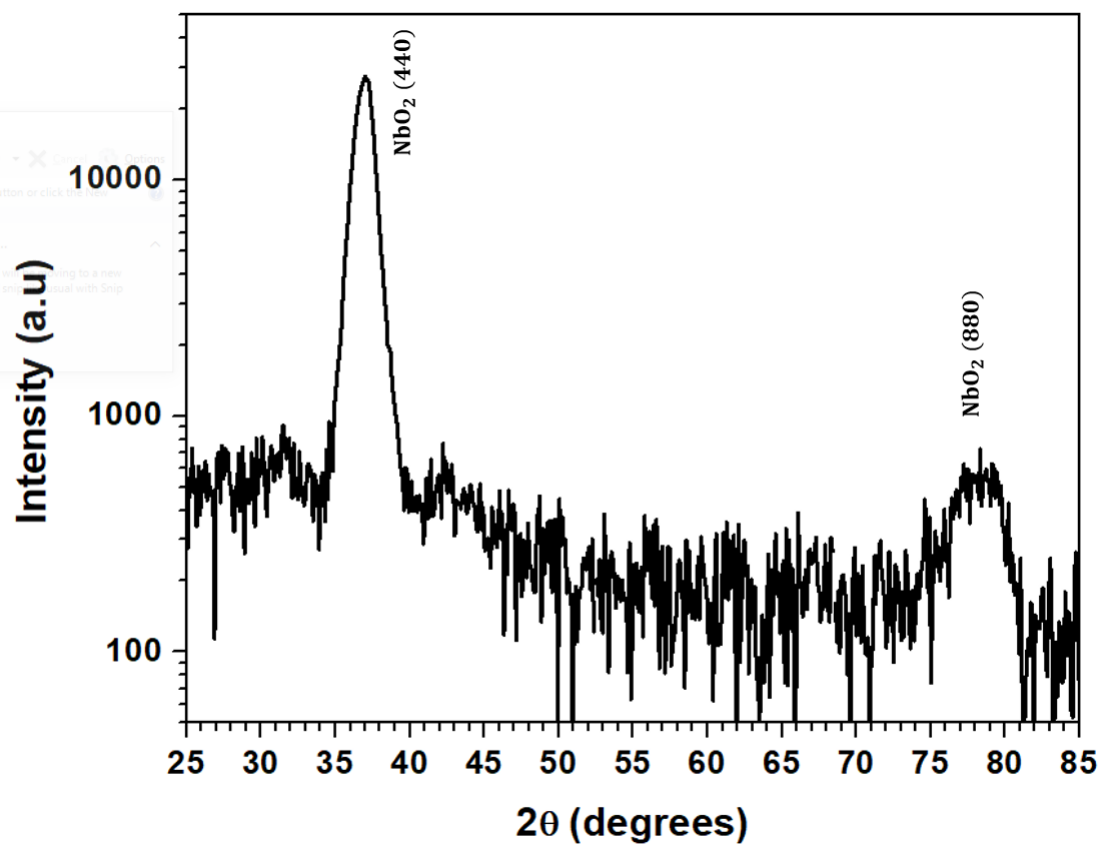


Figure 3.12: The x-ray diffraction pattern of the 125 nm film after oxidation. (XRD was performed using Cu K α_1 radiation)

3.5 Summary on Ambient Nb Thin Film Oxidation

Initially, we chose to deposit polycrystalline metallic thin films of Nb and search for favorable oxidation conditions in an attempt to fabricate NbO₂. Annealing in air at a relatively low temperature (constrained below the transition temperature $T_g = 550 - 600^\circ\text{C}$ [188] of soda-lime glass) reached by a gradual ramp while monitoring the film resistance resulted in step-like increases in film resistance corresponding to oxidation. However, these increases were not uniformly reproducible and differed from one sample to another, and we obtained amorphous thin films where the Nb oxidation state was impossible to identify either by XRD or by Raman spectroscopy. Nevertheless, the oxidation was not homogeneous. We also attempted flash annealing or rapid heating (few seconds) the polycrystalline metallic films directly to a temperature of 500°C in air. This resulted in the appearance of dark localized spots of NbO₂ crystallites of several micron diameter (identified by Raman spectroscopy) which however did not evolve into a uniform NbO₂ film.

These inconclusive attempts led us to use magnetron sputtering with a stoichiometric NbO₂ target to prepare NbO₂ films on various substrates.

The diagram in figure 3.13 shows a summary of the approach of obtaining NbO₂ films by oxidation of Nb.

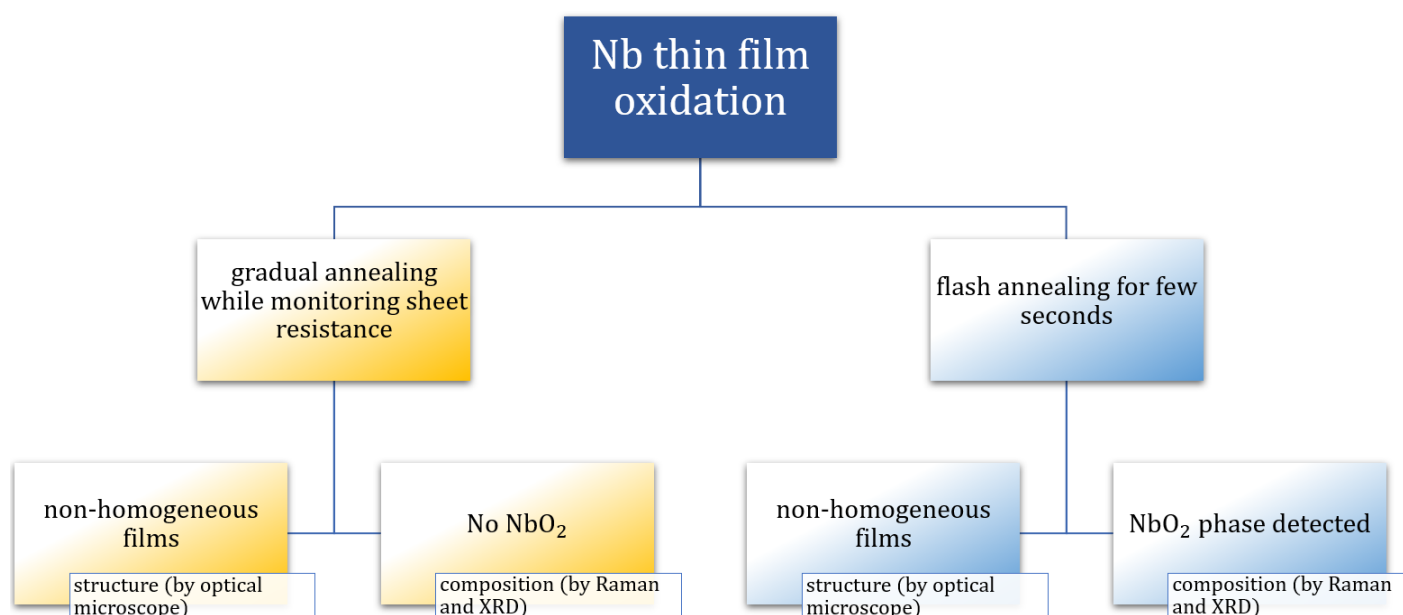


Figure 3.13: A diagram showing the previous methods performed in attempt to oxidize Nb thin films into NbO₂.

3.6 NbO₂ Thin Films by RF-Magnetron Sputtering

As stated in the introduction of this chapter, earlier work has revolved around sputtering in a controlled partial pressure of oxygen or argon [178, 189]. However, in general post-annealing to induce or improve crystallization has also been necessary [1, 190]. The lack of success of our low temperature oxidation attempts backed by past work on NbO₂ oxidation [1, 28, 44, 79, 172–174, 179, 182, 182–185] led us to believe that below roughly 530°C [190] the modification of the oxidation state of bulk NbO_x does not happen. This opened the possibility of using a stoichiometric NbO₂ target to directly deposit stoichiometric NbO₂ on the substrate with argon gas being the process gas of the sputtering experiment, avoiding partial gaseous pressure (oxygen or a mixture of oxygen and hydrogen) during deposition. We decided to concentrate on optimizing conditions for deposition (sputtering rate, substrate temperature, Ar pressure), followed by post-annealing for crystallization.

The stoichiometric target, 100 mm diameter × 3 mm thickness with a backing copper plate of 117 mm diameter × 6.5 mm thickness, was obtained from EDGETECH INDUSTRIES LLC. It is important to verify that the target presents a uniform dark blue-grey color (see figure 3.14) which implies the NbO₂ phase. A light colored target is a sign of oxidation during the sintering phase of the target even if the powder precursor is stoichiometric NbO₂, and at least one target was rejected by us for this reason. The NbO₂ phase of the chosen target was verified by Raman spectroscopy (figure 3.15) and XRD (figure 3.16) before mounting in the sputtering chamber.

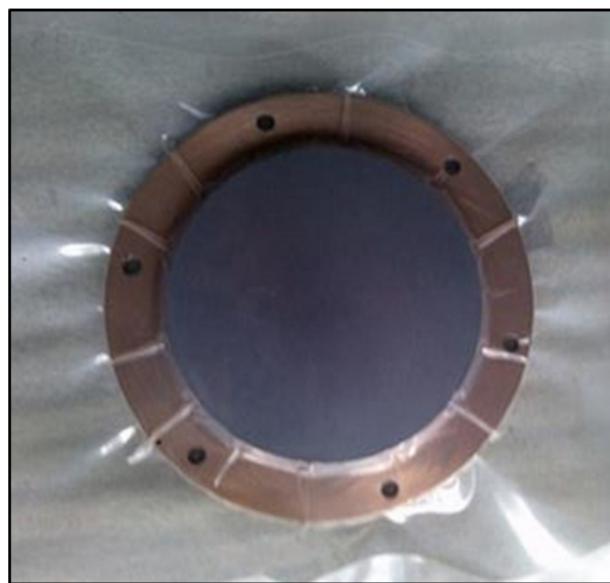


Figure 3.14: A photo of the purchased target. The dark blue-grey color is a sign of stoichiometric NbO₂ phase.

The Raman spectrum of the target was taken using the 50× objective as the target surface is large and with a laser of 532 nm wavelength. The obtained Raman spectrum resembles those found in epitaxial NbO₂ films by Wang et al. [173] and Wong et al. [179]. Note that the measurement was done while the target was still sealed in its vacuum plastic cover (which does not have any Raman active phonons). However, after removing the sealing

cover and taking other Raman spectra in different regions, the results were different from the NbO₂ spectrum seen in figure 3.15. This means that the NbO₂ target surface is highly sensitive to oxidation.

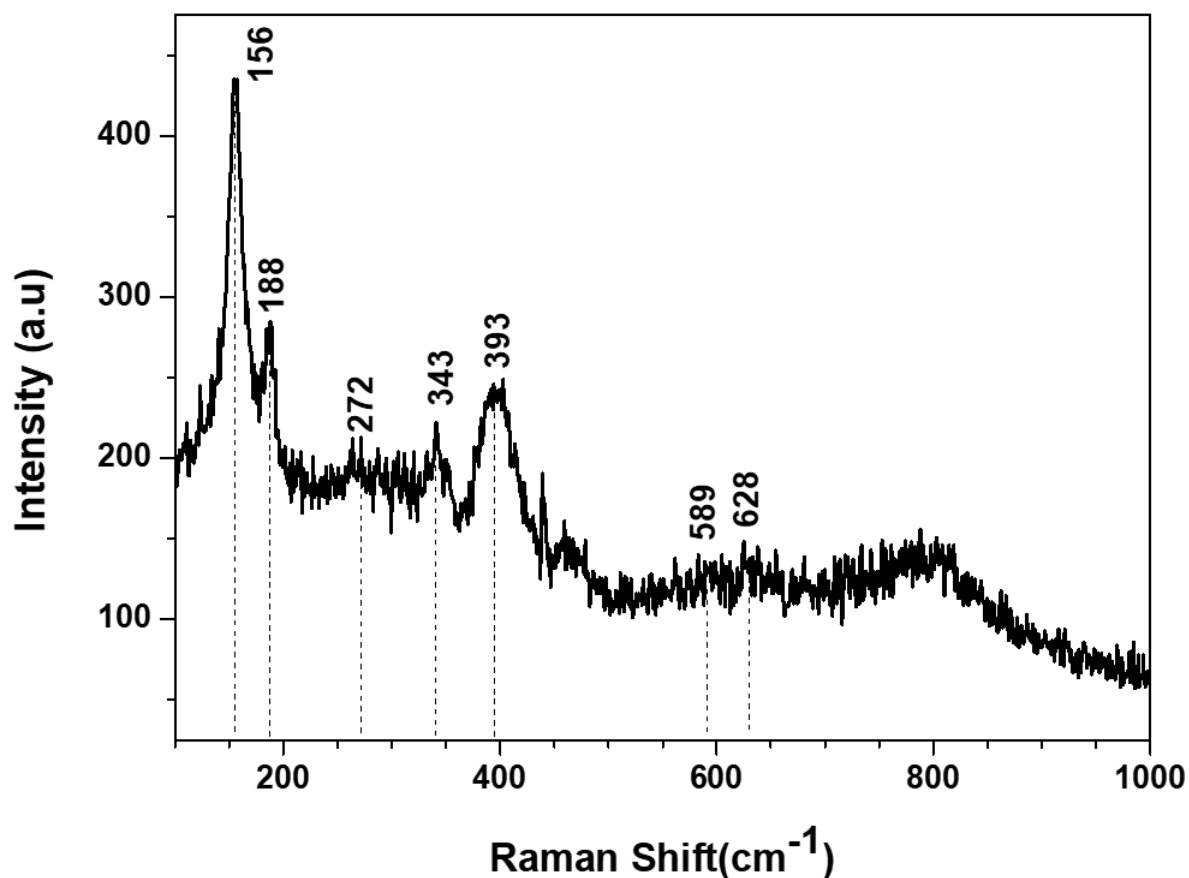


Figure 3.15: Raman spectrum of the purchased NbO₂ target while sealed in its vacuum protection sac.

As for the XRD measurements shown in figure 3.16, they were performed using a cobalt x-ray tube, and thus the x-rays produced were of wavelength $\lambda_{Co} = 1.789\text{\AA}$. As compared to Nb [191–193], NbO [191, 194, 195], NbO₂ [191, 196–200], Nb₂O₅ [191, 201–205] and Nb₁₂O₂₉ [206] diffractograms, it was found that the diffraction pattern has a majority of NbO₂ peaks though less intense than many others of different phases. NbO, Nb₂O₅ and Nb₁₂O₂₉ were also present and intensive in certain directions. The existence of other niobium oxide phases could have originated during the sintering or annealing process if the target were obtained by “hot pressing” or due to the use of bad initial powders in case the target was fabricated by cold pressing. Indeed, nominal stoichiometry for the target does not imply phase purity and maybe the reason why oxygen or argon, and in some cases hydrogen [190] partial pressure has been necessary in earlier experiments. However, oxidation or reduction during film deposition is a delicate adjustment which can also influence deposition dynamics. Despite the multi-phase surface of the sputtering target in hand, we were able to optimize the sputtering parameters which lead to pure phase NbO₂.

An important aspect of our methodology was to ensure a similar fabrication process for films on three different substrates, sodalime glass, single crystal Si and single crystal

Si topped by a 285 nm layer of poly-crystalline oxide. Of these, the glass substrate constrains post-annealing to temperatures below 600°C, while the other substrates may be post-annealed at higher temperatures. The parameters varied to optimize the quality of the deposited films were total magnetron power, the process gas (Ar) pressure and sample target distance which control the sputtering rate and substrate temperature which can alter deposition dynamics and notably help crystallization. As stated earlier we only used in-vacuum sputtering with a base pressure of $\sim 1 \times 10^{-6}$ mbar. Several runs were made with the three kinds of substrates by varying the parameters stated above. Details of the depositions are discussed below.

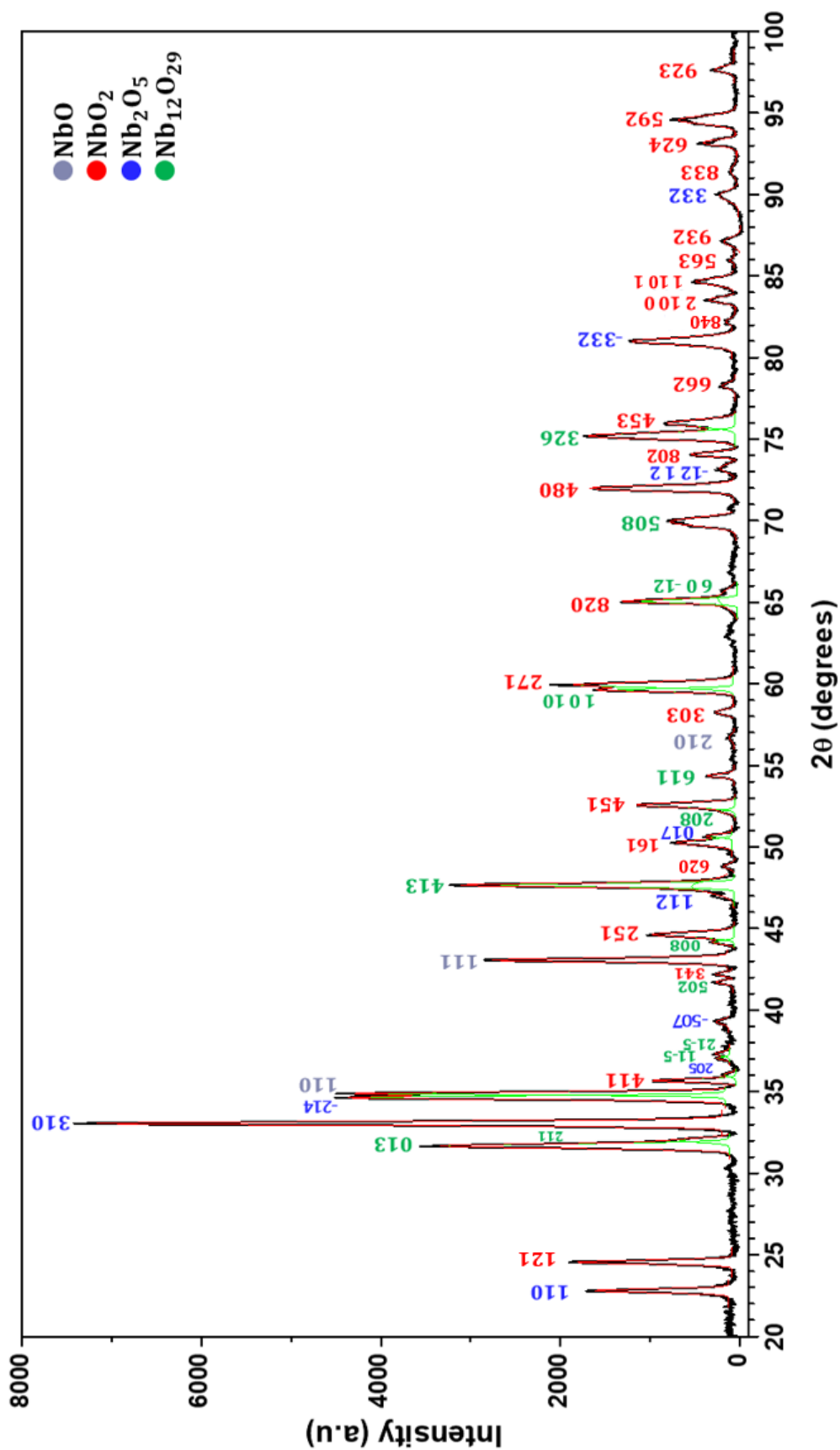


Figure 3.16: X-ray diffraction pattern of the purchased NbO₂ target taken in ambient conditions. The green curves represent Gaussian fittings added up to fit an asymmetric diffraction peak. (XRD was performed using Co K α_1 radiation).

3.7 Sputtering Experiments

In seeking the favorable and optimized parameters for depositing NbO₂ films, different RF-magnetron sputtering experiments were made while varying initial conditions. Studies for the effect of target-substrate distance, Ar pressure and substrate temperature were made. Note that all sputtered films were amorphous, and post annealing was required to crystallize the films. The results of such experiments are presented below.

3.7.1 Effect of Target-Substrate Distance $H_{\text{substrate}}^{\text{target}}$

Initially we chose to change the distance separating the target and the substrate with the other parameters chosen moderately according to previous magnetron sputterings depositions used to synthesize NbO₂ films. The sputtering parameters are shown in table 3.3.

Deposition	P(Watts)	p _{Ar} (mbar)	T _{substrate} (°C)	t _{deposition} (min)	$H_{\text{substrate}}^{\text{target}}$ (cm)
A	200	0.1	500	10	6.5
B	200	0.1	500	10	7.5
C	200	0.1	500	10	8.5
D	200	0.1	500	10	9.0

Table 3.3: Sputtering parameters for testing the effect of target-substrate distance on the film quality.

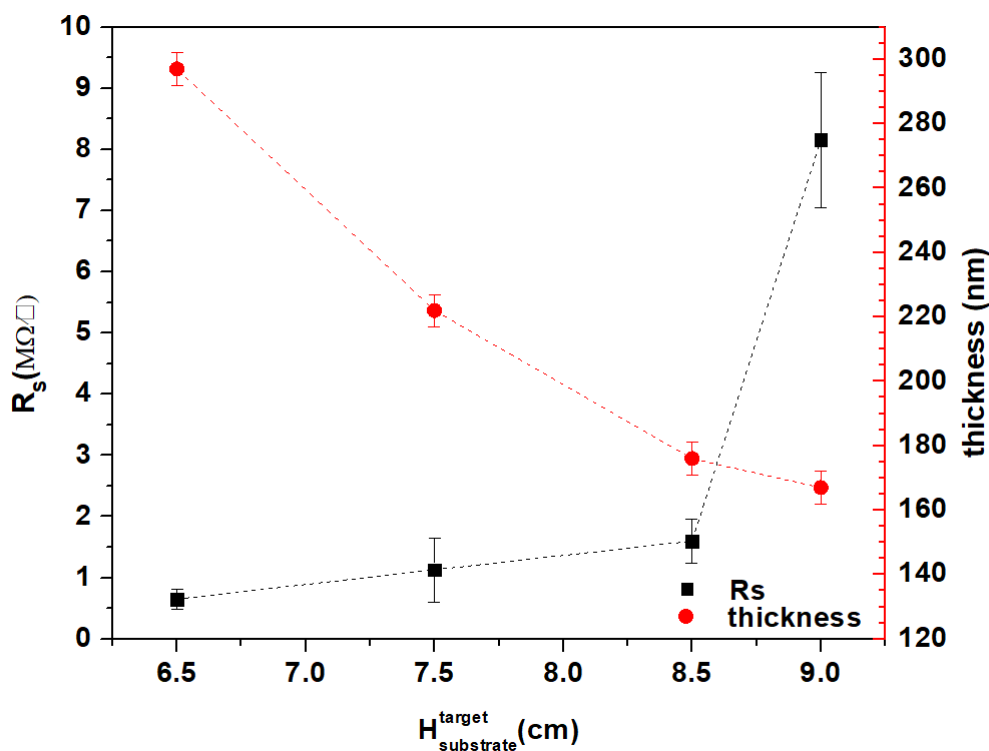


Figure 3.17: Graph showing the sheet resistance R_s and the thickness as a function of the target-substrate distance.

After the deposition, the film's thicknesses and sheet resistance were measured, and the results are shown in figure 3.17. We expect that the thickness of the film will decrease the farther the substrate's position is from the target since the solid angle decreases. This is clearly shown in the graph. What is also expected is that the thinner the film is, the higher the sheet resistance it will have. This is also clear in the figure.

One can argue that the bigger the target-substrate distance, the more the oxygen content in the film. There are several arguments for this claim based on composition and structural considerations.

First, at the level of atomic bombardment, the number of oxygen atoms in the target (supposing it perfect NbO_2 after etching it) is double that of the Nb atoms and hence it is more likely that when Ar^+ ions strike the target to extract more oxygen atoms than Nb, not to mention that the oxygen atom is lighter than Nb atom which means that the energy transferred to oxygen after the collision is more than that transferred to Nb assuming the collisions are elastic. Secondly, when the atoms are released from the target, the small oxygen atoms (96 pm in diameter) are less likely to be scattered before reaching the substrate than the big niobium atoms (396 pm) [207]. Indeed, the equation of the mean free path is [208]:

$$\lambda = \frac{R T}{\sqrt{2} \pi d^2 N_A P} \quad (3.2)$$

where R is the universal gas constant, T is the temperature, d is the diameter of the atom, N_A is Avogadro's number and P is the pressure. Considering that from the point of view of an oxygen or a niobium atom all parameters other than the diameter are the same, then the mean free path of oxygen is 16 times greater than that of Nb, which means that in its way to the substrate the oxygen atom will encounter less collisions than a niobium atom. One more remark to add concerning this figure is that we noticed that as we were increasing the target-substrate gap, the sheet resistance was increasing lightly; however, when moving from 8.5 cm to 9 cm, we saw that there was a *jump* in the sheet resistance although the film's thickness decreased less than in the former experiments. This again justifies that the oxygen content in the film increases with the increase in the distance taking into account the sizes of the O and Nb atoms building the film. Thus, to achieve a better stoichiometry, it was better to keep the separation between the target and substrate small, and as stated earlier all sputtering depositions gave niobium oxide films which were amorphous having the Raman spectra like the ones shown in figure 3.18.

After the deposition, the films were annealed for 2 hrs at 600°C . The optical microscopic photos in figure 3.19 and the Raman spectra in figure 3.20 taken before and after the annealing do not show any change.

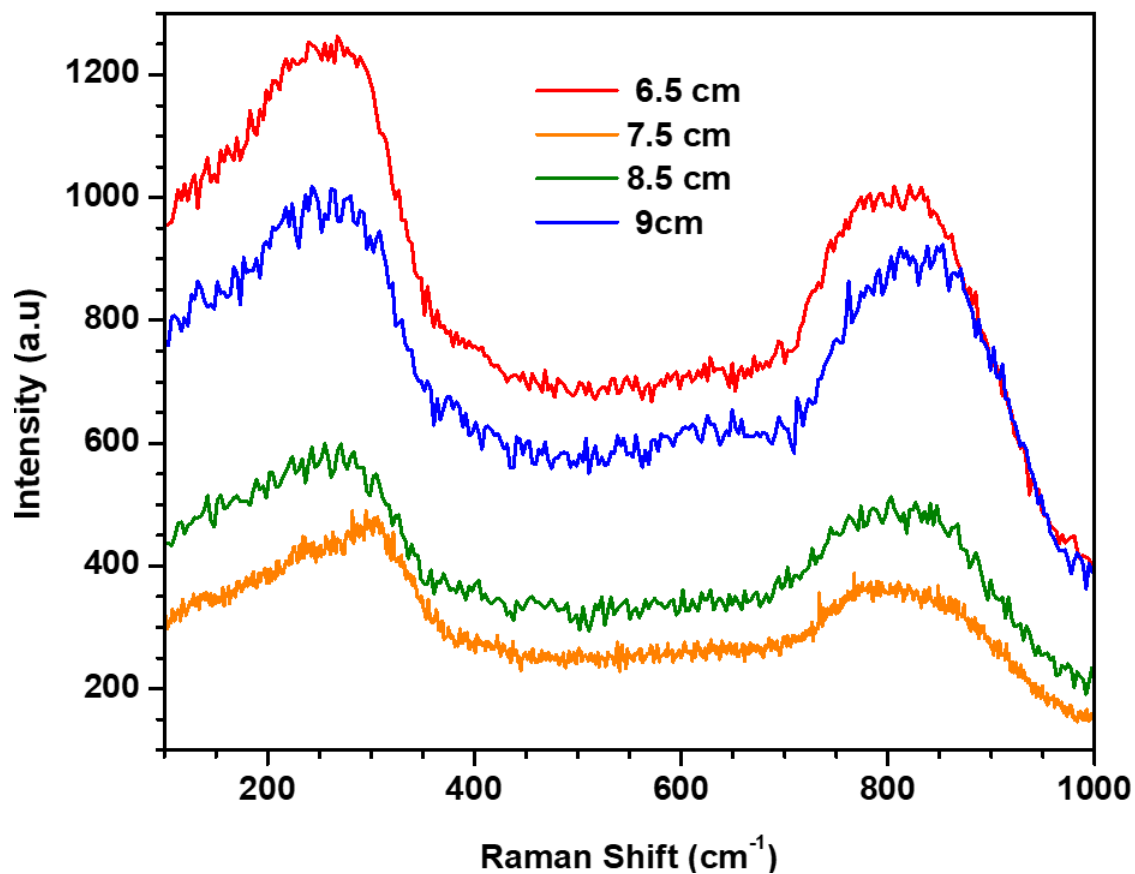


Figure 3.18: Raman spectra of the as-deposited niobium oxide films sputtered at different target-substrate distances.

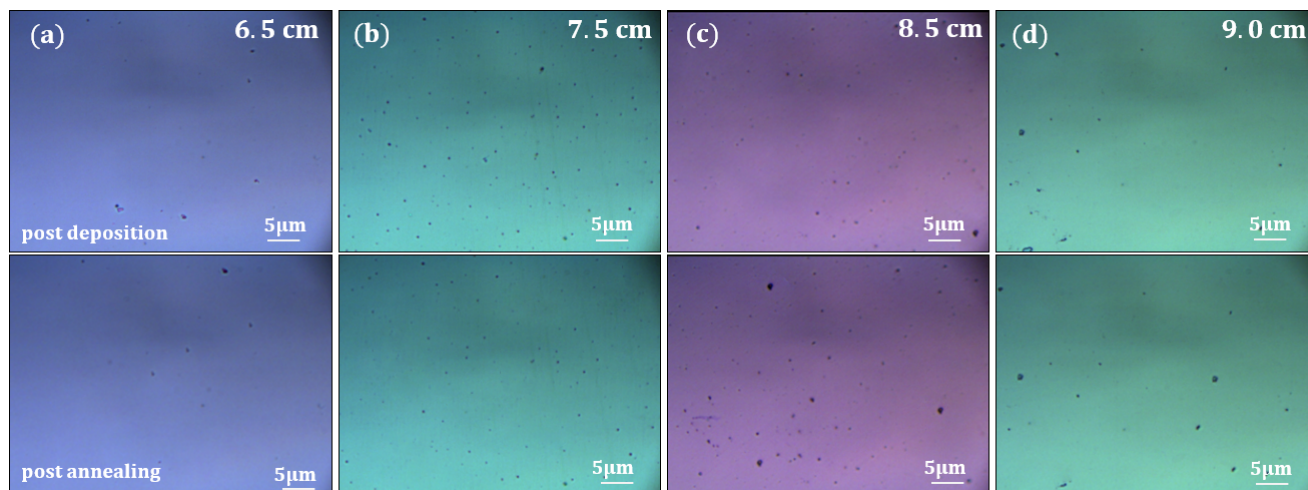


Figure 3.19: Optical photos of the samples before and after annealing at different target-substrate distances (a) 6.5 cm (b) 7.5 cm (c) 8.5 cm and (d) 9 cm.

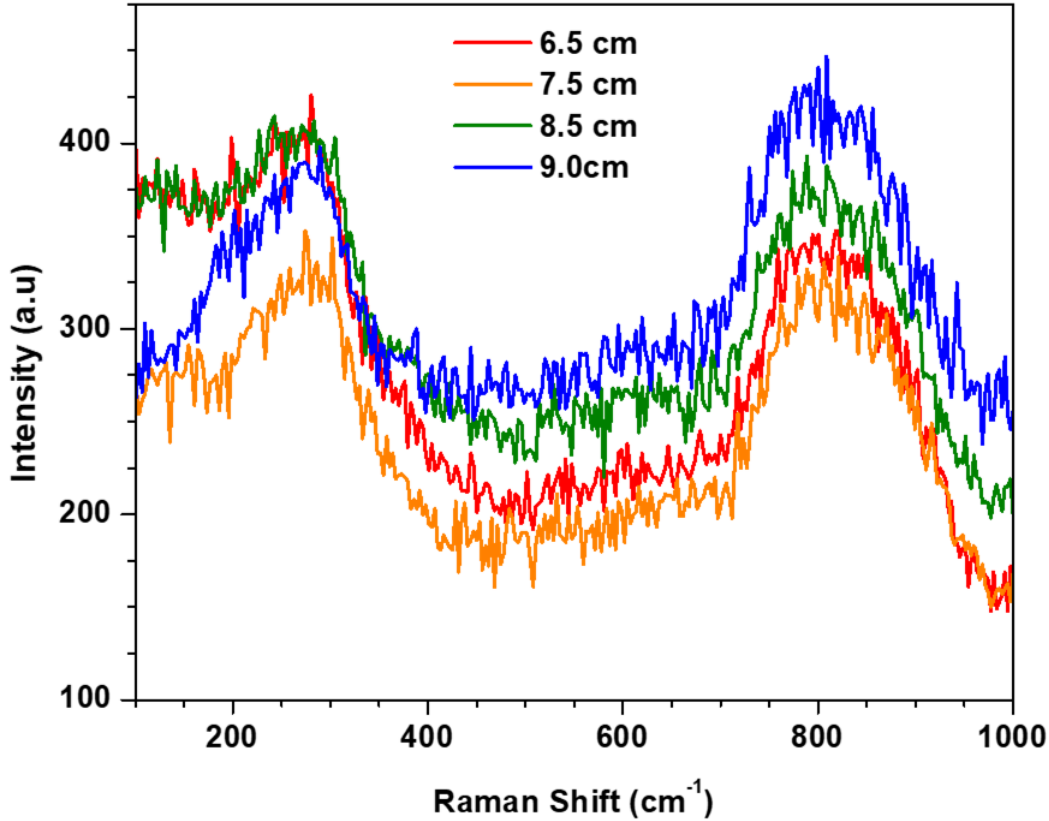


Figure 3.20: Raman spectra of the post annealed niobium oxide films originally sputtered at different target-substrate distances.

3.7.2 Effect of Substrate Temperature T_{sub}

The other parameter that we have varied is the substrate temperature T_{S} . The parameters used are shown in table 3.4.

Deposition	P(Watts)	p_{Ar} (mbar)	$T_{\text{substrate}}(^{\circ}\text{C})$	$t_{\text{deposition}}$ (min)	$H_{\text{substrate}}^{\text{target}}$ (cm)
E	200	0.1	450	10	6.5
F	200	0.1	500	10	6.5
G	200	0.1	600	10	6.5

Table 3.4: Sputtering parameters for testing the effect of substrate temperature on the film quality.

The same procedure was done as the previous experiments, i.e. the thickness and the sheet resistance were measured, and the results are shown in graph 3.21.

From the obtained results, we notice that the substrate temperature does not influence the film quality significantly. Only a small difference can be seen in the thickness and sheet resistance of the tested samples. However, we chose to work with a temperature of 550°C in our experiments as, in general, a higher substrate temperature leads to a better

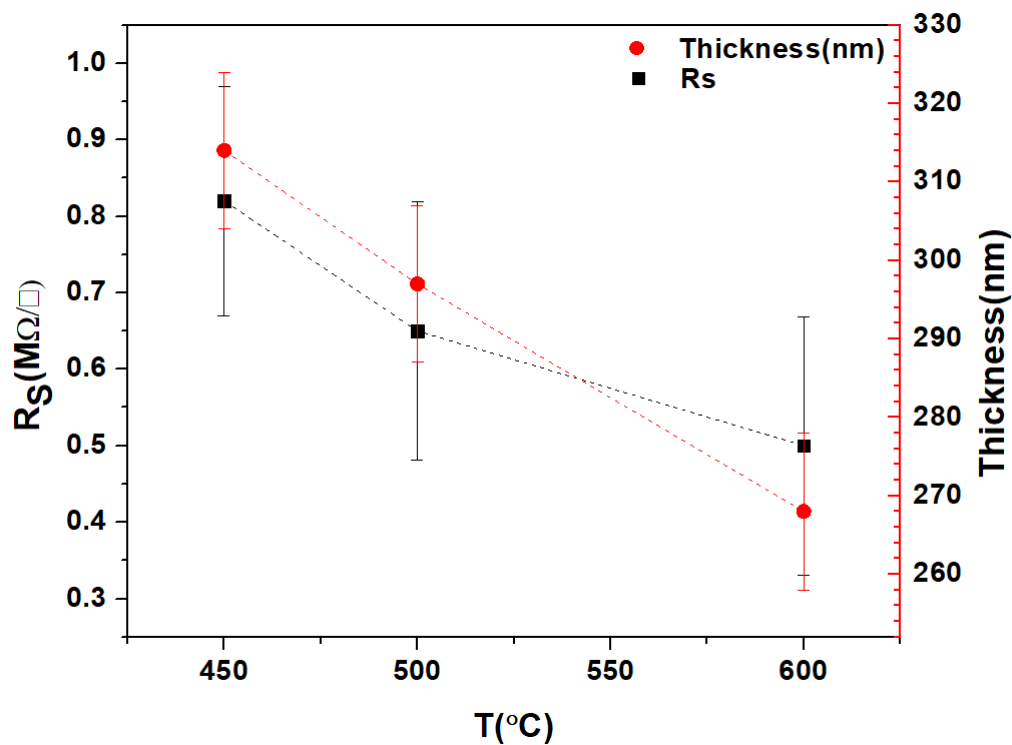


Figure 3.21: Graph showing the sheet resistance R_S and the thickness as a function of the substrate temperature T_S .

crystallinity. A temperature higher than that would be risky as we are already working in the vicinity of the glass softening temperature.

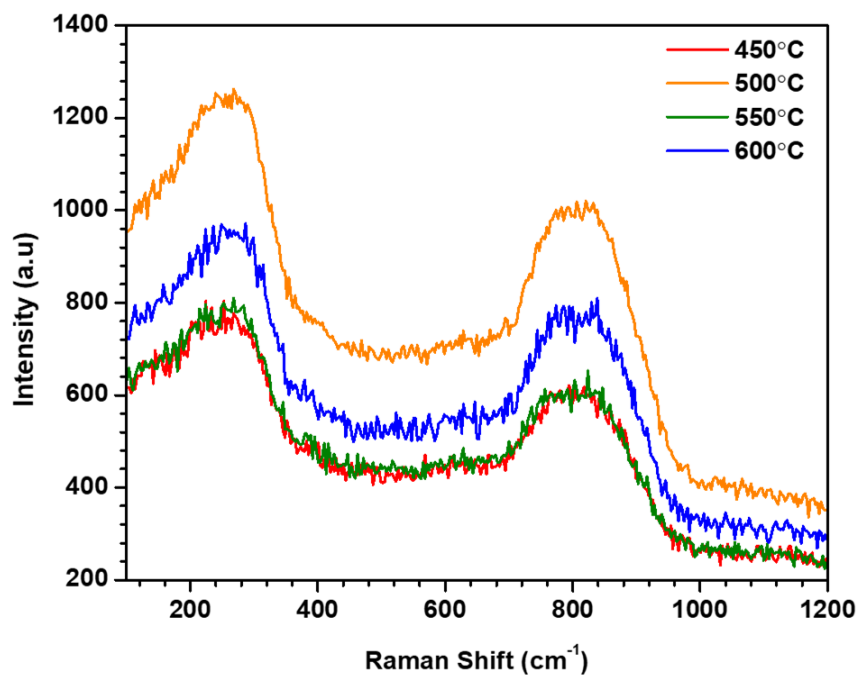


Figure 3.22: Raman spectra of the as-deposited niobium oxide films sputtered at different substrate temperatures.

3.7.3 Effect of Process Gas Pressure P_{Ar}

With the variation of earlier parameters the required phase could not be obtained. A final parameter to be varied is the pressure of the Ar introduced into the chamber bombarding the target. The parameters chosen for the experiments are presented in table 3.5, and the film thickness and sheet resistance were also measured and shown in figure 3.23.

Deposition	P(Watts)	p_{Ar} (mbar)	$T_{\text{substrate}}(^{\circ}\text{C})$	$t_{\text{deposition}}(\text{min})$	$H_{\text{substrate}}^{\text{target}}(\text{cm})$
H	200	0.1	550	10	6.5
I	200	0.2	550	10	6.5
J	200	0.5	550	10	6.5

Table 3.5: Sputtering parameters for testing the effect of Ar pressure on the film quality.

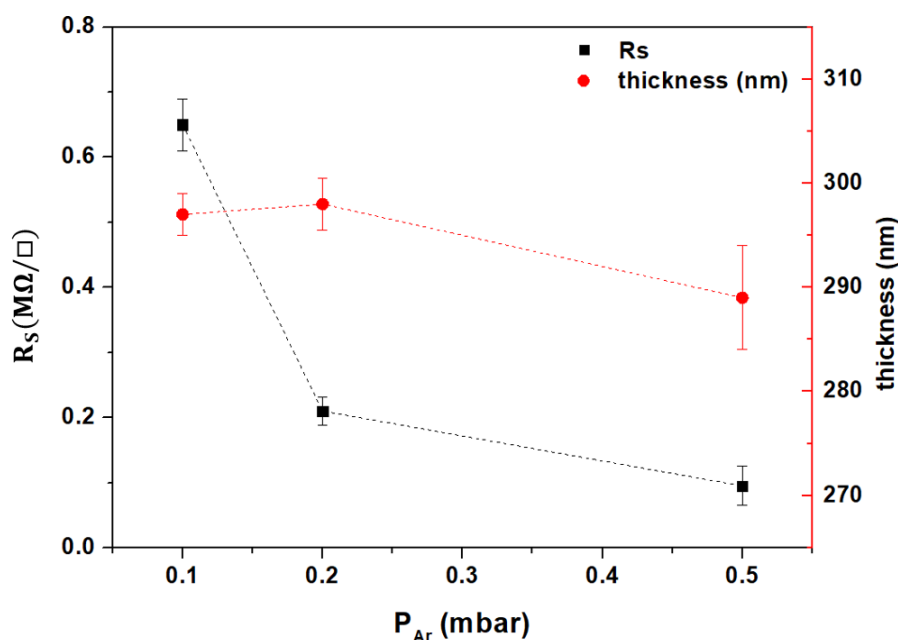


Figure 3.23: Graph showing the sheet resistance R_s and the thickness as a function of the substrate temperature P_{Ar} .

From figure 3.23, we can see that while there is little variation in the film thickness there is a more than five-fold decrease in the sheet resistance for the higher Ar pressure. This is indicative of a stoichiometry or phase change. After deposition, Raman spectroscopy was performed and the results are shown in figure 3.24. Similar to all other experiments, whatever conditions were chosen, no crystallinity was detected in the films prior to annealing.

The samples were annealed for 2 hrs at 600°C . Earlier work [1] shows that annealed films which are amorphous after deposition can lead to a crystalline transition. Nakao et al. [1] showed that NbO_2 thin films can be grown with pulsed laser deposition from a stoichiometric target in a partial pressure of oxygen. To attain crystallinity they annealed their samples in vacuum after deposition at a temperature of 600°C for 1 hr. We also chose

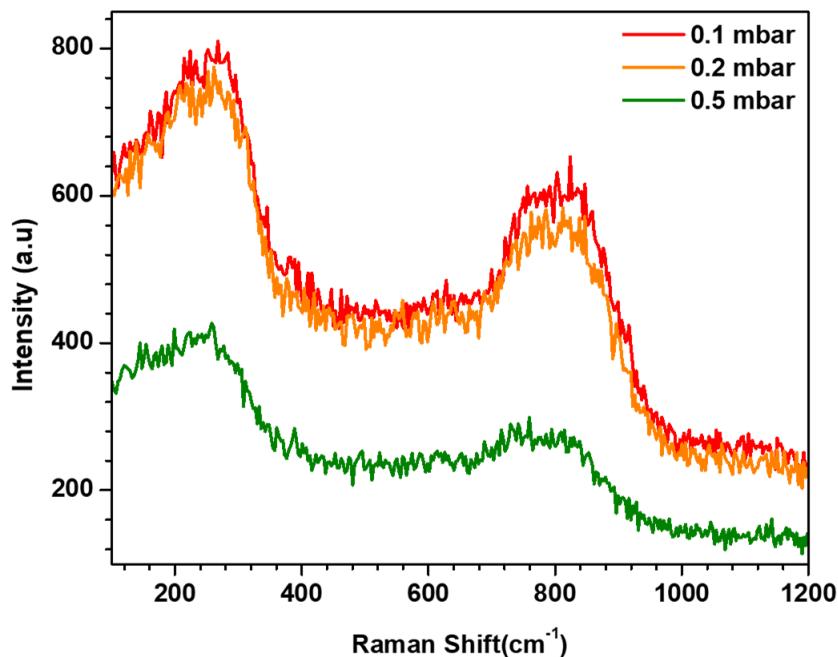


Figure 3.24: Raman spectra of the as-deposited niobium oxide films sputtered at different process gas pressure P_{Ar} .

vacuum annealing because we do not want or expect any stoichiometry changes at these temperatures but hope for a structural, amorphous/crystalline transition. The optical photos of the samples before and after annealing are shown in figure 3.25 and the Raman spectra of the post annealed samples are shown in figure 3.26. All the regions on the film of figure 3.25 (b) where the Ar pressure was 0.5 mbar show NbO_2 phase Raman peak.

The fact that we are using a transparent substrate (glass) allows us to verify that the film is crystallized through the whole thickness. Figure 3.27 shows an optical image of the sample taken through the substrate along with the Raman spectra taken using $50\times$ objective as there are focal limitations using the $100\times$ objective. Of course, the signal is not as good as taken from the top of the sample as the laser has to pass through the relatively thick glass before reaching the film and eventually higher substrate signal will be collected, yet it was a good verification to assure that the film is characterized at the film-substrate interface. Also, notice that the island structures are not only a surface feature of the film, but also extends within the depth of the sample. In addition, an AFM image was taken for the sample (of course from the right side) and the image is shown in figure 3.28. The surface roughness was measured and has a r.m.s. of ~ 0.85 nm which is not a very smooth surface, but considering the peaks and troughs coming from the islands spaces between the trenches, it looks reasonable, and the grains have a size in the order of few tens of nanometers.

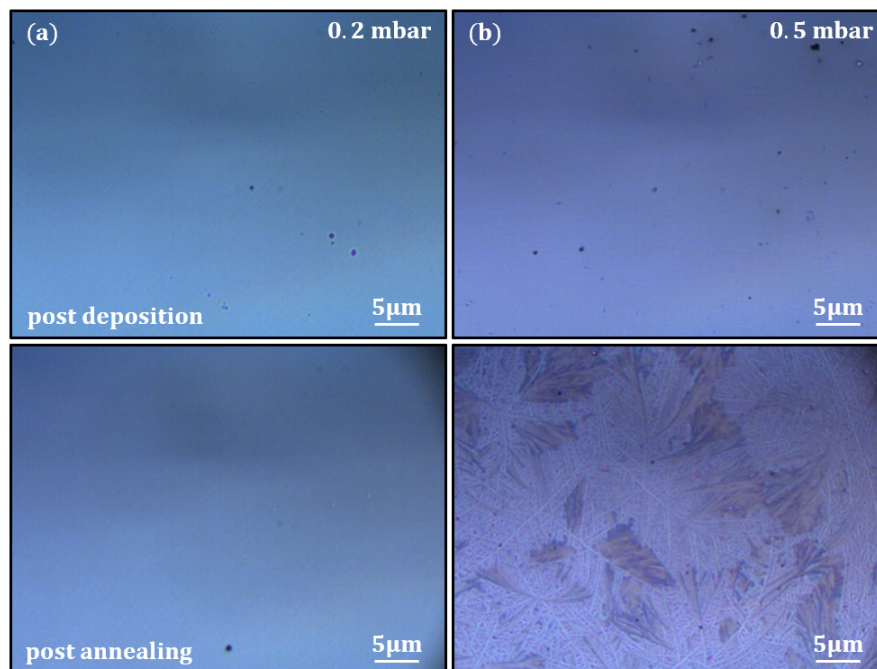


Figure 3.25: Optical photos of the samples before and after annealing at different argon pressures (a) 0.2 mbar and (b) 0.5 mbar.

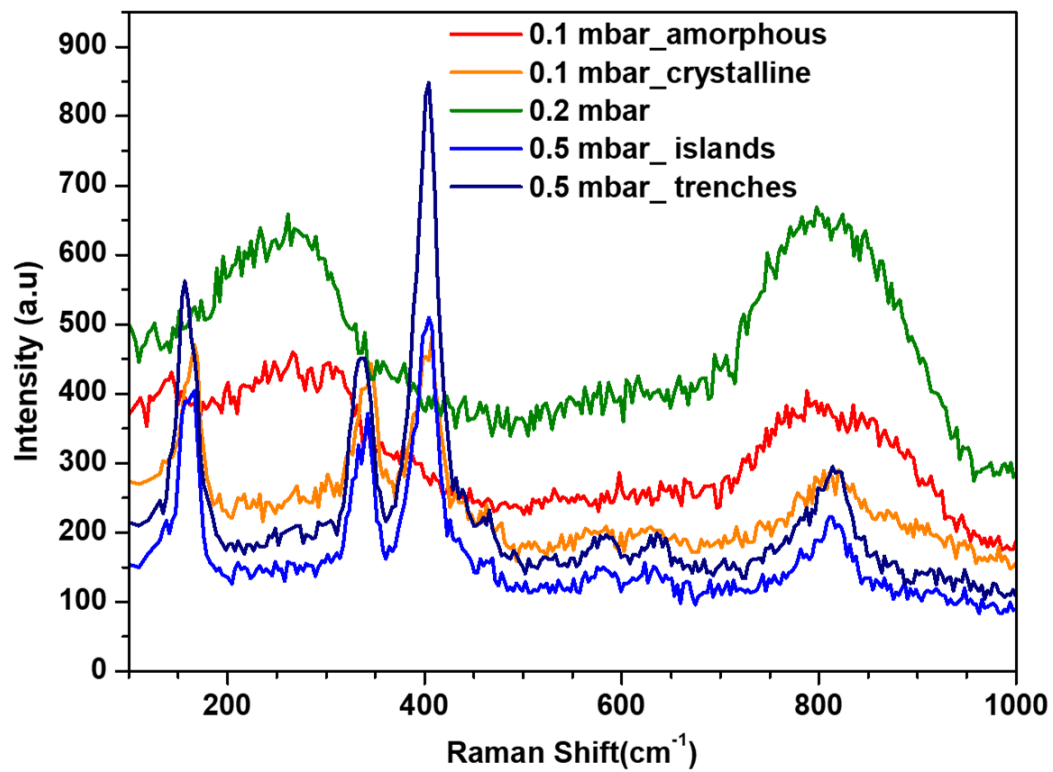


Figure 3.26: Raman spectra of the post annealed niobium oxide films originally sputtered at different argon pressure.

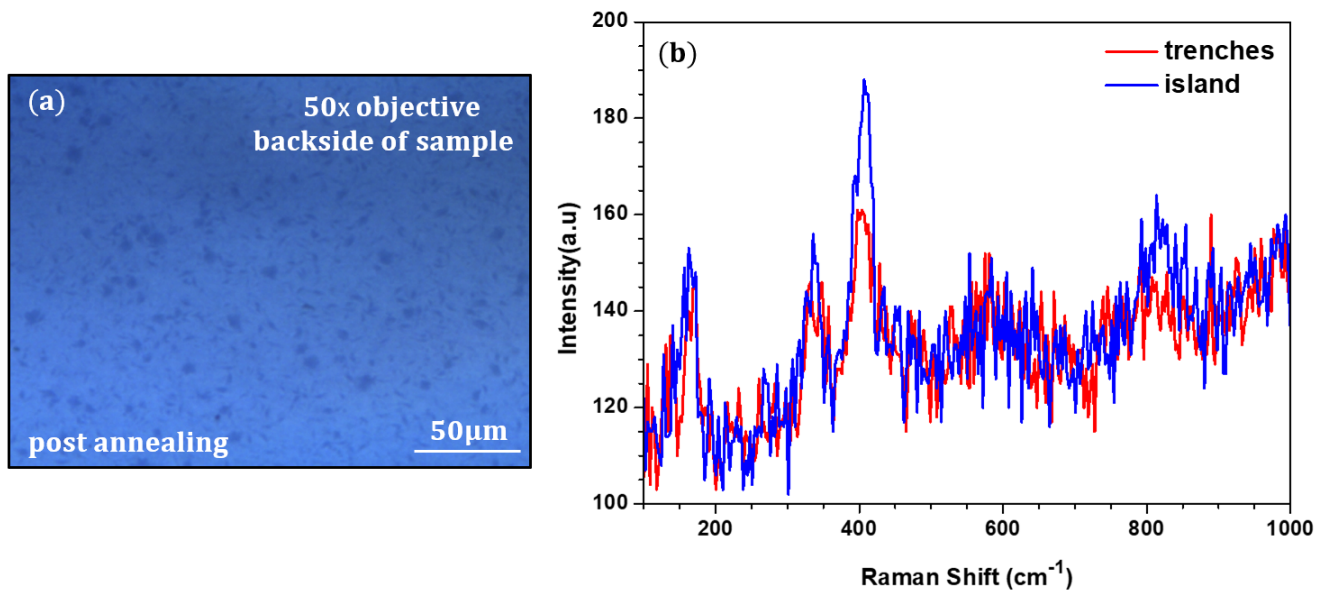


Figure 3.27: (a) Optical photo taken for a totally crystalline NbO_2 film taken from the opposite side of the film (through the glass substrate). (b) The Raman spectra taken of the trenches and islands taken from the opposite side of the sample.

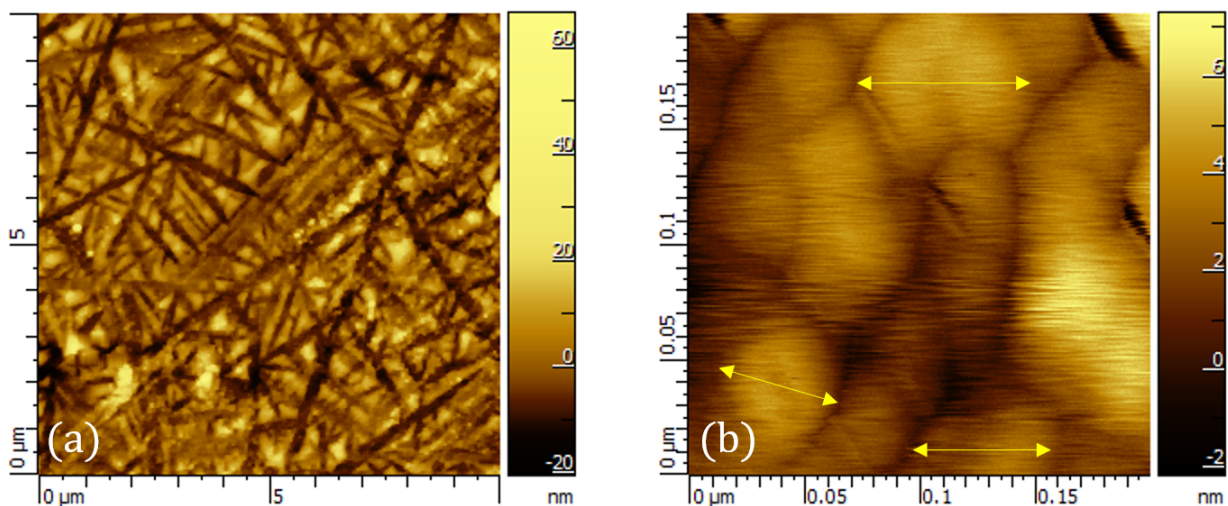


Figure 3.28: (a) 10 μm AFM image of the NbO_2 film showing the trench like structure and nucleated islands. (b) 200 nm AFM image showing the grains size in the film.

A final measure of verification taken after obtaining a fully crystalline NbO₂ film was an XRD test. The XRD performed on the NbO₂ film is shown in figure 3.29 which was taken using a cobalt x-ray source tube and in the Bragg Brentano geometry. Indeed, the XRD peaks show that the film is polycrystalline NbO₂³.

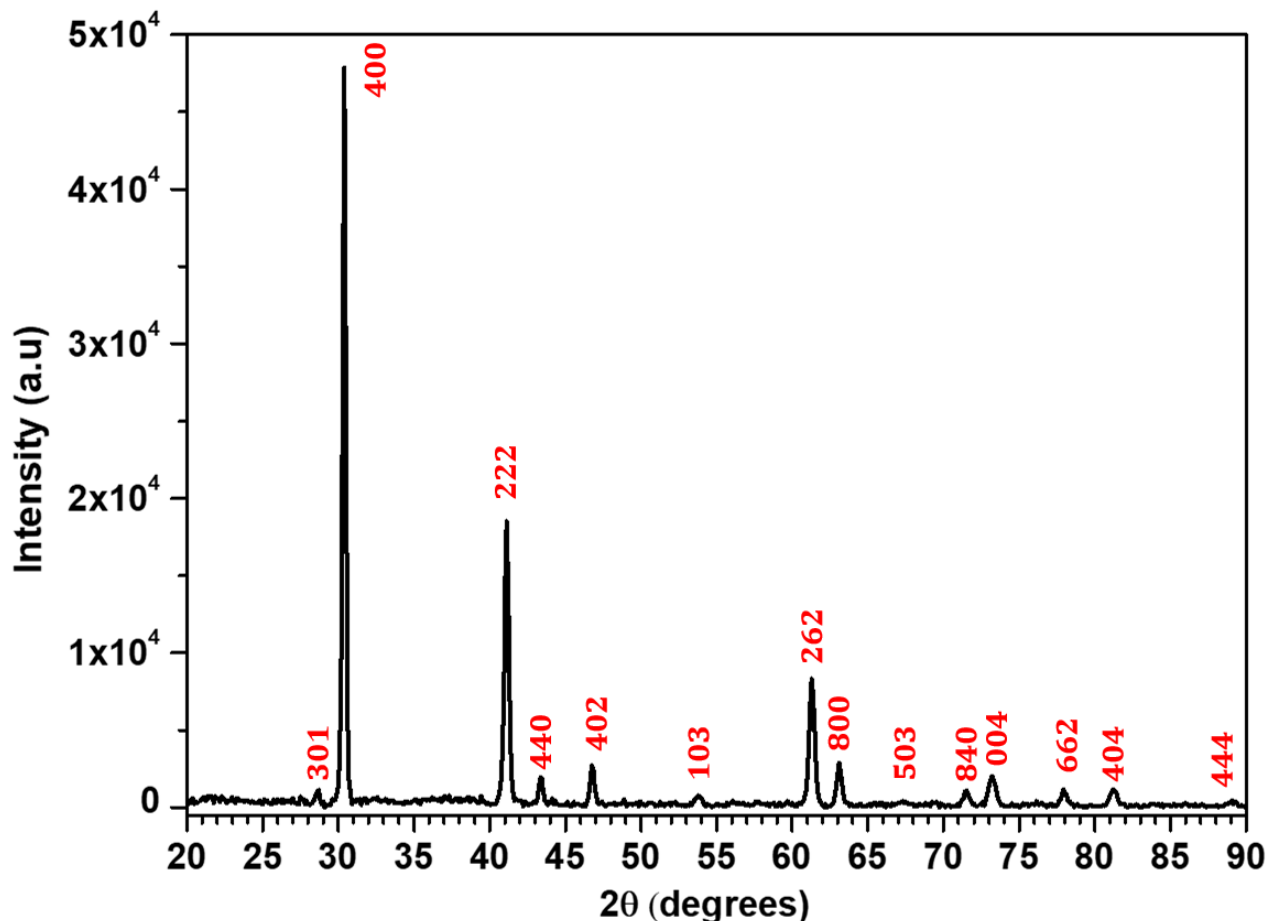


Figure 3.29: X-ray diffraction pattern for the NbO₂ film obtained after annealing for 2 hrs at 600°C. Measurement was taken in the Bragg Brentano configuration. (XRD was performed using Co K α ₁ radiation).

Now that the sputtering parameters for fabricating well polycrystalline NbO₂ films were attained, what remains is to optimize the post annealing process with respect to time and temperature. Therefore, after fabricating NbO₂ films using the parameters of deposition ‘J’ in table 3.5, post annealing for those films were made while varying the two parameters: time and temperature. The studies are discussed in the next section.

³Peak identification will be shown later in a table as to compare with films deposited on silicon substrates.

3.8 Post Annealing Process Optimization

Glass substrates cannot be heated above 600 °C because of structural reasons whereas Si or Si/SiO₂ substrates have no such limitations. The effect of annealing temperature was investigated with Si substrates and that of annealing time with glass substrates. All annealing is done in a vacuum of about 10⁻⁶ mbar.

3.8.1 Effect of Post Annealing Time

Annealing at 600°C for 2 hrs, 4 hrs and 6 hrs does not change the microstructure pattern; however, as the time increased, it was noticed that the trenches became denser as seen in figure 3.30. Also, the Raman signal became more intense as can be seen in figure 3.31 where each curve is an average for several curves taken at different spots on the sample.

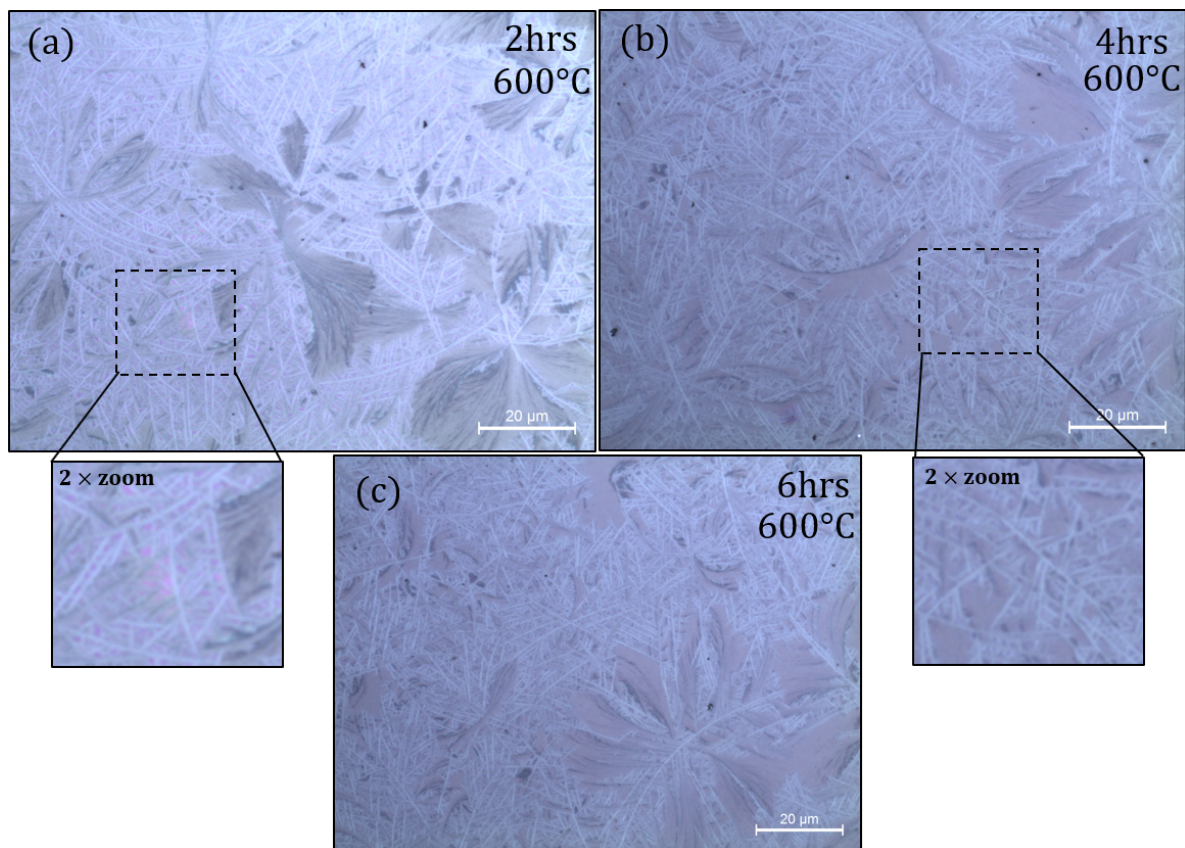


Figure 3.30: Optical photos of NbO₂ films annealed at 600°C at different times (a) 2 hrs (b) 4 hrs and (c) 6 hrs.

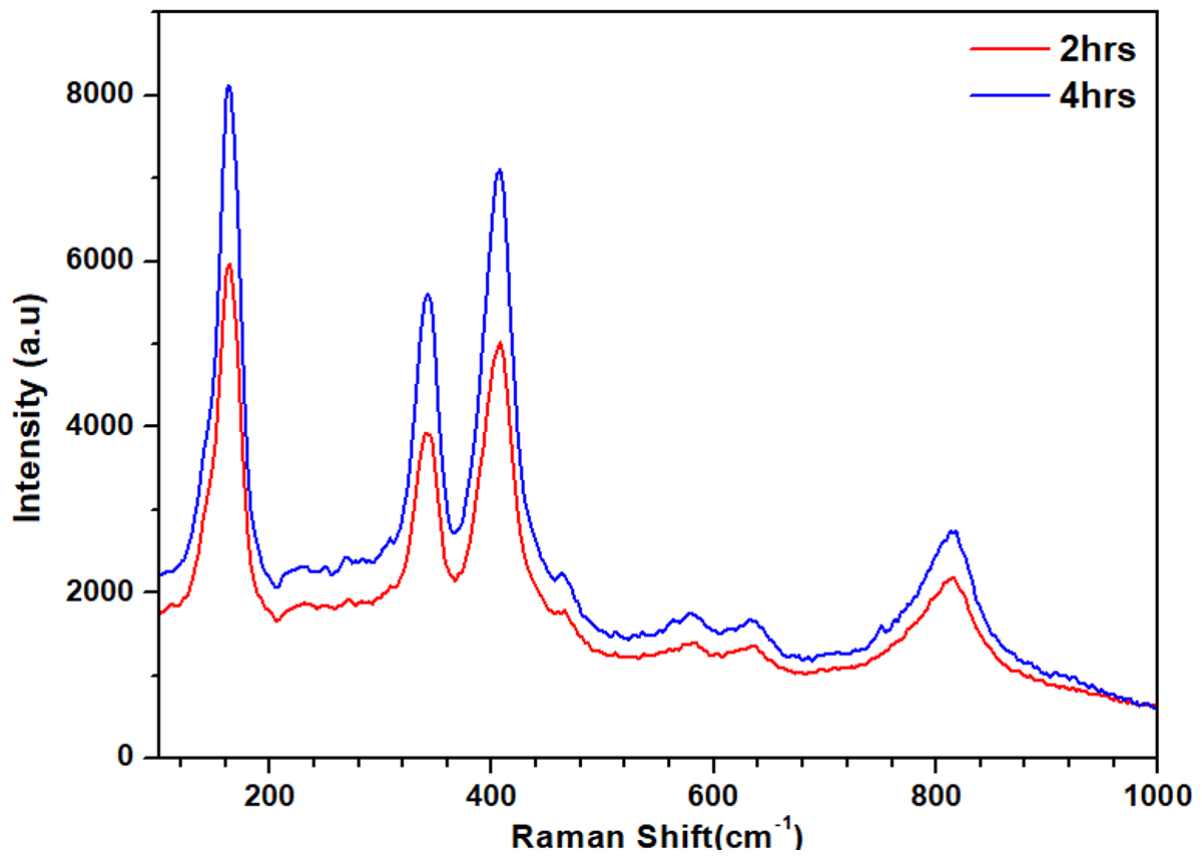


Figure 3.31: Raman spectra of two NbO₂ films one annealed at 600° for 2 hrs and the other for 4 hrs.

3.8.2 Effect of Post annealing Temperature

On Si substrates, amorphous NbO₂ films were deposited and then annealed at different temperatures for 4 hrs. The optical images of the annealed films are show in figure 3.32.

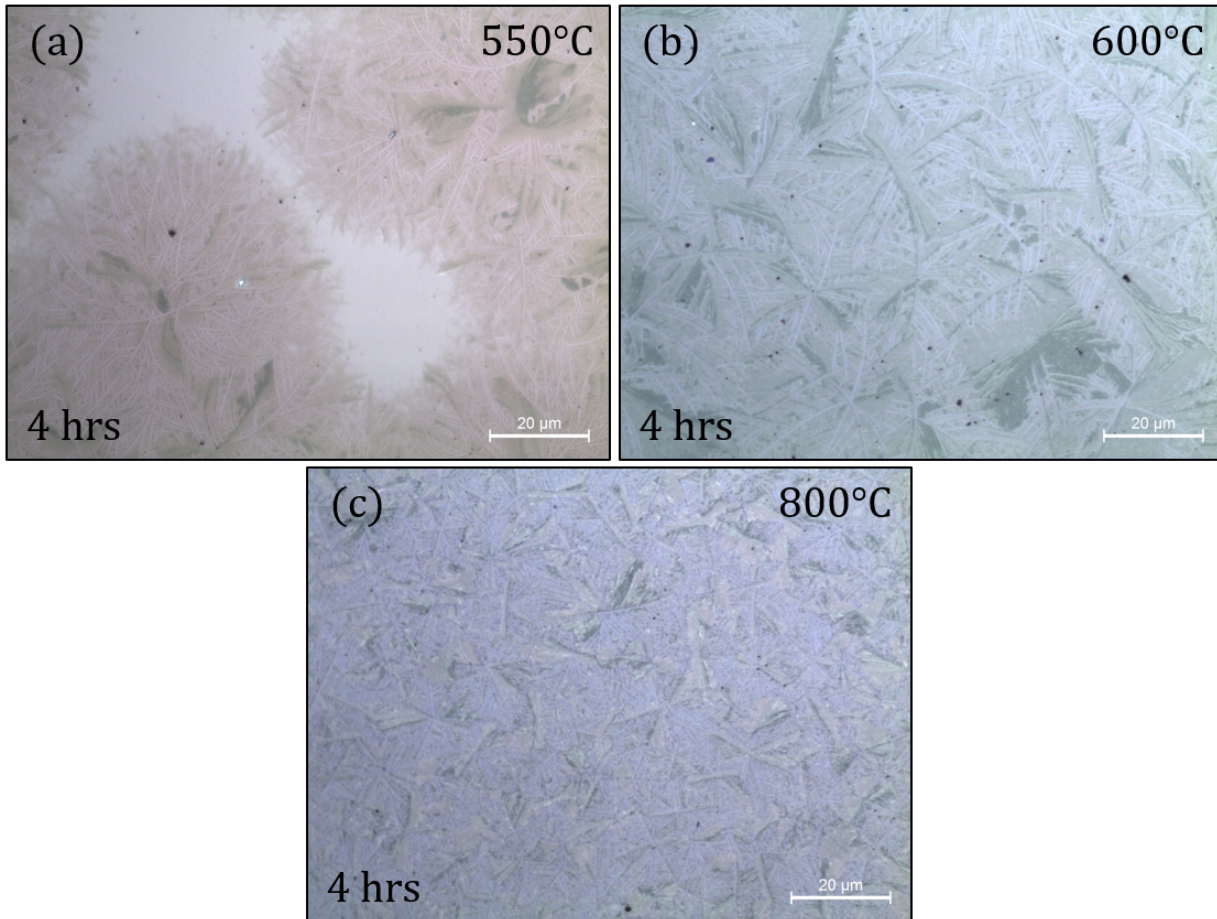


Figure 3.32: Optical photos of NbO₂ films annealed for 4 hrs at (a) 550°C (b) 600°C and (c) 800°C.

We noticed that at 550°C there were regions that were still non crystalline, and as the temperature was increased the trenches seemed to weld together. At 800 °C the trench pattern tend to disappears. Raman spectroscopy was also performed on different regions of each sample and then the average was taken as shown shown in figure 3.33. As the temperature increased the Raman intensity was higher. So, the higher the temperature, the better crystallized the film is, and eventually the better the quality.

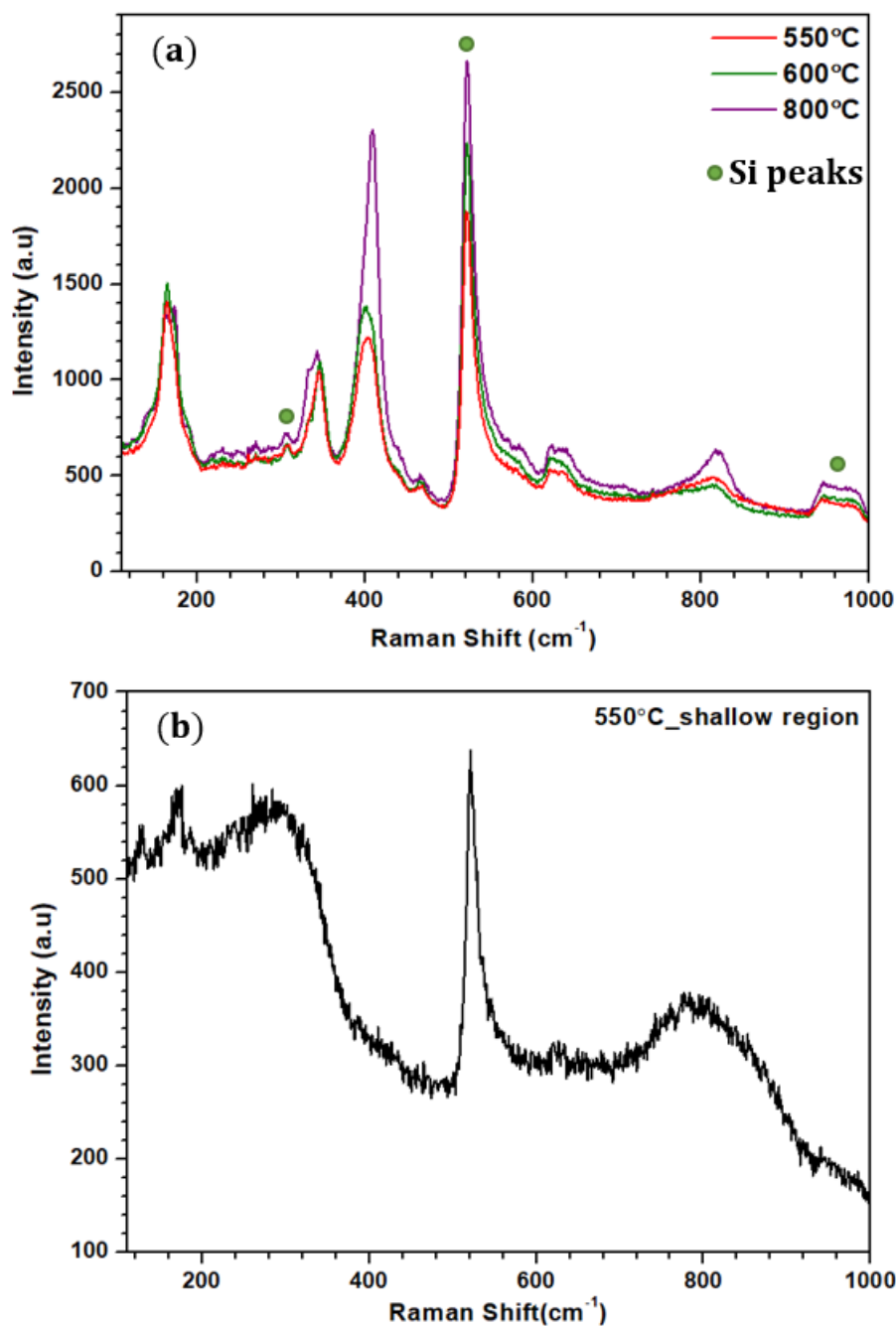


Figure 3.33: (a) Raman spectra of three NbO₂ films on Si substrate annealed for 4 hrs at 550°C, 600°C and 800°C. (b) Raman spectrum of the shallow non-crystalline region in figure 3.32 (a).

Finally, we compare amorphous NbO₂ films grown on different substrates after annealing: film on glass for 2 hrs, on Si and SiO₂ for 14 hrs. Raman spectroscopy comparison is shown in figure 3.34 where the peaks of the films annealed for 14 hrs match the nanostructured NbO₂ films of ref. [172].

X-ray diffraction measurements were also performed on samples with different substrates (glass, Si, SiO₂) before and after annealing. Starting with figure 3.35 (a) which shows the Bragg-Brentano results of the as deposited samples, we see that there are no peaks

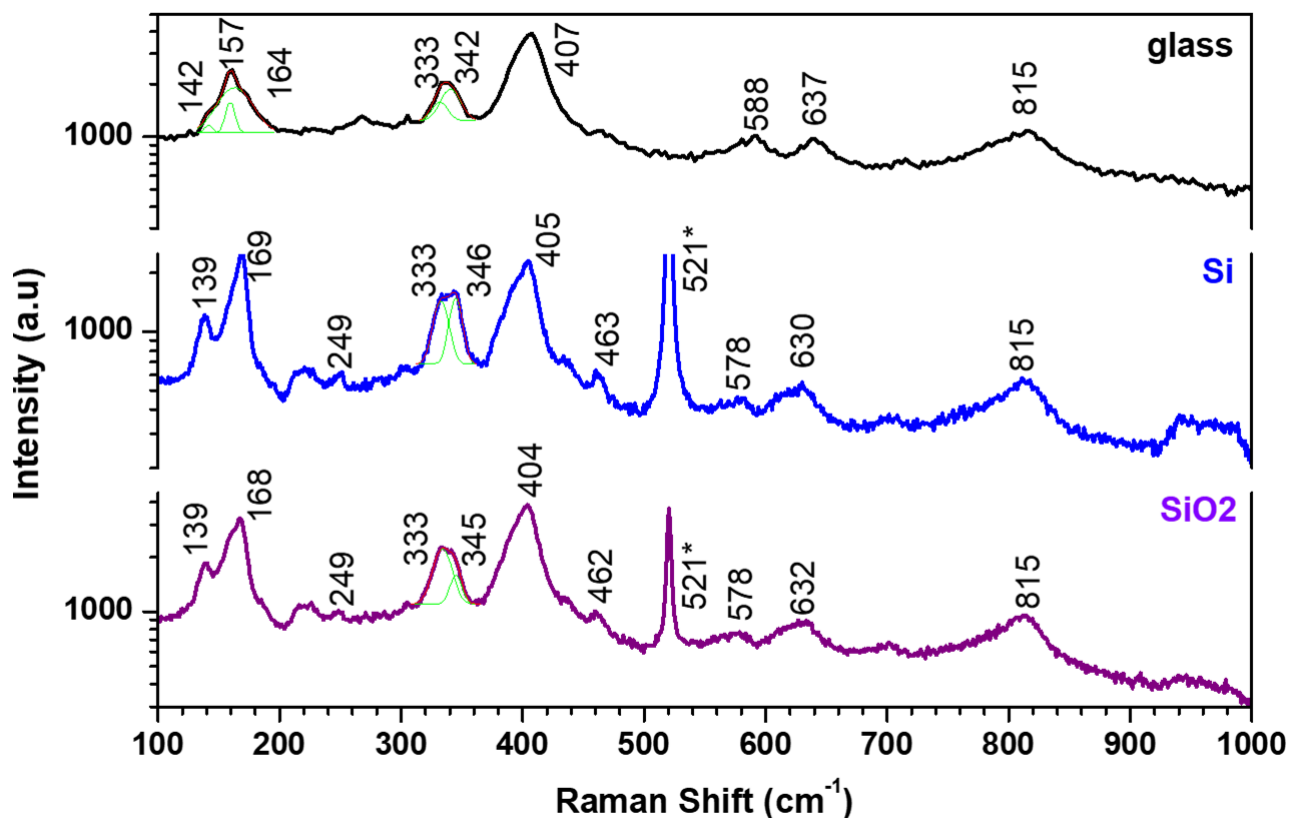


Figure 3.34: Raman spectra of NbO₂ films on different substrates after annealing. In particular Raman spectra of the Si and Si/SiO₂ films match nanostructured NbO₂ films of reference [172]. The green curves represent Gaussian fittings added up to fit an asymmetric peak.

in the sample with glass substrate and only the Si-400 peak appears in the film with Si substrate. This means that the film deposited is amorphous in both samples. In contrary to the former two samples, the film deposited on SiO₂ substrate, did show, in addition to the Si peaks, NbO₂ and Nb₂O₅ peaks. The reason why niobium oxides peaks are present could be attributed to the contribution of oxygen atoms in SiO₂ to the deposited film while the substrate was at 550°C. These peaks could refer to structures formed at the film-substrate interface. Looking, at figure 3.35 (c) where the x-ray measurement is taken in the grazing incidence geometry, we see that all three samples show the presence of a single Nb₂O₅ peak and a pair of NbO₂ peaks. The absence of Si peaks in the Si/SiO₂ samples reveals that the measure is identifying the near surface structure. The film surfaces might have spontaneously crystallized into these phases in air or due to the substrate temperature in the sputtering chamber being aware that the spontaneous formation of Nb₂O₅ thin layer has been previously demonstrated [173]. Also note that the narrow Bragg peak around $2\theta \sim 38.5^\circ$ in Figure 3.35 (a) and (b) is related to the well known double diffraction of the (004) peak of the silicon substrate. Its random appearance in Bragg-Brentano experiments is due to the substrate positioning, which might not be fully in the sample holder plane.

After annealing the films, 2 hrs at 600°C for the one with glass substrate and 14 hrs at 800°C for the other two samples, from figure 3.35 (b) and (d) we see that all three pat-

Peak	$2\theta_{\text{glass}}$	β_{glass}	$L_{\text{glass}}(\text{\AA})$	$2\theta_{\text{Si}}$	β_{Si}	$L_{\text{Si}}(\text{\AA})$	$2\theta_{\text{SiO}_2}$	β_{SiO_2}	$L_{\text{SiO}_2}(\text{\AA})$
301	28.622	0.318	299	28.636	0.425	224	28.651	0.207	216
400	30.389	0.240	398	30.384	0.238	402	30.381	0.222	431
310*	-	-	-	33.22	0.386	249	33.177	0.455	211
002	-	-	-	38.502	0.389	251	38.508	0.160	611
503*	-	-	-	-	-	-	40.440	2.443	40
222	41.122	0.325	303	41.136	0.336	293	41.135	0.310	318
440	43.384	0.285	348	43.390	0.445	223	43.409	0.300	331
402	46.826	0.318	316	46.836	0.322	312	46.847	0.331	304
103	53.950	0.496	209	54.059	0.773	134	54.196	2.525	249
213	-	-	-	56.401	0.376	278	56.377	0.202	518
271	-	-	-	59.857	0.534	196	59.877	0.428	249
262	61.382	0.413	260	61.395	0.419	256	61.393	0.392	274
800	63.104	0.372	291	63.155	0.403	269	63.172	0.346	313
503	67.344	0.743	149	-	-	-	67.354	0.222	497
523	-	-	-	69.422	0.606	185	69.225	0.313	358
840	71.571	0.455	250	71.621	0.339	336	71.574	0.470	242
004	73.304	0.551	209	73.336	0.922	125	73.334	0.117	650
453	-	-	-	-	-	-	75.338	0.325	359
671	-	-	-	-	-	-	76.316	0.268	438
662	77.964	0.465	255	78.021	0.430	276	78.340	0.945	126
404	81.229	0.552	220	-	-	-	-	-	-
444	89.063	0.672	192	-	-	-	-	-	-

Table 3.6: Table showing the indices of plane directions with the corresponding XRD peak positions 2θ of thin NbO_2 films deposited on the three substrates: glass, Si, and SiO_2 . β and L are the peak's full width at half maximum and the grain size respectively. The asterisk sign corresponds to Nb_2O_5 peaks.

terns show that the films are almost completely polycrystalline NbO_2 with some traces of Nb_2O_5 in the Si/ SiO_2 based films and eventually on the surfaces of all three samples. Moreover, most of the NbO_2 peaks are commonly present in all three patterns specifically the most intense ones which tells us that such NbO_2 polycrystalline structure can be obtained regardless of the substrate. It has been observed before [173] that the surface of NbO_2 films exposed to air is often oxidized to Nb_2O_5 to a depth of ~ 5 nm. The grain size L of the NbO_2 and Nb_2O_5 crystallites composing the films are estimated using the Scherrer Equation described in the previous chapter and the results are shown in table 3.6. The grain size is in the order of tens of nanometers which is coherent with what was shown from AFM in figure 3.28.

After optimizing the parameters of both fabrication and post annealing processes, electronic properties were also studied for such films.

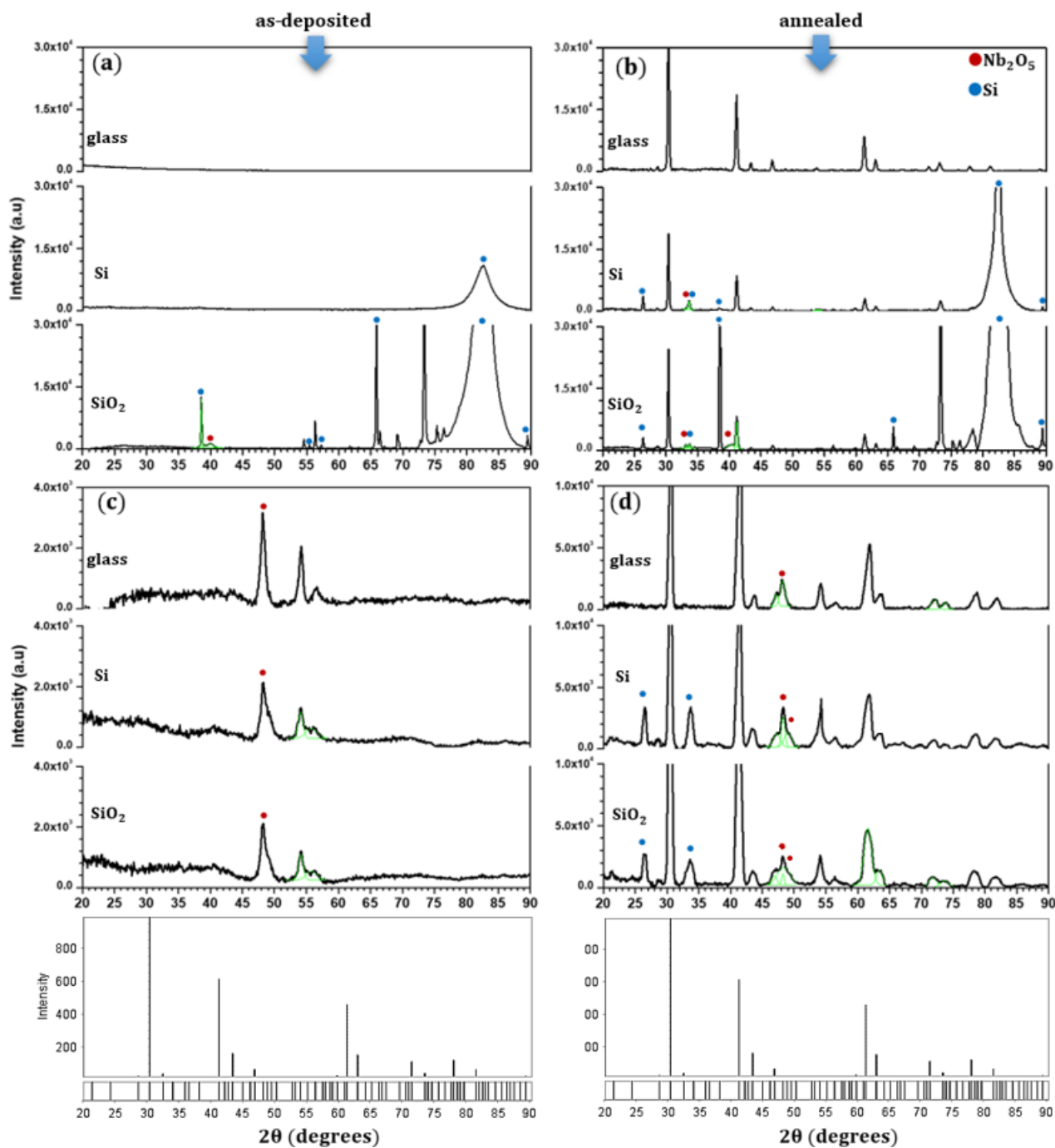


Figure 3.35: X-ray diffractograms of NbO_2 films on different substrates: glass, Si and SiO_2 before and after annealing them. Figures (a) and (b) show the results of experiments done in the Bragg-Brentano configuration, while figures (c) and (d) show the results of experiments done in the grazing incidence geometry. The green curves represent Gaussian fittings added up to fit an asymmetric diffraction peak. (XRD was performed using $\text{Co K}\alpha_1$ radiation).

3.9 Electronic Properties and Doping NbO₂ Thin Films

In the framework of studying the electronic properties of NbO₂, sheet resistance measurements were made on amorphous and crystalline samples from which we can extract the film's resistivities. However, for more precise results, we only used samples with glass substrates to avoid the current leakage within the substrate when using silicon (silicon is less resistive than NbO₂). It is noteworthy to mention that the resistivity of NbO₂ as measured by earlier works lacks consistency. Different studies show different values of crystalline NbO₂ resistivity: 199 Ωcm [1], 2.5 Ωcm [173], ~0.27 Ωcm [178]. Moreover, in some studies such as those done by Nakao. et al. [1] it was shown that the amorphous films were less resistive than the crystalline ones where the resistivity of the amorphous films can be as low as 0.27 Ωcm, i.e about three orders of magnitude less than the crystalline films. The variety in the results can be attributed to the synthesis process and the conditions and parameters used during fabrication since resistivity depends both on the oxygen content and the degree of crystallinity of the film. The results we obtained for room temperature crystalline films were lower than those measured by Nakao et al. [1] in terms order of magnitude where we had: $\rho_{\text{cry}} \sim 50 \Omega\text{cm}$ and that of Nakao's [1] is $\rho_{\text{cry}} = 200 \Omega\text{cm}$, but, our amorphous films were more resistive than theirs: $\rho_{\text{amo}} = 5 \Omega\text{cm}$ for our films $> \rho_{\text{amo}} = 0.27 \Omega\text{cm}$ for [1].

The resistivity between 300 K and 400 K of the amorphous film SL367 (33 nm) and that of the crystalline film SL310 (330 nm) are shown in figure 3.36.

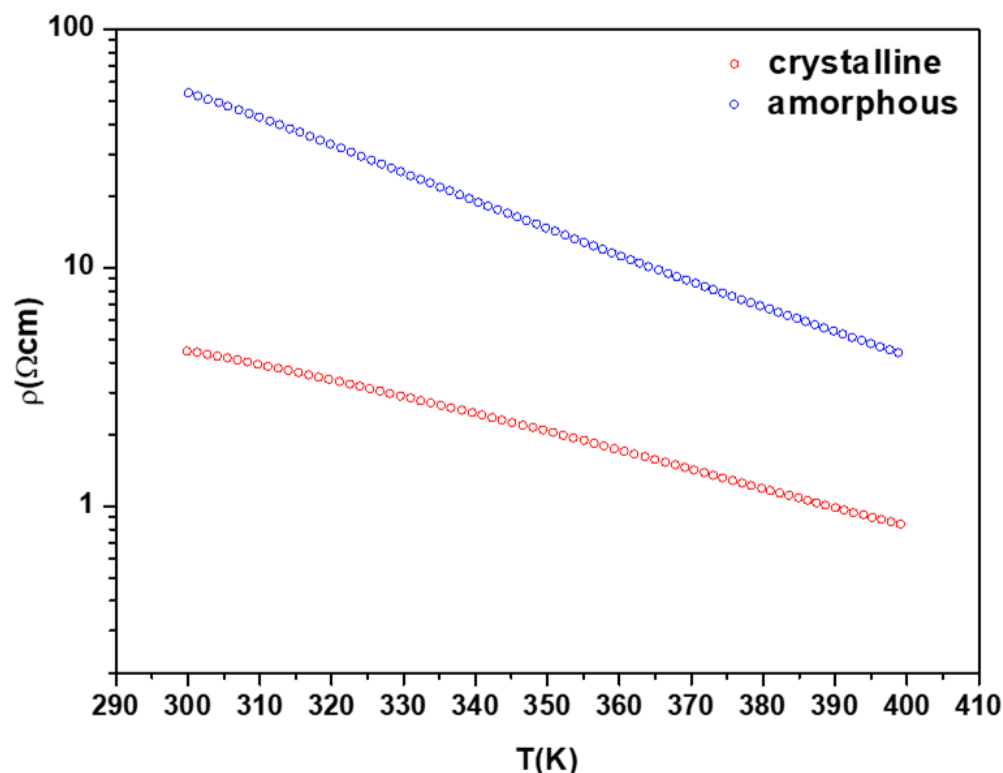


Figure 3.36: The resistivity of an amorphous NbO₂ film and a crystalline NbO₂ film deposited on a glass substrate between 300 K and 400 K.

Figure 3.37 shows the Arrhenius plot of film conductivity, and the fitting to determine activation energy of conduction. If it is assumed that the mobility of the carrier varies rather slowly with temperature, then the conductivity may be written as follows [209]:

$$\sigma = \sigma_0 \exp\left(\frac{-E_a}{k_B T}\right) \quad (3.3)$$

where E_a represent the activation energy, k_B is Boltzmann's constant, σ_0 is the conductivity at zero temperature, and σ is the electrical conductivity.

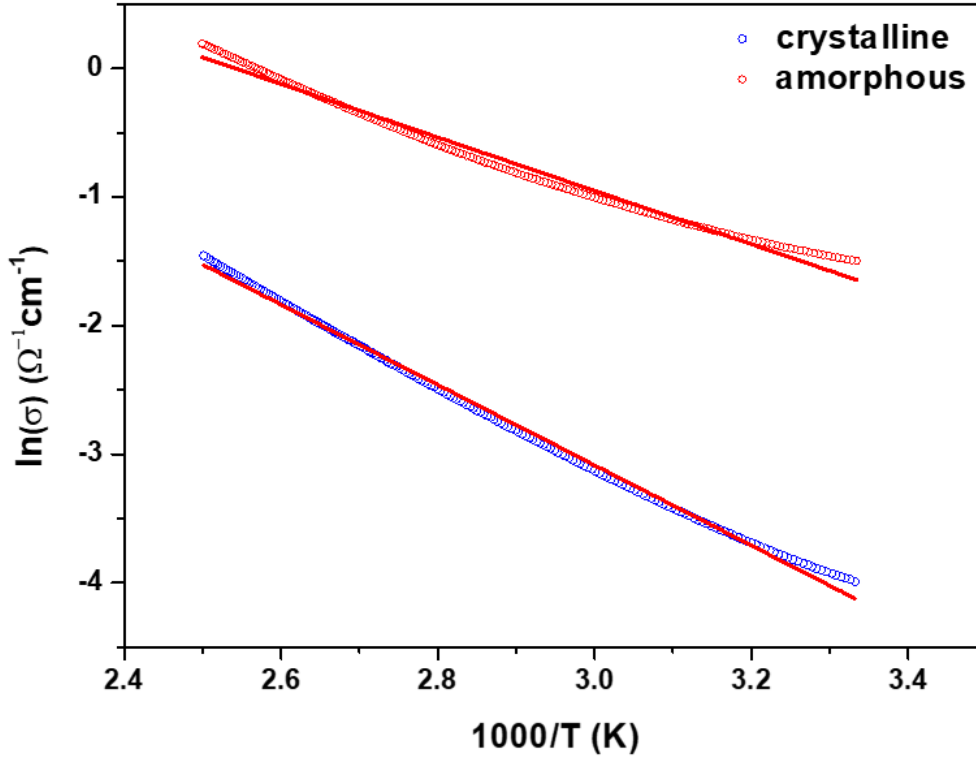


Figure 3.37: Arrhenius plot of film conductivity from 300 K to 400 K.

The activation energy of both the crystalline and amorphous sample was calculated from the slope of the fitting of figure 3.37 and it was found to be ~ 0.269 eV. and 0.178 eV. respectively. The activation energy value of the crystalline sample is close to that found by ref [173], and as expected the higher the conductivity of the sample the lower its activation energy which we see for the amorphous sample as compared to the crystalline.

The measured electrical conductivity in the temperature range (300-400 K) is higher for the amorphous sample. Simulations [178] show that the electronic structure is not very different between crystalline and amorphous NbO_2 , except for localized states in the gap in the amorphous phase. One would expect that the amorphous phase would have lower conductivity because of disorder and Anderson localization. However at non-zero temperature defects in NbO_x control the concentration of the charge carriers. These mainly arise from oxygen vacancies [175] which create trap states within the band gap. Different values of the activation energy in the NbO_x system have been reported ~ 0.23 eV [176], 0.1 eV and $0.5-1$ eV [177], whereas we measure 0.27 eV for the crystalline and 0.18 eV for amorphous phases from temperature dependent resistance measurements,

above room temperature. At non-zero temperature in insulators, it is thermal activation of carriers to the conduction band which determines the conductivity. These energies correspond to activation from in-gap defect states rather than across the gap.

3.9.1 Space Charge Doping of NbO_2 Films

As discussed in section 1.7, we decided to electrostatically dope NbO_2 thin films on glass substrates using the space charge doping method and a field effect transistor configuration to see if an insulator-metal transition could be induced at room temperature. 33 nm thin films were prepared and tested for R_S measurements. Measuring the sheet resistance R_S of these three 33 nm samples SL_{354} , SL_{355} and SL_{356} which were post annealed at 600°C for 6 hrs, 4 hrs and 2 hrs respectively, we found that as the annealing time increased, R_S also increases; $0.3 \text{ G}\Omega$ for SL_{354} , $0.2 \text{ G}\Omega$ for SL_{355} and finally $0.1 \text{ G}\Omega$ for SL_{356} . And as we have seen that the film's resistivity increases when moving from an amorphous phase to a crystalline one, this also verifies that the samples that were annealed for a longer time had better crystallinity.

The SL_{356} sample annealed for 6 hrs was set-up on the cryostat for electrostatic doping. For this the sample and substrate temperature is raised to 400 K to activate the motion of Na^+ ions in the glass substrate. After this gate voltage is applied to the device to induce ionic drift and create a space charge of Na^+ ions beneath the film and eventually dope the film. The result is shown in figure 3.38 which shows the gate voltage applied and the R_S measured as a function of time. Increasing time and gate voltage means an increasing space charge of Na^+ ions and thus an electrostatically induced increased n-doping of the NbO_2 film.

By the time a gate voltage of 250 V is reached, the sheet resistance has decreased by about one order of magnitude, so the film is n-doped. However no electronic phase transition is observed. The same experiment was repeated with both amorphous and crystalline films with similar results. Several reasons can be invoked for this:

Electrostatic doping is very sensitive to the nature and perfection of the glass/ NbO_2 interface. In our films, this interface might not be perfect because:

- 1) at the interface the NbO_2 phase might not be as prominent as in the film bulk. We have no accurate means of verifying this even though our Raman spectra through the glass are satisfactory.
- 2) The annealing temperature is close to the T_g for glass and may induce imperfections or ionic diffusion at the interface.

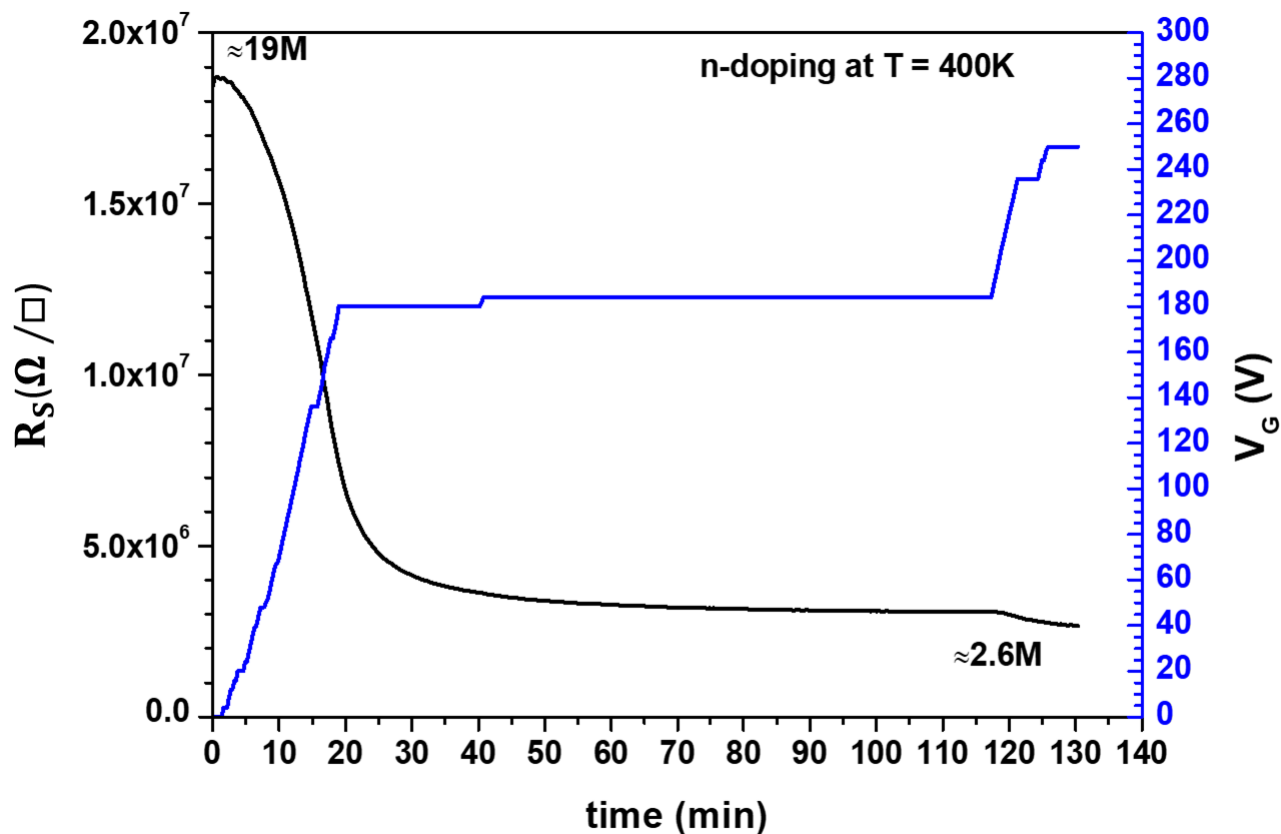


Figure 3.38: N-doping an NbO₂ film at 400 K using Space Charge Doping Technique.

Space charge doped phase transitions were one of the objectives of this thesis which was financed by the Labex MATISSE. In that perspective a collaboration with Dr. Ricardo Lobo of LPEM/ESPCI had been envisaged with the use of infra-red spectroscopy to investigate possible phase transitions in-situ with space charge doping. Some pilot experiments were performed with Dr. Lobo in this direction, but the inconclusive results of space charge doping as outlined above led us to concentrate our remaining efforts on investigating CC-NDR in the material.

3.10 High Temperature Raman Measurements

NbO_2 undergoes a metal insulator transition at $t \sim 800^\circ\text{C}$. This electronic transition is accompanied by a structural transition. We attempted to study this structural transition by in-situ Raman spectroscopy.

We set a crystalline sample NbO_2 sample Si_{35}^{100} in a Linkam sample holder, compatible with the Raman spectrometer and which is a flow water cooled apparatus where temperatures of the order of 1000°C could be reached. It would have been preferable to measure in-vacuum but this was not possible in this apparatus, instead an Ar flow was used to force air out of the Linkam chamber. A $10\times$ objective was used for the Raman measurements. A 513 nm green laser was chosen with a power of 60 mW, and the acquisition time for each measurement was 60 s. Raman measurements were performed at room temperature and then from 100°C to 1000°C with steps of 100°C . A photo of the set-up is shown in figure 3.39. Raman spectra are shown in figure 3.40 along with optical photos of the evolution of the film structure.

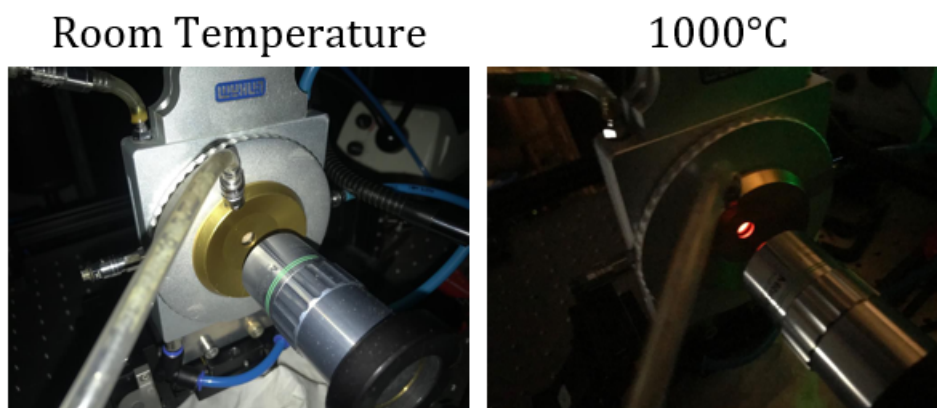


Figure 3.39: Photo of the linkam where the sample was kept during the measurement at RT (left) and at 1000°C (right).

The small dark islands that can be seen on the film in the photos until 600°C disappear when the temperature was raised beyond 600°C indicating that the structure has changed or the film has changed composition. From the Raman spectra we see that after the spectrum at 600°C the NbO_2 peaks disappear and either the film is no more crystalline, or more likely there is a stoichiometry change perhaps due to the presence of residual gases even though there is a continuous Ar flow.

Although we were not able to conserve the film's crystallinity and witness an insulator to metal transition due to apparatus limitations, we were still able to achieve a side quest which is beneficial and can be used as reference for other types of measurements. We studied the shift in the silicon peak's position (peak 521 cm^{-1}) at the different temperatures. The results are shown in figure 3.41. These points can be fitted linearly with the equation:

$$T(E) = -39.7 E + 20704 \quad (3.4)$$

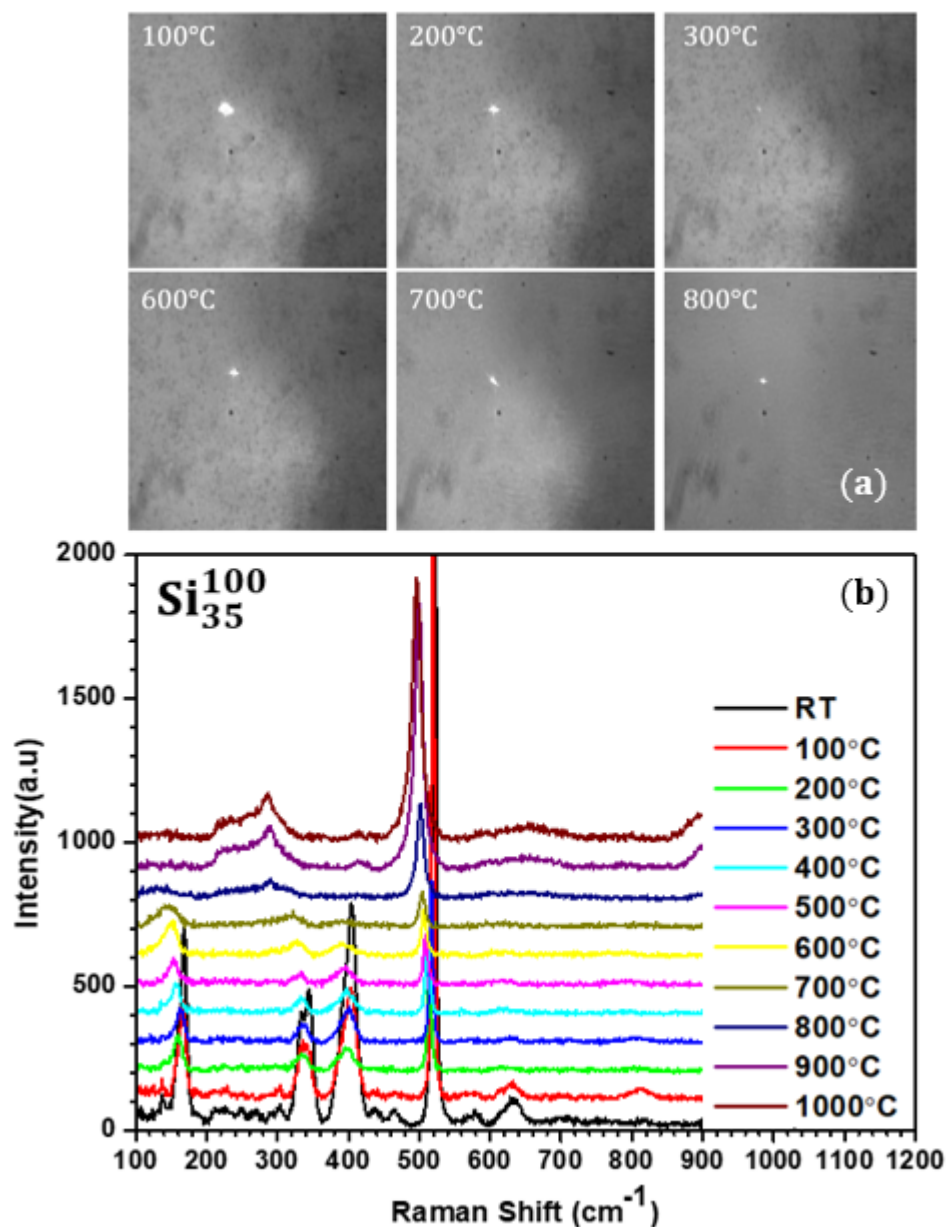


Figure 3.40: (a) Optical photos showing the evolution of the NbO₂ crystalline film. After 700°C the crystallinity disappears. (b) Raman spectra of the NbO₂ film. We notice that the NbO₂ peaks start vanishing at 700°C. After which only the Si peaks appear.

where E is the Raman shift of the peak (in cm^{-1}). The slope of the equation is -39.7 ± 0.6 and the intercept equals 20704 ± 300 K. This equation represents a relation between the main Si Raman peak and the temperature, so it is a good reference which we will use later in this work.

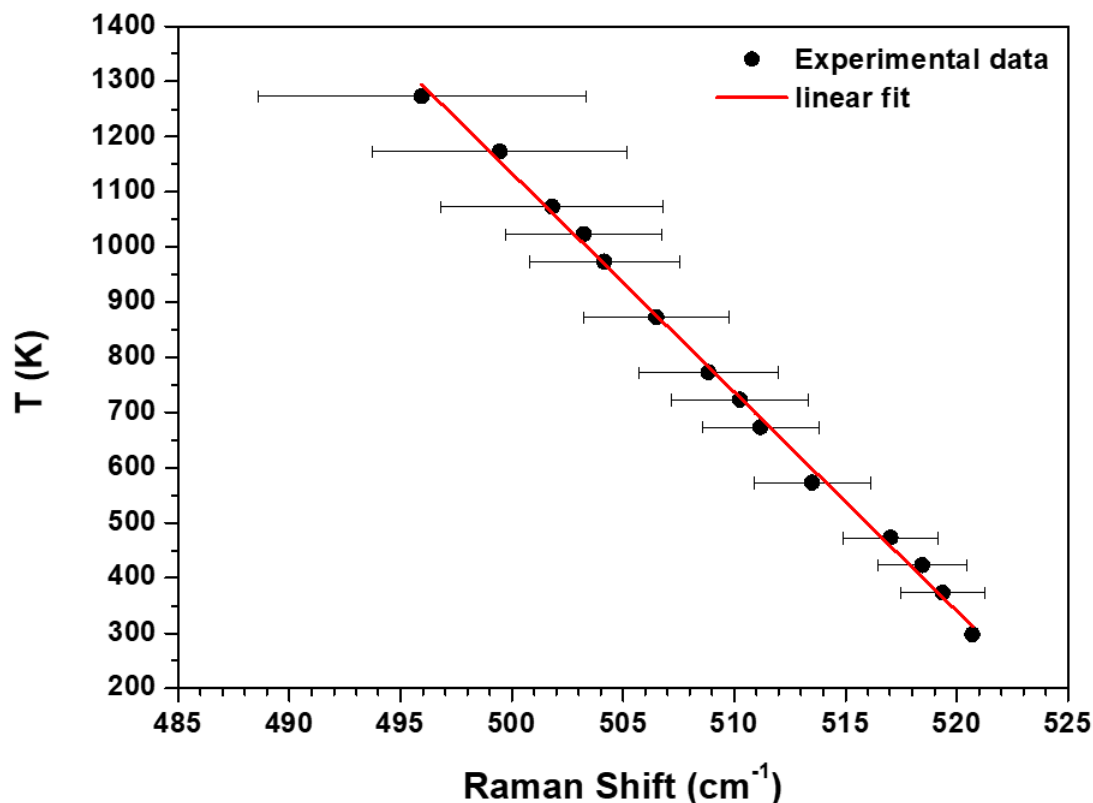


Figure 3.41: A graph showing the variation of temperature as a function of Si peak position.

3.11 Conclusion

We have seen that ex situ oxidation of Nb thin films prepared by sputtering from an Nb target does not work in producing homogeneous and stoichiometric NbO₂. Therefore, an alternative technique adopted was sputtering from a stoichiometric NbO₂ target. Using RF-magnetron sputtering we were able to produce amorphous NbO₂ films on all three different substrates we used. Post annealing of the films was required in order to crystallize the films. We noticed that a longer annealing implied a bigger grain size. Also, annealing at higher temperature lead to a better quality crystallization. These films were characterized by Raman spectroscopy, XRD and transport measurements (some times in situ) and we saw that correct stoichiometry was obtained on all substrates. Finally, from high temperature Raman measurements, we were able to achieve a relation between the temperature and the shifting in the Si raman peaks.

Chapter 4

Negative Differential Resistance in NbO₂: Origins

4.1 Introduction

Threshold switching (TS) in niobium oxides, in which the current abruptly increases at an onset voltage, has been reported as early as 1960's [2]. This phenomenon has been observed not only in stoichiometric NbO₂ [210], but also in metal rich nonstoichiometric phases of NbO_x [211–213]. However, the physical concepts that lie behind the threshold switching mechanism in NbO₂ are still controversial, and different studies attribute this switching to different origins. Some claim that this phenomenon is basically a thermally driven metal insulator transition MIT which originates from Joule's heating with formation of conducting filaments in the bulk material leading to a local drop in the resistance [134,214,215]. Others suggest that the TS is triggered by modifications in the electronic structures by applying an electric field [216–218], while recent work shows that this TS is due to the current and temperature controlled negative differential resistance phenomenon that is present in NbO₂ [24]. Research has concentrated on different designs of NbO₂ devices in order to understand this ambiguous behavior of NbO₂ .

Most studies have concentrated on geometries susceptible to be directly incorporated in devices. Such a geometry often implies a thin layer film of NbO_x (typically few tens of nm), probed vertically across its thickness, with the device area limited laterally by the size of one of the contacts which can also be typically a few tens of nm. This implies a very small NbO₂ volume in the device [24,137]. Wang et al. [173] fabricated Nb/NbO₂/TiN vertical devices and studied the response of NbO₂ to an applied electric field. They report that the obtained MIT demonstrated unipolar threshold switching characteristics, with repeatability up to hundreds of cycles and thermal stability up to 150°C. Moreover, they suggested that the hopping conduction was the dominant conduction process in the NbO₂ insulating state and that the MIT was not thermally driven by Joule heating but rather by changes in the electronic structure. Kumar et al. [24] have also fabricated vertical NbO₂ sandwiched devices. They studied the response of NbO₂ under the application of electric current. In their experiments, they witness two domains where NbO₂ exhibits CC-NDR, one at relatively low temperature and the other at a high one. They concluded that the former NDR is caused by Joule-heating-driven thermal runaway in strongly non-linear conduction, while the latter is a temperature-controlled MIT-driven hysteresis.

In our work, we focus on answering several questions concerning these phenomena in NbO₂ and understand their nature and origin. Is this phenomenon electric field driven? Is it a current controlled or temperature controlled NDR? Are there any structural changes or phase changes accompanying the transition? This chapter is the basis of a manuscript which has been submitted for publication.

4.2 Studies Under Electric Field

Unlike most NbO₂ or NbO_x devices which are used in such studies where a thin film is sandwiched between two conducting contacts, at least one of which is nanometric in size, (Pt/TiN/NbO_x /W [133], Pt/NbO₂ /Pt [219], Nb/NbO₂ /TiN [216]) our film was deposited on an n-doped (by Phosphorus) 280 μm thick silicon substrate Si < 100 > , or on a 500 micron thick soda-lime glass substrate. The Si substrate acts as the bottom electrode and 50 nm of gold is deposited on the NbO₂ film as a top electrode. The gold contacts were deposited in a geometry that allows to access different measurements such as vertical measurements, lateral measurements and sheet resistance measurements. A central square and four peripheral triangular contacts were deposited on top of the NbO₂ film as discussed in chapter 2 and shown in figure 4.1 (b). The parameters of the sputtered NbO₂ film Si₃₆¹⁰⁰ are shown in table 4.1. The films had a thickness of ~ 130 nm. Before gold contact evaporation, the amorphous film was crystallized by annealing in vacuum (10⁻⁶ mbar < p < 10⁻⁵ mbar) for 4 hrs at 600 °C. The electric insulator MgO substrate is used to isolate the substrate from the copper sample holder of a cryostat used for temperature control and a vacuum environment. The device configuration is shown in figure 4.1 (b) as compared to that of Kumar et al.'s [133] in figure 4.1 (a). The central contact is labelled C, the gate gold contact under the silicon or glass substrate G and the peripheral contacts X,Y,Z and T. The choice of the Si substrate allows us to perform both vertical and lateral measurements and avoid the trace Nb₂O₅ phase which can be found on the SiO₂/Si substrate, see section 3.8.

Parameter	Target Etching	Substrate Etching	Deposition
Ar pressure (mbar)	0.5	0.5	0.5
power (Watts)	100	225	225
tension (V)	465	480	500
target-substrate distance (cm)	6.5	6.5	6.5
substrate temperature (°C)	RT	RT	550
time (min)	2	3	4

Table 4.1: Sputtering parameters of sample Si₃₆¹⁰⁰ used in the studies to test the effect of electric field on the NbO₂ transition.

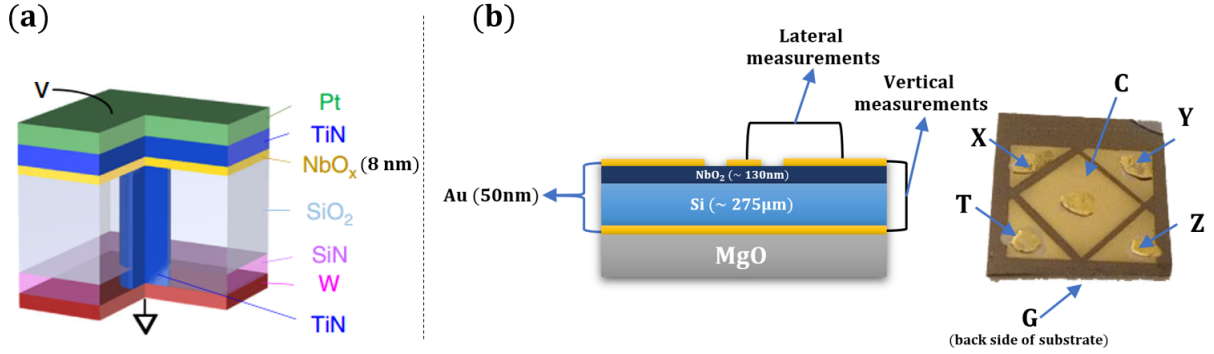


Figure 4.1: (a) A schematic drawing of the device used by Kumar et al. [24]. (b) A schematic of the device used in our work (left) along with its relative photo (right).

4.2.1 Vertical Measurements and Sheet Resistance

4.2.1.1 Vertical Measurements

A sample with silicon substrate was shaped, contacted and mounted in a cryostat as described in section 2.3 and figure 4.1 (b). As a first, step we studied the I-V curves along the vertical direction (between the central contact C and the gate contact at the back of the substrate, and between a peripheral contact and the gate). Voltage was swept from -200 V to 50 V along the central contact with relatively larger area and along a peripheral contact with relatively smaller area, and I-V curves were recorded as shown in figure 4.2. We notice two main features. We observe asymmetric-diode like characteristics depending on the polarity. In a ‘forward-bias’ regime, the device conducts, in a ‘reverse-bias’ regime it does not until a threshold voltage that is subject to hysteresis is reached. This diode-like behavior is a consequence of the semiconductor-semiconductor Si-NbO₂ interface. The ‘reverse-bias’ regime, which is the one probed in all earlier work with a metal-NbO₂ interface contains the switching region which is often identified with a threshold voltage. One immediate conclusion is that this threshold voltage does not correspond to a Zener-like regime. The simple reason is that the threshold is not voltage dependent, and depends on the history of the I-V cycle, ($V_{th1} \neq V_{th2}$).

Since we can control the global temperature of the device we can investigate the effect of temperature on the observed hysteresis. The curves obtained at 320 K, 240 K, 150 K and 50 K are shown in figure 4.3. We notice that as the temperature decreases the hysteresis width ($V_{th1} - V_{th2}$) and the threshold voltage V_{th1} increase. This result is contrary to what Wang et al. [216] see, where the hysteresis, which they attribute to surface Nb₂O₅, shifts to lower voltages and becomes more noticeable at higher temperatures. As for the forward bias, the voltage is barely shifted to a higher one as the temperature decreases.

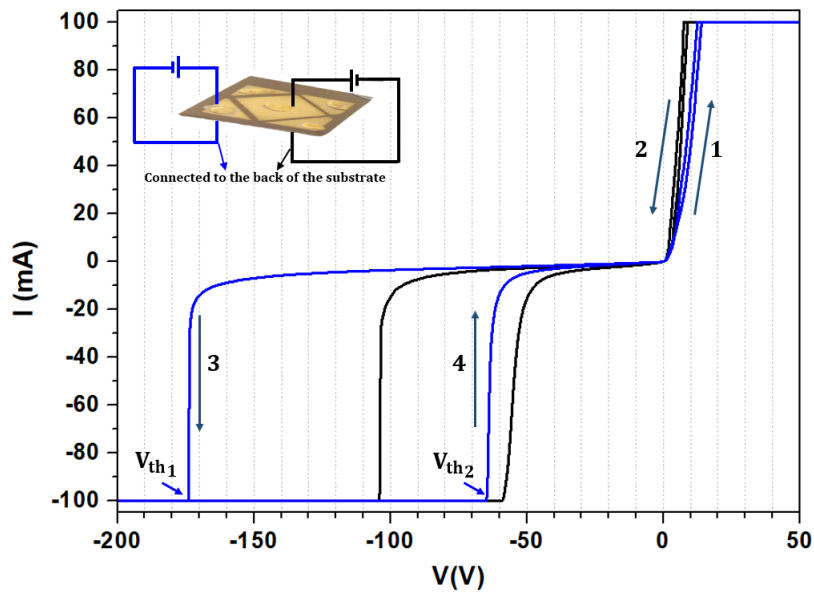


Figure 4.2: I-V curves of the central contact C to the gate contact (black) and of a peripheral contact of relatively smaller area to the gate contact (blue) taken at stabilized temperature of 320 K. Both curves show diode-like characteristics; however, the threshold voltage V_{th1} across the peripheral contact is higher than that across the central one.

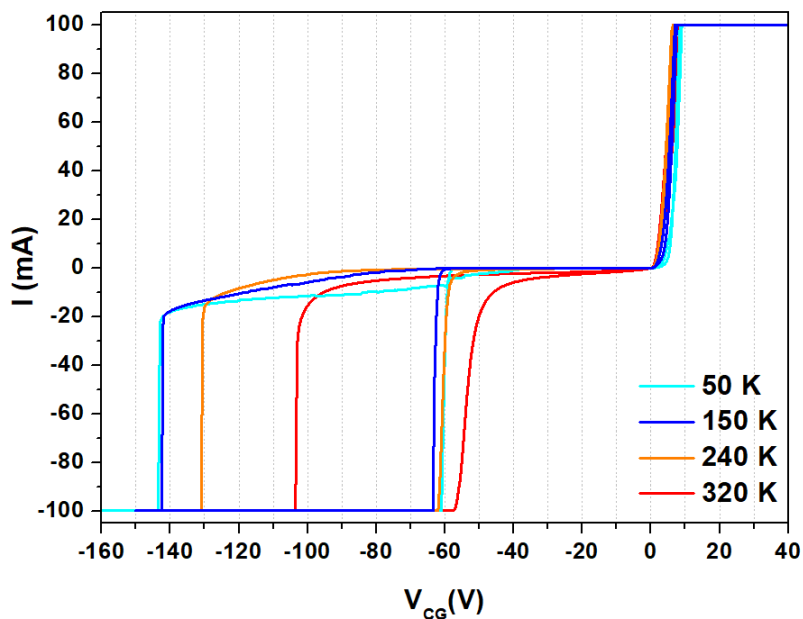


Figure 4.3: I-V curves across the central-gate contacts V_{CG} taken at different stabilized temperatures. The threshold voltage V_{th1} shifts to the right (lower voltages in absolute value), and the hysteresis size becomes smaller as the temperature increases.

4.2.1.2 R_S Measurements

We now examine a possible effect of the electric field on the conductivity of our NbO_2 sample. The same sample as in section 4.2.1.1 is used for this measurement. However, an electric field is applied across the thickness of the NbO_2 film using the silicon substrate as the gate contact and the central C contact. The peripheral X,Y,Z and T contacts are then used to measure the sheet resistance in the van der Pauw configuration. A bias voltage $V_{\text{bias}} = 2\text{ V}$ was applied across the peripheral contacts and the resistance was measured according to the van der Pauw method. A gate voltage was swept along GC from 0 to 100 V (in the ‘reverse-bias’ regime), while R_S across the contacts X, Y, Z and T was measured, and the current compliance was set at 100 mA. The experiment was stabilized at 270 K at the beginning of each measure and the results are shown in figure 4.4.

As the voltage V_{CG} increased, both the current and the sheet resistance increased. R_S increased from $1.2\text{ k}\Omega$ to a maximum of $23.2\text{ k}\Omega$ at 25 V. As the voltage was increased further, R_S started to decrease while the current remained increasing. At 94 V (V_{th1}), a jump occurred in the current where it increased from $\sim 5\text{ mA}$ to saturate at the compliance (100 mA). On the other hand, R_S dropped from $5\text{ k}\Omega$ to reach $265\ \Omega$. While sweeping back, no change was observed until $V_{\text{th2}} = 36\text{ V}$ was reached where both curves showed a sharper drop/jump from 100 mA to $797\ \mu\text{A}$ for the current and from $254\ \Omega$ to $18.6\text{ k}\Omega$ for R_S . We again see a voltage threshold with associated hysteresis. Is this the same phenomenon seen earlier in the I-V measurements? The electric field seems to change the sheet resistance of the film with a dramatic collapse at high gate voltage but the more resistive state is obtained on the down sweep at much lower voltage. Our first step was to investigate the observed hysteresis in these two measurements which is closely associated to the reaching of a compliance limit in the allowed current and may thus have instrumental origins.

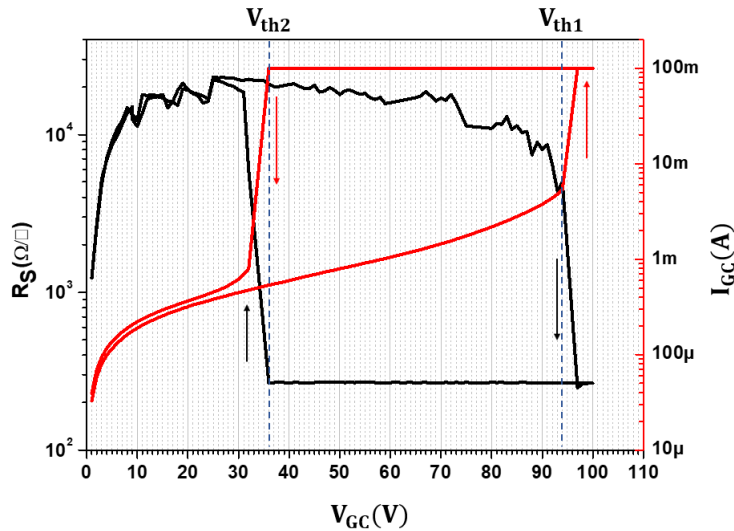


Figure 4.4: Graph showing the variation of R_S (left axis) and the current I_{GC} (right axis) as a function of the voltage V_{GC} . As V increases to 94 V (V_{th1}), the current shows a jump in the curve, while R_S shows a step drop to a less resistive state. Then as V decreases to 36 V (V_{th2}), the current/ R_S display a sharp drop/jump respectively.

4.2.1.3 Hysteresis and Threshold in Voltage Control Mode

This hysteresis seems to be at least partly an instrumental artifact generated by the compliance value on the Keithley source meter.

To clarify this we changed the current compliance values (1 mA, 10 mA, 20 mA, 50 mA and 100 mA). Carried out at the same temperature 270 K, the I-V curves taken at different compliances and the relative sheet resistance measurements are shown in figure 4.5 .

The I-V curves showed that the hysteresis is compliance dependent, figure 4.5 (a), and that it increases as the compliance value is increased. Moreover, the threshold voltages also change, especially V_{th2} . Similarly, the sheet resistance drop to different values for different compliances, figure 4.5 (b).

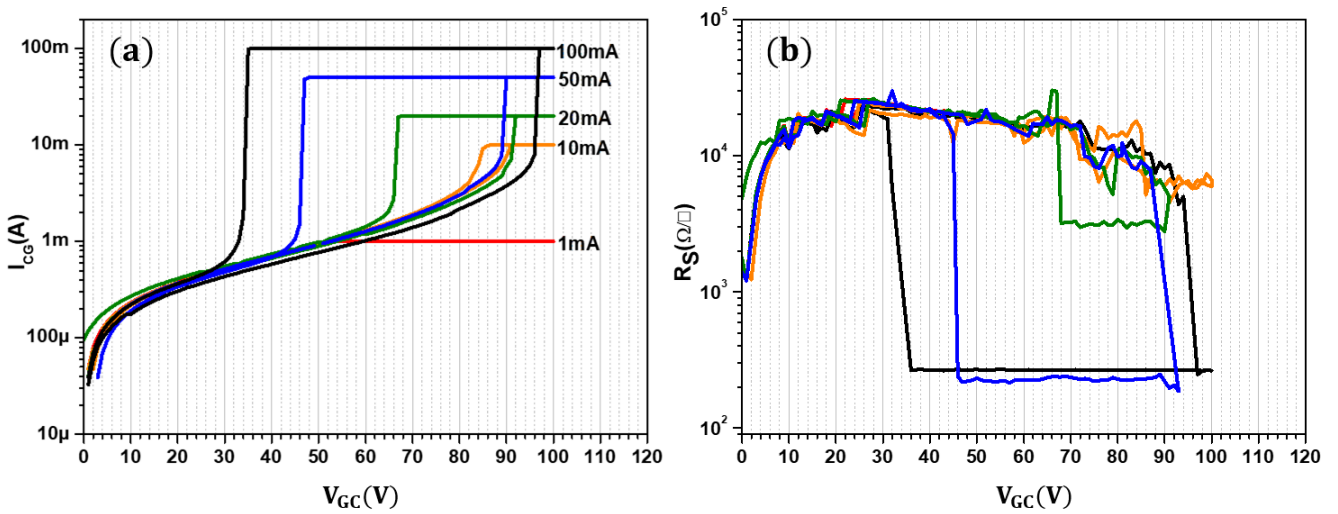


Figure 4.5: (a) I-V and (b) R_S curves of measurements taken across the gate-central contact GC at different compliances. The threshold voltages vary as the compliance varies for I-V and R_S -V curves.

4.2.1.4 Keithley Source Meter Functioning

At this point we have understood that changing the compliance affects the outcome of the experiment. And this is where the second question arose: Is it really the same voltage across the contacts of the sample and as shown on the Keithley source meter in the compliance regime?

To answer this question, we connected a secondary Keithley source meter as voltmeter directly to the sample and measured the sample voltage while the primary Keithley source meter was running the experiment. Figure 4.6 shows that once the voltage applied reaches V_{th1} , the voltage at the sample drops to V_{th2} and remains there, while the voltage displayed on the Keithley keeps increasing to complete a full sweep. The sample voltage remains at V_{th2} until the backward sweep of the primary Keithley reaches V_{th2} where both the sample and Keithley voltages decrease now in parallel.

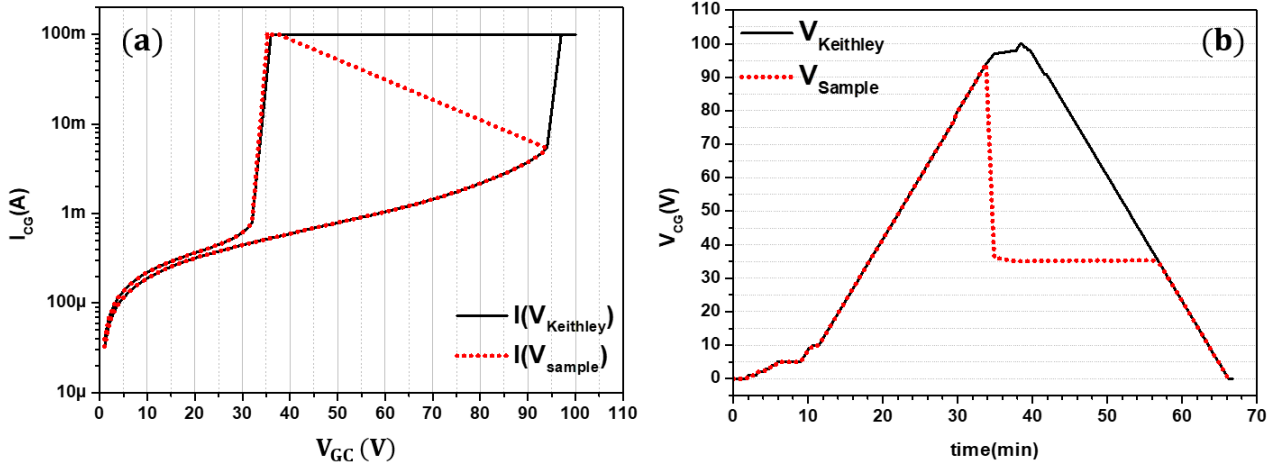


Figure 4.6: (a) I-V curve showing that the hysteresis obtained while sweeping voltage was not a real hysteresis. Testing the voltage at the sample by adding a secondary keithley showed that the actual voltage at the sample after compliance is reached is not the same displayed on the primary keithley. (b) The drop in voltage remains constant at the threshold value V_{th2} until the primary keithley's sweep hits the same value and then both voltages continue to decrease in parallel.

In figure 4.6 (a), we see that the hysteresis measured earlier is an artifact as the voltage values of the sweep after surpassing V_{th1} and before reaching V_{th2} , in the back sweep, were not real. In figure 4.6 (b), we see how the voltage drops from V_{th1} , once reached, to V_{th2} and remains there until the primary keithley voltage hits the value V_{th2} .

4.2.2 Discussion and Conclusion Concerning the Transition by Applying E-Field

In their paper, where they showed that the transition in NbO_2 can be achieved under the application of an electric field, Wang et al. [216] mentioned that they found a dependence of the threshold electric field on the contact area in a way that the threshold field increased as the size of the contact was increased. They also stated that ‘The mechanism for the area dependence of $E_{Threshold}$ is not entirely clear, but may be related to the non-uniform switching near the edges of the rectangular contact, since the distribution of electric field varies near electrodes.’

The immediate conclusion is that, as seen in figure 4.2, hysteresis occurs which means that the threshold appears at different voltages during a cycle for the same sample. This means that the corresponding threshold field changes too, during the measurement. Secondly, on changing the global sample temperature the threshold voltages and hysteresis change. This is a strong indication that the phenomenon is temperature related. Finally, in figure 4.1, the contact area C on the sample is 0.16 cm^2 three times larger than the contact area T which is 0.05 cm^2 . Then if we look at the I-V curves of figure 4.2 we see that the threshold voltage V_{th1} increased as the area decreased, from $V_{th1CG} = 105\text{ V}$ to $V_{th1TG} = 175\text{ V}$, or in terms of electric field, the field increased from $E_{th1} = 8\text{ MV/cm}$ for contact C to $E_{th1} = 13.4\text{ MV/cm}$ for contact T. Assuming that the current is homogeneously crossing the film from one contact to another, we can confirm that there is a

dependence of the threshold voltage or threshold field on the contact size and it decreases as the area increases which is contrary to what Wang et al. have; however, our results are consistent with what Joshi et al. found [137].

The behaviour of the threshold voltage with the contact area suggest it is related to the current density rather than the electric field. Indeed, from Ohm's law:

$$\mathbf{E} = \rho \mathbf{J} \quad (4.1)$$

and from the definition of the current density:

$$\mathbf{J} = \frac{\mathbf{I}}{\mathbf{A}} \quad (4.2)$$

We can clearly see how the electric field changes when the area of the contact changes, so it is the current density which is the central element in this phenomenon rather than the applied voltage. When the area changes, the current density changes and eventually the electric field.

What also brings us to this conclusion is what we saw in figure 4.5 (a) when changing the compliance on the Keithley source meter. If it were the voltage that is causing the transition, then this voltage should be the same regardless of the current compliance as long as the other conditions such as temperature, pressure, contact size... remain the same. However, it was not the case, and we see for example at 50 mA compliance V_{th1} was 90 V less than V_{th1} for 100 mA compliance which is 97 V. Moreover, the transition must have had the same effect on the sheet resistance if it were a real transition. However in figure 4.6 (a), we found that the hysteresis was virtual.

4.3 CC-NDR in NbO₂

From the previous experiment we have learned the following concerning the threshold voltage:

- It is contact dependent.
- It shifts to lower voltages as the temperature increases.
- It is also instrument related and dependent on the compliance value of the current.

Furthermore, the hysteresis seen in the voltage driven experiment is not intrinsic.

The problem is understood if we take a look again at Figure 1.14. NbO₂ is an S type NDR material as shown in Figure 1.14 (b). This means that if a voltage source is used, at the threshold of NDR, the resistance becomes negligible forcing the source meter to go into compliance mode. This is easily resolved by making the measurements with a current source. Therefore, we decided to switch to current source mode measurements. Also, to avoid asymmetric diode-like behavior in the device where one contact is NbO₂/Au and the other is NbO₂/Si, we switched to horizontal measurements so that the NbO₂ region tested is between two gold contacts (lateral, for example any couple excluding the gate contact G). Sweeps between -100 mA and 100 mA were taken with a step of 1 mA and

a step duration of 200 ms. Figure 4.7 shows the V-I curves taken between central gold contact and a peripheral one and between two peripheral contacts.

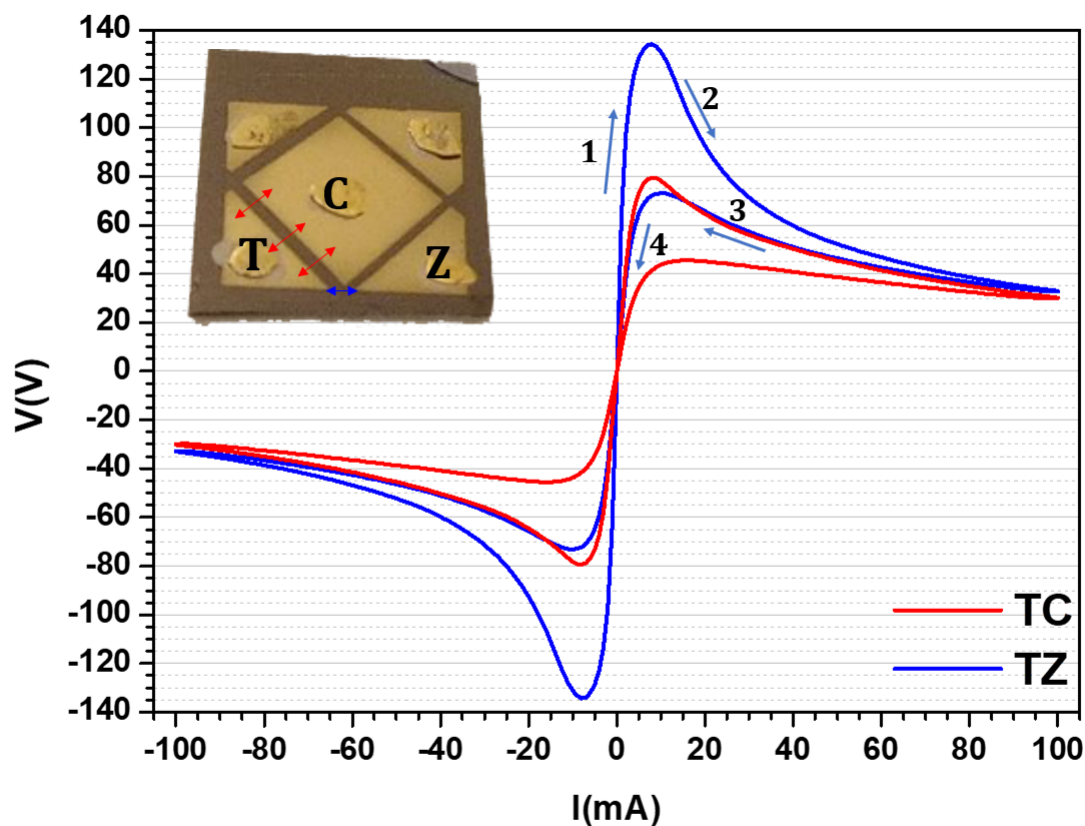


Figure 4.7: $V(I)$ curves between central-peripheral TC and peripheral-peripheral TZ contacts. The $V(I)$ curves show CC-NDR resistance in NbO_2 with a hysteresis. Notice the dependence of the voltage on the path area of the current. Contacts which provide narrower current path (TZ) have higher current density and eventually higher voltages.

The slopes of the curves represent the resistance, and we can clearly see when starting from 0 mA, the slope is very high and then starts to decrease to become negative after ~ 7 mA, whence the name Negative Differential Resistance. As voltage is increased further, the negative slope decreases, and the voltage flattens with the current until the maximum value for the current. On reducing current, the voltage now follows a curve with lower values, though similar shape. Since both current and voltage are well defined in this experiment (no effect of instrumental compliance), the measured hysteresis is real. These results are consistent with what is reported in literature for CC-NDR in NbO_2 [24, 133–135] except that the earlier work does not detect hysteresis. This will be discussed later. Since $V(I)$ curves measured between contact pairs TC and TZ are not identical, this implies that the measured voltage depends on current density.

After confirming that the physical phenomenon taking place in NbO_2 is CC-NDR, we were interested in studying eventual differences between amorphous and crystalline NbO_2 samples and also verify if there are any structural changes that occur during process.

4.4 NDR in crystalline and amorphous NbO₂

Three samples were used in the following experiments. An amorphous NbO₂ sample Si₃₂¹⁰⁰¹ and a crystalline NbO₂ sample Si₃₁¹⁰⁰ each on Si < 100 > substrates (the same substrate previously used) and another sample on soda lime glass substrate SL₃₀₇. The deposition parameters are the same except that on glass the deposition power used was 200 Watts and the deposition time was 10 min. The film thickness was 130 nm and 330 nm for films on Si and glass substrates respectively. Si₃₁¹⁰⁰ was crystallized by annealing in vacuum at 800 °C for 14 hrs and SL₃₀₇ at 600 °C for 2 hrs. The geometry of the gold contacts on the films with Si substrates was different from the earlier experiment since we are not any more interested in vertical measurements. Van der Pauw masks like the ones described in section 2.2.3 were used to deposit gold as seen in figure 4.8. However, only 2 wire measurements were performed.

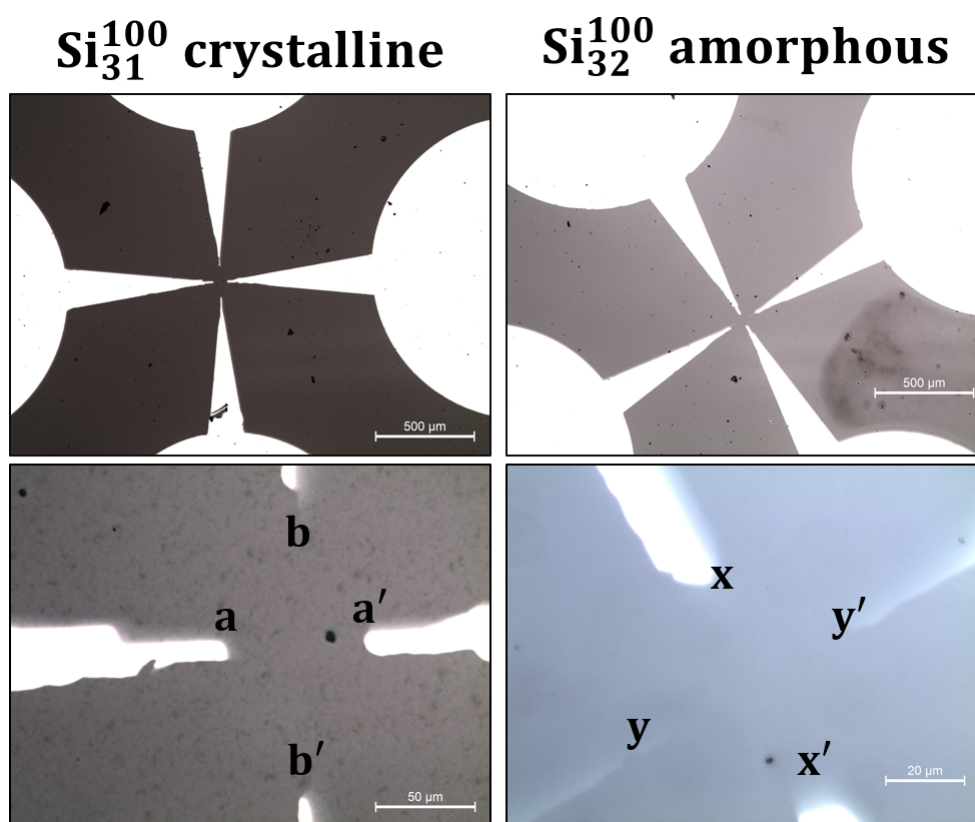


Figure 4.8: Gold contacts deposited on crystalline and amorphous NbO₂ samples.

4.4.1 Hysteresis in the measured NDR

On samples Si₁₀₀³¹ and Si₁₀₀³² V(I) measurements were performed. Sweeps were done between -100 mA and +100 mA, 1 mA step and 200 ms step duration. The voltage compliance was set to 210 V. Figure 4.9 shows the difference obtained in both samples when taking a measurement across aa' and xx' contacts where the gold tip to tip distance is ~ 60 μm.

¹In the sample name X_b^a: X is the substrate used, the super script “a” is the crystalline direction and the subscript “b” is the number of the sample we named. SL stands for soda-lime glass substrate.

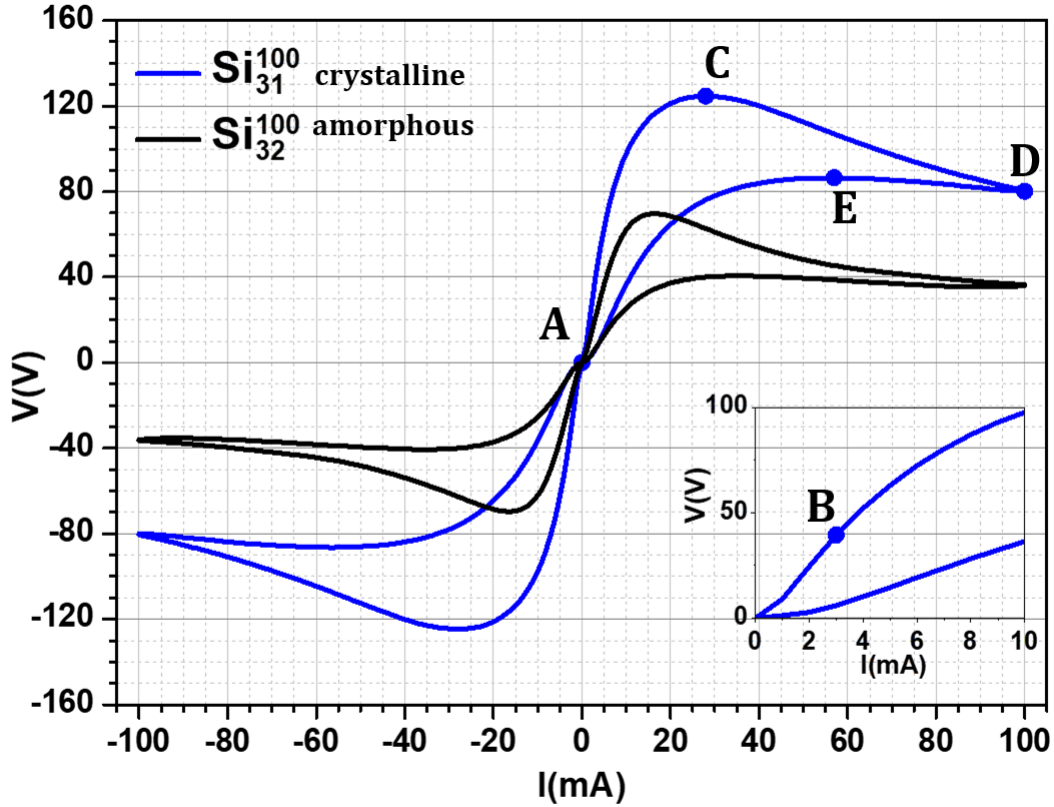


Figure 4.9: $V(I)$ curves for crystalline (Si_{31}^{100}) and amorphous (Si_{32}^{100}) NbO_2 . Both curves show negative differential resistance and also exhibit a hysteresis. The blue curve lies above the black curve indicating that the resistivity of crystalline NbO_2 is higher than that of amorphous NbO_2 .

It is clear that the CC-NDR occurs in both crystalline and amorphous NbO_2 . Earlier in chapter 3, we have seen that the resistivity of crystalline NbO_2 is higher than that of amorphous NbO_2 . This justifies why the curve of the crystalline sample reaches higher voltages than the amorphous one.

Now, consider the points A, B, C, D and E shown in figure 4.9 which correspond to V, I values listed in table 4.2, and which will be used below to interpret the measured curves. Figure 4.10 shows the evolution of the different parameters with respect to the time of a sweep between 0 to 100 mA. The curves are displayed with respect to time because as we can see, aside from the current which we can control by sweeping, all the other parameters V , R and P (or T) are simultaneously changing. As usual the Resistance R is determined from the measured current and voltage as:

$$R = \frac{V}{I} \quad (4.3)$$

and the power is calculated by the equation:

$$P = V \times I \quad (4.4)$$

Of course, in the NDR regime these are simplifications but serve as instantaneous estimates to interpret the phenomenon. As the sweeping time interval are the same, then this means that as the power increases, the heat energy increases as well. Moreover, thermal

Point	I(mA)	V(V)	R (k Ω)	P (Watts)
A	0	0	9	0
B	3	39.4	13.1	0.1
C	28	124.7	4.5	3.5
D	100	80.5	0.8	8.0
E	57	86.4	1.5	4.9

Table 4.2: The different components of critical points on the hysteresis of curves of figure 4.9.

energy is nothing but the temperature T multiplied by the Boltzmann constant k_B , so we can write:

$$T \propto E \propto P$$

With this in mind, the hysteresis curve is interpreted as follows:

(AB): Between points A and B of figure 4.9, the differential resistance dV/dI increases to reach its peak of $\sim 13 \text{ k}\Omega$ at 3 mA where the slope is maximum after which it decreases.

(BC): As the current increases further, more heat is generated due to power dissipation by Joule effect:

$$P = RI^2 \tag{4.5}$$

Even though the differential resistance decreases, the increasing current contributes to dissipation.

(CD): In this negative differential resistance regime, the voltage *decreases* as current increases rendering the differential resistance negative.

(DE and EA): The cycle is completed by decreasing the current to zero. This part should normally be superimposed on the ABC part of the cycle but hysteresis is detected. In the following sections we will explain the origin of this hysteresis as a consequence of temperature evolution during the measurement in the sample volume between the contacts.

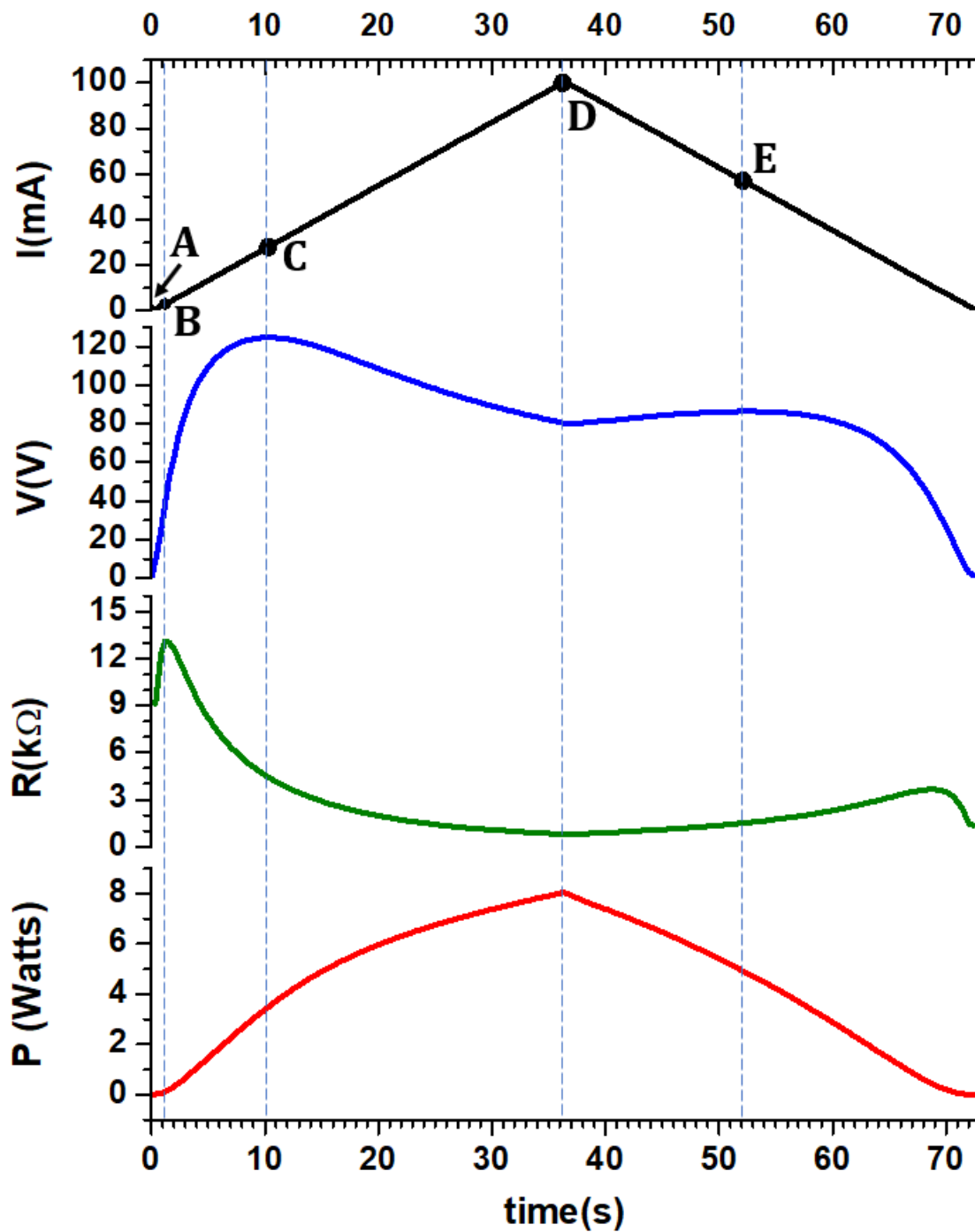


Figure 4.10: Graph showing the different parameters $I(\text{mA})$, $V(\text{V})$, $R(\text{k}\Omega)$ and $P(\text{Watts})$ as a function of time. The power represents the heat dissipated and eventually the change temperature.

4.4.2 Origin of Hysteresis

To investigate the nature of the measured hysteresis we changed the rest time at each measured current from 50 ms to 200 ms and finally to 500 ms. It was noticed that when the rest time increased the hysteresis decreased. Figures 4.11 (a) and (b) show the results of measurements done on the crystalline sample Si_{31}^{100} at two different temperatures 300 K and 320 K respectively. At a fixed current, the longer we wait the smaller is the hysteresis. In other words there is a dynamic effect clearly related to temperature evolution in the sample. A longer rest time at a given current leads to a better estimation of the equilibrium value of the voltage because of an equilibrium temperature in the volume between the measured contacts in the sample.

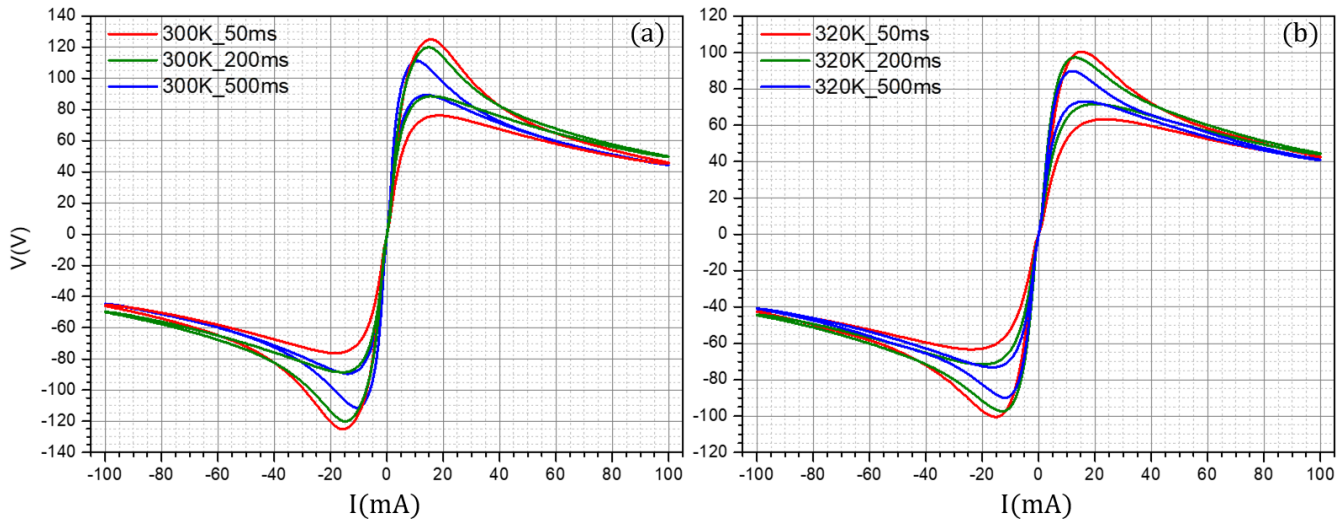


Figure 4.11: $V(I)$ curves obtained at different step size durations at two temperatures (a) 300 K and (b) 320 K.

4.4.3 Hysteresis and Thermal Equilibrium

The question is: How to measure the equilibrium value corresponding to a non-hysteretic curve? The obvious answer is to wait a sufficiently long time at each measured current value so that equilibrium is attained. However, there is a practical problem because it can mean a measurement time for a given curve can extend to hours. So, we first estimated the equilibrium curve by measuring the equilibrium voltage values at a few chosen points, and then opted for a way to estimate the complete equilibrium curve from the faster, dynamic measurement.

Two sets of measurements were made in a cryostat with one set stabilized at a temperature of 320 K and the other set at 400 K². First a control measurement (the black curve in figures 4.12 (a) and (b)) was performed between 0 and 100 mA with a 200 ms step time. Then the experiment was repeated; however, this time once the current reached 5 mA, the measurement was paused, and we waited for the voltage to settle to an equilibrium value. Once the voltage was stabilized, the measurement was resumed at the fast rate. Such pauses were made at different current values (one pause per measurement)

²Raising the temperature to 400 K reduces the impact of the induced heat due to Joule effect.

and the curves were studied in a similar manner. The stabilization values are the end points of the troughs/peaks of the curves depending on whether the measurement was paused while the sweep was going from 0 mA to 100 mA (troughs) or returning from 100 mA to 0 mA (peaks). Note that, between every two measurements we waited for ~ 15 min so that the temperature can go back to the initial temperature 320 K or 400 K depending on the temperature regime of the experiment. Moreover, we noticed that, as the current increased the time needed for reaching equilibrium was shorter. Table 4.3 shows the time needed for achieving equilibrium at the tested currents at 320 K. As can be seen in the figures that the troughs and the peaks more or less converge to a curve (the blue curve in the figures). This curve is nothing but the average of the two portions of the control curve, the upper curve where the current swept from 0 mA to 100 mA and the lower curve when the current was returning from 100 mA to 0 mA to complete the loop. The reason why the end points do not fall exactly on the curve could be attributed to temperature contributions to the dynamical hysteresis in each measurement.

This is a useful result because it means that we can make measurements in the usual fast sweep mode and still compute the equilibrium, non-hysteretic curve. **In what follows we will show this equilibrium non-hysteretic curve only.** Finally, we can also give here the reason why existing literature does not show this hysteresis [133]. The reason is that the sample volume between the contacts is orders of magnitude smaller in earlier work with respect to ours, due to one contact being nanometric in size (see figure 4.1 (a)). Thus thermal equilibrium is instantaneously attained in these devices and no hysteresis is observed.

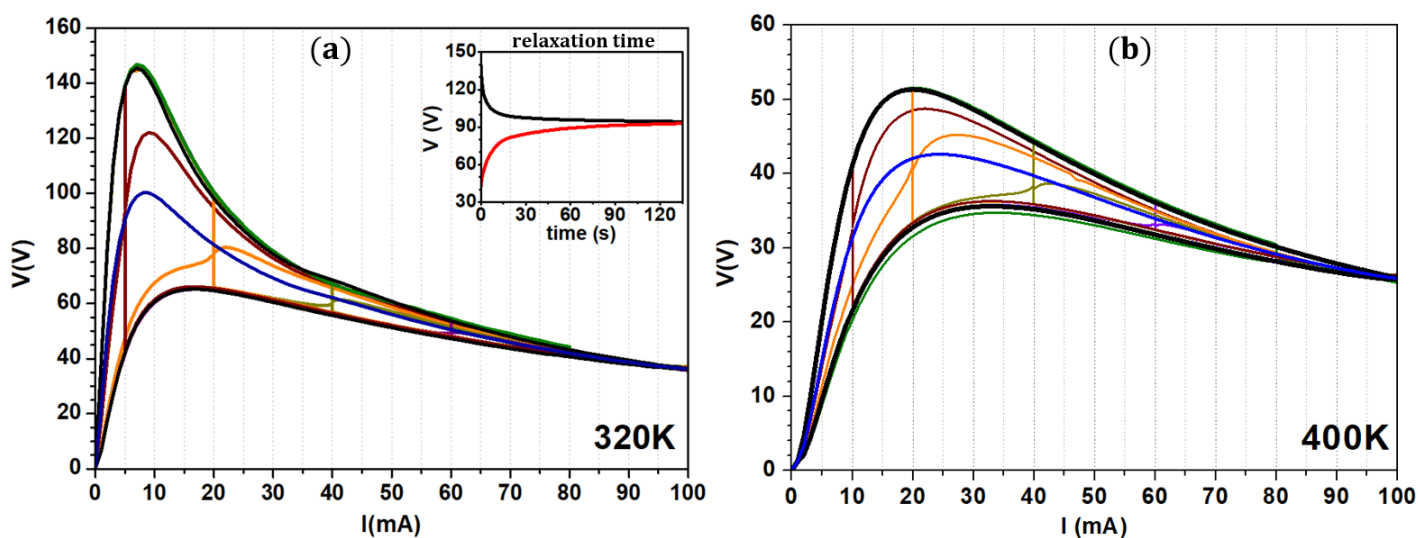


Figure 4.12: $V(I)$ curve results obtained during the thermal equilibrium test at two different temperatures (a) 320 K and (b) 400 K. The different colors in each figure represent different current values at which pauses were made in both forward and backward sweeps. The peaks and troughs at each current represent the stabilization voltage. The inset in panel (a) shows the relaxation of the voltage during the pause at 5 mA during the forward sweep (black) and the backward sweep (red).

Current (mA)	5	20	40	60	80
Time (s)	120	30	16	11	3
Equilibrium voltage (V)	94	78	62	48	36

Table 4.3: The time required for the voltage to stabilize while the measurement was paused at specific current values in a sweep from 0 to 100 mA (at 320 K).

4.4.4 Heat Dissipation and Current Distribution in Sample and Substrate

As we have seen, NDR in NbO_2 is dependent on current density and Joule heating in the sample. Here we discuss the samples introduced in section 4.4 on Si and on glass. The current distribution, and hence the heat dissipation, depends very crucially on the substrate. Indeed, the glass is an insulator more resistive than NbO_2 ; however, the silicon substrates used are highly doped and much more conductive than NbO_2 . It follows that, even though in both cases the measurement geometry is lateral, when the substrate is Si, almost all injected current will flow through the substrate as will be proved in what follows. This means that the current in the NbO_2 is almost exclusively vertical, between the top contact and the bottom Si layer. To verify this, we first simulate the current distribution corresponding to two points of the contact geometry.

A schematic of the device is shown in figures 4.13 (a) and the resulting current density distribution is shown in panel (b). For simplicity in the simulation we suppose the following for material conductivity: Au (500), Si (100) and NbO_2 (1). Taking the numerical values 99.6% of the current goes through the silicon. Furthermore, we can clearly see in figure 4.13 (b) that nearly no current passes through the NbO_2 in between the contacts. Schematic in figures 4.13 (c) and (d) show the difference in current flow path taken in both samples with Si and glass substrates respectively.

On glass, the cross-sectional area of the sample is the thickness of the NbO_2 film multiplied by the effective width between the contacts (so $\sim 100 \text{ nm} \times \sim 10 \text{ }\mu\text{m}$). For the film on the Si substrate, as we have pointed out, the current is vertical and one dimension of the cross-sectional area, corresponding to the lateral extension of the contact is much bigger. This increase in cross sectional area and subsequent decrease in the current density for the same current, with respect to the geometry for the film on the glass substrate, justifies why we see in figure 4.13 (g) that we have currents of few tens of mA in the Si substrate device. This is upto two orders of magnitude higher than what is typically observed in NbO_2 nanometric devices or in our sample SL_{307} which has a glass substrate.

Figures 4.13 (e) and (f) show the electric circuit configuration for the samples on silicon and glass respectively. For the sample on silicon, the diodes represent the asymmetric I-V characteristics measured in section 4.2 in the vertical NbO_2/Si device. The asymmetry disappears here because this geometry, although effectively vertical, is symmetric.

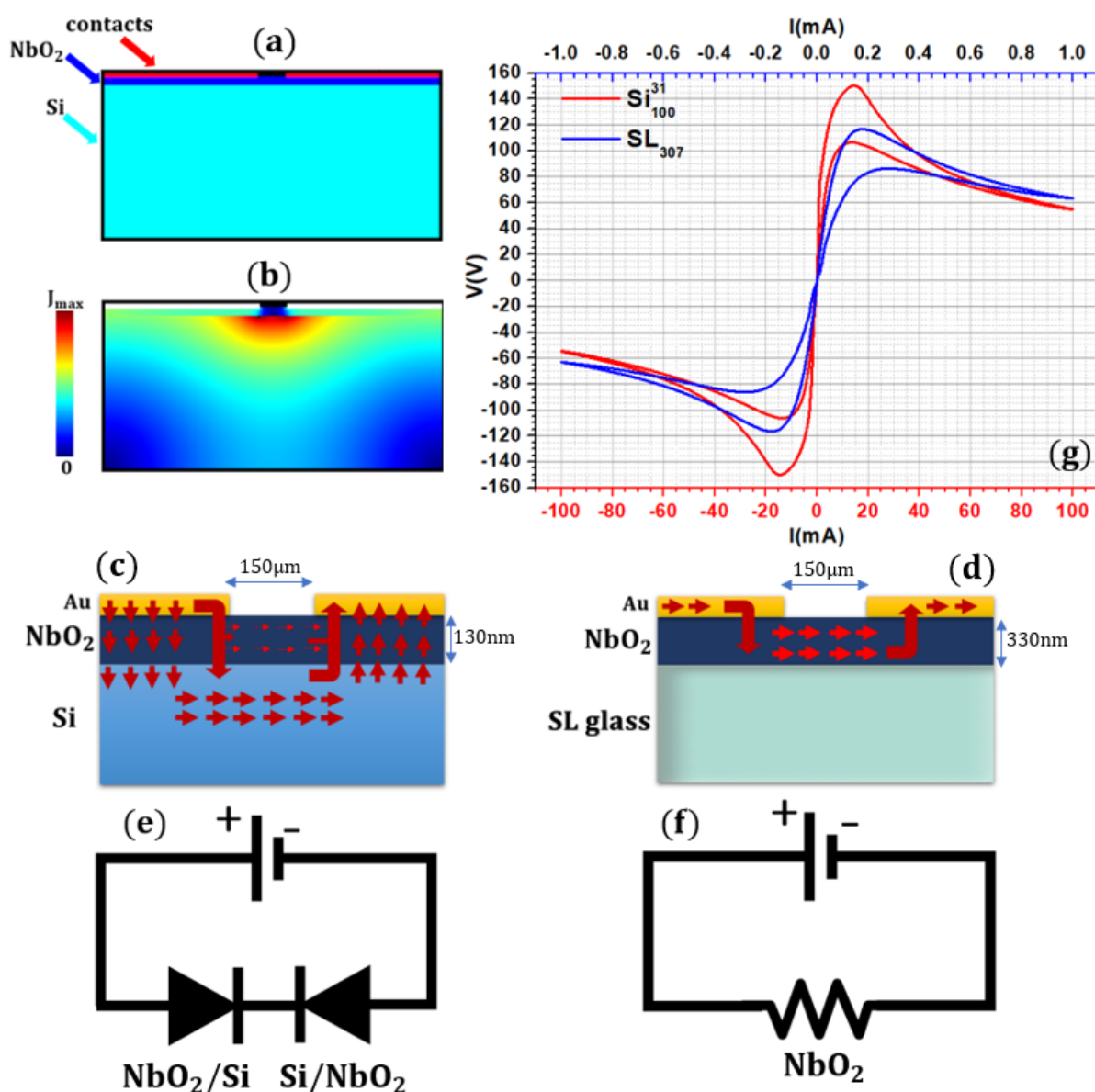


Figure 4.13: (a) Schematic of the cross section of the NbO_2 device with a conductive Si substrate. (b) Calculated current density distribution in the NbO_2 and Si when voltage is applied between the contacts for the geometry defined in (a). The current distribution indicates that most of the current if not all the current passes vertically downwards from the NbO_2 film to the Si substrate and then vertically upwards from the Si substrate to the NbO_2 film. (c) and (d) are schematics that show the differences between the current flow direction in the NbO_2 device on Si and glass substrate respectively. (e) and (f) show the circuit representation of these two devices. (g) $V(I)$ curves showing on NbO_2 devices with Si and glass substrate. In the former a large current is needed for the NDR to occur while in the sample with glass substrate much less current is needed for NDR to happen. The difference in current is due to the different effective cross-sectional areas of the two geometries.

We have also studied the effect of the distance between the contacts on the $V(I)$ curves using sample SL_{307} and contacting the NbO_2 surface directly with aluminum wires by wirebonding. The distances between the contacts kk' , mm' and nn' are $40\ \mu\text{m}$, $200\ \mu\text{m}$ and $450\ \mu\text{m}$, figure 4.14 (a). Sweeps between $-1\ \text{mA}$ and $1\ \text{mA}$ were made with a $10\ \mu\text{A}$ step for $200\ \text{ms}$. The results are shown in figure 4.14 (b).

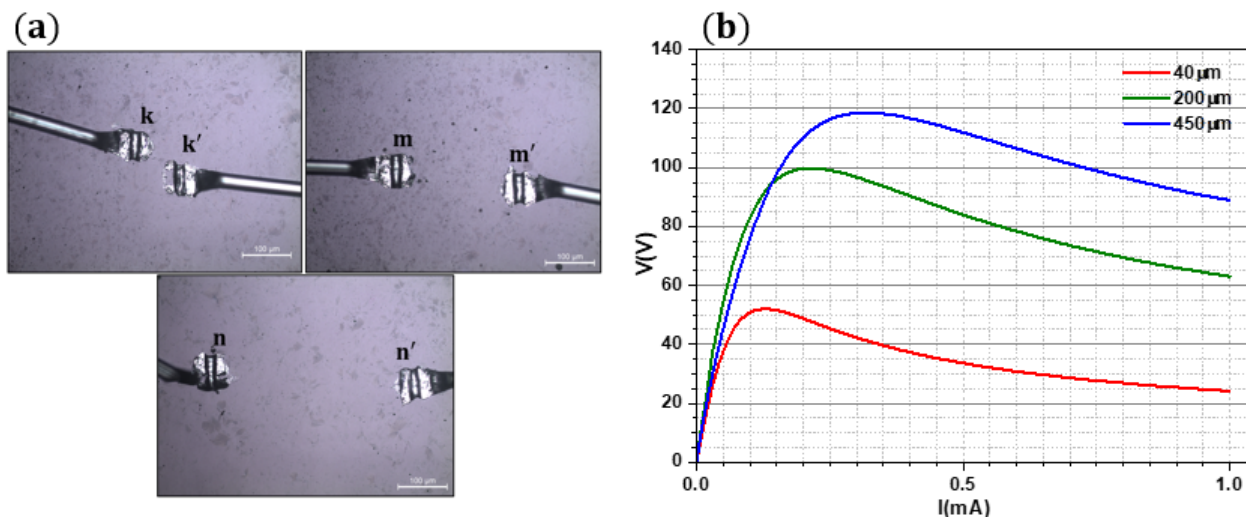


Figure 4.14: (a) Optical photos of the contacts made for the studies of $V(I)$ curves on the glass substrate. (b) $V(I)$ curves obtained at different contact separation. Shorter distance between contacts induced lower maximum voltages in the $V(I)$ curves.

Intuitively, for smaller distances the resistance is reduced and so is the dissipated power. Since NDR is supposedly caused by joule heating, it seemed contradictory with behavior seen in figure 4.14 as the contacts closest to each other show NDR at lower power. However, the hysteresis (not shown) was also lower and tended to disappear as the distance decreased. The reason is most probably that closer contacts confine the current to a smaller volume which at equivalent power heats more rapidly which is why experiments on nano devices show no hysteresis.

4.4.5 NDR and Sample Temperature

Since heat dissipated by current flow in sample causes changes in the sample conductivity an interesting question arises: How is NDR influenced by increasing the sample temperature? To investigate this we measure the equilibrium NDR curves for both the amorphous and crystalline samples which have different electrical and thermal properties.

For both, the crystalline and the amorphous samples, as the temperature increases from $285\ \text{K}$ to $400\ \text{K}$, the $V(I)$ curves shift downwards as shown in figures 4.15 (a) and (b). A similar behavior is found in the current controlled negative differential resistance of $\text{Co}_2\text{FeO}_2\text{BO}_3$ and $\text{Fe}_3\text{O}_2\text{BO}_3$ [226] when the temperature is increased. 4.15 (b), for the amorphous sample, we see that the NDR part of the curve progressively disappears and that at $400\ \text{K}$ the relation between V and I is linear with a positive and well-defined Ohmic resistance. The polycrystalline sample in Figure 4.15 (a) shows the same trend, but $400\ \text{K}$ -the maximum temperature on our measuring system- is not enough to get rid of the NDR regime. However, one can estimate by comparison with the amorphous sample

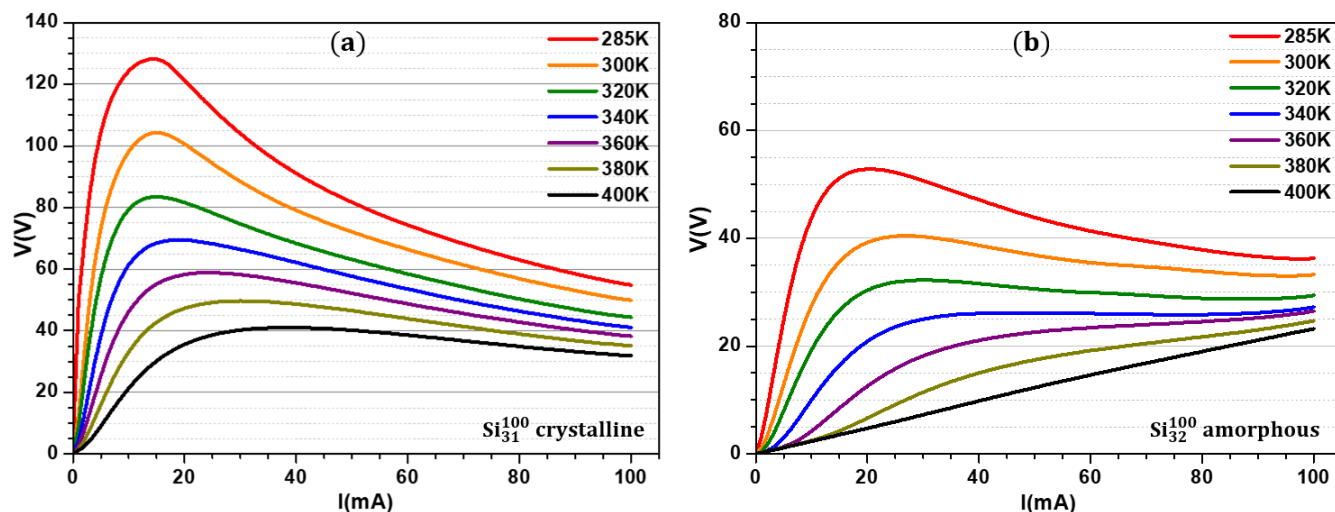


Figure 4.15: Effect of temperature on the $V(I)$ curves of crystalline and amorphous NbO_2 films. For both samples as the temperature increases the hysteresis becomes less and the curves tend to flatten.

that a temperature between 500 and 600K should suffice for getting rid of the NDR regime in this sample. NDR in NbO_2 is thus caused by the variation of electrical conductivity in a feedback loop phenomenon where the power dissipated by the device current determines local temperature. If the device is operated at a temperature where conductivity is already sufficiently high, no NDR is observed. Another important conclusion is that although conductivity increases in both the amorphous and the crystalline sample, there is no electronic phase change. Both samples remain insulators because their resistance decreases as temperature increases.

4.5 NDR and Structural Changes

One interesting question that can be asked is the presence of structural or physical changes in the material during the different regimes of the $V(I)$ curve. One way to answer this question is to make Raman spectroscopy measurements on the device at different points of the NDR curve. To achieve those simultaneous measurements, a cryostat housing with an optical window, specially designed and fabricated by the laboratory's workshop, was used with our Xplora Raman spectrometer, as shown in figure 4.16.

4.5.1 Stable Current Application

In these experiments, instead of sweeping the current, we slowly raised it to the required value for the duration of the Raman measurement. We chose the points so that we had at least one point within each phase of the curve (At point A, near point B, between points B and C, and between points C and D of figure 4.9). The wave length of the Raman laser was 532 nm (green light), the acquisition time was 60 s with two accumulations. A 10 % filter and a 10 \times objective were used. Then the laser was focused to be at the center of the contacts shown in figure 4.1 as the current was being passed through that region. The current was gradually increased to 5 mA and left there to take a measurement, after the measurement was done, the system was allowed to stabilize again to room temperature.

After which the temperature was further increased to 10 mA and another measurement was taken. This process was repeated until until the input current was 100 mA. Results for experiments done on Si_{31}^{100} and Si_{32}^{100} are shown in figure 4.17.

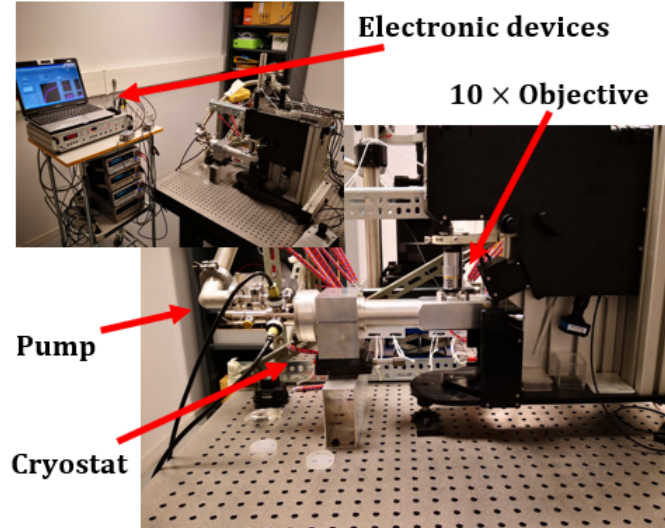


Figure 4.16: Raman apparatus setup used to make Raman spectroscopy on samples while taking $V(I)$ measurements.

Analyzing the spectra, no structural change was detected in the crystalline sample (Figure 4.17 (a)) nor in the amorphous one (Figure 4.17 (b)). In these figures, a slight shift in the Raman peaks to lower energies can be seen which can be attributed to the heating of the sample. We can determine this temperature because the Raman spectra also contain a silicon peak at roughly 520 cm^{-1} whose dependence on temperature was studied earlier in section 3.10. From figure 4.18 (a), which shows the variation of both voltage and temperature (the temperature calculated from the Si-peak shift), it can be estimated that at 100 mA current in the device the temperature reached is 510 K for the more resistive crystalline sample and from figure 4.18 (b) the temperature at 100 mA would be 430 K for the less resistive amorphous sample.

This temperature is however estimated from the silicon volume between the contacts and therefore may be different from the temperature of the volume of NbO_2 receiving electrical current.

The temperature values for the crystalline sample in figures 4.18 (a) and (b) are fitted using Newton's Law of cooling in the static limit [24]:

$$T = T_{\text{amb}} + R_{\text{th}} \times I \times V \quad (4.6)$$

where $T = T_{\text{amb}}$ is the ambient temperature 285 K and R_{th} is the thermal resistance and has an adjusted value of 44 KW^{-1} . This is a reasonable value as compared to the Si thermal resistance [221]; however, the heat is not generated in the silicon substrate itself. Indeed, as described earlier, in this *vertical* geometry, the silicon is sandwiched in series with two parts of the NbO_2 film. Furthermore, as the silicon used is very conductive,

the voltage drop in the silicon part is negligible compared to the voltage drop of the two NbO_2 parts. Therefore, the heat is generated by the power dissipated in the NbO_2 parts and diffused by the good thermal conductivity of the nearby silicon.

In the amorphous sample, the non-linearity is less pronounced, but an equivalent fit yield a thermal resistance value of 36 KW^{-1} close to the one found on the crystalline sample.

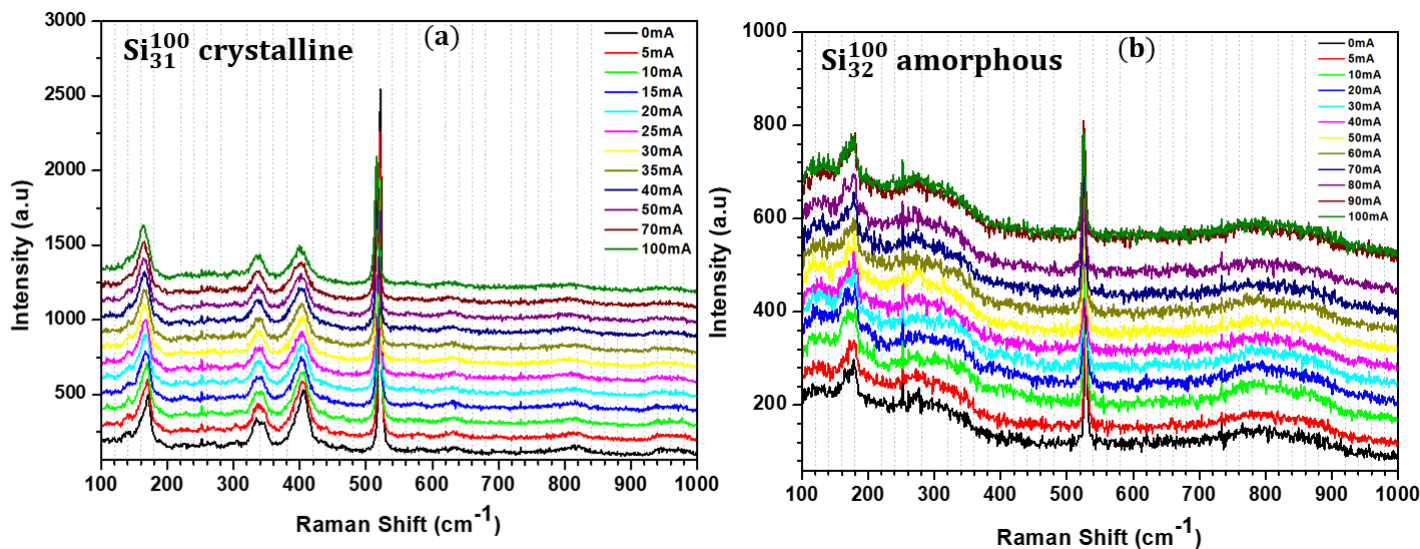


Figure 4.17: Raman spectroscopy at different current values on (a) Si_{31}^{100} (b) Si_{32}^{100} . Both films did not show any structural change during the transport process. However, all peaks shift to lower energies as the temperatures increases due to heat dissipation.

NDR is found in both amorphous and crystalline NbO_2 devices. However, the electrical conductivity of amorphous NbO_2 is different than that of crystalline NbO_2 , which means that the I-V range where NDR is found is different in each material. The amorphous-crystalline transformation sets in between 800 K and 900 K, while the Mott insulator-metal transition happens at 1080 K in the crystalline material. These transitions are not involved in the NDR phenomena in our devices. No phase transition, either structural or electronic, and no irreversible phenomena could be related to NDR in our samples. Moreover, since NDR involves significant variations of electrical conductivity generated by temperature change, it can be found in semiconductors or insulators where such sizable variation is possible through thermal energy. However, for such sizable variation of electrical conductivity to occur, there has to be considerable changes in local temperature through Joule heating. This implies low thermal conductivity in the material. Effectively, NbO_2 has a thermal conductivity which is two orders of magnitude lower than that of silicon, and the electronic contribution to this thermal conductivity is negligible [222].

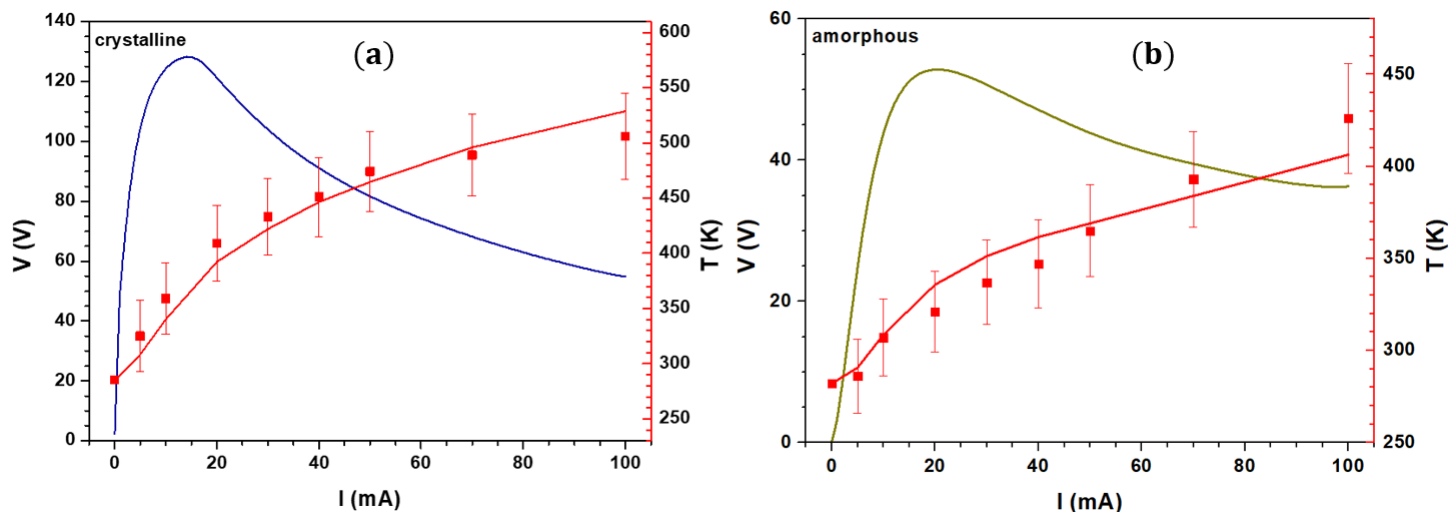


Figure 4.18: The voltage and the temperature variation as a function of current in both (a) crystalline and (b) amorphous samples. The temperature were calculated by studying the Si Raman peak shifts as described in section 3.10.

4.5.2 Pulsed Current Application

Threshold switching and commutation between two states or phases are often thought to be dynamic phenomena where energy deposited in a short time could generate phase transitions. We subjected our devices to current pulses to eventually observe such changes both through Raman spectroscopy and visual observation.

Pulses were applied on both crystalline Si_{31}^{100} and amorphous Si_{32}^{100} samples. That was done by a sudden application of 100 mA to the sample consecutively. The pulse period was 10 ms. Figures 4.19 and 4.20 show the results after pulsing the samples. On the crystalline sample no changes observed optically or in the Raman spectrum even after making 50 pulses, however, the pulses caused intense local heating since they damaged the contacts (Figure 4.19).

On the other hand, by making 10 pulses on the amorphous sample, we were able to see an optical change where the current left an imprint along the directions it traversed. Along xx' and yy' 10×10 ms pulses were made, while along xy' 20×10 ms pulses were made. Figure 4.20 (a) shows the contacts before pulsing and Raman was measured at the center of the contacts. In panel (b), darker tracks are seen between contacts xx' , yy' and xy' after the pulses. The Raman spectra shown in panel (c) correlates these darker tracks with the appearance of Raman peaks indicating that the NbO_2 has crystallized under pulsed current.

From these two test, we can estimate that the temperature on the crystalline film did not surpass the MIT temperature ($\sim 800^\circ\text{C}$) but at least reached the crystallization temperature of $\sim 550^\circ\text{C}$.

This result may seem contradictory with our earlier statement that in these samples the current is going vertically through the NbO_2 to reach the conductive silicon substrate and not laterally through the NbO_2 between the contacts. However, the NbO_2 between

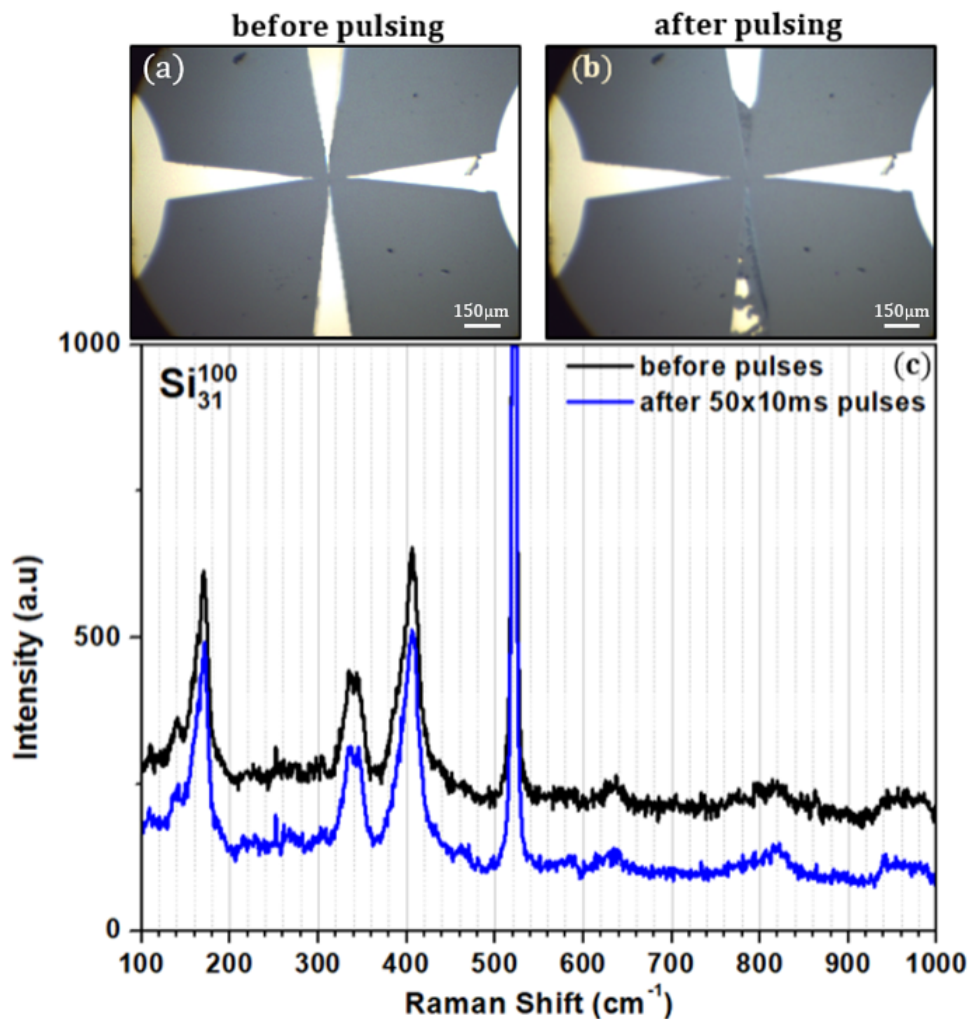


Figure 4.19: (a) and (b) show an optical image of sample Si_{31}^{100} before and after pulsing respectively. (c) Shows the Raman spectra before pulsing and after applying 50 pulses of 100 mA. No noticeable change can be remarked.

the contacts being the most insulating part of the circuit, it behaves as a capacitor in parallel of the silicon. Hence, a pulse of current will go through the NbO_2 .

In addition to Raman spectroscopy, after pulsing sample Si_{32}^{100} a $V(I)$ curve was taken and compared to a curve obtained before pulsing. The curves are shown in figure 4.21. Clearly, after pulsing, the curve has shifted upward (although the tested region is expected to have a higher temperature) and this is because the crystalline NbO_2 has a higher resistivity of the amorphous one.

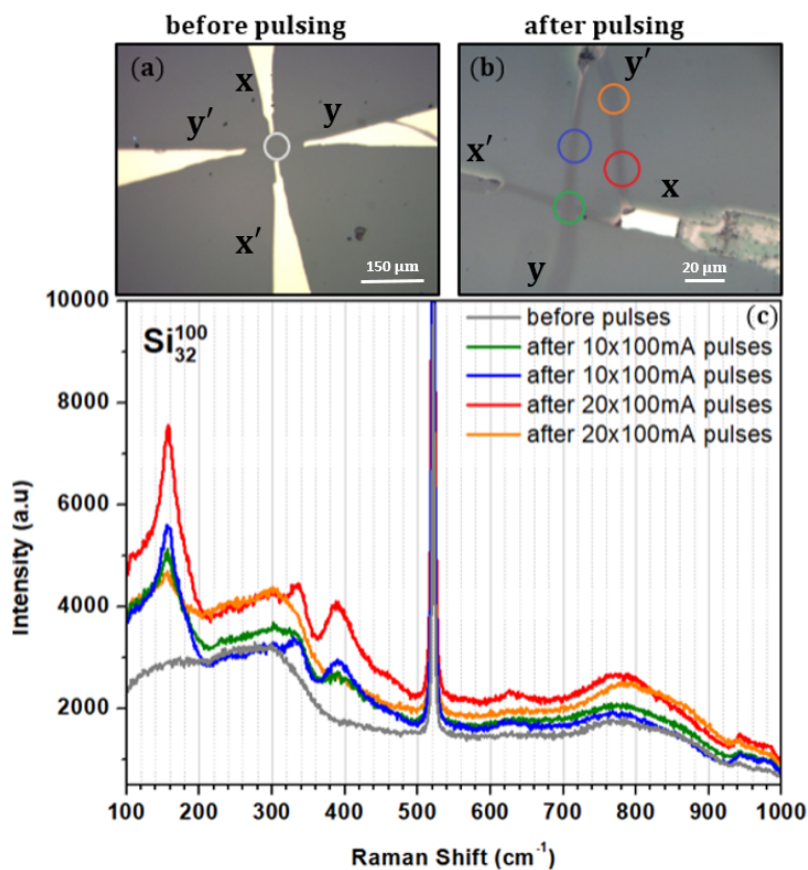


Figure 4.20: (a) and (b) show an optical image of sample Si_{32}^{100} . After pulsing, a track can be seen along the direction of the pulse. (c) Raman spectra of different regions on the sample, it is noticed that the more the pulses, the darker the region, the better the crystallinity and the more intense Raman signal.

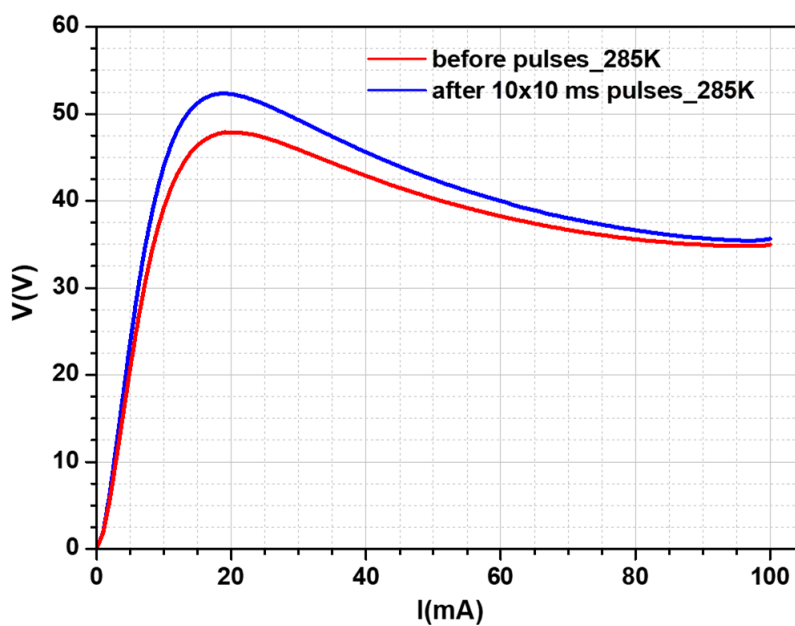


Figure 4.21: $V(I)$ curves of sample Si_{32}^{100} before and after 10 pulses. After pulsing, the $V(I)$ curve shifts upwards due to the higher resistivity of the crystalline NbO_2 compared to that of amorphous.

4.6 Numerical Modeling of CC-NDR in NbO₂

Currently, Joule self heating is the most accepted explanation of the NDR phenomenon. The increase of the current in a sample means that the dissipated power increases and eventually the temperature. This increase in the temperature generates charge carriers and CC-NDR is observed. The increase in conductivity with temperature for a semiconducting material can be simply written using thermal activation across a characteristic activation energy as [223]:

$$\sigma = \sigma_0 \exp\left(-\frac{E_a}{k_B T}\right) \quad (4.7)$$

where σ_0 is the zero temperature conductivity, E_a is the activation energy and k_B is the Boltzmann constant.

When one takes the electric field effects on the conduction mechanism into account (as detailed in section 1.8), the Poole–Frenkel conduction mechanism modifies this conductivity as below [138, 139]:

$$j \propto E \cdot \exp\left(\frac{-q(\Phi_B - \sqrt{qE/(\pi \epsilon)})}{k_B T}\right) \quad (4.8)$$

where j is the current density, E is the applied electric field, q is the elementary charge, Φ_B is the voltage barrier (in zero applied electric field) that an electron must cross to move from one atom to another in the crystal, ϵ is the dynamic permittivity, k_B is Boltzmann's constant, and T is the temperature.

While the standard expression for Poole-Frenkel conduction mechanism assumes that carriers hop in one dimension only, an extended and modified version of Pool-Frenkel conduction mechanism [224, 225] where multiple trapping effects are introduced and the system is three dimensional (3D) has been constructed as given below [15]:

$$j(E, T) = \sigma E = \sigma_0(T) \left(\frac{k_B T}{\beta}\right)^2 \left[1 + \left(\frac{\beta \sqrt{E}}{a k_B T} - 1\right) e^{\frac{\beta \sqrt{E}}{a k_B T}}\right] + \frac{\sigma_0(T) E}{2} \quad (4.9)$$

where

$$\sigma_0(T) = e \mu N_c \left(\frac{N_d}{N_t}\right)^2 e^{-\frac{E_d + E_t}{2k_B T}}$$

Here, $\beta = \sqrt{e^3/(\pi \epsilon_0 \epsilon_i)}$, μ is the electron mobility, N_d and N_t are the volume densities of donors and traps, respectively, and E_d and E_t are their corresponding energies that are added to find an activation energy. N_c is the effective density of states in the conduction band, ϵ_0 and ϵ_i are the vacuum permittivity and the high frequency dielectric constant respectively. The term 'a' added by Young in the prefactor for the exponential term is equal to 1 in the standard Poole-Frenkel and 2 in the modified version [225]. This equation has been used first in [15] with $a = 2$, and later in [24] with $a = 1$ (although with a noticeable error in the equation of the latter).

In all the above models, the dynamic equation for the temperature (which is the state variable) is Newton's law of cooling expressed in terms of device current and voltage,

$$\frac{dT}{dt} = \frac{iV}{C_{th}} - \frac{T - T_{amb}}{C_{th}R_{th}(T)} \quad (4.10)$$

where T_{amb} is the ambient temperature, C_{th} and R_{th} are the thermal capacitance and effective thermal resistance respectively. In the static limit where $\frac{dT}{dt} = 0$ equation 4.10 becomes $T = T_{amb} + R_{th}IV$. The static limit is justified in our case as we are fitting the static non-hysteretic curves.

The parameters used to fit the $V(I)$ curve measured from the film on glass substrate (the simpler device) with the different models (thermal activation, standard Poole-Frenkel, modified Poole-Frenkel with $a = 1, 2$) are stated in table 4.4. The values are the same for all models except for the effective thermal resistance which is summarized in table 4.5 (note : the value of the conductivity constant is changed mathematically by a factor of $8/5$ in the modified Poole-Frenkel model with $a = 2$). The values of R_{th} are reasonable as compared to literature [222]. However, some of the parameters remain estimates and not exact as for example we do not know the exact cross section the current flows through or the exact temperatures.

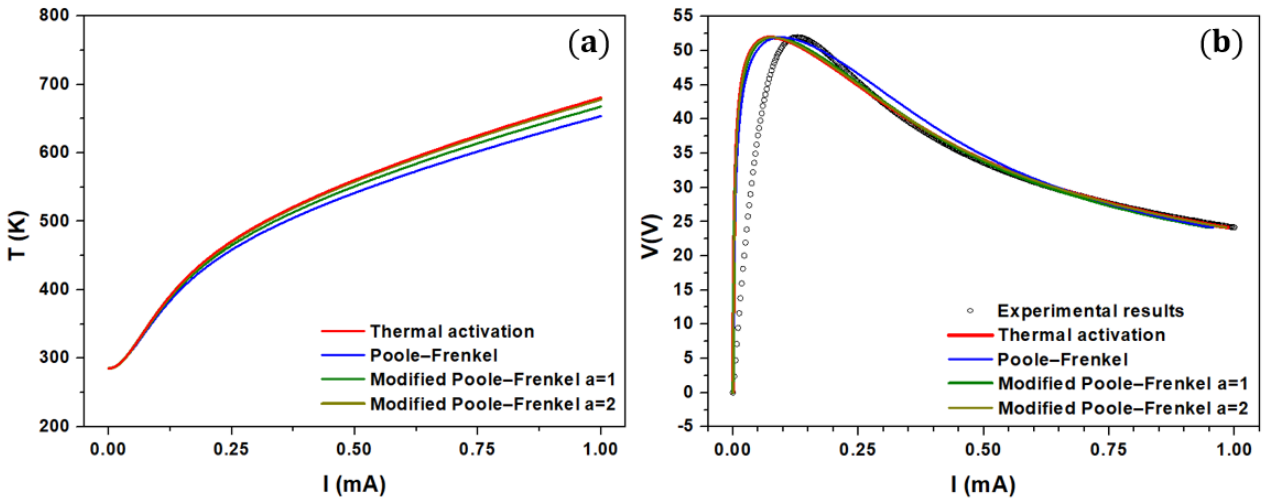


Figure 4.22: (a) Model of the variation of temperature as a function of current using Newton's law of cooling in the static limit. (b) Curves of the different models used to fit the experimental data of $V(I)$ curves.

Several conclusions can be reached by analyzing Figure 4.22:

- 1) The variation of temperature as a function of current as extracted from our fits (4.22 (a)) is similar to the measured temperature variation in figure 4.18 as deduced from the Raman measurement on the Si substrate close to the effective NbO_2 volume. This is an indication that the power dissipation, modeled simply by Newton's law of cooling and the variation of electrical conductivity, is reasonably accurate.
- 2) The modeled temperature curves of figure 4.22 (a) show that the maximum temperature reached in the NbO_2 is roughly between 650 - 700 K. This temperature is higher than the maximum temperature (500 K) as measured from the Raman shift of the Si Raman

Physical quantity	Symbol	Value	Unit
Thermal capacitance	C_{th}	5.5×10^{-11} [24]	WsK^{-1}
Boltzmann's constant	K_{B}	8.617×10^{-5}	eV
Activation energy	E_{a}	0.269	eV
Electron charge	e	1.60×10^{-19}	C
Film thickness	d	40	μm
Active Area	A	1.32×10^{-11}	m^2
Vacuum permittivity	ϵ_0	8.85×10^{-12}	Fm^{-1}
High frequency dielectric constant	ϵ_i	45 [16]	
conductivity constant	σ_0	12100*	S/m

Table 4.4: List of parameters used in the conduction models for fitting the V(I) curves. *The fitting parameter σ_0 for Poole-Frenkel model with $a=2$ is multiplied by a factor of $8/5$ [15] so it becomes 19360.

Model	$R_{\text{th}}(\text{KW}^{-1})$
Thermal Activation	16390
1d Poole-Frenkel	15263
3d Poole-Frenkel ($a=1$)	15838
3d Poole-Frenkel ($a=2$)	16281

Table 4.5: Effective thermal resistance of the different models used to fit our measured data.

lines. This can be understood because firstly the two samples are different, the first one on a glass substrate while the second is on a Si substrate. Secondly, the temperature of the sample on the Si substrate is estimated by the temperature of Si which is heated only by thermal conduction and is at a lower temperature than the effective volume of NbO_2 where the current passes.

3) An important conclusion concerns the mechanism of CC-NDR. We have used three models for estimating the variation of electrical conductivity as a function of current, the simple thermal activation model, and the more complex 1D and 3D Poole-Frenkel models which account for more complex mechanisms of transport dependent on the applied electrical field and trapped states. All three models, as shown in figure 4.22 (b) show a very similar thermally induced variation of conductivity with current. All three reproduce the general variation in the experimental curve but show differences from it in the low current region.

4) In our opinion the difference with respect to the experimental data is essentially due to the extended geometry of our structure where none of the contacts are nanometric, leading to non-uniformity of the current and temperature in the effective NbO_2 volume. This should then not be an intrinsic problem and with a more compact device structure, such as those used in literature, a better agreement could be found.

5) However we find that the simpler thermal activation model gives results equivalent to the more complicated Poole-Frenkel models. This validates the basic correctness of the thermal activation phenomenon being at the root of the observed behavior, coupled

with very low thermal conductivity. This puts into doubt the necessity of invoking more complex phenomena.

4.7 Conclusion

We worked on macroscopic devices which can be better characterized as to stoichiometry and crystalline structure. We showed that hysteresis in CC-NDR is due to temperature inhomogeneity (this hysteresis is not observed in nanometric devices). We reiterate that there is no phase transition (the phase is always insulating). Moreover, we showed that there is a similar temperature driven change in conductivity in both the amorphous and the crystalline samples, no Mott physics. In addition, the amorphous sample is a better electronic conductor as is already known. Finally, we proved that the CC-NDR may be simply explained by the creation of carriers by temperature in a semiconductor, without the need for invoking more complicated transport mechanisms.

Chapter 5

Conclusion

In this thesis we chose to work on NbO₂ thin films which are potential components of future memristor devices because of peculiar conductivity variations observed as a function of device current. A characteristic of NbO₂ is that it undergoes an insulator to metal transition at a high temperature ~ 1080 K. NbO₂ also exhibits a current controlled negative differential resistance (CC-NDR) regime in the V(I) characteristics. We asked ourselves which phenomena intervene and to what extent when NbO₂ undergoes changes in conductivity in typical device conditions? How does the structure (amorphous, crystalline) influence electronic properties? Do structural or electronic phase transitions take place? How can observed changes be modeled simply?

To answer these questions we fabricated both amorphous and crystalline stoichiometric NbO₂ thin films. Because of the existence of several intermediate and non-stoichiometric oxides this particular step turned out to be difficult and long. We then made simple devices which do not replicate the geometry used in memristor devices but allow a better control of the material, its phase and its electrical and spectroscopic characterization. This work included I-V characterization and sheet resistance measurements with control of temperature, Raman spectroscopy including during electrical characterization, and finally, the use of some simple models to verify the nature of the changes leading to current controlled negative differential resistance in NbO₂.

Initially, we attempted to fabricate NbO₂ thin films by sputtering Nb films followed by ex situ oxidation. However, we found that ex situ oxidation of Nb thin films prepared by sputtering from an Nb target does produce homogeneous and stoichiometric NbO₂ thin films. Therefore, the alternative technique adopted was sputtering from a stoichiometric NbO₂ target. RF-magnetron sputtering was used to synthesize NbO₂ thin films on different substrates: glass, Si and SiO₂. After optimizing the sputtering parameters, we found that annealing the amorphous as-deposited films for at least two hours was required to crystallize the films into crystalline NbO₂. A longer annealing time implied a bigger grain size. Also, annealing at higher temperature lead to a better crystallinity, keeping in mind the temperature constraints on the samples with glass substrates. The thin films on the different substrates were characterized using Raman and XRD which showed satisfying results concerning structure and stoichiometry. Electronic characterization was also done using various transport measurements in a cryostat which can go to low vacuum ($\sim 10^{-6}$ mbar) and has a temperature range of 3-400 K. From sheet resistance measurements we concluded that the resistivity of crystalline NbO₂ is $\sim 50 \Omega \text{ cm}$, about one order of

magnitude larger than that of the amorphous $\sim 5 \Omega \text{ cm}$. From the Arrhenius plots of each film we extracted the activation energy of crystalline NbO_2 and that of amorphous which are $\sim 0.27 \text{ e.V}$ and 0.18 e.V respectively. Attempts to electrostatically dope the crystalline and amorphous films on glass substrates using Space Charge Doping technique yielded expected changes in resistivity with doping, but no phase changes which could have been expected from the calculated electronic structures. Many reasons can be put forward to explain this observation. Electrostatic doping (like chemical doping) can be ineffective if the chemical potential is pinned to trapped states in the gap such that it cannot be brought to coincide with an electronic band. Also phase changes may also be unattainable due to the mobility edge often encountered in disordered samples. Finally, a non-ideal sample substrate interface can also hinder the efficiency of electrostatic doping.

Further measurements were made to investigate the origins of the threshold switching and the negative differential resistance phenomena that occur in NbO_2 . In the voltage controlled regime, we showed, both through I-V characteristics and through sheet resistance measurements as a function of gate voltage that instrumental limitations often introduce threshold-switching-like effects and that it is necessary to make measurements in conditions where these can be avoided. This can be done by controlling the current in the device and measurements in this regime led us to observe current-controlled negative differential resistance in NbO_2 .

Systematic measurements on devices on Si and glass substrates allowed us to conclude that:

- No electronic or structural phase change is observed in NbO_2 thin films in the CC-NDR mode. In particular, even in the NDR domain where large changes in the resistivity occur, both crystalline and amorphous samples remain insulating since their resistance always decreases with increase in temperature.
- Eventual phase changes observed in literature may be due to the amorphous-crystalline change which occurs above 550°C . The metal insulator transition which occurs at about 800°C is probably never observed in such devices.
- Temperature is the parameter which induces this change in resistivity through thermal activation of carriers. Temperature changes are locally induced because of power dissipated by the current in the device and the intrinsically low thermal conductivity of NbO_2 .
- Measured and extracted (from parameter fitting) changes in temperature and conductivity are in reasonable agreement indicating that the phenomenon is reasonably well understood. However, the simplest thermal activation model accounts for the observations without the need of invoking more complex models.

NDR in NbO_2 is caused by the variation of electrical conductivity by thermally generated charge carriers in a feedback loop phenomenon where the power dissipated by the device current determines local temperature. If the device is operated at a temperature where thermally generated charge carriers are sufficiently numerous, no NDR is observed. For amorphous NbO_2 , this temperature is as low as 400 K and presumable about 100 K

higher for crystalline NbO₂.

NDR is found in both amorphous and crystalline NbO₂ devices. However, the electrical conductivity of amorphous NbO₂ is more than that of crystalline NbO₂, which means that the I-V range where NDR is found is different in each material. The amorphous-crystalline transformation sets in between 800 K and 900 K, while the Mott insulator-metal transition happens at 1080 K in the crystalline material. These transitions are not involved in the NDR phenomena in our devices. No phase transition, either structural or electronic, and no irreversible phenomena could be related to NDR in our samples.

Since NDR involves sizable variations of electrical conductivity generated by temperature change, it can be found in semiconductors or insulators where such sizable variation is possible through thermal energy. But for sizable variation of electrical conductivity to occur, considerable changes in local temperature should be possible through Joule heating. This implies low thermal conductivity in the material. Effectively, NbO₂ has a thermal conductivity which is two orders of magnitude lower than that of silicon and the electronic contribution to this thermal conductivity is negligible.

Appendices

Appendix A

Raman Spectra on Target Before and After Unsealing

Figure A.1 shows a comparison between the Raman spectra before unsealing the target and exposing it to air, and after doing so. Notice that as target gets exposed to air the NbO₂ raman peaks start to shrink until they disappear and a completely different amorphous phase appears. This shows how sensitive the NbO₂ phase is to oxidation though the Raman measurements were very short (1 min each measurement).

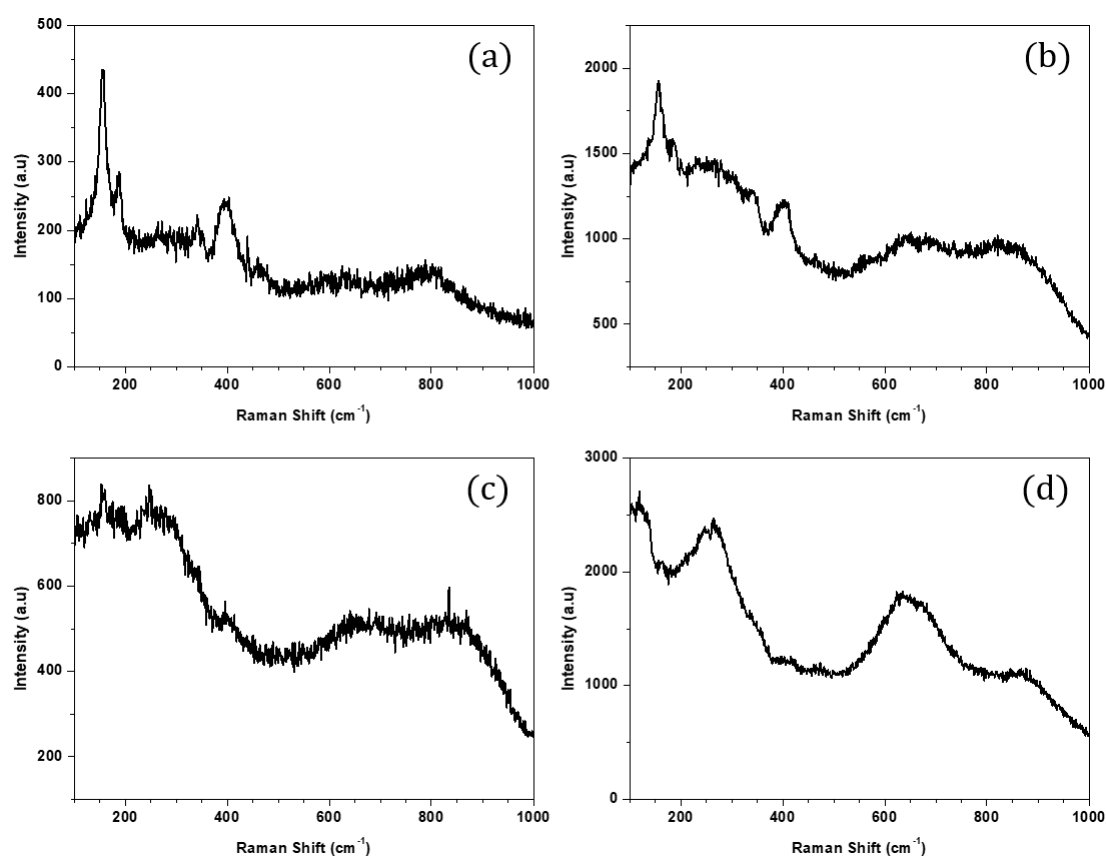


Figure A.1: (a) Raman spectrum before unsealing the target. (b), (c) and (d) Successive Raman spectra taken after unsealing the target.

Bibliography

- [1] S. Nakao, H. Kamisaka, Y. Hirose¹, T. Hasegawa, Structural, electrical, and optical properties of polycrystalline NbO₂ thin films grown on glass substrates by solid phase crystallization. *Phys. Status Solidi A* 214, No. 3, (2017) 1600604.
- [2] D. V. Geppert, A new negative-resistance device, *Proc. IEEE*, vol. 51, no. 1, (1963) 223.
- [3] Y. Chen, L. Goux, S. Clima, B. Govoreanu, R. Degraeve, G. Kar, A. Fantini, G. Groeseneken, D. Wouters, M. Jurczak, Endurance/retention tradeoff on cap 1T1R bipolar RRAM, *IEEE Trans. Electron Devices*, 60(3), (2013)1114–1121.
- [4] S. Jung, J. Shin, H. Hwang, Effect of ZrO_x/HfO_x bilayer structure on switching uniformity and reliability in nonvolatile memory applications, *Appl. Phys. Lett.*, 97, (2010) 172105.
- [5] H. Lee, P. Che, T. Wu, Y. Che, C. Wan, P. Tzen, C. Lin, F. Chen, C. Lien, M. Tsai, Low power and high speed bipolar switching with a thin reactive Ti buffer layer in robust ZrO_x/HfO₂ based RRAM, In *Electron Devices Meeting, IEEE International*, (2008) 1–4.
- [6] F. Chudnovskii, L. Odynets, A. Pergament, G. Stefanovich, Electroforming and switching in oxides of transition metals: the role of metal-insulator transition in the switching mechanism, *J. Solid State Chem.*, 122(1), (1996) 95–99.
- [7] A. Pergament, A. Crunteanu, A. Beaumont, G. Stefanovich, A. Velichko, Vanadium Dioxide: Metal-Insulator Transition, Electrical Switching and Oscillations, A Review of State of the Art and Recent Progress. presented as an oral talk at the Energy Materials and Nanotechnology (EMN) Meeting on Computation and Theory, Istanbul (Turkey) 9-12/11, (2015).
- [8] S. Nandi, Resistive Switching in Transition Metal Oxides for Integrated Non-volatile Memory, Thesis Report (2017).
- [9] A. Guha, A. Raychaudhuri, A. Raju, C. Rao, Nonlinear conduction in Pr_{0.63}Ca_{0.37}MnO₃: effect of magnetic fields, *Phys. Rev. B* 62 (2000) 5320–5323.
- [10] A. Asamitsu, Y. Tomioko, H. Kuwahara, Y. Tokura, Current switching of resistive states in magnetoresistive manganites, *Nature* 388 (1997) 50–52.

- [11] A. Alexandrov, A. Bratkovsky, B. Bridle, S. Savel'ev, D. Strukov, R. Williams, Current-controlled negative differential resistance due to Joule heating in TiO_2 , *Appl. Phys. Lett.* 99 (2011) 202104.
- [12] D. Kim, T. Grant, Z. Fisk, Limit cycle and anomalous capacitance in the Kondo insulator SmB_6 , *Phys. Rev. Lett.* 109 (2012) 096601.
- [13] C. Funck, S. Menzel, N. Aslam, H. Zhang, A. Hardtdegen, R. Waser, S. Hoffmann-Eifert, Multidimensional simulation of threshold switching in NbO_2 based on an electric field triggered thermal runaway model. *Adv. Electron. Mater.* 2, (2016) 1600169.
- [14] S. Shin, T. Halpern, P. Raccach, High-speed high-current field switching of NbO_2 , *J. Appl. Phys.* 48, (1977) 3150–3153.
- [15] G. Gibson, S. Musunuru, J. Zhang, K. Vandenberghe, J. Lee1, C. Hsieh, W. Jackson, Y. Jeon, D. Henze, Z. Li, R. Williams, An accurate locally active memristor model for S-type negative differential resistance in NbO_x , *Appl. Phys. Lett.* 108, (2016) 023505.
- [16] S. Slesazek, H. Mahne, H. Wylezich, A. Wachowiak, a J. Radhakrishnan, A. Ascoli, R. Tetzlaffb, T. Mikolajickab, Physical model of threshold switching in NbO_2 based memristors. *RSC Adv.*, 5, (2015) 102318.
- [17] M. Pickett, G. Medeiros-Ribeiro, R. Williams, A scalable neuristor built with Mott memristors, *Nat. Mater.* 12, (2012) 114–117.
- [18] X. Liu, S. Li, S. Nandi, D. Venkatachalam, R. Elliman, Threshold switching and electrical self-oscillation in niobium oxide films, *J. Appl. Phys.* 120, (2016) 124102.
- [19] G. Vezzoli, Recovery curve for threshold-switching NbO_2 , *J. Appl. Phys.* 50, (1979) 6390–6395.
- [20] Y. Zhou, S. Ramanathan, Mott memory and neuromorphic devices, *Proc. IEEE* 103, (2015) 1289–1310.
- [21] B. Murdoch, D. McCulloch, R. Ganesan, D. McKenzie, M. Bilek, J. G. Partridge, Memristor and selector devices fabricated from $\text{HfO}_{2-x}\text{N}_x$. *Appl. Phys. Lett.* 108, (2016) 143504.
- [22] E. Cha, J. Park, J. Woo, D. Lee, A. Prakash, H. Hwanga, Comprehensive scaling study of NbO_2 insulator-metal-transition selector for cross point array application, *Appl. Phys. Lett.* 108, (2016) 153502.
- [23] K. Kim, J. Zhang, C. Graves, J. Yang, B. Choi, C. Hwang, Z. Li, R. Williams, Low power, self-rectifying, and forming-free memristor with an asymmetric programming voltage for a high density crossbar application. *Nano. Lett.* 11, (2016) 6724–6732.
- [24] S. Kumar, Z. Wang, N. Davila, N. Kumari, K. Norris, X. Huang, J. Strachan, D. Vine, A. Kilcoyne, Y. Nishi, R. Williams, Physical origins of current and temperature controlled negative differential resistances in NbO_2 , *Nature Communications*, 8, (2017) 658.
- [25] J. Barth, G. Costantini, K. Kern, Engineering atomic and molecular nanostructures at surfaces, *Nature* 437, (2005) 671.

- [26] Y. Xia, P. Yang, Y. Sun, Y. Wu, B. Mayers, B. Gates, Y. Yin, F. Kim H. Yan, One-Dimensional Nanostructures: Synthesis, Characterization, and Applications, *Adv. Mater* 15, No.5 (2003) 353-389.
- [27] Y. Arakawa, H. Sakaki, Multidimensional quantum well laser and temperature dependence of its threshold current. *Appl. Phys. Lett.* 40, (1982) 939.
- [28] A. O'Hara, T. Nunley, A. Posadas, S. Zollner, A. Demkov, Electronic and optical properties of NbO₂. *J. of Appl. Phys.* 116, (2014) 213705. <https://doi.org/10.1063/1.4903067>.
- [29] P. Diener, E. Janod, B. Corraze, M. Querre, C. Adda, M. Guilloux-Viry, S. Cordier, A. Camjayi, M. Rozenberg, M. P. Besland, and L. Cario, How a dc Electric Field Drives Mott Insulators Out of Equilibrium, *Phys. Rev. Lett.* 121,(2018) 016601.
- [30] W. Fogle, J. Perlstein, Semiconductor-to-Metal Transition in the Blue Potassium Molybdenum Bronze, K_{0.30} MoO₃; Example of a Possible Excitonic Insulator, *Phys. Rev. B* 6, (1972) 1402.
- [31] M. Greenblatt, Molybdenum oxide bronzes with quasi-low-dimensional properties, *Chem. Rev.* 88, (1988) 31.
- [32] C. Sellier, F. Boucher, E. Janod, Crystal structure and charge order below the metal–insulator transition in the vanadium bronze β-SrV₆O₁₅, *Solid State Sci.* 5, (2003) 591.
- [33] P. Marley, A. Stabile, C. Kwan, S. Singh, P. Zhang, G. Sambandamurthy, S. Banerjee, Charge Disproportionation and Voltage-Induced Metal–Insulator Transitions Evidenced in β-Pb_xV₂O₅ Nanowires, *Adv. Funct. Mater.* 23, (2013) 153.
- [34] J. Torrence, P. Lacorre, A. Nazzal, E. Ansaldo, Ch. Niedermayer, Systematic study of insulator-metal transitions in perovskites RNiO₃ (R=Pr,Nd,Sm,Eu) due to closing of charge-transfer gap *Phys. Rev. B* 45, (1992) 8209.
- [35] M. Medarde, Structural, magnetic and electronic properties of RNiO₃ perovskites (R = rare earth), *J. Phys. Condens. Matter* 9, (1997) 1679.
- [36] J. Alonso, M. Martinez-Lope, J. Garcia Munoz, and M. Fernandez-Diaz, Room-temperature monoclinic distortion due to charge disproportionation in RNiO₃ perovskites with small rare-earth cations (R=Ho, Y, Er, Tm, Yb, and Lu): A neutron diffraction study, *Phys. Rev. B* 61, (2000) 1756.
- [37] A. Paradisi, J. Biscaras, A. Shukla, Space Charge Induced Electrostatic Doping of Two-Dimensional Materials: Graphene as a Case Study, *Appl. Phys. Lett.*, 107, (2015) 143103.
- [38] A. Alexandrov, A. Bratkovsky, B. Bridle, S. Savel'ev, D. Strukov, R. Williams, Current-controlled negative differential resistance due to Joule heating in TiO₂, *Appl. Phys. Lett.* 99, (2011) 202104.
- [39] A. Alves, A. Coutinho, The Evolution of the Niobium Production in Brazil, *Materials Research*,18(1), (2015) 106-112.

- [40] W. Luo, D. Roundy, M. Cohen, J. Morris, Jr., Ideal strength of bcc molybdenum and niobium, *Phys. Rev. N* 66, (2002) 094110.
- [41] R. Grill, A. Gnadenberger, Niobium as mint metal: Production-properties-processing, *International Journal of Refractory Metals and Materials*, 24 (2006) 275-282.
- [42] C. Nico, T. Monteiro, M. Graça, Niobium oxides and niobates physical properties: Review and prospects, *Progress in Materials Science* 80 (2016) 1–37.
- [43] H. SCHÄFER, , D. BERGNER, R. GRUEHN, Die thermodynamische Stabilität der sieben zwischen 2,00 and 2,50 O/Nb existierenden Phasen. *Z. anorg. Allg. Chem.* 365, (1969) 31-50.
- [44] K. Naito, N. Kamegashira, N. Sasaki, Phase equilibria in the system between NbO₂ and Nb₂O₅ at high temperatures. *J. Solid State Chem.* 35, (1980) 305-311.
- [45] R. Elliott, Columbium-oxygen system, *Trans. Am. Soc. Metals* 52, (1960) 990-1014.
- [46] J. Hulm, C. Jones, R. Hein, ; J. Gibson, Superconductivity in the TiO and NbO systems, *Journal of Low Temperature Physics*, 7 (3–4), (1972) 291.
- [47] W. Wahnsiedler, Energy band structure and electronic transport properties of niobium monoxide, *J. of Solid State Chemistry* 49, (1983) 195.
- [48] A. Okaz and P. Keesom, Specific heat and magnetization of the superconducting monoxides: NbO and TiO, *Phys. Rev. B* 12, (1975) 4917.
- [49] Y. Qiu , D. Smyth, J. Kimmel, The stabilization of niobium-based solid electrolyte capacitors, *Acta Passive Electron Components* 25(2), (2002) 201–9.
- [50] T. Karnik, Ceramic powder for use in forming an anode of an electrolytic capacitor, GB (A), (2009) 2454049.
- [51] T. Karnik, Doped ceramic powder for use in forming capacitor anodes. Patent US 7760487 B2; (2010).
- [52] C. Nico, M. Soares, J. Rodrigues, M. Matos, R. Monteiro, M. Graça, M. Valente, F. Costa, T. Monteiro, Sintered NbO powders for electronic device applications, *J. Phys. Chem. C* 115, (2011) 4879–86.
- [53] S. Forghany, J. Anderson, Reduction and polymorphic transformation of B-Nb₂O₅. *J. Chem. Soc., Dalton Trans*, (1981) 255–61.
- [54] A. Le Viet, R. Jose, M. Reddy, M. Chowdari, S. Ramakrishna, Nb₂O₅ photoelectrodes for dye-sensitized solar cells: choice of the polymorph, *J. Phys. Chem.*, C114, (2010) 21795–800.
- [55] R. Brayner, F. Bozon-Verduraz, Niobium pentoxide prepared by soft chemical routes: morphology, structure, defects and quantum size effect, *Phys. Chem.*, 5, (2003) 1457–66.
- [56] H. Schäfer, R. Gruehn, F. Schulte, The modifications of niobium pentoxide, *Angew. Chem. Int. Ed. Engl.* 5, (1966) 40–52.

- [57] V. Shamrai, Y. Blagoveshchenski, A. Gordeev, A. Mitin, I. Drobinova, Structural states and electrical conductivity of oxidized niobium nanopowders, *Russ. Metall. Met.*, (2007) 322–6.
- [58] L. Reznichenko, V. Akhnazarova, L. Shilkina, O. Razumovskaya, S. Dudkina, Invar effect in $n\text{-Nb}_2\text{O}_5$, $\text{aht-Nb}_2\text{O}_5$, and LNb_2O_5 , *Crystallogr. Rep.* 54, (2009) 483–91.
- [59] C. Valencia-Balvín, S. Pérez-Walton, G. Dalpian, J. Osorio-Guillén, First-principles equation of state and phase stability of niobium pentoxide, *Comput. Mater. Sci.* 81 (2014) 133–40.
- [60] R. Rani, A. Zoolfakar, A. O’Mullane, M. Austin, K. Kalantar-Zadeh, Thin films and nanostructures of niobium pentoxide: fundamental properties, synthesis methods and applications, *J. Mater. Chem. A* 2, (2014) 15683.
- [61] T. Massalski, A. International, Binary alloy phase diagrams. 2nd ed. Materials Park (OH): ASM Intl; 1990.
- [62] Ph.D. of David Bach, EELS investigations of stoichiometric niobium oxides and niobium-based capacitors, (2009).
- [63] R. Pynn, J. Axe, R. Thomas, Structural distortions in the low-temperature phase of NbO_2 , *Phys. Rev. B* 13, (1976) 2965.
- [64] A. Bolzan, C. Fong, B. Kennedy, and C. Howard, A Powder Neutron Diffraction Study of Semiconducting and Metallic Niobium Dioxide, *J. Solid State Chem.* 113, (1994) 9.
- [65] S. Shapiro, J. Axe, G. Shirane, P. Raccach, Neutron scattering study of the structural phase transition in NbO_2 , *Solid State Commun.* 15, (1974) 377.
- [66] V. Eyert, The metal-insulator transition of Formula : An embedded Peierls instability, *Europhysics letters* 58 (6), (2002) 851.
- [67] T. Sakata, K. Sakata, and I. Nishida, Study of Phase Transition in NbO_2 , *Phys. Status solidi* 20, (1967) K155.
- [68] A. Cheetham and C. Rao, A neutron diffraction study of niobium dioxide, *Acta Cryst.* B32, (1976) 1579.
- [69] G. Thornton, A. F. Orchard, and C. N. R. Rao, An x-pes study of the semiconductor-metal transition in NbO_2 , *Phys. Lett.* 54, (1975) 235.
- [70] M. DELHEUSY, Thèse présentée pour obtenir le grade de Docteur en Sciences de l’Université Paris XI Orsay: X-ray investigation of Nb/O interfaces, (07-2008).
- [71] H. Bethe, Termaufspaltung in Kristallen, *Annalen der Physik* (in German), 395 (2), (1929) 133–208.
- [72] J. Van Vleck, Theory of the Variations in Paramagnetic Anisotropy Among Different Salts of the Iron Group, *Phys. Rev.* 41 (2), (1932) 208–215.
- [73] J. Goodenough, The Two Components of the Crystallographic Transition in VO_2 , *J. Solid State Chem.* 3, (1971) 490-500.

- [74] F. Wong, N. Hong, S. Ramanathan, Orbital splitting and optical conductivity of the insulating state of NbO_2 . *Phys. Rev. B* 90, (2014) 115135.
- [75] [https://chem.libretexts.org/Bookshelves/InorganicChemistry/SupplementalModules\(InorganicChemistry\)CrystalFieldTheory/CrystalFieldTheory](https://chem.libretexts.org/Bookshelves/InorganicChemistry/SupplementalModules(InorganicChemistry)CrystalFieldTheory/CrystalFieldTheory).
- [76] D. Adler, Mechanisms for metal-nonmetal transitions in transition-metal oxides and sulfides, *Rev. Mod. Phys.*, (1968) 714–736.
- [77] M. Yousuf, B. Kuliyeu, B. Lalevic, Investigation of trapping centers in single-crystal niobium dioxide by admittance spectroscopy, *J. Appl. Phys.* 53, (1982) 8647.
- [78] Y. Sakai, N. Tsuda, T. Sakata, Electrical properties of semiconducting NbO_2 , *J. Phys. Soc. Jpn.*, 54(4), (1985) 1514–1518.
- [79] A. Posadas, A. O'Hara, S. Rangan, R. Bartynski, and A. Demkov, Band gap of epitaxial in-plane-dimerized single-phase NbO_2 films, *Appl. Phys. Lett.* 104, (2014) 092901.
- [80] H. Kuwamoto, J. Honig, J. Appel, Electrical properties of the $(\text{V}_{1-x}\text{Cr}_x)_2\text{O}_3$ system, *Phys. Rev. B*, 22,(1980) 2626.
- [81] E. Janod, J. Tranchant, B. Corraze, M. Querré, P. Stoliar, M. Rozenberg, T. Cren, D. Roditchev, V. Phuoc, M. Besland, L. Cario, Resistive Switching in Mott Insulators and Correlated Systems, *Adv. Funct. Mater.*, 25, (2015) 6287–6305.
- [82] M. Imada, A. Fujimori, Y. Tokura, Metal-insulator transitions, *Rev. Mod. Phys.* 70, (1998) 1039.
- [83] S. Hassan, A. Georges, H. Krishnamurthy, Publisher's Note: Sound Velocity Anomaly at the Mott Transition: Application to Organic Conductors and V_2O_3 *Phys. Rev. Lett.*, 94, (2005) 036402.
- [84] Y. Zhou, S. Ramanathan, Correlated electron materials and field effect transistors for logic: a review, *Critical Reviews in Solid State and Materials Sciences*, 38(4), (2013) 286-317.
- [85] N. Mott, Metal-insulator transitions, *Cryst. Res. Technol.* 26, (1991) 788.
- [86] M. Imada, A. Fujimori, Y. Tokura, Metal-insulator transitions, *Reviews of Modern Physics*, 70(4), (1998) 1039.
- [87] N. Mott, Metal-insulator transition, *Reviews of Modern Physics*, 40(4), (1968) 677.
- [88] P. Anderson, Absence of diffusion in certain random lattices, *Phys. Rev.*, 109, (1958) 1492–1505.
- [89] N. Mott, The mobility edge since 1967, *J. Phys. C Solid State Phys.*, 20, (1987) 3075.
- [90] M. Fowler, *Electrons in One Dimension: the Peierls Transition* (2007).
- [91] V. Eyert, The metal-insulator transition of NbO_2 : An embedded Peierls instability, *Europhys. Lett.*, 58(6), (2002) 851–856.

- [92] A. O'Hara, A. Demkov, Nature of the metal-insulator transition in NbO_2 , *Phys. Rev. B* 91, (2015) 094305.
- [93] Y. Yang, Influence of Chemical Doping on Microstructures and Superconducting Properties of MgB_2 Wires and Bulk Samples, Dissertation (2016).
- [94] H. Yuan, H. Shimotani, A. Tsukazaki, A. Ohtomo, M. Kawasaki, and Y. Iwasa, High-density carrier accumulation in ZnO field-effect transistors gated by electric double layers of ionic liquids, *Adv. Funct. Mater.*, 19, (2009) 1046–1053.
- [95] H. Wong, Beyond the conventional transistor, *IBM J. Res. Develop.* 46, (2002) 133–168.
- [96] F. Wong, S. Ramanathan, Electrical transport in transition metal oxides, *Resistive Switching: From Fundamentals of Nanoionic Redox Processes to Memristive Device Applications*, (2016) 165–196.
- [97] A. Miller, E. Abrahams, Impurity conduction at low concentrations, *Phys. Rev.*, 120, (1960) 745–755.
- [98] P. Anderson, Absence of diffusion in certain random lattices, *Phys. Rev.*, 109, (1958) 1492–1505.
- [99] N. Mott, E. Davis, *Electronic processes in non-crystalline materials*, OUP Oxford, (2012).
- [100] Y. Wang, Metal-Insulator Transition in Niobium Dioxide Thin Films, thesis dissertation (2017).
- [101] I. Shlimak, *Is hopping a science?: selected topics of hopping conductivity*, World Scientific, (2015).
- [102] M. Pollak, A percolation treatment of dc hopping conduction, *J. of NonCrystalline Solids*, 11(1), (1972)1-24.
- [103] E. Hamilton, Variable range hopping in a non-uniform density of states, *Philosophical Magazine*, 26(4), (1972) 1043–1045.
- [104] B. Shklovskii, A. Efros, *Electronic properties of doped semiconductors*, vol. 45, Springer Science and Business Media, (2013).
- [105] R. William, S. Amos, G. Dummer, *Newnes Dictionary of Electronics*, 4th Ed. Newnes. (1999) 211.
- [106] R. Graf, *Modern Dictionary of Electronics*, 7th Ed. Newnes. (1999) 499.
- [107] D. Shanefield, *Industrial Electronics for Engineers, Chemists, and Technicians*. Elsevier, (2001) 18–19.
- [108] J. Carr, *Microwave and Wireless Communications Technology*, USA: Newnes, (1997) 313–314.
- [109] J. Groszkowski, *Frequency of Self-Oscillations*, Warsaw: Pergamon Press - PWN (Panstwowe Wydawnictwo Naukowe), (1964) 45–51.

- [110] O. Aluf, Ofer. *Optoisolation Circuits: Nonlinearity Applications in Engineering*, World Scientific. (2012) 8–11.
- [111] I. Gottlieb, *Practical Oscillator Handbook*, Elsevier, (1997) 75–76.
- [112] R. Kaplan, Equivalent circuits for negative resistance devices, Technical Report No. RADC-TR-68-356. Rome Air Development Center, US Air Force Systems Command: (1968) 5–8.
- [113] M. Shahinpoor, H. Schneider, *Intelligent Materials*, London: Royal Society of Chemistry. (2008) 209.
- [114] M. Golio, *The RF and Microwave Handbook*, CRC Press. (2000) 5.91.
- [115] H. Beneking, *High Speed Semiconductor Devices: Circuit aspects and fundamental behaviour*, Springer, (1994) 114–117.
- [116] L. Chua, , Memristor—The Missing Circuit Element, *IEEE Transactions on Circuit Theory*, CT-18 (5), (1971) 507–519.
- [117] I. Sinclair, *Sensors and transducers*, 3rd Ed. Newnes, (2001) 69–70.
- [118] Y. Rybin, *Electronic Devices for Analog Signal Processing*, Springer, (2011) 155–156.
- [119] M. Fogiel, *The electronics problem solver*, Research and Education Assoc., (1988).
- [120] M. Radmanesh, *Advanced RF and Microwave Circuit Design* (2009).
- [121] R. Rao, *Microwave Engineering*, PHI Learning Pvt. Ltd., (2012) 440.
- [122] F. Brown, *Engineering System Dynamics*, (2006) 43.
- [123] K. Kaiser, *Electromagnetic Compatibility Handbook*, (2004) 13–52.
- [124] U. Kumar, Design of an indiginized negative resistance characteristics curve tracer, *Active and Passive Elect. Comp.*, Vol.23 Corp, 23 (2000) 13–23.
- [125] R. Gilmore, L. Besser, *Practical RF Circuit Design for Modern Wireless Systems*, Vol. 2, (2003) 27–29.
- [126] A. Kumar, *Pulse and Digital Circuits*, (2004) 274, 283–289.
- [127] M. Fogiel, *The electronics problem solver*, Research and Education Assoc. (1988) 1032.
- [128] C. Kidner, I. Mehdi; J. East; J. Haddad (March 1990), Potential and limitations of resonant tunneling diodes, *First Int. Symp. on Space THz Technology*, Ann Arbor, MI, (1990) 85.
- [129] K. Du, M. Swamy, *Wireless Communication Systems: From RF Subsystems to 4G Enabling Technologies*, Cambridge Univ. (2010) 438.

- [130] J. Wu, T. Hu, Y. Yin, J. Li, W. Zhou, Y. Gao, L. Jiang, Z. Huang, J. Chu, Current-controlled negative differential resistance in small-polaron hopping system, *AIP Advances* 9, (2019) 055223.
- [131] R. Franz, Use nonlinear devices as linchpins to next-generation design, *Electronic Design Magazine*, (2010).
- [132] G. Abraham, Multistable semiconductor devices and integrated circuits". *Advances in Electronics and Electron Physics*, Vol. 34–35, (1974) 270–398.
- [133] Z. Wang, S. Kumar, R. Williams, Y. Nishi, H. Wong, Intrinsic limits of leakage current in self-heating triggered threshold switches, *App. Phys. Lett.*, 114, (2019) 183501-1.
- [134] M. Pickett, R. Williams, Sub-100 fJ and sub-nanosecond thermally driven threshold switching in niobiumoxide crosspoint nanodevices, *Nanotechnology* 23, (2012) 215202.
- [135] S. Kumar, J. Strachan, R. Williams, Chaotic dynamics in nanoscale NbO₂ Mott memristors for analogue computing, *Nature* vol. 548, (2017) 318-321.
- [136] G. Gibson, Designing Negative Differential Resistance Devices Based on Self-Heating, *Adv. Funct. Mater.*, 28, (2018) 1704175.
- [137] T. Joshi, P. Borisov, D. Lederman, Structural and electrical characterization of NbO₂ thin film vertical devices grown on TiN-coated SiO₂/Si substrates, *J. Appl. Phys.*, 124, (2018) 114502.
- [138] R. Ongaro, A. Pillonnet, Poole-Frenkel (PF) effect high field saturation, *Revue de Physique Appliquee*, 24 (12), (1989) 1085-1095.
- [139] P. Rottlander, M. Hehn, A. Schuhl, Determining the interfacial barrier height and its relation to tunnel magnetoresistance, *Phys. Rev. B* 65 (2002) 054422.
- [140] S. Swann, Magnetron Sputtering, *Phys. Technol.*, 19 (1988).
- [141] A. Chaoumead, Y. Sung, D. Kwak, The Effects of RF Sputtering Power and Gas Pressure on Structural and Electrical Properties of ITiO Thin Film, *Advances in Condensed Matter Physics* (2012) 1-7 651587.
- [142] F. Oudrhiri-Hassani, L. Presmanes, A. Barnabe, P. Tailhades, Microstructure, porosity and roughness of RF sputtered oxide thin films: Characterization and modulation, *Appl. Surface Science* 254 (2008) 5796–5802.
- [143] A. Barnabe, A. Chapelle, L. Presmanes, P. Tailhades, Copper and iron based thin film nanocomposites prepared by radio frequency sputtering. Part I: elaboration and characterization of metal/oxide thin film nanocomposites using controlled in situ reduction process, *J. Mater. Sci.* 48, (2013) 3386–3394.
- [144] A. Ahmed, M. Devarajan, N. Afzal, Effects of substrate temperature on the degradation of RF sputtered NiO properties, *Materials Science in Semiconductor Processing* 63 (2017) 137–141.
- [145] T. Bui, H. Trong, L. Presmanes, A. Barnabé, C. Bonningueab, P. Tailhades, Thin films of $Co_{1.7}Fe_{1.3}O_4$ prepared by radio frequency sputtering – the first step towards their spinodal decomposition, *Cryst. Eng. Comm.* 16, (2014) 3359.

- [146] C. Carlisle, T. Fujimoto, W. Sim, D. King, Atomic imaging of the transition between oxygen chemisorption and oxide film growth on Ag{1 1 1}, *Surface Science* 470, (2000) 15–31.
- [147] A. Fromhold, JR. and E. Cook, Kinetics of Oxide Film Growth on Metal Crystals: Electron Tunneling and Ionic Diffusion, *Phys. Review* vol. 158 no. 3, (1967) 600-612.
- [148] G. V. Chandrashekhar, J. Moyo, AND J. M. Honig, Electrical Resistivity of NbO, *J. Solid State Chem.* 2, (1970) 528-530.
- [149] J. Gallego, C. Thomas, Preparation and Characterization of Thin Films of NbO₂, *Thin Solid Films*, 98 (1982) 11-22.
- [150] M. Graça, A. Meireles, C. Nico, M.A. Valente, Nb₂O₅ nanosize powders prepared by sol-gel – Structure, morphology and dielectric properties, *J. of Alloys and Compounds* 553 (2013) 177–182.
- [151] R. Singh, C.V. Raman and the Discovery of the Raman Effect, *Physics in Perspective (PIP)*, 4(4), (2002) 399-420.
- [152] S. Rajinder, F. Riess, The Nobel Prize for Physics in 1930 – A close decision?, *Notes and Records of the Royal Society of London.* 55 (2), (2001) 267–283.
- [153] G. Binnig, H. Rohrer, Scanning tunneling microscopy- From Birth to Adolescence. *Reviews of Modern Physics*, Vol. 5, No. 3, (1987) Part I.
- [154] G. Binnig, C. Quate, Atomic force microscope, *Phys. Rev. Lett.* 56(9), (1986) 930-933.
- [155] P. Huang, C. Ruiz-Vargas, A. van der Zande, W. Whitney, M. Levendoff, J. Kevek, S. Garg, J. Alden, C. Hustedt, Y. Zhu, J. Park, P. McEuen, D. Muller, Grains and grain boundaries in single-layer graphene atomic patchwork quilts, *Nature*, 469(7330), (2011) 389–392.
- [156] J. Welker, F. Giessib, Revealing the Angular Symmetry of Chemical Bonds by Atomic Force Microscopy, *Science* 336, 44 (2012).
- [157] K. Nanda, S. Sarangi, S. Sahu, Measurement of surface roughness by atomic force microscopy and Rutherford backscattering spectrometry of CdS nanocrystalline films, *Appl. Surface Science*, 133 (1998) 293–297.
- [158] Y. Kuznetsov, A. Malkin, T. Land, J. DeYoreo, A. Barba, J. Konnert, A. McPherson, Molecular Resolution Imaging of Macromolecular Crystals by Atomic Force Microscopy, *Biophysical Journal* Volume 72, (1997) 2357-2364.
- [159] P. Hartley, H. Thissen, T. Vaithianathan, H. Griesser, A Surface Masking Technique for the Determination of Plasma Polymer Film Thickness by AFM, *Plasmas and Polymers*, Vol. 5, No. 1, (2000).
- [160] W.H. Bragg, W.L. Bragg, The Reflection of X-rays by Crystals, *Proc. R. Soc. Lond.* A. 88 (605), (1913) 428-438.

- [161] A. Patterson, The Scherrer formula for X-ray particle size determination, *Phys. Rev.*, 56(10), (1939) 978-982.
- [162] L. van der Pauw, A method of measuring specific resistivity and Hall effect of discs of arbitrary shape, *Philips Technical Review*, 20, (1958) 220-224.
- [163] J. Webster, *The Measurement, Instrumentation and Sensors handbook*. New York: CRC Press LLC. (1999) 1339.
- [164] M. Raskovic, J. Upadhyay, L. Vuskovic, S. Popovic, A-M. Valente-Feliciano, L. Phillips, Plasma treatment of bulk niobium surface for superconducting rf cavities: Optimization of the experimental conditions on flat samples, *Phys. Rev., ST Accel. Beams* 13, (2010) 112001.
- [165] P. Walker, W. Tarn, *Hand Book of Metal Etchants*, (1991) 881.
- [166] Micro. Chem. data sheet, NANOTM PMMA and Copolymer (2001).
- [167] HARDIE POLYMERS, polymers, PMMA or acrylic useful Data, Melt temperature. <https://www.hardiepolymers.com/polymers/pmma-or-acrylic/>
- [168] H. Mehrer, A. Imre, E. Tanguet-Nijokep, Diffusion and Ionic Conduction in Oxide Glasses. *Journal of Physics: Conference Series* 106 (2008) 012001.
- [169] E. Sterpetti, J. Biscaras, A. Erb, A. Shukla, Comprehensive phase diagram of two-dimensional space charge doped $\text{Bi}_2\text{Sr}_2\text{CaCu}_2\text{O}_{8+x}$, *Nature Comm.* 8, (2017) 2060.
- [170] K. Jung, Y. Kim, Y. Park, W. Jung, J. Choi, B. Park, H. Kim, W. Kim, J. Hong, H. Im, Unipolar resistive switching in insulating niobium oxide film and probing electroforming induced metallic components, *J. Phys. D: Appl. Phys.* 48 (2015) 335308.
- [171] K. Jung, Y. Kim, Y. Park, W. Jung, J. Choi, B. Park, H. Kim, W. Kim, J. Hong, H. Im, Journal of Physics D: Applied Physics Paper Preparation, characterization, and electrical properties of epitaxial NbO_2 thin film lateral devices, *J. Phys. D: Appl. Phys.* 48 (2015) 335308.
- [172] Y. Zhao, Z. Zhang, Y. Lin, Optical and dielectric properties of a nanostructured NbO_2 thin film prepared by thermal oxidation, *J. Phys. D* 37, (2004) 3392.
- [173] Y. Wang, R. B. Comes, S. Kittiwatanakul, S. A. Wolf, J. Lu, Epitaxial niobium dioxide thin films by reactive-biased target ion beam deposition, *J. Vac. Sci. Technol. A* 33, (2015) 021516-1.
- [174] A. Bonakdarpour, R. Tucker, M. Fleischauer, N. Beckers, M. Brett, D. Wilkinson, Nanopillar niobium oxides as support structures for oxygen reduction electrocatalysts, *Electrochim. Acta* 85, (2012) 492.
- [175] R. Rani, A. Zoofakar, A. O'Mullane, M. Austina, K. Kalantar-Zadeh, Thin films and nanostructures of niobium pentoxide: fundamental properties, synthesis methods and applications, *J. of Materials Chem. A*, 2 (2014) 15683.
- [176] J. Shank, M. Tellekamp, M. Wahila, S. Howard, A. Weidenbach, B. Zivasatienraj, L. J. Piper, W. Doolittle, Scalable memdiodes exhibiting rectification and hysteresis for neuromorphic computing, *Nature*, (2018) 12935.

- [177] E. Greener, D. Whitmore, M. E. Fine, Electrical Conductivity of Near-Stoichiometric α - Nb_2O_5 , *The J. of Chemical Phys.*, 34, 3 (1961) 1022.
- [178] D. Music, R. W Geyer, Theoretical and experimental study of NbO_2 nanoslice formation, *J. Phys. D: Appl. Phys.* 48 (2015) 305302.
- [179] C. Nico, T. Monteiro, M. Graca, Niobium oxides and niobates physical properties: Review and prospects, *Prog. Mater. Sci.* 80, (2016) 1.
- [180] F. J. Wong and S. Ramanathan, Heteroepitaxy of distorted rutile-structure WO_2 and NbO_2 thin films, *J. Mater. Res.* 28, (2013) 2555.
- [181] A. Foroughi-Abari, K. C. Cadien, Growth structure and properties of sputtered niobium oxide thin films, *Thin Solid Films* 519, 3068 (2011) 73.
- [182] M. Pickett, G. Medeiros-Ribeiro, R. Williams, A scalable neuristor built with Mott memristors, *Nature Mater.* 12, (2013) 114.
- [183] R. Ohnishi, Y. Takahashi, A. Takagaki, J. Kubota, and K. Domen, Niobium Oxides as Cathode Electrocatalysts for Platinum-free Polymer Electrolyte Fuel Cells, *Chem. Lett. Vol.37*, (2008) 838-839.
- [184] L. Zhang, L. Wang, C. Holt, T. Navessin, K. Malek, M. Eikerling, D. Mitlin, Oxygen Reduction Reaction Activity and Electrochemical Stability of Thin-Film Bilayer Systems of Platinum on Niobium Oxide, *J. Phys. Chem. C* 114, (2010) 16463.
- [185] L. Zhang, L. Wang, C. Holt, B. Zahiri, Z. Li, K. Malek, T. Navessin, M. Eikerling, D. Mitlin, Highly corrosion resistant platinum–niobium oxide–carbon nanotube electrodes for the oxygen reduction in PEMfuel cells, *Energy Environ. Sci.* 5, (2012) 6156.
- [186] D. Kowalski, Y. Aoki, H. Habazaki, Characterization of amorphous anodic Nb_2O_5 nanofilm for gas sensing, *ECS Transactions*, 16 (48), (2009) 57-65.
- [187] Neil W. Ashcroft, N. David Mermin. *Solid State Physics.* (1976) Chapter 6.
- [188] B. Aktas , M. Albaskar , S. Yalcin , K. Dogru, Optical properties of soda-limesilica glasses doped with peanut shell powder. *Archives of Materials Science and Engineering Volume 82*, (2016) 57-61.
- [189] K. Fujiwara, A. Tsukazaki, Formation of distorted rutile-type NbO_2 , MoO_2 , and WO_2 films by reactive sputtering, *J. Appl. Phys.* 125, (2019) 085301.
- [190] J. M. GALLEGO AND C. B. THOMAS. PREPARATION AND CHARACTERIZATION OF THIN FILMS OF NbO_2 . *Thin Solid Films*, 98 (1982) 11-22.
- [191] Inorganic Crystal Structure Database (ICSD) using POWD-12 + + (2004).
- [192] M. Marlene, H. McMurdie, E. Evans, B. Paretzkin, H. Parker, N. Pyrras, Standard X-ray Diffraction Powder Patterns section 190 Data for 51 Substances, *Natl. Bur. Stand. (U. S.) Monogr.* 25 19, (1982) 67.
- [193] N. Terao, Structures des Oxydes de Niobium, *Jpn. J. Appl. Phys.* 2, (1963) 156.

- [194] A. Bowman, T. Wallace, J. Yarnell, R. Wenzel, The crystal structure of niobium monoxide, *Acta Crystallogr.* 21, (1966) 843.
- [195] A. Miura, T. Takei, N. Kumada, S. Wada, E. Magome, C. Moriyoshi, Y. Kuroiwa, Bonding preference of carbon, nitrogen, and oxygen in niobium-based rock-salt structures, *Inorg. Chem.* 52, (2013) 9699.
- [196] A. Bolzan, C. Fong, B. Kennedy, C. Howard, A powder neutron diffraction study of semiconducting and metallic niobium dioxide, *J. Solid State Chem.* 113, (1994) 9.
- [197] A. Magnéli, G. Andersson, G. Sundkvist, Note on the crystal structure of niobium dioxide, *Acta Chem. Scand.* 9, (1955) 1402.
- [198] A.V. Arakcheeva, V.V. Grinevich, V.F. Shamrai, M. Meyer, , G. Chapuis, KNb₄O₅F and NbO₂ crystal structures. Structural aspect of chemical decomposition of K_{2-x}Nb₄O₃(O,F)(3)F in the melt of sodium and potassium chlorides *Crystallogr. Rep.* 44, (1999) 2-7.
- [199] A. Arakcheeva, V. Grinevich, V. Shamrai, M. Meyer, Chapuis, G. Golden Book of Phase Transitions, Wroclaw 1, (2002) 1.
- [200] R. Pynn, J. D. Axe, R. Thomas, Structural distortions in the low-temperature phase of NbO₂, *Phys. Rev. B* 13, (1976) 2965.
- [201] T. Ercit, Golden Book of Phase Transitions, Wroclaw 1, (2002) 1.
- [202] T.S. Ercit, Refinement of the structure of zeta-Nb₂O₅ and its relationship to the rutile and thoreaulite structures, *Mineralogy and Petrology* 43, (1991) 217.
- [203] H. McMurdie, M. Morris, E. Evans, B. Paretzkin, W. Wong-Ng, Y. Zhang, Methods of producing standard x-ray diffraction powder patterns, *Powder Diffr.* 1, (1986) 342.
- [204] J. Waring, R. Roth, , H. J. Parker, Temperature-pressure phase relationships in niobium pentoxide, *Res. Natl. Bur. Stand., Sect. A* 77A, (1973) 705.
- [205] B. Gatehouse, A. Wadsley, The crystal structure of the high temperature form of niobium pentoxide, *Acta Crystallogr.* 17, (1964) 1545.
- [206] J. . Waldron, M. Green, D. Neumann, Structure and electronic properties of monoclinic Nb₁₂O₂₉, *J.Phys. Chem. Solids* 65, (2004) 79.
- [207] E. Clementi, D. Raimondi, W. Reinhardt, Atomic Screening Constants from SCF Functions. II. Atoms with 37 to 86 Electrons, *J. Chem. Phys.* 47, (1967) 1305.
- [208] Chapter 2. Rohlf, James William, *Modern Physics from a to Z* , Wiley, (1994).
- [209] M. Omar, *Elementary Solid State Physics*, 2nd. Edition, John Wiley and Sons Inc., New York (1975).
- [210] G. Vezzoli, S. Levy, B. Lalevic, M. Shoga, Threshold switching polycrystalline NbO₂: Decay and recovery of the on state at room and low temperatures and its relationship to trapping centers, *J. Appl.Phys.*, vol. 54, no. 10, (1983) 5828–5838.

- [211] J. Bae, I. Hwang, Y. Jeong, S. Kang, S. Hong, J. Son, J. Choi, J. Kim, J. Park, M. Seong, Q. Jia, B. Park, Coexistence of bi-stable memory and mono-stable threshold resistance switching phenomena in amorphous NbO_x films, *Appl. Phys. Lett.*, vol. 100, no. 6, (2012) 062902.
- [212] X. Liu, S. Sadaf, M. Son, J. Park, J. Shin, W. Lee, K. Seo, D. Lee, H. Hwang, Co-occurrence of threshold switching and memory switching in Pt/ NbO_x /Pt cells for crosspoint memory applications, *IEEE Electron Device Lett.*, vol. 33, no. 2, (2012) 236–238.
- [213] X. Liu, S. Sadaf, J. Park, S. Kim, E. Cha, G. Jung, D. Lee, H. Hwang, Complementary resistive switching in niobium oxidebased resistive memory devices,” *IEEE Electron Device Lett.*, vol. 34, no. 2, (2013) 235–237.
- [214] H. Philipp, L. Levinson, NbO_2 devices for subnanosecond transient protection, *J. Appl. Phys.*, vol. 50, no. 7, (1979) 4814–4822.
- [215] S. Li, X. Liu, S. Nandi, D. Venkatachalam, R. Elliman, Temperature dependence of threshold switching in NbO_x thin films, in *Proc. Optoelectron. Microelectron. Mater. Devices*, Perth, WA, Australia, (2014) 138–140.
- [216] Y. Wang, R. Comes, S. Wolf, (Member, Ieee), J. Lu (Member, IEEE), Threshold Switching Characteristics of $\text{Nb}/\text{NbO}_2/\text{TiN}$ Vertical Devices, *Journal of the Electron Devices Society* (2015).
- [217] G. Vezzoli, S. Levy, B. Lalevic, M. Shoga, Threshold switching polycrystalline NbO_2 : Decay and recovery of the on state at room and low temperatures and its relationship to trapping centers, *J. Appl. Phys.*, vol. 54, no. 10, (1983) 5828–5838.
- [218] S. Shin, T. Halpern, P. Raccach, High-speed high current field switching of NbO_2 , *J. Appl. Phys.*, vol. 48, no. 7, (1977) 3150–3153.
- [219] S. Kim, J. Park, J. Woo, C. Cho, W. Lee, J. Shin, G. Choi, S. Park, D. Lee, B. Lee, H. Hwang, Threshold-switching characteristics of a nanothin- NbO_2 -layer-based Pt/ NbO_2 /Pt stack for use in cross-point-type resistive memories, *Microelectronic Engineering* 107 (2013) 33–36.
- [220] Y. Wang, Metal-Insulator Transition in Niobium Dioxide Thin Films. A dissertation Presented to the faculty of the School of Engineering and Applied Science. University of Virginia, (2017).
- [221] C. Glassbrenner, G. Slack, Temperature dependence of thermal conductivity for high purity Si (1964).
- [222] H. Cho, G. Kimb, T. Onozato, H. Jeenc, H. Ohta, Thermal conductivity tensor of NbO_2 . *International Journal of Heat and Mass Transfer* 137, (2019) 263–267.
- [223] Abdul-Aziz, O. Musa Mohammed, A. Al-Ameer, and Fuaad Sh. Hashim. Determined the energy gap and activation energies of some transition metal complexes of liquid crystalline Schiff base, *Iraqi National J. of Chem.* 30, (2008) 323-329.
- [224] J. Hartke, The Three-Dimensional Poole-Frenkel Effect, *J. Appl. Phys.* 39, (1968) 4871.

-
- [225] P. Young, dc electrical conduction in thin Ta_2O_5 films. I. Bulk-limited conduction, *J. Appl. Phys.* 47, 235 (1976).
- [226] E. dos Santos, D. Freitas, I. Fier, J. Fernandes, M. Continentino, A. de Oliveira, L. Walmsley, Current controlled negative differential resistance behavior in $\text{Co}_2\text{FeO}_2\text{BO}_3$ and $\text{Fe}_3\text{O}_2\text{BO}_3$ single crystals, *Journal of Physics and Chemistry of Solids* 90 (2016) 65–68.